HIGH POWER PHASED ARRAY AND TAILORED GAIN SEMICONDUCTOR LASERS

Thesis by
Christopher Paul Lindsey

In Partial Fulfillment of the Requirements
for the Degree of
Doctor of Philosophy

California Institute of Technology
Pasadena, California
1987

(Submitted July 2, 1986)

Dedication

to
Yahweh

Who gave me strength
when I needed it most.

Seek first the Kingdom of Heaven and its righteousness,
and all else will be *added* unto you.

— *Matthew 6:33*

Acknowledgments

I would like to thank my advisor, Dr. Amnon Yariv, for his support of my work, and especially so during that trying period of time when more single lobed farfield patterns were coming out of the computer models of arrays than came from the devices themselves. I consider it a privilege to have been part of such an exciting, dynamic, and prolific group as his.

I would like to express my great appreciation in particular to (the future Dr.) David Mehuys. I have benefited greatly from our collaboration, and I sincerely hope that he has enjoyed learning from me as much as I have enjoyed learning from him. I wish — and expect — for him nothing but the best.

The early stages of this work were performed in collaboration with Drs. Yossi Katz, Eli Kapon, and Shlomo Margalit. I would expressly like to thank Dr. Katz for inviting me to join with him in his investigation of phased array semiconductor lasers, and to Dr. Margalit for sharing his unwavering enthusiasm and prolific outpouring of interesting ideas with me. Most of all, I am grateful to him for the constant encouragement he gave me throughout our time together at Caltech.

I would like to acknowledge many very helpful discussions I have had with Drs. Josi Salzman, Zeev Rav-Noy, Stephen Smith, Robert Lang, Kerry Valhala, T. R. Chen, Christoph Harder, and (future Drs.) Michael Mittelstein and Pamela Derry. I will miss the excitement of their company and look forward to their continued success (and perhaps collaboration with them) in future years.

A word of thanks also to my Thesis Committee, Drs. Amnon Yariv, William Bridges, William Johnson, David Rutledge, and Donald Cohen for taking the time to read and critique my work.

The ability to quickly fabricate some unusual photolithographic masks played a promenant role in several stages of this work. I would like to acknowledge and thank Drs. David Rutledge, Dean Neikirk, and Chung-En Zah for the time and effort they put into developing a very useful mask making facility.

The experimental work described in this thesis benefited greatly from the excellent and continuing efforts of Desmond Armstrong and Ali Ghaffari to improve our epitaxial growth, fabrication, and testing facilities. Lou Johnson, Norm Keidel, and Larry Begay gave excellent assistance with machine shop work, while Dana Roth was especially helpful with library matters.

A glance through this thesis will immediately reveal the importance of the assistance I have received from the computing and graphics arts departments. I would especially like to thank Albert Chang and Edith Huang at the Computing Center for continually giving me cheerful and highly competent advice. Thanks also to Glenn Gribble, Calvin Jackson, and Dave Gillespie for putting a lot of work into developing the Chipmunk TEX system which makes typesetting so easy and fun. The beautiful figures interspersed throughout this work are the talented artistry of Pat Marble, Bob Turring, Alejandro Soza, and Pat Lee. I thank them for patiently enduring the many corrections and revisions I requested.

I would also like to take a moment to thank all the many unnamed support staff, students, and faculty at Caltech who have, either directly or indirectly, made my years here more pleasant and productive.

Although a Ph. D. thesis is necessarily a technical document, in my case it would not have been possible without some outstanding support from some (relatively!) nontechnical people. I would especially like to thank our group secretary, Mrs. Jana Mercado, for her always encouraging words which helped me so much during some discouraging times.

It is not an easy thing to pursue a Ph. D. while supporting a wife and child, and there is no doubt that I could not have done so without the help of Carol Mastin and her friendly crew in the Graduate Office. I am deeply indebted (both figuratively and financially!) to them for their assistance with loans and fellowships. I would also especially like to thank the women of the ARCS Foundation for their very generous financial support during my years at Caltech, and to acknowledge research support from the Office of Naval Research, the Air Force Office of Scientific Research, the National Science Foundation, and the National Areonautics and Space Administration.

Finally, I would like to thank some very, very special people without whose behind-the-scenes support this work would not have been possible. To my parents, many thanks for nurturing my early interest in science, for their never ending support and encouragement over the years, and for giving me a "home away from home" when I needed to get away from Caltech. To that very special man, Dr. Robert Borrelli of Harvey Mudd College, I extend my great gratitude for having faith and confidence in me, and for helping me begin to "see things in the soft haze of a spring day" and to know that I could bring them to fruition.

And finally, to that most special, and most wonderful person of all, my dear wife Yvonne: how can I thank her enough for her unfailing support, encouragement, and love during what has been the most trying time of our lives together? From the bottom of my heart I extend to her my very deepest gratitude and love, and pray that God may richly reward her for her patience and perseverence.

To my son Gregory (and, someday, other children): may he come to discover, as I have, that Physics is a whole lot of fun.

Thanks to all of you for making it possible.

We grow great by dreams. All big
men are dreamers. They see things in
the soft haze of a spring day or in the
red fire of a long winter's evening.
Some of us let these great dreams die,
but others nourish and protect them,
nurse them through the bad days till they
bring them to the sunshine and light
which comes always to those who sincerely
hope that their dreams will come true.

WOODROW WILSON

Abstract

Most phase locked semiconductor laser arrays suffer from undesirable twin lobed farfield patterns, making them unsuitable for many applications. In this thesis we make a detailed theoretical and experimental study of this problem, and solve it by tailoring the spatial gain profile across the array. We demonstrate a *tailored gain chirped array* which emits $450mW$ into a single beam $3\frac{1}{2}^\circ$ wide.

Stripe geometry lasers for use in phased arrays are examined in Chapter 2, as are design considerations for evanescently coupled phased arrays. A powerful numerical method for analyzing a nearly arbitrary one-dimensional dielectric waveguide with gain and/or loss is described.

Chapter 3 analyzes in detail the simplest array of two adjacent waveguides, both real index and gain guided and both weakly and strongly coupled. Chapter 4 discusses why a uniform array has a twin lobed farfield pattern, and introduces the concept of a nonuniform real index guided *chirped array* of lasers with widths which increase monotonically across the array. Real index guided chirped arrays can, in principle, be made to lase with a single lobed farfield pattern. Since such arrays are difficult to fabricate, and will be at least partially gain guided, we concentrate on gain guided structures. The combination of gain tailoring and a high interchannel gain in a proton implanted chirped array enables us to achieve our goal of fabricating a high power array with the single lobed farfield pattern described above.

Such arrays are actually *tailored gain broad area* lasers. Chapter 5 demonstrates another method for gain tailoring, the "halftone" process, which can create nearly arbitrary *two-dimensional* spatial gain profiles in an optoelectronic device, thereby offering a new degree of freedom to the designer of semiconductor lasers.

Single lobed nearly diffraction limited beams from tailored gain broad area lasers $50\mu m$ wide are obtained.

Asymmetric tailored gain waveguides have several unusual properties. the technique of Path Analysis for analyzing these complex waveguides is introduced. Fundamental Fourier Transform relationships relating device structure to farfield patterns yield additional insights. Finally, we close with a measurement of the antiguiding parameter and briefly examine some design criteria for practical tailored gain broad area lasers.

Table of Contents

List of Figures

Chapter 1. Introduction and Overview

Chapter 2. Single Element Lasers

Chapter 3. Two Coupled Lasers

Chapter 4. Phased Array Lasers

Chapter 5. Tailored Gain Broad Area Lasers

CHAPTER
ONE
Introduction and Overview

In five minutes you will say it is all so absurdly simple.

—Sherlock Holmes, *The Adventure of the Dancing Men*
Sir Arthur Conan Doyle

§1.1 Historical Background

Laser action was first predicted by Schawlow and Townes in 1958,[1] and first observed by Maiman[2] in the ruby system in 1960. In 1962, less than 2 years later, stimulated coherent emission from semiconductor $GaAs$ $p-n$ junctions was first observed nearly simultaneously by four groups.[3–6] Within six years, lasing action had been obtained in a wide variety of semiconductor materials covering the wavelength range between 0.5μm to 20μm. Semiconductor lasers were not capable of room temperature operation until the introduction of the $GaAs/GaAlAs$ heterojunction in 1969. Continuous Wave (CW) lasing of $GaAlAs$ laser diodes at room temperatures was not achieved until 1970.[7] Since then, progress has been exceedingly rapid because of the tremendous commercial importance of semiconductor lasers as highly efficient, compact, and inexpensive light sources, particularly for use in optical fiber lightwave communication systems.

It is a tribute to modern technological research that in the fifteen or so years since the advent of the first room temperature CW laser diode, the state of the art has advanced enormously. Degradation rates of $10^{-6}hr^{-1}$ at $100°C$ temperature and extrapolated lifetime in excess of 10^7 hours at room temperature have been obtained.[8] Lasers that are capable of emitting up to $40mW$ into a stable beam with a very narrow spectral linewidth are commercially available. Semiconductor lasers are extremely efficient converters of electrical to optical energy. Differential power efficiencies of 80% have been measured,[9] and threshold currents as low as $2.5mA$ (corresponding to a power dissipation of $5mW$) have been reported.[10] Amplitude and phase fluctuations in the best laser structures have been shown to be near the quantum limit.[11]

Naturally, no one laser design is capable of simultaneously achieving all of these attributes. Since different applications require different laser characteristics, device design has been directed towards specific applications. Historically, the most important application is that of optical fiber communication. Lasers for fiber communications require high modulation bandwidths with very clean beam profiles and exceptionally pure spectral characteristics at wavelengths near the 1.5μm absorption and dispersion minimum in silica glass fibers. $GaAlAs$ lasers are unsuitable for such applications due to their relatively short $\sim 0.85\mu$m lasing wavelength, and so most lasers intended for fiber communications use the $InGaAsP$ system. As a result of having been optimized for their spectral and modulation properties, such lasers are limited to a few milliwatts of optical power output and have beamwidths between 10° and 30°.

Recently, some potentially important applications of semiconductor lasers have emerged which require substantially higher output power at $GaAs$ wavelengths. These include freespace nonfiber optical communication (*e.g.*, between satellites in space), optical disk recording, laser printing, and possibly even some medical applications. Although probably not quite as large as the market for communications lasers, these latter markets are still substantial, and interest in achieving high power output, perhaps as great as several watts, is rapidly increasing. Furthermore, it should be possible to concentrate this several watts of optical power into a single narrow beam less than a degree wide.

However, there is an upper limit on the width of conventional semiconductor lasers, and so several new approaches for achieving high power operation with narrow beams have emerged within the past few years. Two of the most promising include *unstable resonator*[12] and *phased array*[13] semiconductor lasers. The latter topic forms the subject of this thesis.

Phased array semiconductor lasers are fabricated by placing many single-element lasers close enough together so that the entire assembly acts as one unit. The first laser arrays were reported as early as 1968 by Birbeck,[14] but the impetus for their development did not really come until the team of Streifer, Scifres, and Burnham at the Xerox Corporation made some major contributions to the field.[15–18] In 1983 this group set a high power record of 2.6W CW emission from a laser diode which stood unbroken for many years.[19] In 1985, Harnagel, Scifres, *et al.* at Spectra Diode Laboratories broke the old record, reporting 5.4W of CW power from a phase locked array.[20]

Unfortunately, high power operation did not come without its price: almost all of the arrays reported to date have suffered from double lobed farfield patterns.[21,22] The two beams, typically separated by about ten degrees, make such arrays unsuitable for many applications. As a result, substantial effort has gone into understanding the source of this problem and devising methods for its elimination.

Most of the early work on phase locked arrays used *uniform arrays* of identical elements on equidistant centers. In 1984 Kapon, Katz, and Yariv at Caltech[23] introduced the concept of array supermodes, and showed that the twin lobed farfield patterns were the result of the lossy interchannel regions inherent in the design of most uniform arrays. Kapon, Lindsey, *et al.* then proposed the concept of *nonuniform* chirped arrays.[24] In mid 1984 Lindsey demonstrated the first chirped array based on this principle, which was capable of nearly diffraction limited 2° single lobed operation.[25] About one year later, in mid 1985, Welch and Scifres used a minor variation of this design, and achieved CW power outputs of about $\frac{1}{2}W$ into single lobed beams only one degree wide.[26]

More recently, there has been a renewed interest in semiconductor lasers that achieve high power, single lobed operation without resorting to either array or unstable resonator structures. In particular, in 1985, Lindsey, *et al.* showed that the nonuniform chirped array reported earlier might better be described as a broad area laser with a *nonuniform* spatial gain profile.[27] He then demonstrated a *tailored gain broad area laser* which achieved nearly diffraction limited single lobed, high power ($200mW$ into $2\frac{1}{2}°$) operation from a truly broad area laser about 50μm wide.[28,29]

The scope of this thesis therefore begins with a discussion of the reasons why a uniform array has an undesirable twin lobed farfield pattern, proposes and demonstrates nonuniform tailored gain chirped arrays, and concludes with a demonstration and analysis of tailored gain broad area lasers.

§1.2 Semiconductor Lasers

In order to achieve laser action, the three requirements, shown schematically in Figure 1.1, must be met. First, it is necessary to provide a means of exciting electrons into higher energy states more rapidly than the rate at which they decay into lower energy states. In a semiconductor laser, this is achieved by sufficiently forward biasing a $p-n$ junction in a direct band gap material such as $GaAs$.[30]

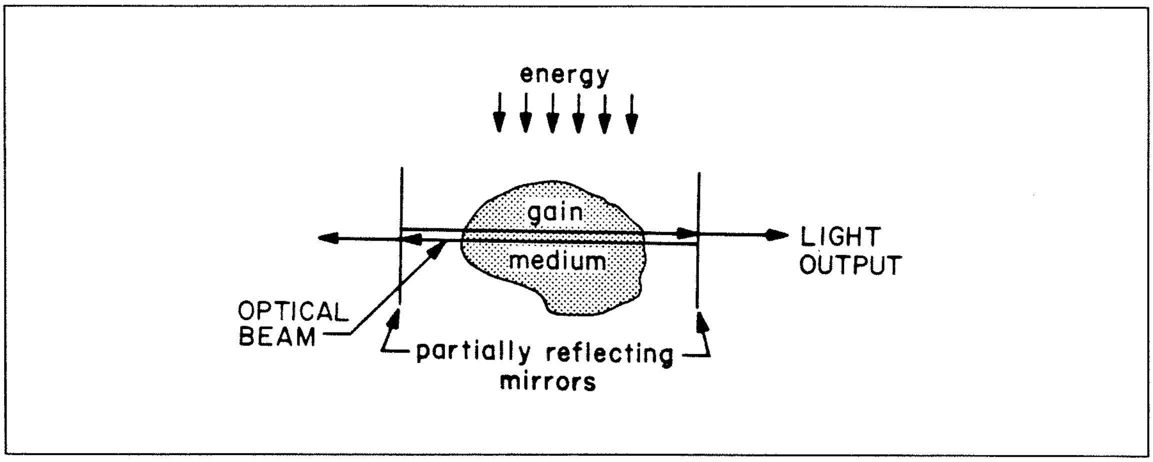

FIGURE 1.1 Requirements for laser action.

The spontaneous and stimulated recombination of the electrons and holes at the junction create photons, some of which escape the device in the form of useful light output. Secondly, provision must be made for confining the light which is generated so that the spontaneous emission rate is negligible compared to the stimulated emission rate.[31] In a $GaAs$ laser this is achieved by means of a dielectric waveguide[32] formed by a $GaAlAs/GaAs/GaAlAs$ double heterostructure. Finally, it is necessary to provide optical feedback so that a stable optical mode can build up in the device. In most semiconductor lasers, this is achieved by cleaving the semiconductor crystal to form a Fabry-Perot cavity.[33]

The $GaAlAs/GaAs/GaAlAs$ heterostructure in the vertical direction is created by sandwiching a thin (typically $\sim 0.1\mu m$) $GaAs$ active layer between two $Ga_{1-x}Al_xAs$ cladding layers where x is typically $\sim 0.2 - 0.4$. To form the $p-n$ junction the upper $GaAlAs$ layer is usually doped p type, the lower layer is n type, while the active layer is often left undoped. Figure 1.2a shows that when the $p-n$ junction is forward biased, the smaller energy band gap of $GaAs$ relative to that of $GaAlAs$ causes both electrons and holes to be confined to the thin $GaAs$ active

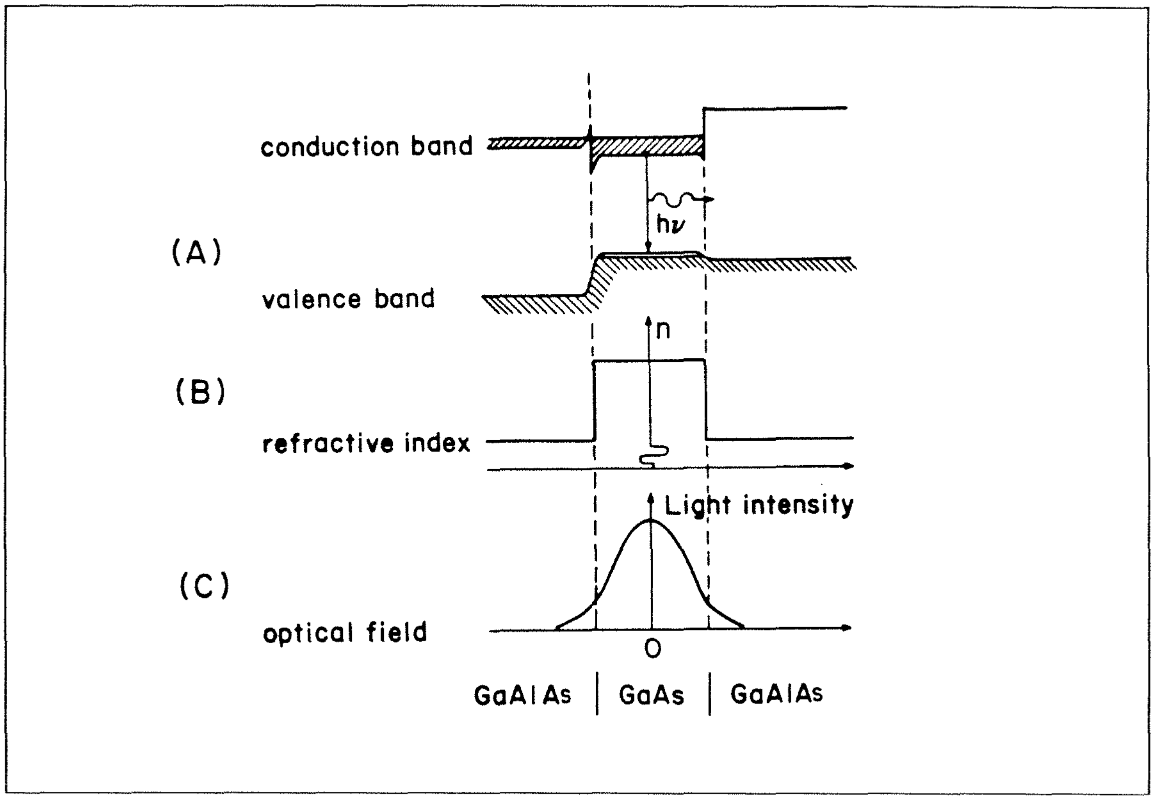

FIGURE 1.2 *GaAlAs/GaAs/GaAlAs* double heterojunction (a) band energy diagram for forward biased $p-n$ junction (b) refractive index profile (c) optical field intensity.

layer, thus leading to the very high inversion densities (*i.e.*, gain) characteristic of semiconductor lasers.

Figure 1.2b shows that since the index of refraction of the *GaAs* core region is greater than that of the *GaAlAs* cladding, the double heterojunction not only confines the carriers, but also forms a dielectric optical waveguide as well. In general, such a dielectric waveguide can guide many optical modes.[34] The shape of the optical mode is referred to as the mode's ***nearfield pattern***, while the radiation pattern that this mode makes when it emerges from the laser is referred to as the mode's ***farfield pattern.*** Almost all applications of semiconductor lasers require a clean, single lobed farfield pattern. This can be achieved by making the thickness of the *GaAs* core region small enough so that only the fundamental mode in the vertical direction will be guided. Figure 1.2c shows schematically the mode shape for the fundamental mode. We see that the optical energy is concentrated in the high gain region of the waveguide. This combination of good carrier and optical confinement makes possible the fabrication of semiconductor lasers capable of low threshold, room temperature operation.

In order to achieve low threshold currents, it is necessary to confine the carriers and optical field in the longitudinal (along the junction plane), transverse (vertical, perpendicular to the junction plane), and lateral (horizontal, parallel to the junction plane) directions. In almost all semiconductor lasers, confinement in the longitudinal direction is provided by the cleaved edge of the crystal, and in the vertical direction by the heterostructure. Almost all the variation in semiconductor laser device design results from the many techniques for providing carrier and optical confinement in the horizontal (lateral) dimension. Of particular interest to this work are the various methods of providing lateral confinement for the optical field.

(a) Uniform Gain Broad Area Lasers

The simplest laser based on these principles is the *broad area* semiconductor laser, illustrated in Figure 1.3a, which has a *uniform* lateral and longitudinal spatial gain profile. No provision for lateral optical and carrier confinement is made other than that provided by the edges of the wafer. Although such lasers have the advantages of being very easy to fabricate and are capable of high power operation, they are useless for almost all applications because, as illustrated in Figure 1.3b, they have very wide, highly irregular, and unstable farfield patterns. These undesirable farfield patterns result from two physical effects.

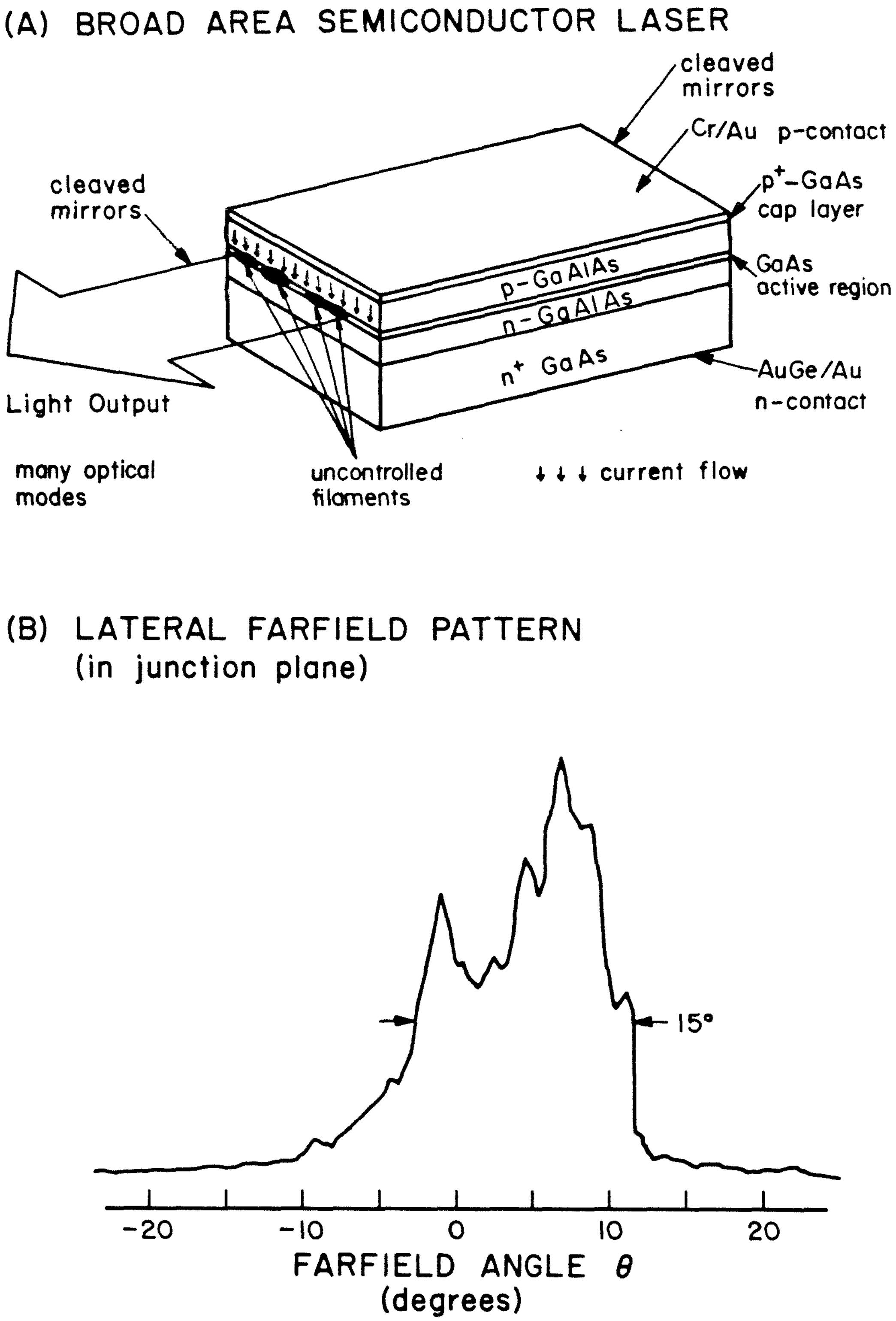

FIGURE 1.3 (a) Schematic diagram of a broad area semiconductor laser (b) typical farfield pattern for a broad area laser ~ 50μm wide. Compare with Figures 1.9 and 1.10.

<i> *The Filamentation Control Problem*

First, the presence of a nonlinear interaction between the carriers and the optical field in a conventional semiconductor laser with a uniform spatial gain profile produces *filaments*,[35] so-called because a photomicrograph of an operating device exhibits small areas of enhanced optical intensity with a filamentary structure.

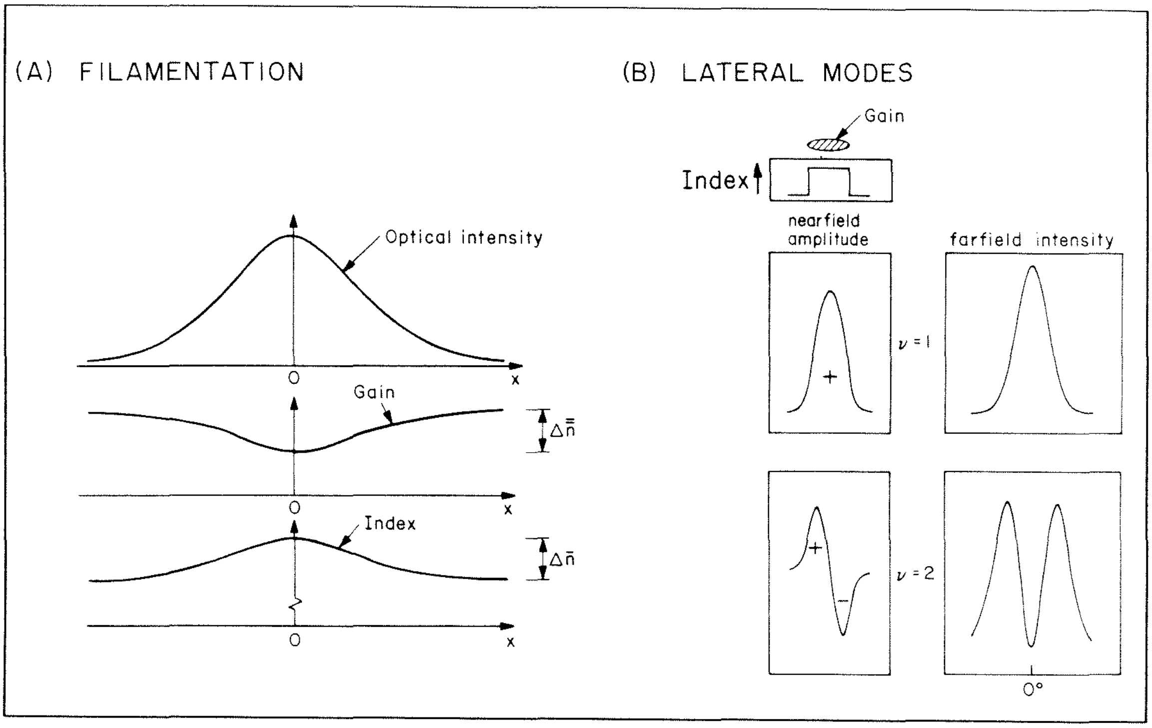

FIGURE 1.4 Problems with broad area lasers (a) filament formation (b) higher order lateral modes.

Since the real part of the refractive index is related to its imaginary part (*i.e.*, the spatial gain) through the Kramers-Kroenig[36] relationship, and also due to the free carrier plasma effect,[37] an *increase* in the gain at any point within the waveguide produces a *decrease* in the real part of the refractive index; this is referred to as the antiguiding effect.[38] Conversely, if a small localized "hot spot" of increased optical intensity should develop as a result of a fluctuation within the waveguide, the increased stimulated emission will deplete the gain,[39] thus creating an *increase* in the local index of refraction. As illustrated in Figure 1.4a, this interaction effectively forms a small waveguide 3 to 12μm wide[35] within the larger waveguide defined by the entire broad area laser.

As a result of the translational invariance within a conventional uniform gain broad area laser, the filaments become unstable and move about randomly. The complicated motions and interactions of the many filaments in a conventional uniform gain broad area laser are one cause of the poor beam quality characteristic of these devices. If a broad area laser's farfield pattern is to be improved, some method of stabilizing the filaments must be found. In conventional semiconductor lasers, this is usually achieved by making the laser's width narrow enough, typically less than at most ten to fifteen microns, so that only one filament can form.

<ii> The Lateral Mode Control Problem

The second problem that must be overcome in a broad area laser comes about because the optical field must be guided in the horizontal (lateral) direction as well as the vertical one. Since the width of a typical broad area laser is perhaps 50 to 100 times the lasing wavelength, the lateral waveguide in a broad area laser will support many *lateral* optical modes. In a conventional broad area laser in which the current injection throughout the device is *uniform*, only the lateral fundamental mode will have a predominantly single lobed farfield pattern.(§2.6) This is illustrated schematically in Figure 1.4b, which shows the waveguide model of a dielectric waveguide that supports two guided modes. (The mode shapes in a *gain guided* waveguide are very similar; see §2.6(a).) The lasing of the higher order modes thus increases the width of the farfield pattern, possibly making it multilobed. To make the laser's farfield pattern single lobed and diffraction limited (*i.e.*, as narrow as possible), the fundamental mode must be the only lasing mode. All other modes must be suppressed. This is not possible in conventional broad area lasers due to the nearly uniform spatial gain profile. Therefore, the conventional method of achieving single lobed farfield operation is to make the laser narrow enough so that the waveguide supports only the fundamental mode, making it the sole lasing mode.

(b) Single Element Stripe Geometry Lasers

We see that the twin problems of filamentation and lateral mode control may be solved by the simple expedient of limiting the width of the laser, typically to 5μm to 10μm. One type of ***stripe geometry*** laser diode is illustrated in Figure 1.5a; it is similar to the broad area semiconductor laser of Figure 1.3a except that the surface resistivity of the entire wafer has been increased everywhere but along a thin stripe by implanting high energy protons into the surface of the crystal.

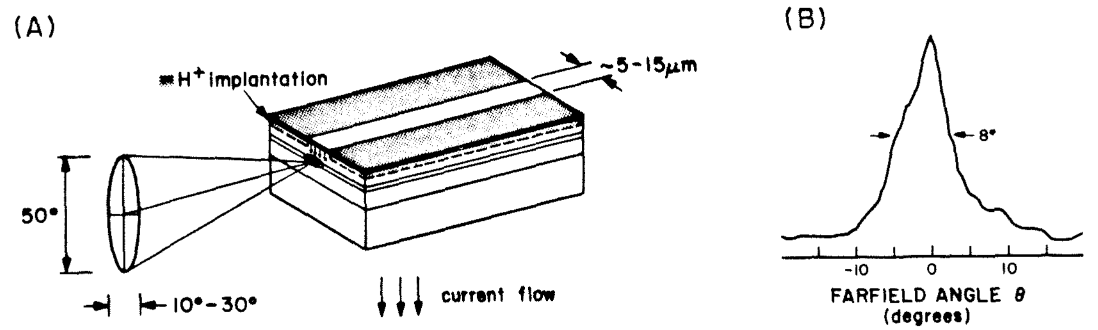

FIGURE 1.5 (a) Proton implanted stripe geometry semiconductor laser (b) typical farfield pattern for a strip geometry laser ~ 5μm wide.

Thus current is injected only into the narrow stripe. The optical field is then confined in the horizontal direction by the presence of the lossy unpumped $GaAs$ active region at the edges of the stripe.

Since unprotected $GaAlAs$ laser mirrors cannot sustain an incident power density greater than about $5MW/cm^2$ without damage,[40] limiting the width of the laser stripe also limits the laser's maximum power output to $\sim 50mW$ and, as shown in Figure 1.5b, also limits its minimum beamwidth to $\sim 10^\circ$. New semiconductor laser designs which achieve high power operation by increasing the laser's width must therefore solve both the filamentation and lateral mode control problems.

In this thesis, we are particularly interested in phased arrays of semiconductor lasers that use single-element stripe geometry lasers as building blocks to form the array. We therefore lay the groundwork for our discussion of arrays with a discussion of some simple waveguide models that describe a semiconductor laser. A waveguide in the lateral direction may be formed either by variations in the real part of the index of refraction (*real index guided*) or by variations in the spatial gain distribution (*gain guided*). We consider several classes of laser structures based on the strength of real index guiding which are candidates for use in phased arrays in §2.2. Due to some fundamental and technological constraints, practical evanescently coupled phased arrays are either gain guided or at best very weakly index guided (§2.4). However, since such structures are notoriously difficult to analyze analytically, we proceed by breaking the problem down into smaller, more manageable parts by starting with simple waveguides and gradually working towards more complicated structures.

In §2.6 we briefly review the properties of the simplest of all possible dielectric waveguides, the symmetric three layer slab structure which forms the basic building block we will use throughout this thesis. Although other, more accurate modes for gain guided lasers have been introduced,[38,41] this simple "box" waveguide has the great advantage that it may be used to display the essential physics without undue mathematical and computational complexity. Many of the other types of waveguides we will encounter have such complicated refractive index and gain profiles that their analytical analysis becomes intractable. We therefore introduce some very simple yet powerful numerical methods for finding the optical modes of a nearly arbitrary waveguide in §2.7, and make extensive use of these methods in Chapters 3 and 4.

(c) Phased Array Lasers

As noted in §1.1, one promising method of achieving high power semiconductor laser operation is to place many lasers in close proximity so that their optical fields overlap sufficiently to bring about "phase locking." In a phase locked array, the optical fields of each laser add coherently, thus potentially providing the dual benefits of high power and narrow beamwidth operation.

Figure 1.6a&b shows the simplest example of a phased array semiconductor laser, the ***uniform array***, which is formed by placing several identical lasers on uniformly spaced centers. Increasing the number of lasing elements obviously will increase the optical power output, and will also *decrease* the beam angle into which it is emitted because of the inverse relationship between the width of the nearfield and farfield patterns.[42,43] In such *phase locked semiconductor laser arrays* the filamentation problem has been solved by confining the filaments within the individual laser channels that comprise the array.

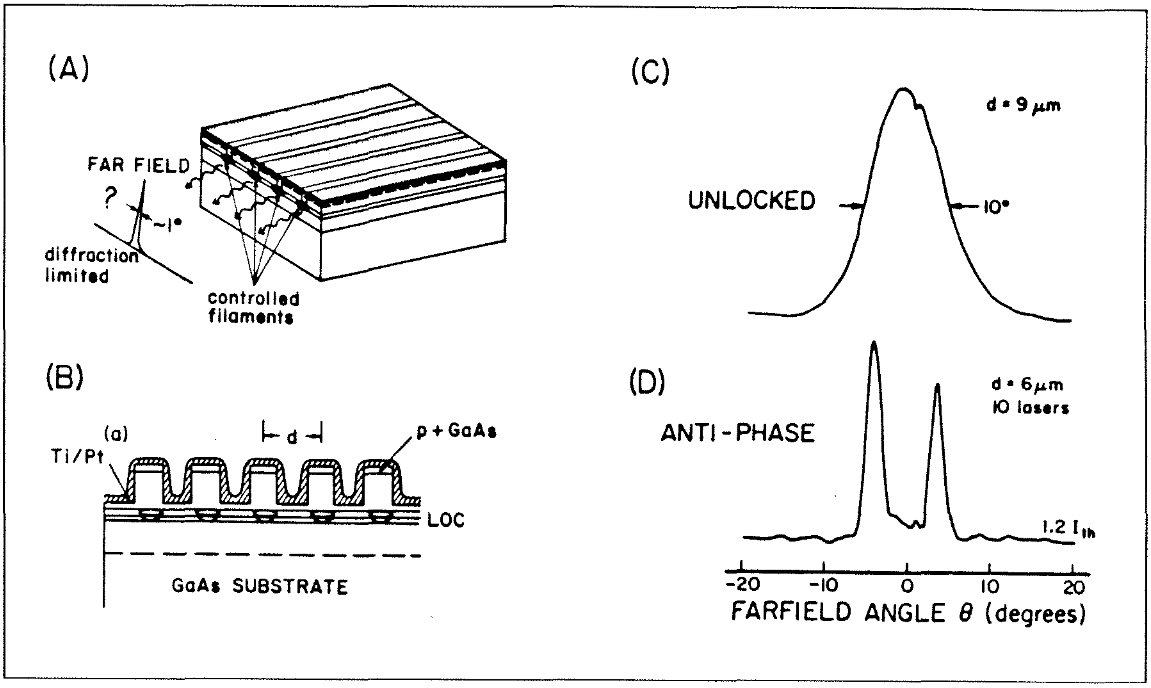

FIGURE 1.6 Uniform array of semiconductor lasers (a) proton implanted (b) air ridge (mesa stripe). Problems with phased arrays (c) not phase locked (wide farfield pattern) (d) anti-phase operation (twin lobed farfield pattern).

However, most uniform arrays suffer from a fundamental problem that makes them unsuitable for many applications. Figure 1.6c&d illustrates the two difficulties with the uniform array that motivated the work described in this thesis. First, Figure 1.6c shows that, if the laser elements comprising the array are too far apart, the lasers do not lock in phase and the optical fields add incoherently.[44,45] The emitted beam then has the same width as that of an individual laser. This implies that the laser elements must be more closely spaced. Second, if the spacing between the elements is decreased, the lasers lock in phase (as evidenced by the narrower beam and deep minima between them in Figure 1.6d), but the farfield pattern is now *twin lobed.* These undesirable twin lobed farfield patterns have been found in uniform arrays with a wide variety of single-element laser designs, and thus appears to be a property of the uniform array structure itself and not of the individual lasers. Understanding the cause of this problem and demonstrating a method of eliminating it form the core of this thesis.

Comparison of the uniform array's experimental farfield pattern of Figure 1.6d and the $\nu = 2$ theoretical farfield pattern of Figure 1.4b suggests that the twin lobed farfield pattern may be due to a high order lateral waveguide mode. We are therefore led to consider waveguiding properties of arrays of box waveguides. One of the very simplest possible arrays consists of two box waveguides placed sufficiently close so that their evanescent fields overlap and the lasers phase-lock. The detailed analytic study of these coupled waveguides forms the subject of Chapter 3. Weakly coupled real index guided waveguides are studied with the help of coupled mode theory in §3.1, while strongly coupled waveguides are considered in §3.2. Coupled mode theory predicts that if the two individual waveguides are single mode, then the composite system will support two "supermodes."[23] In §3.2(a) we find (and explain) the interesting result that when the spatial overlap between the elemental fields becomes large, one of these supermodes disappears, leaving only a new single mode system.

Central to the understanding of systems of coupled waveguides is the concept of the *phase matching wavelength*.(§3.1) From the point of phased array semiconductor laser design, the primary significance of the phase matching wavelength is that at this wavelength equal power flows in each waveguide (*i.e.*, the *admixture factor* is unity). In §3.3 we show that not all coupled waveguides will have a phase matching wavelength, and in §3.1(a) we present a simple method of designing a two waveguide system around a predetermined phase matching wavelength (*e.g.*, the peak in the spectral gain curve of $GaAs$).[46,47]

§1.2(c) Phased Array Lasers

Coupling between two waveguides is illustrated in Figure 1.7. Figure 1.7a shows the nearfield and farfield patterns for two closely spaced identical real index waveguides —*i.e.*, a two-element uniform array. We find that if we assume that each of the individual waveguide channels supports only the fundamental mode, the composite structure supports two supermodes which we label the $\nu = 1$ (++) and $\nu = 2$ (+−) supermodes, where (++) refers to the inphase addition of the individual modes and (+−) refers to antiphase addition. Notice that if the gain is concentrated in the core regions (as indicated by the hatched ovals), the interchannel region between the waveguides is relatively lossy.

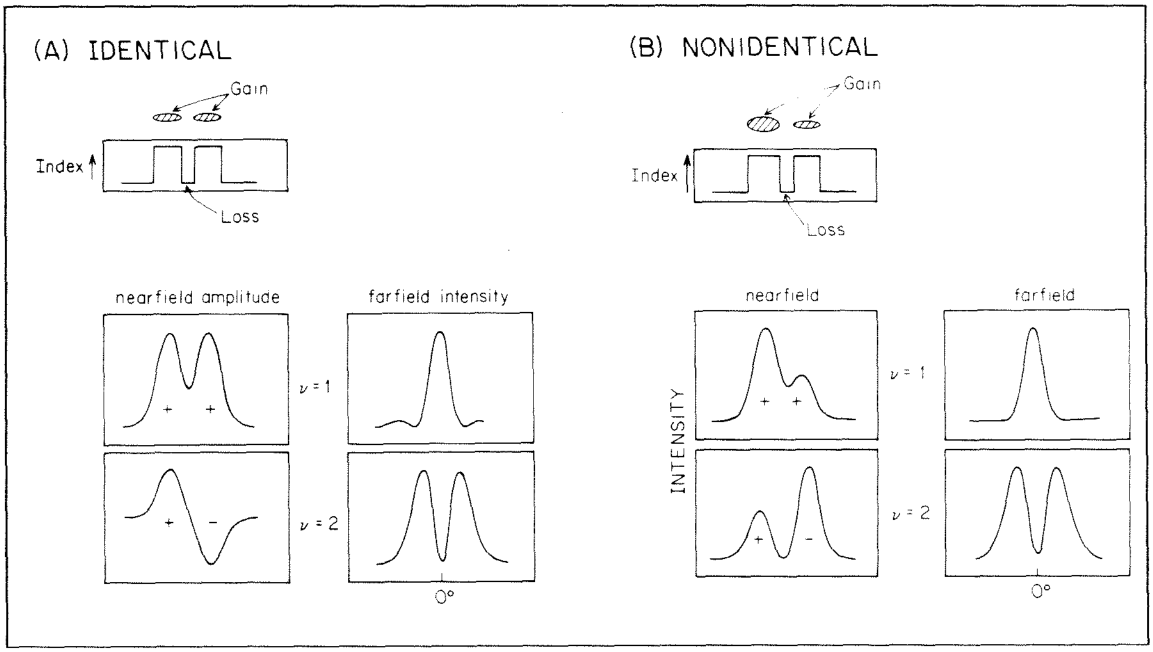

FIGURE 1.7 (a) Supermodes of two identical coupled waveguides. The lossy interchannel region causes the high order (+−) supermode to lase, leading to a twin lobed farfield pattern. (b) Supermodes of two nonidentical coupled waveguides. Greater gain in the left channel than in the right one favors the fundamental (++) supermode, potentially leading to a single lobed farfield pattern.

Since the twin lobed $(+-)$ supermode has a null in the lossy interchannel region, it will be relatively more concentrated in the high gain channel regions than will the single lobed $(++)$ mode; it therefore will be amplified more as it travels down the guide (*i.e.*, it has a higher modal gain) because it is attenuated less by the lossy interchannel regions. The mode with the highest modal gain will be the lasing mode at threshold, and thus near threshold, the farfield pattern will be twin lobed. The above threshold behavior is very complicated, and must be solved using the rate equations.[48] This latter topic is beyond the scope of this work.

We find it interesting to note that the very feature which makes good single lasers with low threshold currents (*i.e.*, placing the gain where the light intensity is greatest) is the very cause of the undesirable twin lobed farfield patterns in a uniform array.

Figure 1.7b shows the supermodes for two phase mismatched *nonidentical* waveguides which have the same index step but *different widths.* As before, we have a $(++)$ and $(+-)$ supermode with single and double lobed farfield patterns respectively, but now we notice a difference between the $(++)$ and $(+-)$ supermode: the $(++)$ supermode is more concentrated in the *wider* guide, while the $(+-)$ supermode is more concentrated in the *narrower* guide.(§3.3) Thus, if it were possible to have more gain in the wider laser than in the narrower (as indicated by the differently sized hatched ovals), the $(++)$ supermode should have the greatest overlap with the gain distribution, and would then be the lasing mode — leading to a single- lobed farfield pattern.

Although the presence of gain has been indicated only schematically in Figure 1.7, we are able to examine its effects on the admixture factor for both weakly and strongly coupled waveguides. For the weakly coupled case (§3.4), the major effect is that if the gain mismatch between the two waveguides is sufficient, equal power will *never* flow in each waveguide, even at the phase matching wavelength. For the case of two strongly coupled gain induced waveguides (§3.5), we find the surprising and unexpected result that while we might expect to find either one or two supermodes for two coupled single mode waveguides, we actually find *four*. We discuss this interesting result in terms of gain guided "leaky" modes in §3.5(b) and the special nature of the complex coupling between two gain guided lasers in §3.5(c).

In Chapter 4 we utilize the ideas of Chapter 3 in our quest to design and fabricate a phase locked array with a single lobed farfield pattern by using a *nonuniform* array structure based on the idea of Figure 1.7b. Chapter 4 tells how the actual implementation of these ideas into a working device came to resemble a rather exciting detective story which starts with the single clue of two phase mismatched waveguides, and evolves as we work out its extension to more elements, discover the limitations of the theoretical results of Chapter 3, modify our ideas, and try again — and again... until we finally arrive at a working device. Along the way, we will also discuss a variety of waveguides relevant to phased array lasers so that the reader will emerge (we hope) with a good understanding of the lateral mode control problem in evanescently coupled phased array semiconductor lasers.

We start our discussion of multi-element arrays by considering a uniform array in §4.1 and real index guided nonuniform chirped arrays in §4.2.

Figure 1.8a shows the nearfield patterns for a five-element uniform array. Notice that the envelope function (shown by the dashed line) for the $\nu = 1$ $(+++++)$ supermode is identical to that of the $\nu = 5$ $(+-+-+)$ supermode, and as in the case of the two-element laser, the two modes differ only in the lossy interchannel

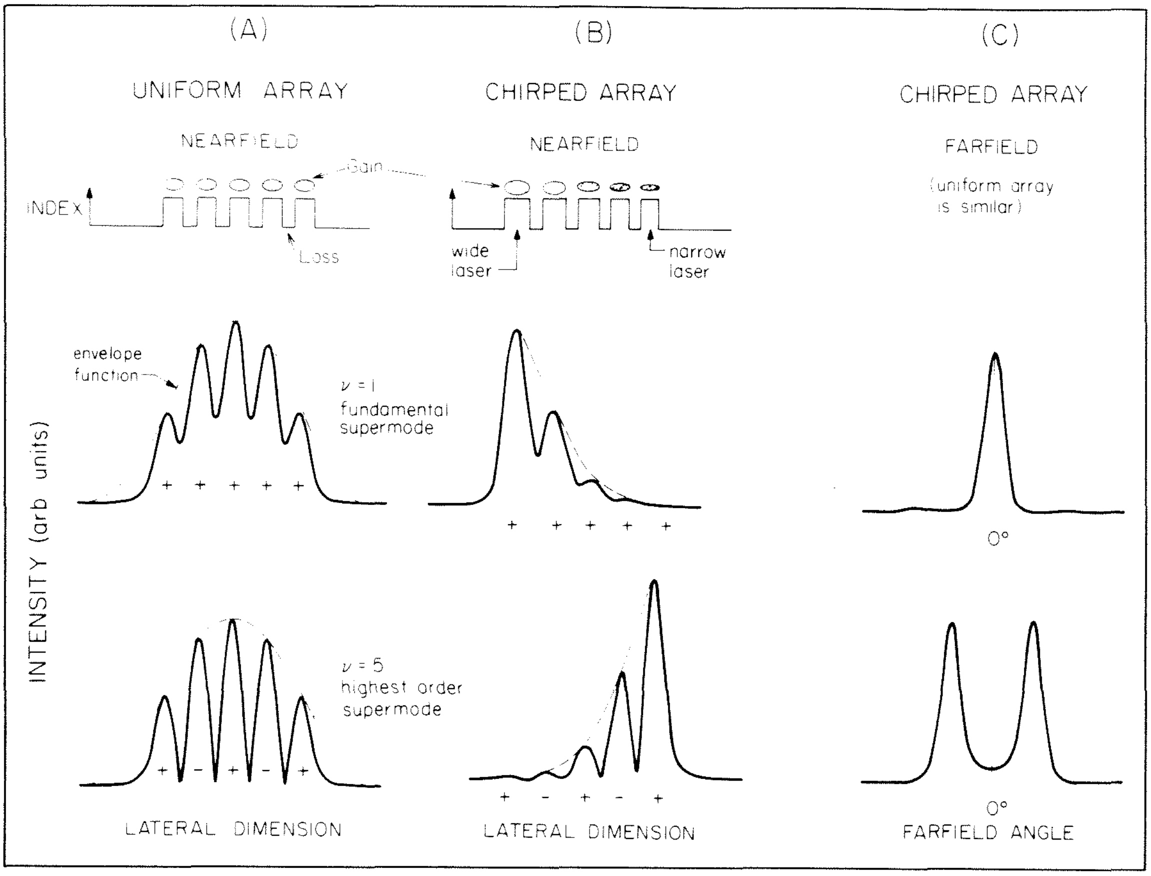

FIGURE 1.8 Supermodes of real index guided arrays (a) uniform array (b) chirped array (c) farfield patterns for the chirped array. (The farfield pattern for the uniform array is very similar.)

region, thus implying that the twin lobed $\nu = 5$ supermode will be the lasing mode. This explains the twin lobed farfield patterns of the uniform array of Figure 1.6c.

Figure 1.8b shows the nearfield pattern for a nonuniform *chirped array* in which the width of the laser waveguides decrease linearly from left to right. Now we observe a great change in the envelope functions of the fundamental $\nu = 1$ and highest order antisymmetric $\nu = 5$ supermodes: the fundamental supermode is localized at one side of the laser, while the highest order antisymmetric supermode is localized at the other. If it were possible to tailor the spatial gain profile to have approximately the same shape as the fundamental supermode, that mode would become the lasing mode because it best utilizes the available gain, thus yielding an array with the desired single lobed farfield pattern.

Prior to this work, there was no known way to easily tailor the spatial gain profile within a semiconductor laser array without using complicated multilevel metallizations.[49] The invention of two different methods for easily achieving such gain tailoring in §4.5(a) and §5.2 forms one of the major contributions of this thesis.

Although we have described the concept of a nonuniform array in terms of a real index guided structure, in §4.2(a) we show that a real index guided chirped array suffers from some fundamental and technological limitations which make its fabrication exceedingly difficult, if not impossible. Consequently, towards the end of Chapter 4 we turn our attention to arrays of nonuniform *gain guided* lasers and discover that gain tailoring may be easily achieved in a chirped array of proton implanted lasers.(§4.5(a)) We are thus led to the concept of the *tailored gain chirped array* presented in Figure 1.9. However, as shown in Figure 1.9a, in order to achieve the desired single lobed farfield pattern, it is necessary to make the interchannel gain so large that the coupling between the array elements becomes so strong that the distinction between an array and broad area laser becomes blurred.(§4.5(b),4.6) Figure 1.9b demonstrates a tailored gain chirped array with a 1.5° wide single lobed diffraction limited beam; other devices were capable of high power ($450mW$ into $3\frac{1}{2}°$) essentially single lobed operation.(§4.5(b))

We have therefore achieved our goal of demonstrating a semiconductor laser array capable of single lobed high power operation.

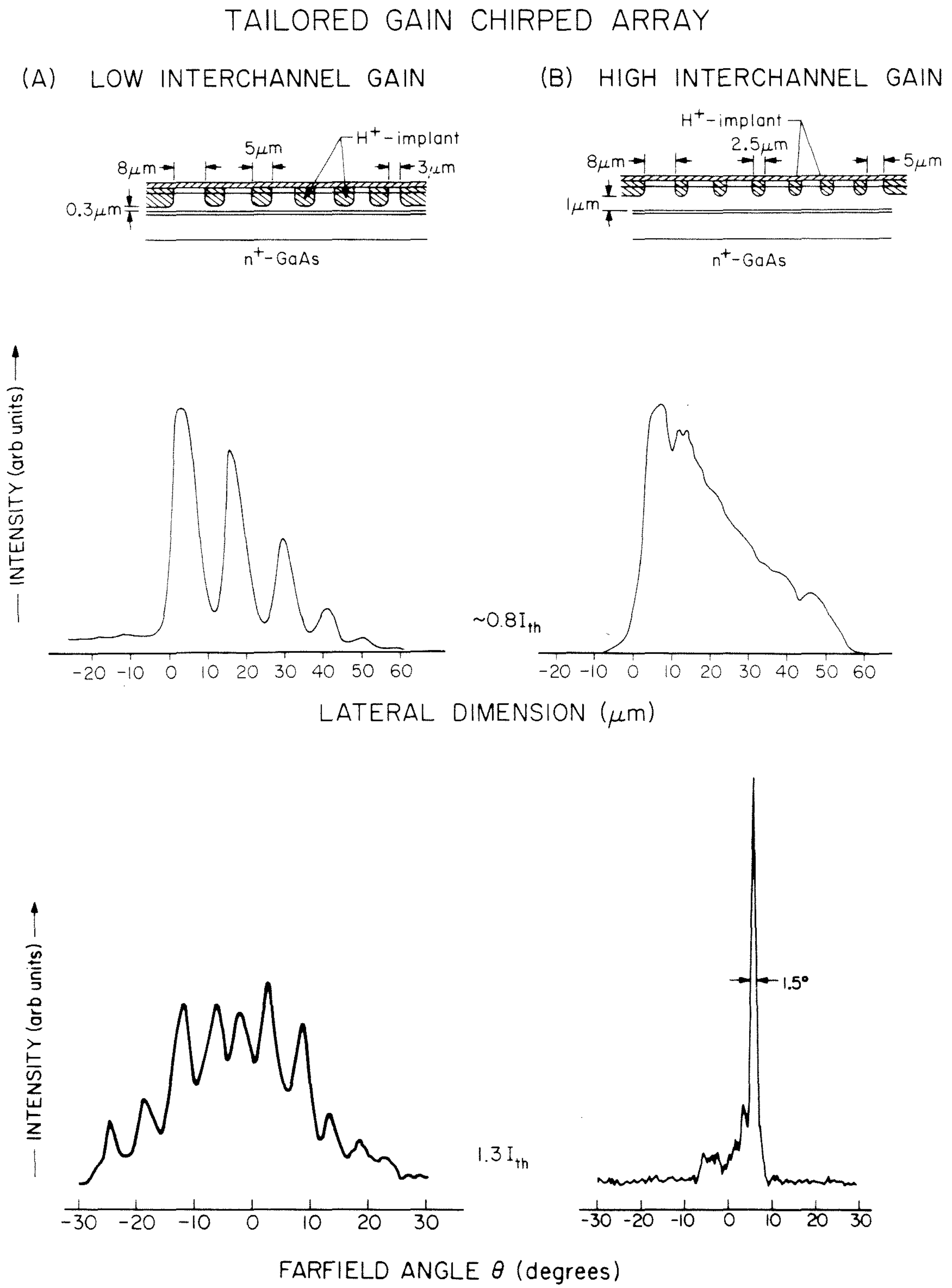

FIGURE 1.9 Tailored gain chirped array with (a) low interchannel gain (b) high interchannel gain, showing diffraction limited single lobed farfield operation.

(d) Tailored Gain Broad Area Lasers

It is interesting to note that although the schematic diagram of the strongly coupled tailored gain phased "array" of Figure 1.9b superficially resembles an array, examination of its gain profile via the spontaneous emission pattern below threshold reveals that the effect of the array has been nearly, if not completely, obliterated by current spreading in the upper cladding layer between the channels. Therefore, in §4.6 we consider whether or not it is actually more proper to refer to such a device as a tailored gain *broad area* laser rather than as an array.

However, it is possible that, despite the beneficial effects of the gain tailoring, the improved performance was due to some residual effect of the array structure. In Chapter 5 we propose, demonstrate, and analyze a very versatile innovation, referred to as the "halftone process," for achieving nearly arbitrary *two-dimensional* spatial gain profiles within an optoelectronic device such as a broad area semiconductor laser and use it to fabricate an entirely new type of semiconductor laser, a *tailored gain broad area laser*, in which all traces of the array structure have been removed.$^{(\S 5.2)}$ This laser is illustrated in Figure 1.10a. The various sized black dots represent areas on the surface of the laser where current is injected, while the white regions represent insulating regions.$^{(\S 2.2(e))}$ As may be seen from this figure, the fractional surface coverage of the injecting contact decreases approximately linearly across the laser, and so, to a first approximation, does the injected current density and hence spatial gain profile. This is confirmed by a plot of the nearly linear, highly asymmetric spontaneous emission pattern below threshold in Figure 1.10b. Figure 1.10c presents the single lobed farfield pattern of this laser which was nearly 50μm wide and emitted 200mW into 2.3°.

Chapter 5 also contains a discussion of the optical modes of a linear asymmetric tailored gain waveguide. We introduce the method of Path Analysis[29] for

§1.2(d) Tailored Gain Broad Area Lasers

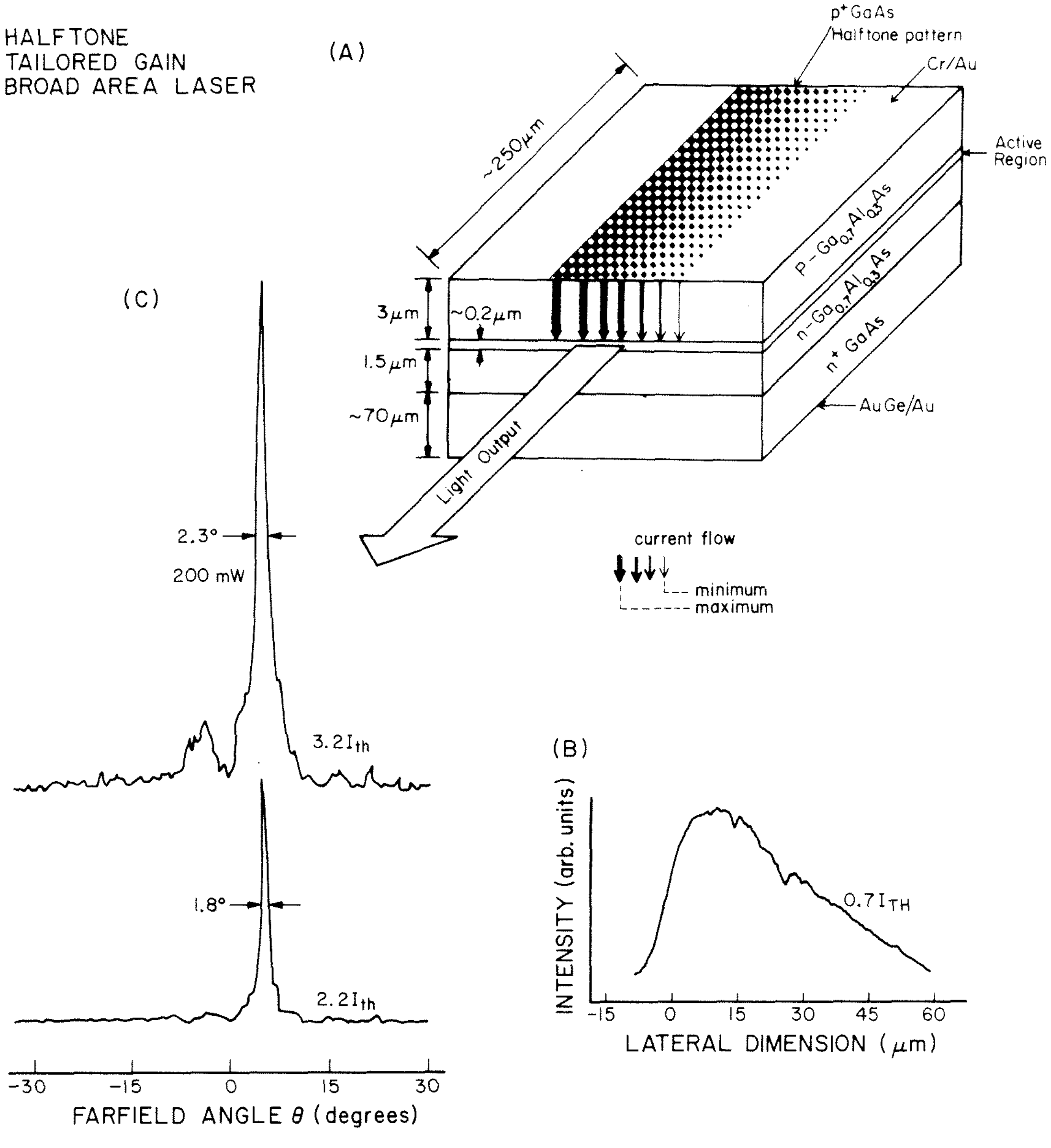

FIGURE 1.10 Halftone tailored gain broad area laser (a) schematic plan view (b) spontaneous emission below threshold showing asymmetric linear spatial gain profile (c) farfield pattern, showing high power single lobed farfield operation.

analyzing nonuniform gain induced waveguides which greatly eases the analysis of these structures, and makes possible the calculation of many waveguide properties using only simple algebraic and geometric arguments.(§2.6(c),5.4,5.8) We find that the modes of asymmetric tailored gain broad area lasers have several very interesting properties. First, the mode discrimination (*i.e.*, difference in the modal gains) between the fundamental and other higher order modes is much better than it is in a uniform gain waveguide.(§5.6) Second, it is well known that symmetric waveguides and real index waveguides have higher order modes with *nulls* in the nearfield patterns.(§4.2) This is not true for asymmetric tailored gain waveguides. The nearfield patterns of the modes of this latter structure all null-less.(§5.10) Finally, the higher order modes of either symmetric or real index guided waveguides have *multilobed* farfield patterns,(§4.2) while *all* of the modes of a linear asymmetric tailored gain waveguide have *single lobed* farfield patterns.(§5.11) We show that these unusual properties result from the complex nature of the electric field made possible by gain guiding and the lack of left-right inversion symmetry in the asymmetric tailored gain structures.(§5.12) We then discuss the effect of these unusual properties on device design, and briefly present some of the engineering tradeoffs involved in designing tailored gain broad area lasers.(§5.14)

In this work, we consider only asymmetric tailored gain waveguides for two reasons. First, although higher powers may, in principle, be obtained from a symmetric structure with twice the width of an asymmetric one, the available experimental evidence suggests that asymmetric structures show better single lobed farfield operation at higher powers than do their symmetric counterparts.[50]Second, asymmetric gain induced waveguides have properties very different from other, more commonly known, structures. We therefore concentrate on asymmetric structures, and remark that the extension of this work to symmetric waveguides is straightforward.

§1.3 Applications and Future Extensions of This Work

Halftone tailored gain broad area lasers are very simple to fabricate, and are thus well suited to large scale processing techniques. We anticipate that they may find application wherever high power single lobe operation of a laser is desired, provided that the lack of spectral purity associated with gain guided lasers is not objectionable.

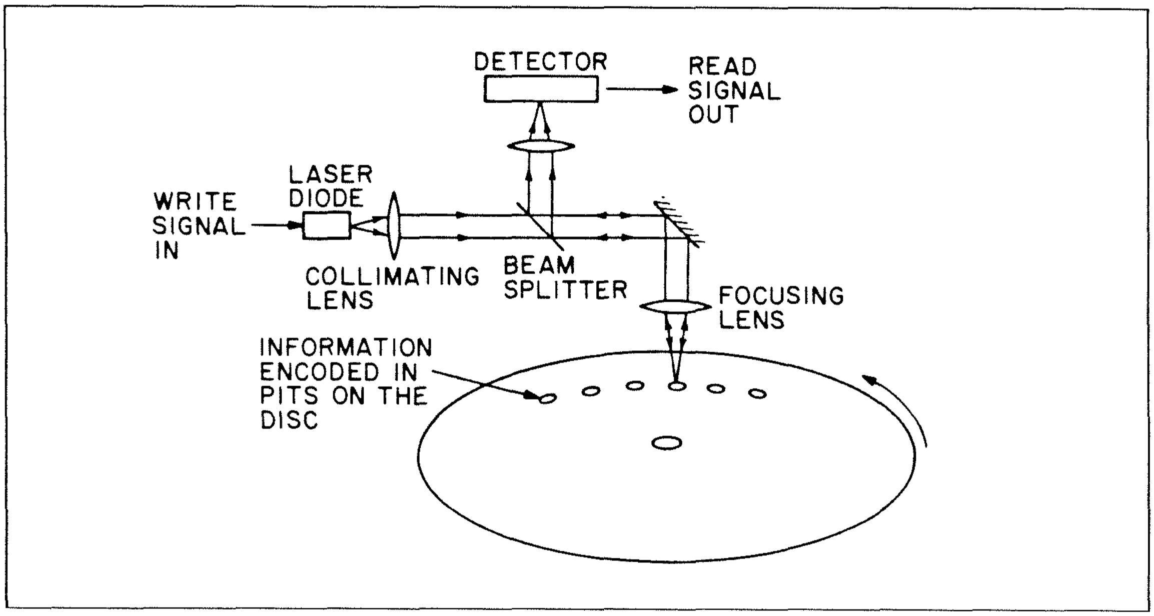

FIGURE 1.11 Optical recording.

Figure 1.11 shows a possible application of asymmetric tailored gain broad area lasers to optical data recording. A semiconductor laser and detector is used to measure the amount of light reflected from microscopic pits on the surface of the disc. In optical data recording, it is necessary to steer the laser beam to the correct track on the optical disc. A closed loop servo mechanism is used to insure that the optical beam will stay centered on the track even if it is not exactly concentric with the axis of rotation. Conventionally, this is done using electromechanical techniques. Figure 1.12 shows how the beam emission angle from an asymmetric tailored gain broad area laser depends on the value of the spatial gain gradient. However, it should be possible to utilize asymmetric tailored gain broad area lasers to *electronically* steer the laser beam onto a track much more rapidly than with conventional electromechanical methods.

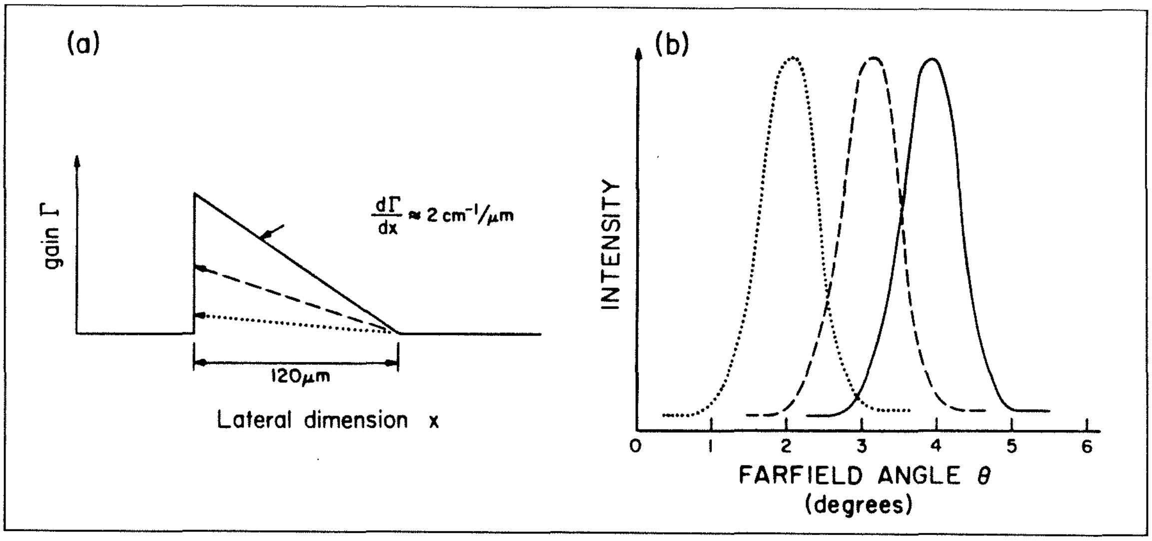

FIGURE 1.12 (a) Tailored gain broad area waveguides with varying gain gradients (b) farfield patterns showing potential for beam steering.

Although electromechanical methods would probably still be required for gross positioning of the beam, the ability to rapidly adjust the precise position of the beam, combined with the high power output of a tailored gain broad area laser, could potentially increase the optical bandwidth of the unit. Thus, we anticipate that asymmetric tailored gain broad area lasers merit further development work.

§1.4 Conclusion

In conclusion, we have come full circle. We started by stating that a uniform gain *broad area laser* was unsuitable for many applications due to the filamentation and lateral mode control problems. The filamentation problem was solved by using an array structure, while the lateral mode control problem was solved by introducing gain tailoring. However, we discovered that in order to make gain tailoring work, it was necessary to increase the interchannel gain to the point where the device resembled a broad area laser more than it did an array. We then demonstrated a tailored gain *broad area laser* (!) which is capable of single lobed, high power operation.

It is interesting to note that, although we began by assuming that an array was necessary for high power operation, we have found that the introduction of gain tailoring makes the array structure superfluous. In fact (as we will show in §4.5(b)), it may be that since the modulation of the laser's nearfield pattern introduced by the array structure increases the power present in the sidelobes and decreases the ability of the device to operate in a phase locked mode, it may well be advantageous to consider other structures which resemble broad area lasers more than they do arrays of individual lasers. In particular, it would be very interesting to combine the present work with gain tailoring with new methods of tailoring the *real* part of the refractive index to create *tailored index tailored gain* broad area lasers that would potentially combine some of the benefits of both real index and tailored gain structures. Furthermore, in one sense what we have done in this thesis is essentially to redefine the maximum upper width of a semiconductor laser from $10\mu\text{m} - 15\mu\text{m}$ to perhaps $60\mu\text{m} - 100\mu\text{m}$. One might then speculate about the possibility of creating *arrays* of *broad area* semiconductor lasers!

However, one crucial question remains unanswered: what is the role of filamentation in a tailored gain broad area laser? Do filaments exist at all, and if so, why don't they degrade device performance? Unfortunately, the resolution of these exceedingly interesting questions are beyond the scope of this thesis.

Finally, Figure 1.13 presents an overall flow chart for the work of this thesis and for some possible future extensions.

§1.5 Conventions Used Throughout This Thesis; References

Here we summarize conventions used throughout this thesis.

(1) The real part of a complex quantity q will be denoted by either $\bar{q}$ or $\Re e\{q\}$; the imaginary part will be denoted by either $\bar{\bar{q}}$, by $\Im m\{q\}$, or by a different symbol. Since the symbol x is used to denote the lateral dimension along a waveguide or laser, we will refer to the real axis of the complex z−plane as the ξ axis.

(2) A plane wave moving in the $+z$ direction is denoted by $e^{i(\beta z-\omega t)}$, where β is the propagation constant and ω is the free space radian frequency of the wave. N.B.: some authors, [40] for example, use $e^{-i(\beta z-\omega t)}$ to represent the same wave. See §2.6 for a brief discussion of this difference.

(3) When we make a waveguide model of a gain guided laser, we assume a loss in the unpumped $GaAs$ active region of 200cm^{-1}.$^{(\S 5.13)}$ The peak gain within the waveguide is set by the requirement that at threshold the power modal gain γ exactly equal the mirror losses, which we assume to be 40cm^{-1} for a device 250μm long.[51] Unless we are attempting to model an actual device, we will ignore the effect of the antiguiding parameter b. This parameter relates the decrease in the real part of the refractive index due to the presence of

§1.4 Conclusion

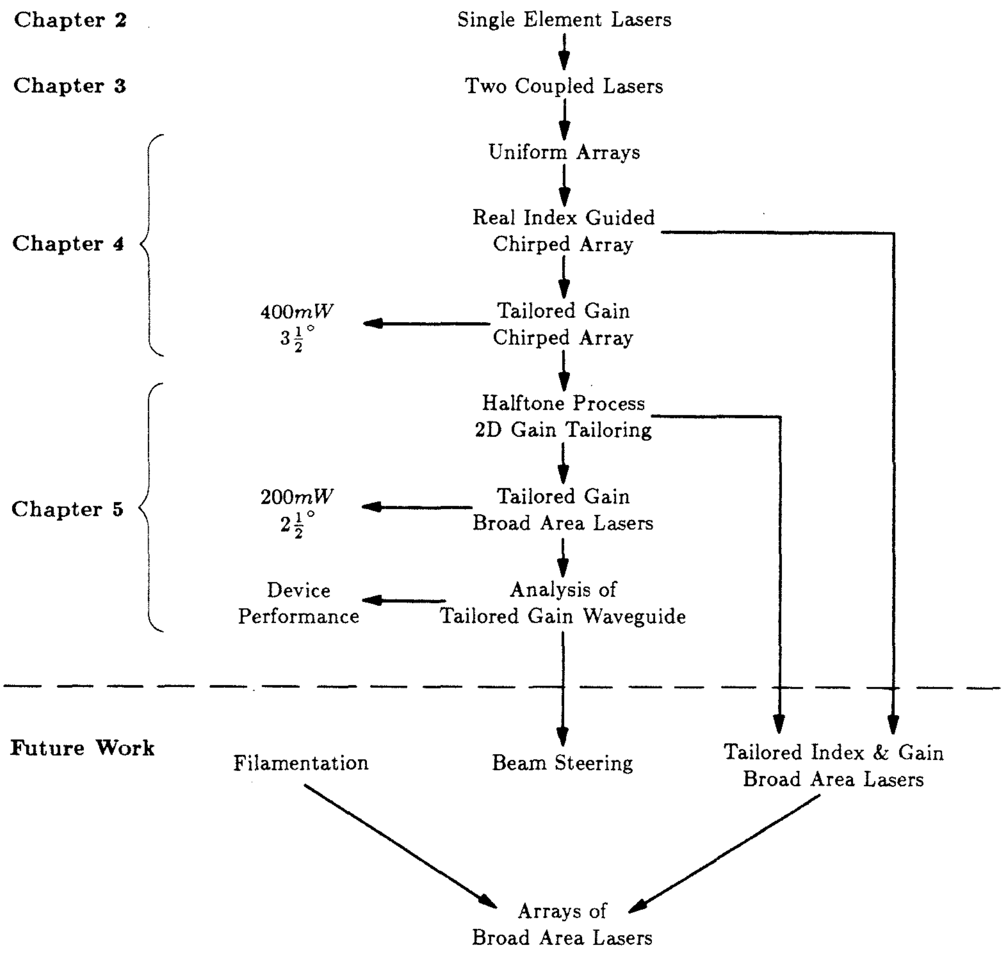

FIGURE 1.13 Flowchart for work described in this thesis.

gain. When it is included, we use a value $b \equiv \frac{\Delta \bar{n}}{\Delta \bar{\bar{n}}} = 3.0$.[52] The $e^{i\beta z}$ convention described above implies that $b > 0$.

(4) Unless otherwise noted, the figures plot intensity nearfield and farfield patterns. The phase plots for gain guided modes are in radian units. In order to simplify the labeling of the axes, $3.41^{0\ 1\ 2 \cdots}$ is used to represent 3.410, 3.411, 3.412, etc.

Throughout this work, a familiarity with the fundamentals of laser theory, and of that of semiconductor lasers in particular, is assumed. An excellent elementary treatment of both topics may be found in the book by Yariv,[33] while more advanced treatments may be found in the comprehensive works by Yariv,[31] Casey and Panish,[40] Kressel and Butler,[53] and Thompson.[34] An elementary knowledge of waveguiding in dielectric media is also assumed. Tamir[32] provides a good introduction to waveguiding in real index media as well as to the field of integrated optics. Marcuse[54,55] gives an advanced treatment of (mostly) real index guided waveguides, with particular applications to optical fibers. A good introductory article on semiconductor lasers is that by Panish,[56] and a reasonably complete review of recent advances in phased arrays has been published by Botez and Ackley.[13]

Finally, while each chapter in this thesis leads naturally into the next, the extensive cross-referencing should make it possible to read each chapter independently of the others.

CHAPTER TWO

Single-Element Stripe Geometry Lasers

'Excellent!' I cried. 'Elementary,' said he

—Sherlock Holmes, *The Adventure of the Crooked Man*
Sir Arthur Conan Doyle

§2.1 Introduction

Before considering arrays of semiconductor lasers, in §2.2 we review several classes of single-element stripe geometry lasers which are potentially suitable for use in phased arrays. These include strongly index guided structures such as the buried heterostructure (§2.2(a)) and buried crescent lasers (§2.2(b)), buried ridge (§2.2(c)) and air ridge (mesa stripe) lasers (§2.2(d)), and two types of gain guided lasers, proton implanted and Schottky isolated (§2.2(e)). We find that technological limitations make fabrication of strongly index guided lasers such as the buried heterostructure unsuitable for use in evanescently coupled phased arrays, so we next consider weakly index guided ridge structures. These latter structures are really neither entirely gain nor index guided; we briefly examine the interplay between gain and real index guiding in §2.3. Finally, we summarize this information by discussing some design considerations for evanescently coupled phased arrays in §2.4.

In §2.5 and §2.6 we summarize the properties of the simplest possible optical model for a single-element laser, that of the symmetric three layer "box" waveguide which forms the basic building block for all of our subsequent work. Finally, in

§2.7 we describe a powerful numerical method for finding the modes of a one-dimensional waveguide with a nearly arbitrary index and gain profile; we will make extensive use of a computer program based on this technique to check the validity of the analytical results of Chapter 3 and also to analyze the complicated array waveguides of Chapter 4.

§2.2 Semiconductor Lasers for Use in Phased Arrays

While almost all semiconductor lasers utilize a double heterostructure to achieve carrier and optical confinement in the vertical direction(§1.2), the variety of methods of achieving carrier and optical confinement in the horizontal (lateral) dimension is almost unlimited. We consider three broad classes of semiconductor lasers which are potentially suitable for use in phased arrays: material index guided, effective index guided, and gain guided. The primary difference between these types of lasers is the strength of the index of refraction difference between the core and cladding regions which form the waveguide.

The index of refraction $\bar{n}$ of $GaAs$ is 3.59, while that of $Ga_{1-x}Al_xAs$ is approximately given by[1] $\bar{n} = 3.590 - 0.710x + 0.91x^2$. Due to the possibility of nonradiative recombination in $Ga_{1-x}Al_xAs$ with $x > 0.45$,[2]the mole fraction of aluminum is usually limited to $x \leq 0.4$. Thus, maximum feasible index step for the $GaAs/GaAlAs$ system is about $\Delta\bar{n} \approx 0.25$.

Throughout this thesis, we will make waveguide models of both single-element and multiple-element arrays of semiconductor lasers. In order to reduce the discussion to the fundamental physical principles that apply to phased array lasers, we will make use of the simplest possible model for a single-element waveguide, that of the symmetric three layer slab waveguide shown schematically in Figure 1.4b.

For obvious reasons, we will refer to this simple structure as a "box" waveguide; extension of our work to more accurate waveguide models is straightforward. [3,4]

(a) Buried Heterostructure Lasers

Material index guided lasers provide the largest index difference, and hence the tightest confinement of the optical field. They make use of the differing material properties of a $GaAs/Ga_{1-x}Al_xAs$ heterojunction with the mole fraction of Al $x = 0.2$ to 0.4 in a manner entirely analogous to the double heterostructure configuration in the vertical direction. A typical laser of this type is the ***buried heterostructure***[5,6] illustrated in Figure 2.1.

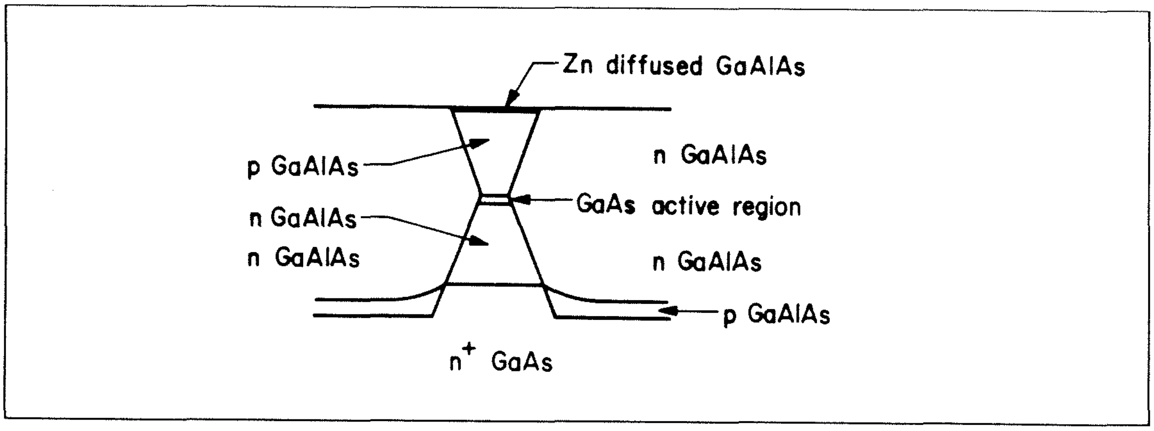

FIGURE 2.1 Buried heterostructure laser.

The distinguishing feature of a buried heterostructure laser is that the $GaAs$ active layer is surrounded on all sides by $GaAlAs$. Figure 2.2a shows the lateral waveguide model for a buried heterostructure laser 1.5μm wide with $x = 0.3$, while Figure 2.2b presents the intensity nearfield and farfield patterns of this waveguide for the fundamental mode.

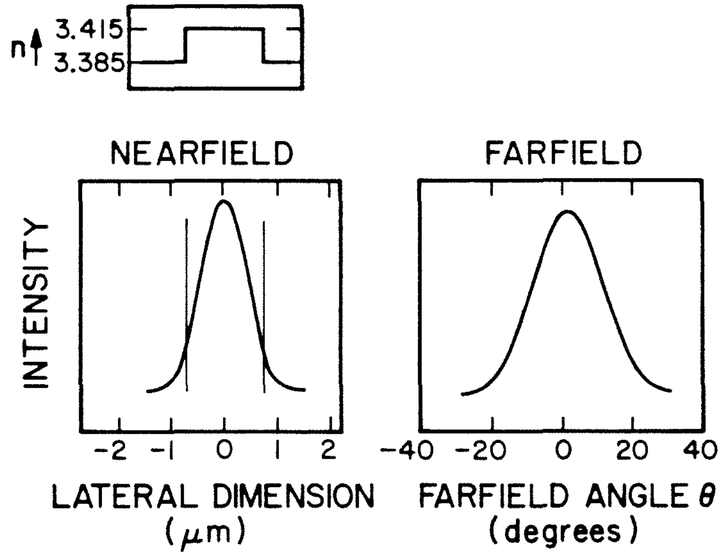

FIGURE 2.2 (a) Lateral waveguide model for a buried heterostructure laser with a cladding *Al* mole fraction $x = 0.3$ and a width of 1.5μm. (b) Nearfield and farfield for the fundamental mode. Note the very wide farfield pattern.

Notice that as a result of the large index of refraction difference between *GaAs* and *GaAlAs* the field is very well-confined. This, in conjunction with the large energy band gap difference between *GaAs* and *GaAlAs*, provides excellent carrier and optical confinement in both the horizontal and vertical directions, thus leading to threshold currents as low as $15mA$.[7] However, if the laser is to have a single lobed farfield pattern the widths of a buried heterostructure laser are limited to about 1μm.[8] This limits the typical power output of buried heterostructure lasers to a few milliwatts.

Strongly real index guided lasers such as the buried heterostructure have the very desirable property that their spectral width is very much smaller than that of a gain guided structure. This is of crucial importance in optical fiber applications, and especially so for heterodyne detection methods.[9] Therefore, it would be highly advantageous to be able to fabricate phased locked arrays of strongly index guided lasers. Unfortunately, due to the techniques necessary to fabricate a buried heterostructure laser, it is not currently possible to place two such lasers closer than $2\mu\text{m} - 3\mu\text{m}$ apart. Figure 2.2b shows that as a result of the large index step that tightly confines the field the overlap between the fields of adjacent lasers will be very small, and thus an array of buried heterostructure lasers is not likely to operate in a phased locked mode.[10,11] It is possible to slightly decrease the refractive index step by using smaller mole fractions x of aluminum in the cladding layer. However, decreasing the mole fraction below $x = 0.2$, causes the threshold current to rise dramatically because the carriers are no longer well-confined.[12] We therefore conclude that despite their great advantages of a low threshold current and very pure spectral output, buried heterostructure lasers are unsuitable for use in evanescently coupled phased arrays.

(b) Buried Crescent (Channeled Substrate) Lasers

Providing slightly less of an index step difference is the buried crescent (channeled substrate or V groove) laser of Figure 2.3.[13] This device takes advantage of the differential growth rate of $GaAs$ and $GaAlAs$ inside and outside an etched groove to create an active region that is thicker towards the center of the groove than towards the edge, thus providing the good carrier confinement characteristic of a double heterostructure.

It is possible to achieve some degree of control of the active layer thickness between the elements, and thus control both the size of the lateral index variation as well as the coupling between the lasers. Although the index step in these lasers approaches that available in a buried heterostructure laser, the smooth variation in the effective index profile provides improved mode discrimination between the

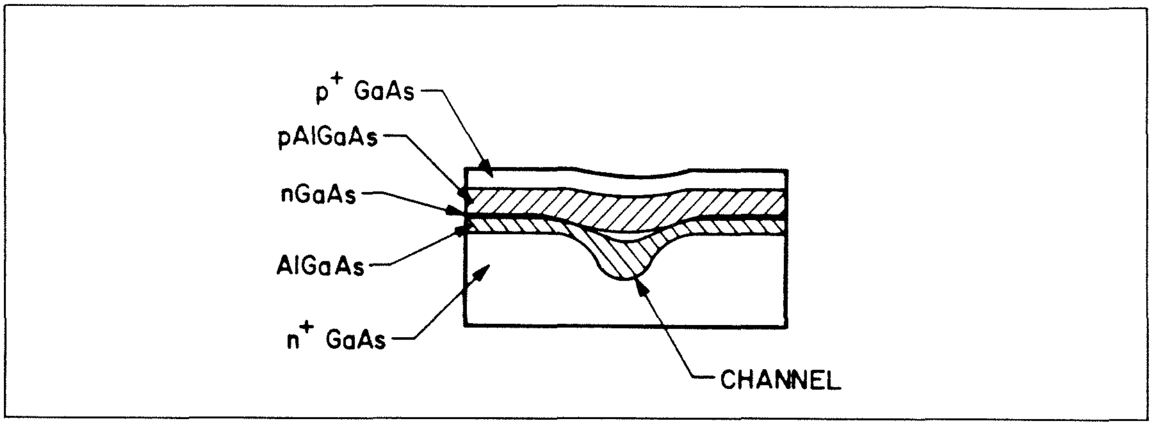

FIGURE 2.3 Buried Crescent (Channeled Substrate) Laser.

fundamental and higher order modes in a single-element waveguide. These lasers are attractive candidates for *uniform* phased arrays but not for nonuniform arrays because it is not easy to obtain controllable growth using grooves of different sizes.[14] We will therefore not consider such arrays in this work. We note, however, that arrays of identical buried crescent lasers with variable *spacing* between the array elements have shown promising results.[15]

(c) Buried Ridge (Strip-Loaded) Lasers

Another method of confining the optical field in the horizontal direction makes use of the "effective index" effect in a ridge guided structure.[16] The refractive index differences associated with effective index guided structures may vary widely depending upon the particular details. Two such possible structures are shown schematically in Figures 2.4 and 2.5. In each case, the optical mode tends to concentrate in the high index region of the waveguide, which is indicated by the dotted ovals in the figures. The first structure is referred to as a *buried ridge* or sometimes as a strip-loaded waveguide, while the second is referred to as an *air ridge* or mesa stripe laser.

§2.2(c) Buried Ridge (Strip-Loaded) Lasers

Buried ridge structures are difficult to fabricate in the $GaAs/GaAlAs$ system because it is virtually impossible to obtain good regrowths over air exposed $Ga_{1-x}Al_xAs$ with a mole fraction x of aluminum greater than 0.1.[17] This fact, in conjunction with the difficulty of controlling etching depths to a precision of better than about 0.2μm, limits the smallest obtainable index step to about $\Delta n \approx 0.03$.

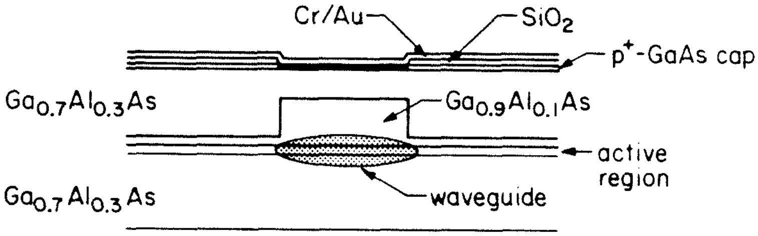

FIGURE 2.4 Buried ridge laser.

The largest index step is limited to $\Delta n \approx 0.1$ by the requirement that the laser's farfield pattern be single lobed in the *vertical* direction as well. Nevertheless, despite the difficulties with the regrowth process, buried ridge structures also provide excellent candidates for phased array lasers, and in fact have been used with some success.[18]

We note that many laser waveguides, while technically not single lobed, do lase with a single lobed farfield pattern. For example, a buried heterostructure waveguide will support only a single mode if its width is less than about 0.5μm, yet many actual devices about 1μm wide show clean, single lobed farfield patterns, suggesting that a better practical condition be that the $\nu = 3$ mode be cut off. The improved performance probably results from the fact that the $\nu = 2$ mode has a null at the high gain region in the center of the waveguide. (This is one instance in which our simplification of the actual waveguide to a box structure is inappropriate.) This new criterion effectively doubles the useful width of the waveguide, and places an upper limit of about $2\mu m - 3\mu m$ on the width of a buried ridge waveguide.

However, while this is a good design rule for an *isolated* laser, it is not clear that it holds for the elements in an *array* of lasers. For a given index step, as the width of the laser increases the fields become more tightly confined, but it is *always* true that the higher order modes with multilobed farfield patterns are less well-confined than the single lobed fundamental. If the individual laser waveguides support more than one mode, the coupling between the higher order modes in the array will be *greater* than it will be for the fundamental mode, thus exacerbating the tendency of the array to operate in an undesirable multilobed farfield pattern. Therefore, it is probably advantageous to use single mode waveguides whenever possible. This more stringent criterion would limit the width of the buried ridge waveguide to about $1\mu m$, with wider waveguides being marginally satisfactory.

(d) Air Ridge (Mesa Stripe) Lasers

An air ridge waveguide[19,20] such as that of Figure 2.5 may be used to obtain arbitrarily small index steps. These devices are sometimes referred to as *mesa stripe* lasers because they are fabricated by etching a mesa into a four layer heterostructure which is similar to the three layer heterostructure described in §1.2 except for the addition of top p^+GaAs cap layer. The metal to $GaAs$ interface forms a good ohmic contact, thus providing better injection into the laser than does the metal to $GaAlAs$ interface.

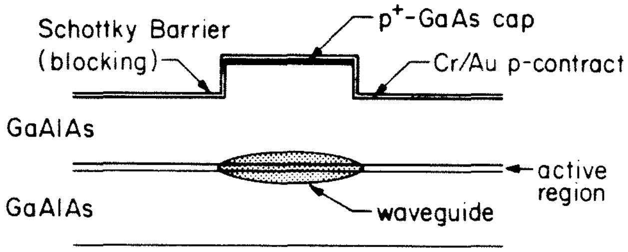

FIGURE 2.5 Air Ridge (Mesa Stripe) Laser.

The maximum index step obtainable is limited by the precision with which the etching action can be halted very close to the active region, typically about $\sim 0.2\mu m$ (although our experience indicates that it is very difficult to obtain uniform results when working to these tolerances; a better practical limit is probably $0.3\mu m - 0.4\mu m$). This places an upper limit on the the refractive index step of about $\Delta\bar{n} \approx 0.02$; the lower limit is, of course, zero, and corresponds to no etching at all.

(e) Proton Implanted and Schottky Isolated Gain Guided Lasers

A gain guided laser is usually considered to be a laser waveguide in which there is no intentionally introduced real index guiding. Waveguiding is provided solely by the gain distribution.[21,22] There are a variety of types of gain guided structures; we will make extensive use of both proton implanted[23] and Schottky isolated lasers[24] in Chapters 4 & 5.

Figure 2.6 presents a schematic diagram of such a gain guided proton implanted laser. The crystal damage caused by the implanted protons[25] creates high resistivity regions in the upper cladding layer, thereby blocking injection everywhere except at the laser stripe that has been protected from the protons by a thick ($\sim 3\mu$m) photoresist stripe.

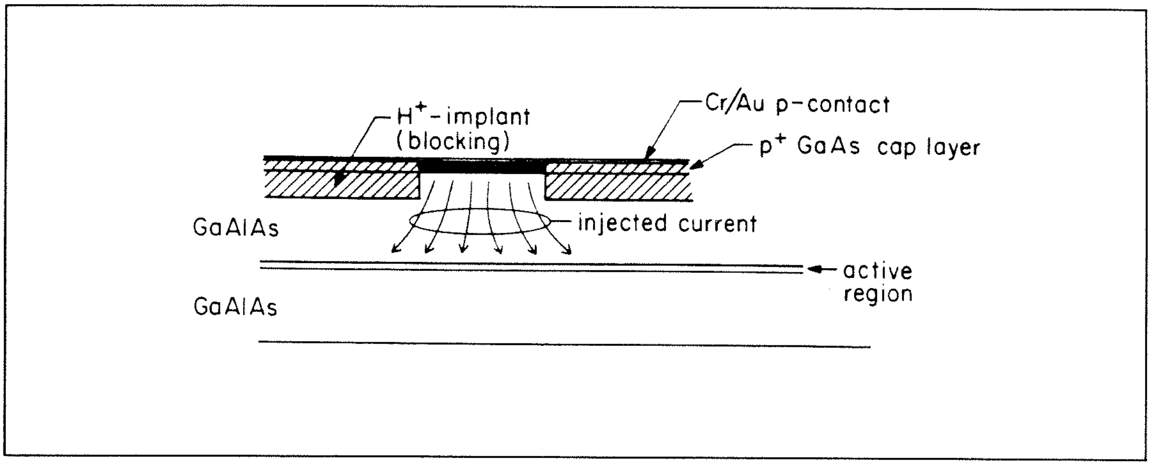

FIGURE 2.6 Proton implanted laser.

Typical implantion dosages are $5 \times 10^{16} cm^{-3}$. The implanation depth, and hence depth of the insulating region, depends upon the proton energy. Proton implanted lasers have been extensively studied, and offer several advantages over other types of lasers from the point of view of phased array semiconducor laser design (see §4.3). However, due to the thick photoresist pattern, it is difficult to achieve feature sizes much smaller than 3μm $-$ 5μm, and especially so for deeply implanted devices.

A schematic diagram of another useful type of gain guided laser, a Schottky isolated laser, is illustrated in Figure 2.7. It consists of a standard three layer heterostructure with the 0.2μm $p^{+}GaAs$ cap layer. After growth, photoresist stripes are deposited on the surface of the wafer, and the thin $p^{+}GaAs$ cap layer is etched away from the unprotected areas using a a noncritical wet chemical etch. This type of laser is actually an "air ridge" laser with a zero etching depth. The shallow etching depth does not affect the real refractive index profile, but does control current injection into laser.

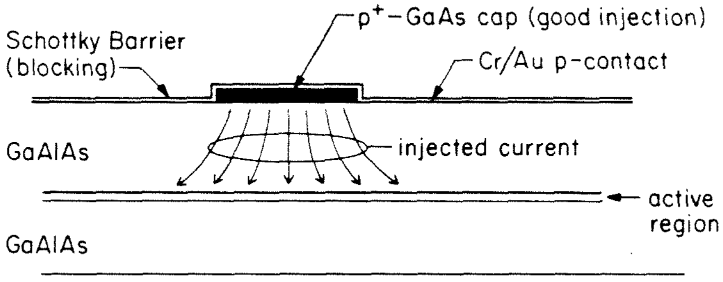

FIGURE 2.7 Schottky isolated laser.

After removing the photoresist, a metal is deposited over the entire surface of the device. The metal to p^+GaAs interface (shown in black) forms an injecting ohmic contact, while the metal to $p\,Ga_{1-x}Al_xAs$ interface (shown in white) forms a Schottky blocking contact. Thus current is injected only into the region under the p^+GaAs stripe. The very thin cap layer allows the feature size to approach the technological limit of about 2μm.

It is important to note that in both structures, at any given point on the surface of the wafer, current is either injected into the crystal or it isn't; there is no simple method for achieving partial injection and hence arbitrarily controlled variations in the spatial gain profile. However, we will return to this point in §5.2 when we demonstrate the halftone process for achieving nearly arbitrary *two-dimensional* spatial gain profiles within a broad area semiconductor laser.

In an actual gain guided laser, the free carriers in the active region, and the change in the electronic band edge due to the gain they introduce, leads to a decrease in the real part of the refractive index within the core region; this is known as the antiguiding effect.(§1.2(a.i)) The ratio $b = |\Delta\bar{n}/\Delta\bar{\bar{n}}|$ is referred to as the antiguiding parameter. Figure 2.8a shows the waveguide model for a gain guided laser 6μm wide. The gain in the core region is fixed by the requirement that at threshold the modal gain of the fundamental mode be equal to the mirror losses.(§1.5)

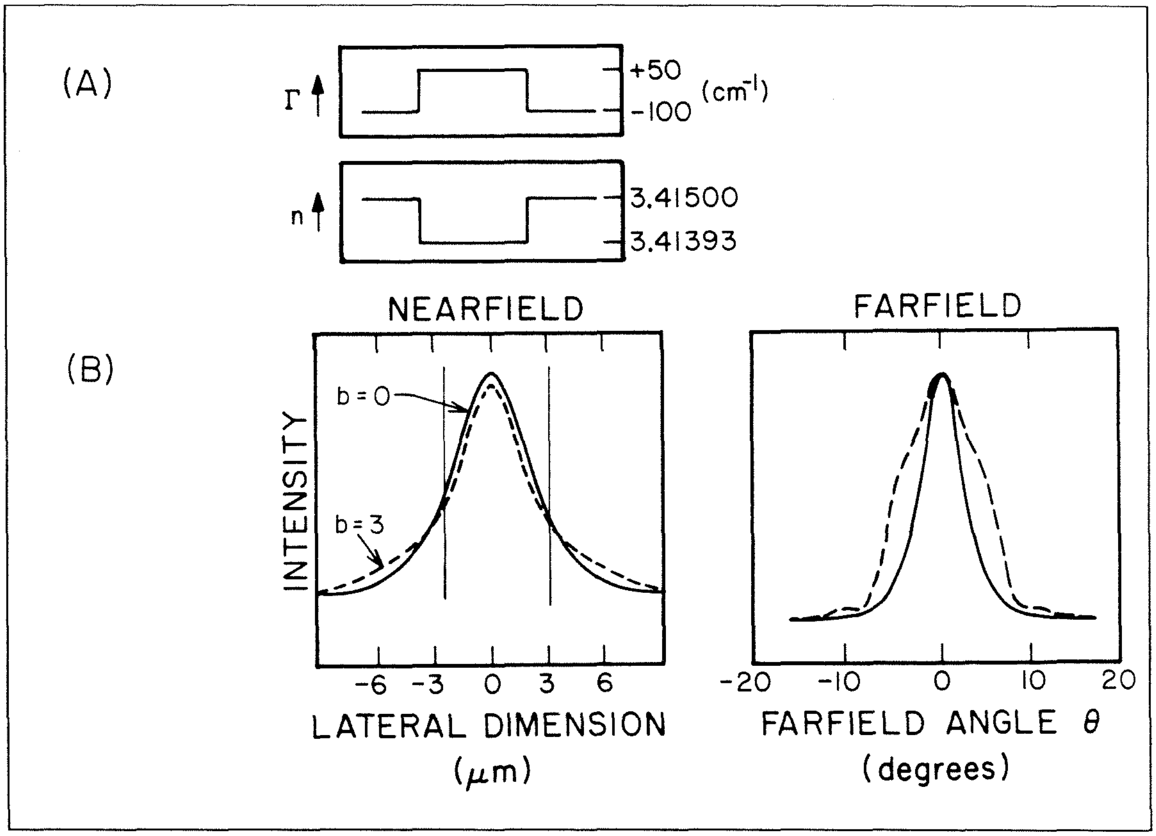

FIGURE 2.8 (a) Waveguide model showing the effect of antiguiding parameter b. (b) Nearfield and farfield patterns for $b = 0$ (solid curve) and $b = 3$ (dashed curve).

Figure 2.8b shows the nearfield and farfield patterns for this mode with no antiguiding ($b = 0$, solid line) and with an antiguiding parameter $b = 3$ (dashed line).[4] Note that the nearfield patterns are very similar. Throughout this thesis our waveguide models will therefore ignore the antiguiding parameter unless we are attempting to model an actual device.$^{(\S 4.5(b),\S 5.13)}$

Finally, we remark that most gain guided structures show single filament operation$^{(\S 1.2(a.i))}$ only if they are narrower than about $10\mu\text{m} - 15\mu\text{m}$.[26]

§2.3 Interplay Between Real Index and Gain Guiding

If the etching depth in an air ridge structure is too small, the effect of the real index guiding becomes weaker than the effect of the gain guiding, and the laser loses the advantages of a real index guided structure (low thresholds and spectral purity). There is no clear dividing line separating a weakly real index guided laser from a gain guided one. We therefore adopt the criterion that, to be considered index guided, the size of the intentionally introduced refractive index step must be approximately equal to the change in the *imaginary* part of the complex refractive index in an otherwise equivalent purely gain guided laser.

The waveguide model for such a comparison is shown in Figure 2.9a. We write the complex index of refraction step$^{(\S 2.5)}$ as $\Delta n = \Delta \bar{n} + i\,\Delta \bar{\bar{n}}$ with $\Delta \bar{\bar{n}} = -\Delta\Gamma/2k_0$ and $\Delta\Gamma = \Gamma_0 - \Gamma_e$. We assume a loss due to the unpumped *GaAs* active region $-\Gamma_e \approx 200\text{cm}^{-1}$, and require that the peak gain Γ_0 inside the core region of the waveguide be just large enough to give the fundamental mode a modal gain just sufficient to balance the mirror losses of $40\text{cm}^{-1}$$^{(\S 1.5)}$

A waveguide $6\mu\text{m}$ wide a peak gain $\Gamma_0 \approx 50\text{cm}^{-1}$ has a gain step $\Delta\Gamma = 250\text{cm}^{-1}$. The peak gain Γ_0, and hence $|\bar{\bar{n}}|$, increases slightly as the guide becomes narrower because the field extends farther into the lossy region. 250cm^{-1} corresponds to a change in the magnitude of the imaginary part of the index of refraction of $\Delta\bar{\bar{n}} = \Delta\Gamma/2k_0 = 0.0018$. Figure 2.9b shows the superimposed intensity nearfield and farfield patterns for the two equivalent ($\Delta\bar{n} = |\Delta\bar{\bar{n}}| = 0.0018$) waveguides

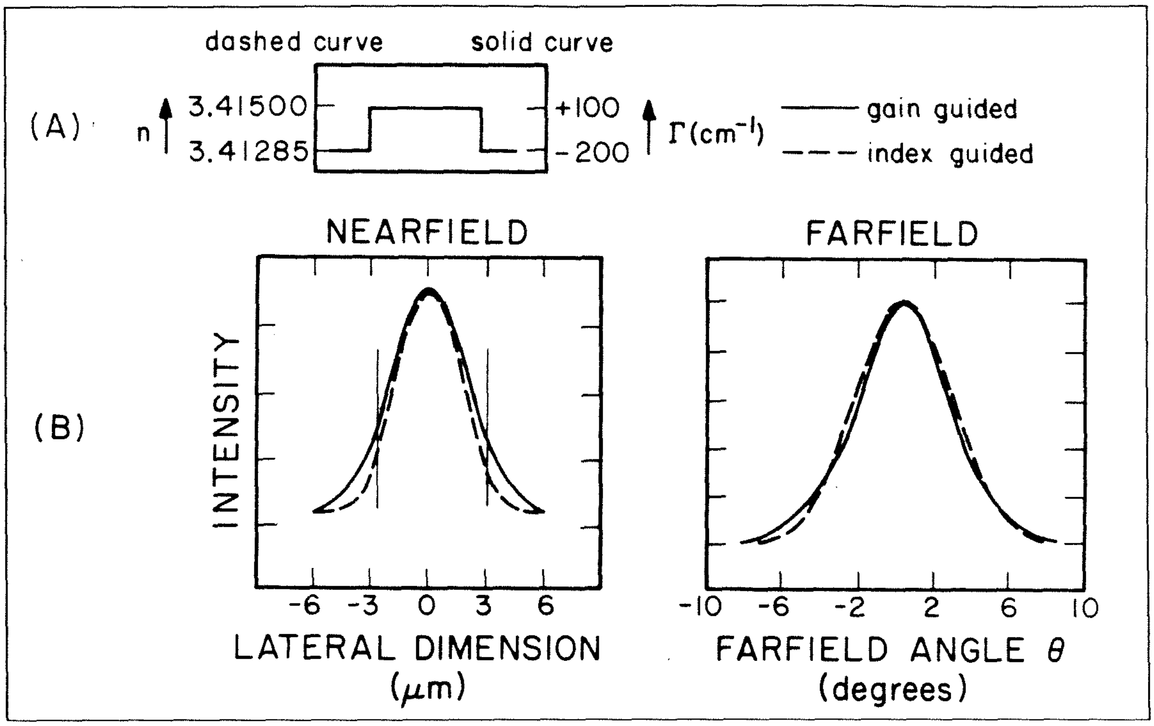

FIGURE 2.9 Waveguide model for gain guided (solid line) and equivalent real index guided (dashed line) structure with $\Delta n = \Delta\bar{n} = 0.0018$.

6μm wide. The gain guided fields are indicated by the solid curves while the index guided fields are indicated by the dashed curves. The gain guided nearfield pattern is very slightly wider than the index guided nearfield, but because of the phase front curvature due to gain guiding,(§2.6(*b*)) the farfield patterns are virtually identical. This indicates that using the criterion $\Delta n = |\Delta\bar{n}|$ as a dividing line to distinguish a real index guided laser from a gain guided one is not an unreasonable one.

In the preceding analysis, we have neglected the effect of the antiguiding factor b which accounts for the depression in the index of refraction due to the free carrier and band edge effects.(§1.2(*a.i*)) The antiguiding effect *reduces* the size of the effective index step by about three times $|\bar{n}|$.[4] Therefore, we propose that for an actual device to be considered as real index guided, it is necessary that

$\Delta\bar{n} \geq \Delta\bar{\bar{n}} + 3\left|\bar{\bar{n}}\right| \approx 0.003$ in order to offset the antiguiding effect. In an air ridge waveguide, this corresponds to an upper cladding thickness of about 0.4μm — which is near the technoloical limit with which etching can be controlled. We therefore conclude that almost all air ridge waveguides will be more or less gain guided structures. We will refer to them as quasi-real index guided lasers.

Finally, we the presence of a metal film so close to the active layer will introduce additional loss into the interchannel regions of an air ridge phased array, thus promoting the tendency of the array to operate with a twin lobed farfield pattern$^{(\S 4.1)}$.

§2.4 Design Considerations for Evanescently Coupled Arrays

Figure 2.10 presents a graphical summary of the information presented in the previous sections. We have plotted the waveguide width ℓ *vs.* the size of the intentionally introduced real index step $\Delta\bar{n}$. Lasers with widths narrower than those indicated by the light dashed line support only the single fundamental mode, while those wider than the heavy dashed line support more than two modes and are hence probably unsuitable for use in phased array lasers. Lasers with widths between the two lines support two modes and are therefore marginally suitable.

The vertical light dotted line indicates the approximate location of the regime where $\Delta\bar{n} \approx \Delta\bar{\bar{n}}$ *i.e.*, the dividing line between gain guided and real index guided lasers if the antiguiding factor were to be ignored. The vertical heavy dotted line accounts for the antiguiding factor of about three by indicating the approximate location of the regime where $\Delta\bar{n} \geq \Delta\bar{\bar{n}} + 3\left|\bar{\bar{n}}\right|$. We consider lasers to the left of the light dotted curve to be gain guided, those between the light and heavy dotted curves to be quasi-real index guided, and those to the right of the heavy dotted line to be real index guided.

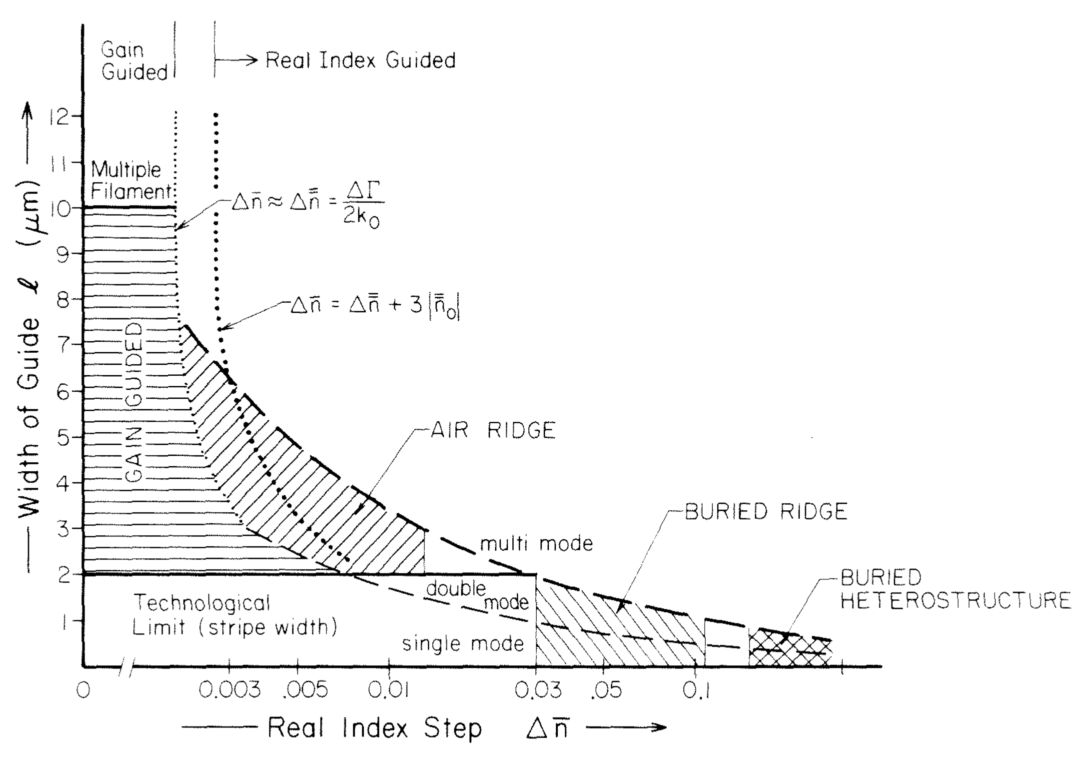

FIGURE 2.10 Design considerations for evanescently coupled phased array lasers. Ideally, an array element should be real index guided and single mode. Current technological limitations make this difficult, so we emphasize gain guided arrays in this work.

Finally, the upper limit on the width of a gain guided laser of about 10μm and the technological limit corresponding to the smallest practical feature size of about 2μm are indicated by the horizontal heavy solid lines.

This figure shows that the only candidates for truly real index guided arrays are the buried heterostructure and buried ridge lasers, both of which will probably support at least two modes. As discussed in §2.2(a), such waveguides are probably unsuitable for use in evanescently coupled arrays requiring single lobed farfield patterns. Almost all air ridge lasers are only weakly real index guided at best. Given the current technological limit of about 2μm feature size and the difficulty of fabricating buried ridge waveguides, we conclude that the laser most suitable for use in arrays will likely be either gain guided or at best partially gain and partially index guided air ridge structures, and that even these will not be single mode waveguides. For this reason, as well as others discussed in §4.2(a), most of the experimental work of this thesis will be with gain guided lasers (also see §4.3).

We remark that these results indicate that many of the so-called "real index guided" air ridge lasers described in the literature[27,28] are not truly real index guided lasers as the term is commonly used. In particular, the on-axis farfield pattern in Reference [28] is probably due to the symmetry of the waveguide, not necessarily to the fact that they are real index guided. The effect of the gain guiding is masked by the symmetry of the structure (see §4.2(a), especially Figure 4.5b, and §5.12).

§2.5 The Helmholtz Equation

Having discussed some of the index of refraction profiles appropriate to semiconductor lasers suitable for use in phased arrays, we now summarize some of the relevant properties of the optical modes of these waveguides.

The optical field $\mathbf{E}(\mathbf{r},t)$ inside any waveguide satisfies Maxwell's wave equation[29]

$$\nabla^2\mathbf{E} - \frac{n^2(\mathbf{r})}{c^2}\frac{\partial^2\mathbf{E}}{\partial t^2} = 0 \tag{2.5.1}$$

where c is the speed of light in a vacuum, and $n(\mathbf{r})$ is the index of refraction in the medium. $n(\mathbf{r})$ is, in general, a complex number[30]

$$\begin{aligned} n(\mathbf{r}) &= \bar{n}(\mathbf{r}) + i\bar{\bar{n}}(\mathbf{r}) \\ &= \bar{n}(\mathbf{r}) - i\Gamma(\mathbf{r})/2k_0 \end{aligned} \tag{2.5.2}$$

and $i = \sqrt{-1}$. The ordinary (real) index of refraction is denoted by $\bar{n}(\mathbf{r})$, while $\Gamma(\mathbf{r}) = -2k_0\bar{\bar{n}}(\mathbf{r})$ is the spatially dependent power gain experienced by an optical wave propagating through the point $\mathbf{r}$. In the unpumped *GaAs* absorbing regions of the waveguide, $\Gamma(\mathbf{r})$ is a negative number.

In a semiconductor laser, $\mathbf{E}(\mathbf{r},t)$ is a complicated superposition of many transverse, lateral, and longitudinal modes oscillating at several different frequencies. We simplify the problem by considering only one oscillation frequency (thus eliminating the longitudinal modes), and make the usual effective index approximation[16] (thereby eliminating the transverse modes). Furthermore, we consider only TE waves[31] traveling in the $+z$ direction. After making these approximations, the electric field of a lateral mode may be written as

$$\mathbf{E}(\mathbf{r},t) \simeq \hat{\mathbf{x}} E(x) e^{i(\beta z - \Omega t)} \qquad \beta = k_0 \eta \tag{2.5.3}$$

where $E(x)$ is now a scalar electric field in the $\hat{\mathbf{x}}$ direction, $k_0 = 2\pi/\lambda$ is the free-space wavevector, $\Omega = c\, k_0$ is the circular frequency of the wave.

Substituting (2.5.3) into (2.5.1) yields the scalar Helmholtz equation:[32]

$$\frac{d^2}{dx^2} E + k_0^2 (n^2(x) - \eta^2) E = 0 \ . \tag{2.5.4}$$

Solutions of this equation are referred to as *modes* of the waveguide. The effective index of the mode is given by the constant η; the propagation constant $\bar{\beta}$ in the z direction is then given by $\bar{\beta} = k_0 \bar{\eta}$. A very important quantity is the *power modal gain* $\gamma = -2k_0 \bar{\bar{\eta}} = -2\bar{\bar{\beta}}$. The intensity of an optical wave which is an eigenmode of Equation (2.5.4) will grow with z as $e^{\gamma z}$. In a laser, the lateral mode with the highest modal gain will be the lasing mode at threshold.

Throughout this work, we will solve this equation for various refractive index profiles $n(x)$. In a real index guided waveguide, there is no gain or loss present, and so the refractive index profile, the eigenmodes, and the electric fields are all real quantities. In particular, we note that the phase ϕ of the electric field $E = |E|\, e^{i\phi}$

is restricted to either 0 or π. On the other hand, in a gain guided structure, variations in the *imaginary* part of the index of refraction determine the modal properties more than do variations in the real part of the refractive index profile. In this case, the eigenvalues are complex, the real part being the effective index and the imaginary part being the modal gain as described by Equation (2.5.2). In a gain guided waveguide, the phase ϕ of the electric field is no longer restricted to either 0 or π and may take on any value.

We remark that the terms "real index guided" and "gain guided" refer to two limiting cases in which variations in one part of the complex index of refraction dominate the other. As we have seen in §2.3, an important class of lasers suitable for use in phased arrays, the air ridge structures, may be considered to be either gain or index guided. Such waveguides will play an important role at one point in our work, and will be further discussed in §4.2(a).

§2.6 Symmetric Three Layer "Box" Waveguides

The simplest possible single-element waveguide is the symmetric three layer slab "box" waveguide illustrated in Figure 2.11 and Figure 2.12, which has a refractive index profile described by

$$n(x) = \begin{cases} n_e & \text{(cladding region) } -\infty < x < -\frac{\ell}{2} \\ n_0 & \text{(core region) } -\frac{\ell}{2} < x < +\frac{\ell}{2} \\ n_e & \text{(cladding region) } \frac{\ell}{2} < x < \infty \ . \end{cases} \tag{2.6.1}$$

The quantities n_0 and n_e are, in general, complex. For waveguiding to occur, it is necessary that in a real index guided laser $n_0 > n_e$, while in a gain guided laser $\Gamma_0 > \Gamma_e$, where $\Gamma_{0,e}$ is related to the imaginary part of the complex index of refraction through Equation (2.5.2). The properties of the real index guided version of this waveguide have been extensively discussed in the literature,[33-35] while the gain guided version has been somewhat less well studied.[22] In this work we will introduce only selected aspects of the theory of these waveguides necessary to aid our understanding of phased array semiconductor lasers.

In general, a waveguide will support many optical modes $E^{\nu}(x)$ where ν is the *mode number*. For the box waveguide of width ℓ illustrated in Figure 2.11, $E^{\nu}(x)$ is given by

$$E(x) = \begin{cases} Be^{g(x+\ell/2)} & -\infty < x < -\frac{\ell}{2} \\ A\begin{cases}\cos kx & \text{symmetric modes } \nu = 1,3,5,\ldots \\ \sin kx & \text{antisymmetric modes) } \nu = 2,4,6,\ldots\end{cases} & \frac{\ell}{2} < x < +\frac{\ell}{2} \\ Be^{-g(x-\ell/2)} & \frac{\ell}{2} < x < \infty \end{cases} \tag{2.6.2}$$

where the normalization constants A and B are given by

$$A = \left[\frac{Z_0}{\eta}\frac{2P}{\ell/2+g^{-1}}\right]^{\frac{1}{2}} \qquad B = A\cos\frac{k\ell}{2} \tag{2.6.3}$$

with $Z_0 = \sqrt{\mu_0/\epsilon_0}$ the impedance of free space and P the power flowing in the mode; this gives the conventional electromagnetic normalization[36]

$$\int_{-\infty}^{\infty} E_i(x)E(j(x)\,dx = 2\frac{\omega\mu_0}{\beta}\delta_{ij} = 2\frac{Z_0}{\beta}k_0\delta_{ij} \tag{2.6.4}$$

with δ_{ij} the Kronecker delta function. The lateral wavevector k inside the core region and the evanescent wavevector g in the cladding region are given by

$$\begin{aligned} k &= \frac{2\pi}{\lambda}(n_0^2 - \eta^2)^{1/2} \\ g &= \frac{2\pi}{\lambda}(\eta^2 - n_e^2)^{1/2} \end{aligned} \tag{2.6.5}$$

where λ is the free space optical wavelength. The eigenvalue η is determined by the roots of the secular equation

$$\tan(k\ell/2) = \begin{cases} -k/g & \text{symmetric modes } \nu = 1,3,5,\ldots \\ -g/k & \text{antisymmetric modes) } \nu = 2,4,6,\ldots \end{cases} \tag{2.6.6}$$

Equation (2.6.2) to (2.6.6) are valid for both real index guided and gain guided box waveguides. The nearfield pattern is given by the magnitude of Equation (2.6.2), while the farfield pattern is given by a slightly modified Fourier Transform of the amplitude nearfield pattern.[37,38]

Note that Equation (2.7-7) of Reference [37] uses the $e^{-i\beta z}$ convention, leading to the $(+i)$ transform of (2.7-28). Our use of the $e^{+i\beta z}$ convention in (2.5.3) implies the use of a $(-i)$ transform to obtain the farfield pattern. Furthermore, through Equation (2.5.2), it also implies that the antiguiding factor b is greater than zero.

(a) Real Index Box Waveguides

For guided modes in a real index waveguide, $n_e < \eta < n_0$. When $\eta < n_e$ the mode is cut off and is no longer guided. Figure 2.11a presents a typical real index box waveguide. Figure 2.11b shows the intensity nearfield and corresponding farfield patterns for the first five low order modes, while Figure 2.11c consists of a plot of the effective index η for each of the eight guided modes. Notice that all the higher order modes have nulls in their nearfield patterns, and that the intensity of each maximum is the same. It is of particular interest to note that only the fundamental mode has a single lobed farfield pattern; the farfield patterns of all higher order modes are multilobed and symmetrical about 0°(§5.12)

(b) Gain Guided Box Waveguides

Figure 2.12 presents the corresponding plots for a gain guided box waveguide. Since the refractive index is now a complex quantity, so also is the modal eigenvalue η. As discussed in §2.5, the real part of the eigenvalue, denoted by $\bar{\eta}$ or $\Re\mathrm{e}\{\eta\}$, is the effective index for the mode, while the imaginary part, denoted by $\bar{\bar{\eta}}$ or $\Im\mathrm{m}\{\eta\}$, defines the power modal gain $\gamma = -2k_0\bar{\bar{n}}$. We therefore present the eigenmodes of

§2.6 Symmetric Three Layer "Box" Waveguides

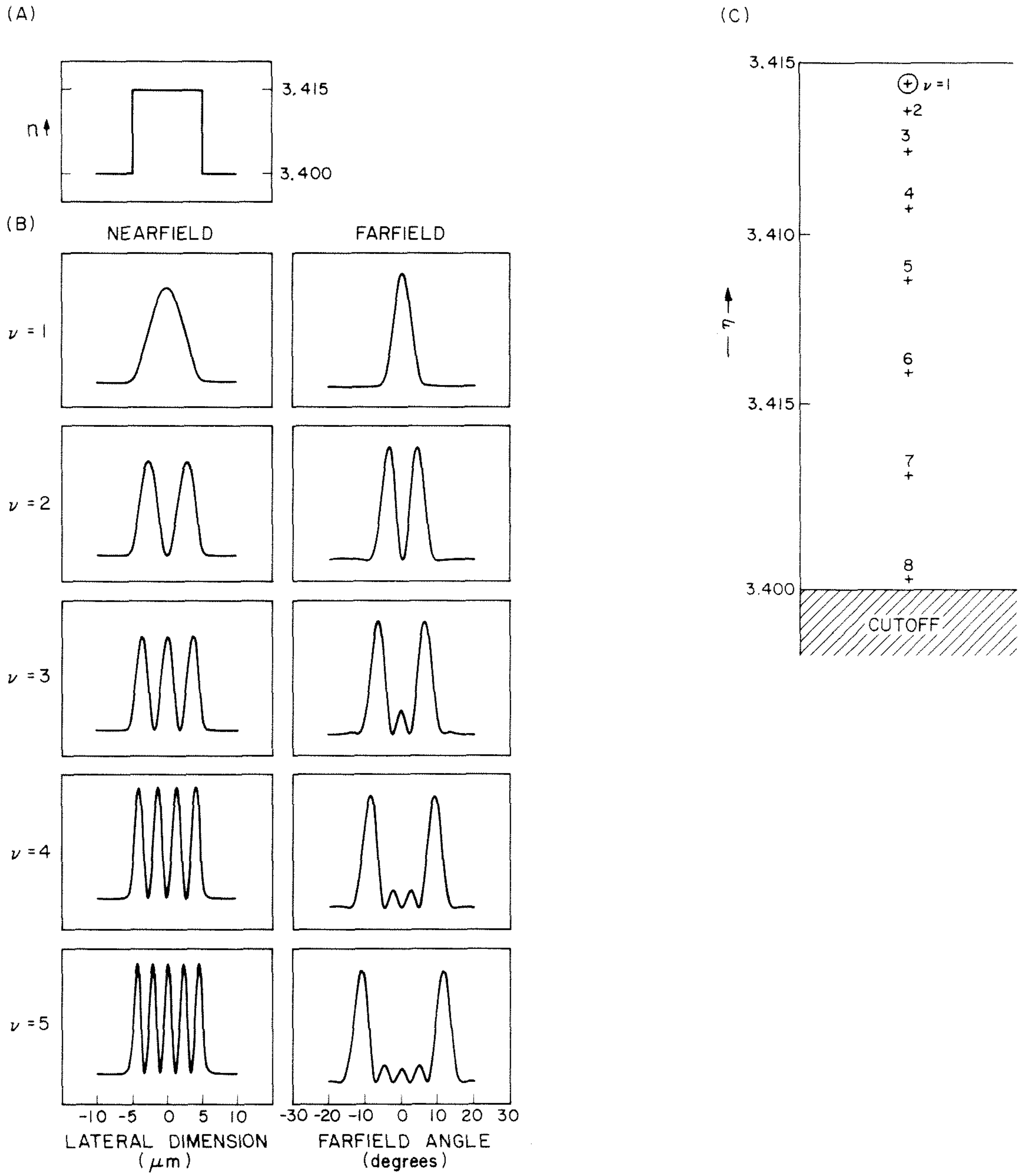

FIGURE 2.11 Modes of the real index box waveguide (a) refractive index profile (b) nearfield and farfield intensity patterns for the first five modes (c) mode structure. Note the nulls in the nearfield patterns and the multilobed farfield patterns for all except the fundamental mode.

§2.6(b) Gain Guided Box Waveguides

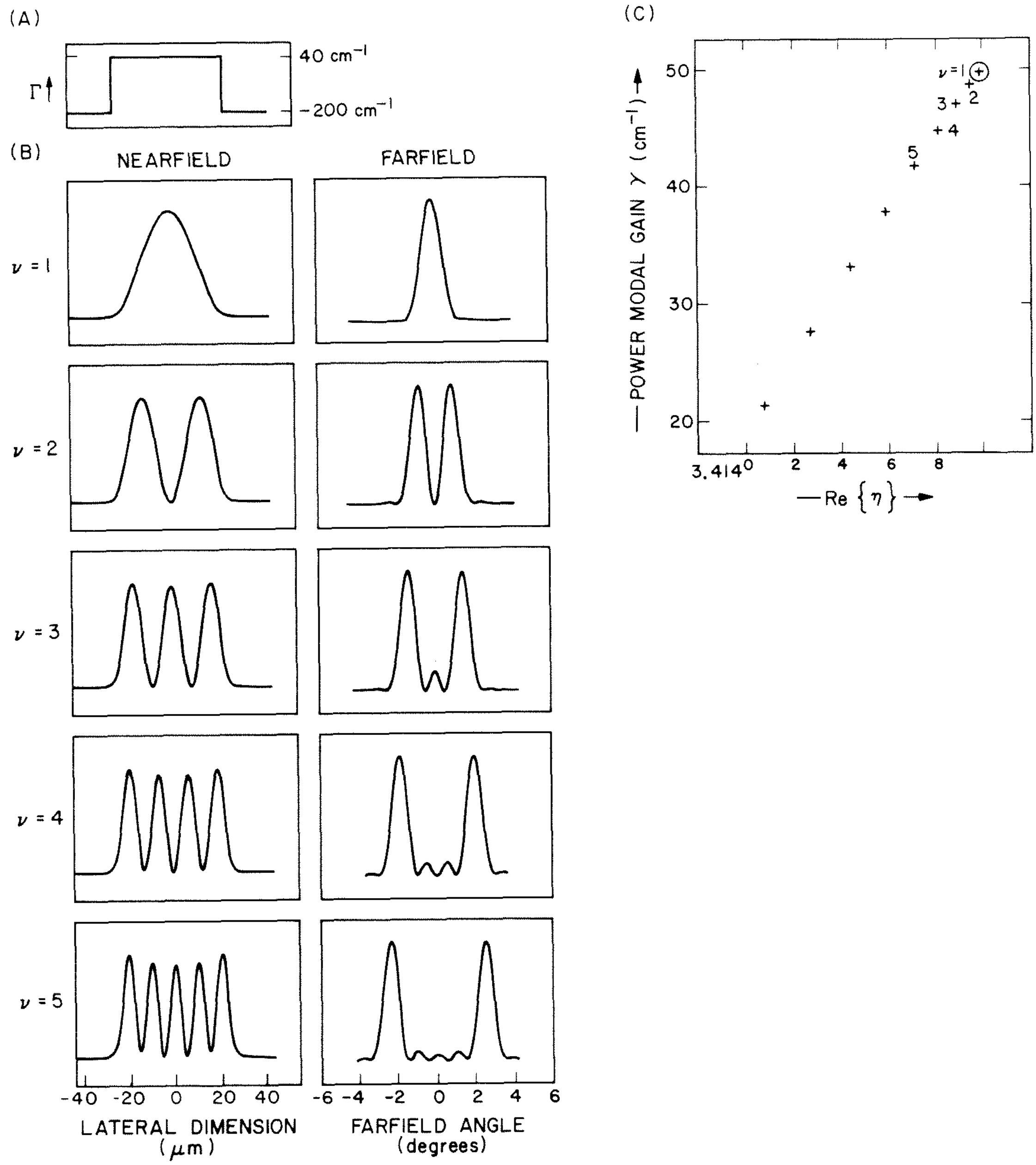

FIGURE 2.12 Modes of the gain guided box waveguide (no antiguiding) (a) gain profile (b) nearfield and farfield intensity patterns for the first five modes (c) mode structure. Note the slight differences from the modes of the real index box waveguide of Figure 2.11.

a waveguide with gain in a *modal diagram* which plots γ *vs.* $\bar{\eta}$. The modal diagram for the waveguide of Figure 2.12a is presented in Figure 2.12b. The modal gain of a mode is approximately related to the overlap between the optical field and the gain distribution within the waveguide. This implies that since the lower order modes are more well-confined, they have higher modal gains than do the higher order modes.

Another effect of the gain is to make the wavevectors k and g complex, and to introduce curvature into the phase fronts of a mode, reflecting the fact that power flows from the high gain region of a mode (inside the core region) towards a low gain region (in the cladding region).[39] The phase front curvature (and hence astigmatism) will therefore be less for the fundamental mode in a very wide waveguide than it will be in a narrow waveguide in which the fundamental has a modal gain much less than the peak modal gain. Unfortunately, because of the poor mode discrimination, the higher order modes of a wide laser will also lase; this is one cause of the poorly characterized farfield patterns of conventional uniform gain semiconductor lasers$^{(\S1.2(a.ii))}$. (The effect of the complex wavevectors will be further discussed in §3.5(c); also see §5.10).

Figure 2.12b presents the corresponding intensity nearfield and farfield patterns for the first five modes of a gain guided box waveguide. Comparison of nearfield patterns of the real index box waveguide of Figure 2.11 with that of the gain guided box waveguide of Figure 2.12 shows that unlike the real index guided case, the gain guided structure has deep minima in the nearfield patterns. The only exact null occurs only at the center of the waveguide. Furthermore, the intensity peaks in the nearfield pattern are no longer uniform but increase slightly towards the edge of the waveguide.

(c) Path Analysis of Box Waveguides

These differences between real index and gain guided box waveguides may be easily understood by introducing a new, very powerful method for analyzing waveguide modes. In brief, the method consists of following the path of the argument of the optical eigenfunction (*e.g.*, kx in the sine or cosine functions of Equation (2.6.2)) throughout the complex plane; hence the name "Path Analysis." We will use this method to analyze the uniform box waveguide in this chapter; however, the real power of Path Analysis will not become apparent until we begin our study of the asymmetric linear tailored gain waveguide in Chapter 5, where we will see that it allows analytical calculation of waveguide properties using some simple geometric and algebraic arguments.

In general, a waveguide eigenmode must be described in terms of a linear combination of the two linearly independent solutions of the second order differential Helmholtz equation (2.5.4) inside the waveguide. In the case of the uniform box waveguide, these are the sine and cosine functions. The boundary conditions then determine the relative contribution of each of the two linearly independent solutions to the optical field on each side of the interface. However, it is often possible to simplify the analysis by eliminating one of the independent solutions by suitable choice of the coordinate system. For example, if the origin is taken to be at the center of the box waveguide, symmetry implies that each eigenmode has a definite parity, either even or odd, corresponding to the cosine or sine functions, respectively. Thus, the symmetry of the waveguide allows the eigenmode to be described entirely in terms of the properties of either the cosine function (symmetric modes) or sine function (antisymmetric modes).

Figure 2.13 illustrates the use of Path Analysis for the simple case of a real index box waveguide. The boundary conditions require (1) that $E(x)$ and $\frac{dE(x)}{dx}$

be continuous at the edges $\pm\ell/2$ of the waveguide, and (2) that the electric field outside the waveguide be an evanescent exponential.

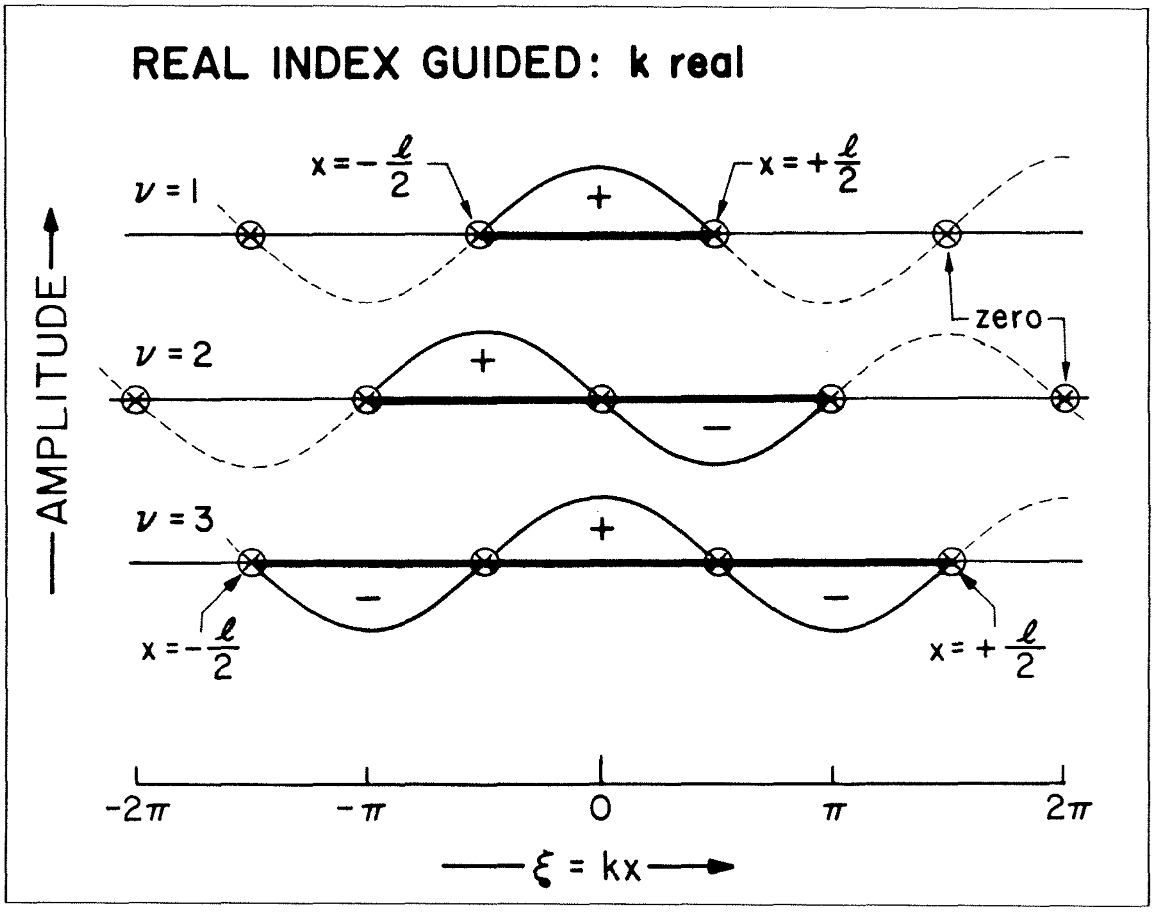

FIGURE 2.13 Path analysis for a wide real index guided box waveguide showing the path of the argument kx of the sine or cosine function along the real axis for the first three modes.

For a well-confined mode, the argument kx must be approximately equal to a zero of the cosine or sine function when $|x| = \frac{\ell}{2}$. This is shown by the endpoints of the heavy solid horizontal line in Figure 2.13. This line plots the line $\mathcal{L}$ that the argument $\xi = kx$ of the sine or cosine function follows along the real axis for the first three modes in a wide real index waveguide with many well-confined modes. For the fundamental mode, the line starts near $\xi = -k\ell/2 \approx -\pi/2$ and ends near $\xi = +k\ell/2 \approx +\pi/2$. Equation (2.6.5) shows that the length of the line $\mathcal{L}$ increases with the mode number ν. In a real index waveguide, k is real so that $\mathcal{L}$ is restricted to the real axis.

Figure 2.13 also plots the sine and cosine functions using a solid line for the first three modes, thus yielding the $\nu = 1, 2, 3$, modes of Figure 2.11. Since the sine and cosine function vary between 0 and ±1 along the real axis, the minima of the electric field will all be exact nulls, while the intensity maxima will be the same for each peak across the guide, as shown in Figure 2.11b.

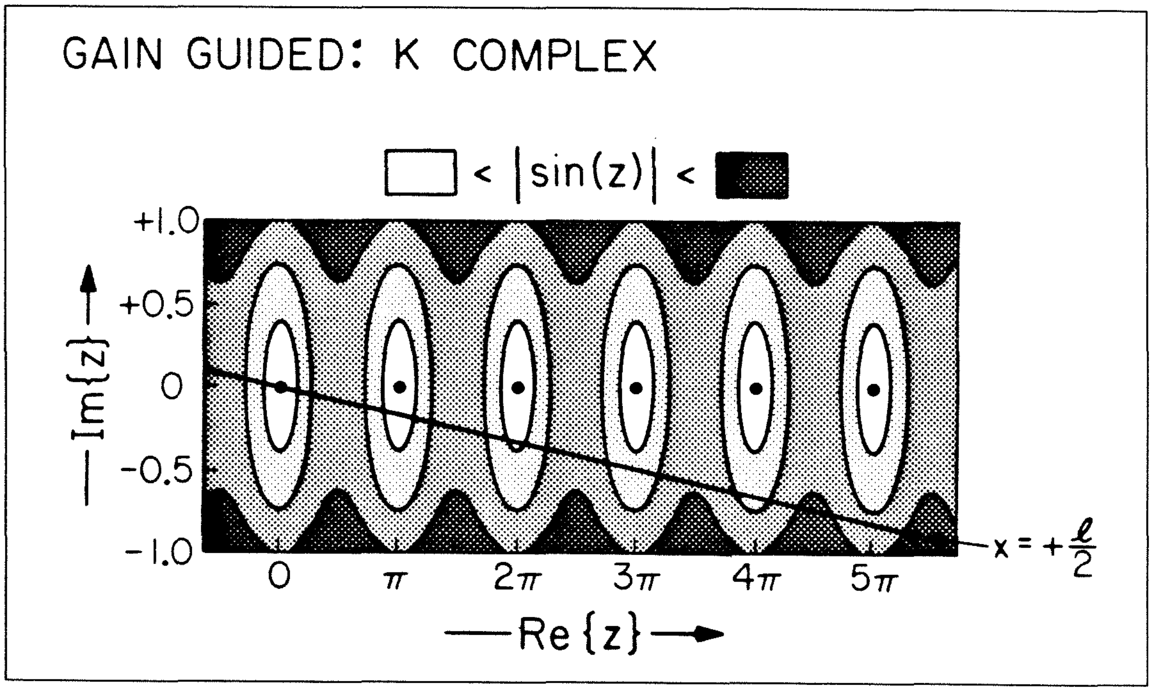

FIGURE 2.14 Path analysis for a wide gain guided box waveguide showing the path of the argument kx of the sine or cosine function in the complex plane for the $\nu = 11$ mode. The values of the complex sine function are indicated using level lines.

Now consider the case of a *gain guided* box waveguide of Figure 2.12. The eigenvalue η and wavevector k are now complex, and the path of the argument $\mathcal{L} : z = kx$ of the sine or cosine function is no longer restricted to the real ξ axis. It now makes an angle $\theta = \tan^{-1}\frac{\Im m\{k\}}{\Re e\{k\}}$ with the real axis, and will cross it only once at the exact center of the waveguide when $x = 0$. We therefore need to consider $\sin z$ or $\cos z$ as a function of the complex argument $z = (\bar{k} + i\bar{\bar{k}})x$. Figure 2.14 shows a plot of the level lines of $|\sin z|$ near the real axis along with the path $\mathcal{L}$ for the $\nu = 11$ mode of a very wide waveguide. Since the only zeros of the sine and cosine functions occur along the real axis, we see that there will only be one exact null in a gain guided box waveguide at $x = 0$. The exponential growth of the sine and cosine functions *away* from the real axis suggests that the intensity of the optical field will also grow exponentially away from the center of the waveguide.

Physically, this is due the incomplete reflection of the wave at the edge of the waveguide, which in turn leads to net power flow away from the waveguide core into the surrounding lossy media. This causes the phase fronts of the mode in the core region to be curved (see §2.6(b) and 3.5(c.ii)). Mathematically, we can write the electric field intensity inside the waveguide as

$$\begin{aligned} I(x) &= |E(x)|^2 \\ &= \left|\cos(\bar{k} + i\bar{\bar{k}})x\right|^2 \\ &= \cos^2 \bar{k}x + \sinh^2 \bar{\bar{k}}x \ . \end{aligned} \tag{2.6.7}$$

The nearfield pattern of a high order mode have an envelope function which grows exponentially away from the center of the waveguide. These results are plotted in Figure 2.15, which compares the high order $\nu = 11$ mode of a real index and gain guided box waveguide, clearly illustrating the effect of the complex k vector and its effect on the nearfield pattern.

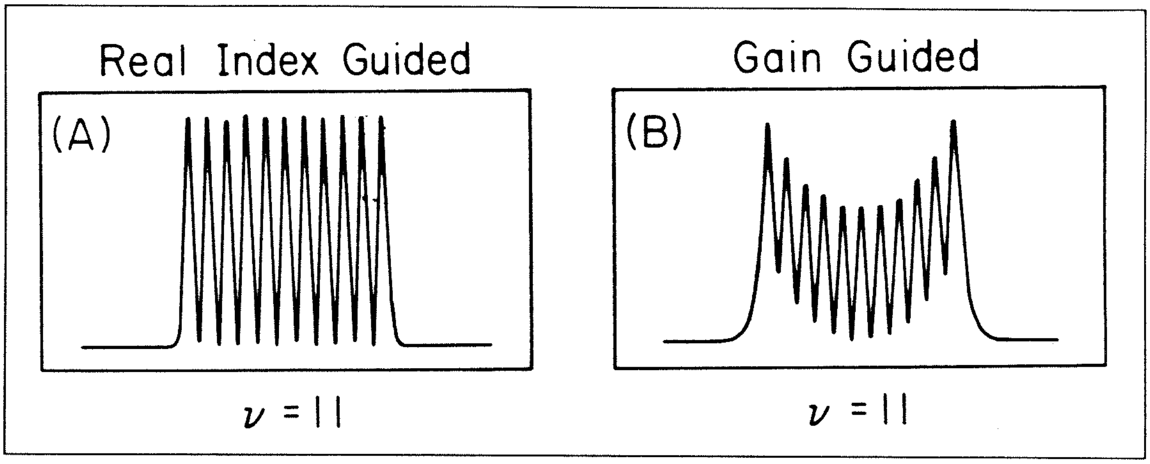

FIGURE 2.15 Comparison of the $\nu = 11$ mode for (a) real index and (b) gain guided box waveguide showing the effect of the complex k vector on the nearfield pattern.

Although the preceding discussion was directed towards waveguides which support many high order modes, we remark that the complex k vector also has an effect on the width of the fundamental mode when compared with an equivalent real index guided mode (see Figure 2.9). The evanescent wavevector g of Equation (2.6.5) is also complex. This has a very important effect on the modes of *coupled* gain guided box waveguides (see §3.5(c.ii)), and may lead to enhanced coupling between the elements in an array of gain guided lasers$^{(\S 3.5(c.ii))}$.

§2.7 Numerical Solutions for Arbitrary Waveguides

The Helmholtz equation (2.5.4) describing optical wave propagation in a dielectric media may be solved exactly over all space only for a few continuous index profiles $n(x)$ such as the quadratic and inverse cosh distributions.[4,4] As we saw in §2.6, the effect of step discontinuities, such as those encountered by the standard double heterostructure, may be included by solving the Helmholtz equation within piecewise continuous regions of space and then requiring that the electric field and its derivative be continuous at the interface. This technique works well for the simple case of a double heterostructure because the eigenfunctions of the free space Helmholtz equations are the sine and cosine functions, which are easy to evaluate numerically.

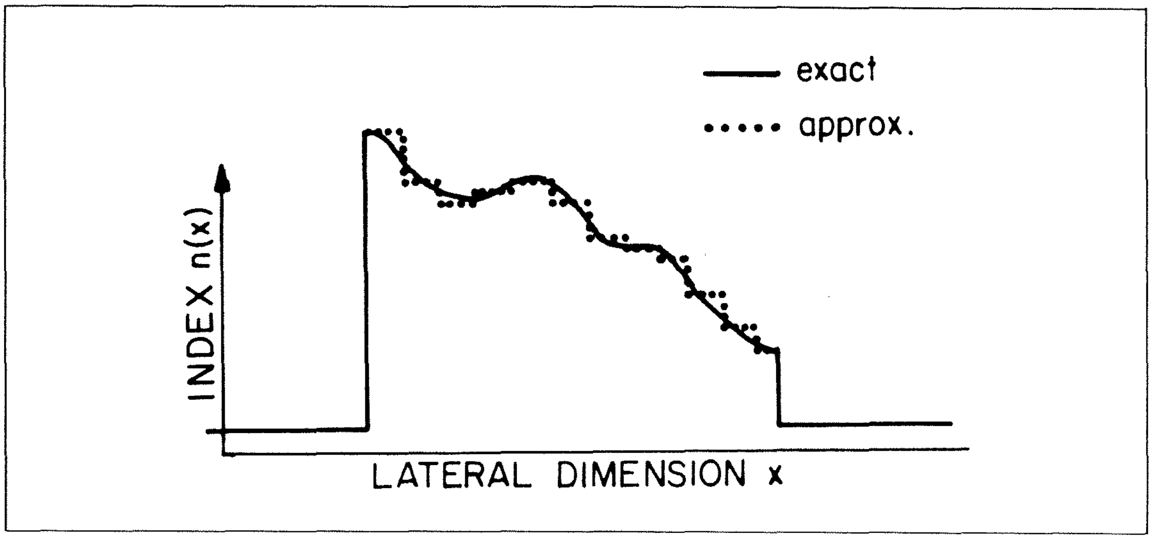

FIGURE 2.16 Numerical approximation for complicated waveguides showing an arbitrary index profile (solid line) and its slab waveguide approximation (dashed line).

As illustrated in Figure 2.16 the same technique may be used to obtain the approximate eigenvalues of waveguides with more complicated index profiles by subdividing a wide waveguide with a continuously varying index of refraction into many smaller contiguous slab waveguides, each having a *constant* index of refraction. The electric field inside each elemental slab waveguide may then be written in terms of the sine and cosine functions (or, alternatively, as complex exponentials). Matching the boundary conditions at each interface and requiring that the field decay evanescently outside the waveguide yields an eigenvalue equation which may be solved numerically. The net effect of this approach is to transform the Helmholtz equation from a second order differential equation into an *algebraic* equation whose roots give approximations for the eigenvalues.

§2.7 Numerical Solutions for Arbitrary Waveguides

We use a matrix propagation technique which has found application in quantum mechanics[40] and in the study of periodically stratified optical media[41] and extend its use to waveguides with arbitrary index and gain profiles. We write the electric field at any point x inside the r^{th} elemental slab waveguide as a superposition of traveling waves moving to the left and right:

$$E_r(x) = \left(a_r e^{+ik_r x} + b_r e^{-ik_r x}\right) e^{i(k_0 \eta z - \Omega t)} \qquad r = 1, 2, \ldots n; \tag{2.7.1}$$

a_r and b_r are constant coefficients, which are, in general, complex. Ω is the angular frequency of the optical wave, and k_r is the spatial lateral wavevector in the r^{th} slab which is defined by

$$k_r = k_0 \sqrt{n_r^2 - \eta^2} \tag{2.7.2}$$

where k_0 is the free space wavevector $\frac{2\pi}{\lambda}$, n_r is the (possibly complex) index of refraction in the r^{th} layer, and η is the effective index of the eigenmode. In what follows, the z and t dependence is superfluous, and so we drop the second exponential product in (2.7.1).

If we write the electric field in Equation (2.7.1) in vector form

$$E_r(x) = \left[e^{+ik_r x} \;,\; e^{-ik_r x}\right] \begin{bmatrix} a_r \\ b_r \end{bmatrix} \tag{2.7.3}$$

and match the boundary conditions at the interface between the r^{th} and $r^{th} + 1$ layer. We can derive a relationship between the a and b coefficients on each side of the interface in terms of a matrix equation

$$\begin{bmatrix} a_{r+1} \\ b_{r+1} \end{bmatrix} = I_r \begin{bmatrix} a_r \\ b_r \end{bmatrix} \tag{2.7.4}$$

where the *interface propagation matrix* I is given by

$$I_r = \frac{1}{2k_{r+1}} \begin{bmatrix} k_{r+1} + k_r & k_{r+1} - k_r \\ k_{r+1} - k_r & k_{r+1} + k_r \end{bmatrix} . \tag{2.7.5}$$

Similarly, after free space propagation a distance l through the layer, the electric field becomes

$$\begin{aligned} E_r(x+l) &= a_r e^{+ik_r(x+l)} + b_r e^{-ik_r(x+l)} \\ &= a_r' e^{+ik_r x} + b_r' e^{-ik_r x} \ . \end{aligned} \tag{2.7.6}$$

The new coefficients a_r' and b_r' are given by the matrix equation

$$\begin{bmatrix} a_r' \\ b_r' \end{bmatrix} = \mathcal{F}_r \begin{bmatrix} a_r \\ b_r \end{bmatrix} \tag{2.7.7}$$

where the *free space propagation matrix* $\mathcal{F}_r$ is given by

$$\mathcal{F}_r = \begin{bmatrix} e^{ik_r l} & 0 \\ 0 & e^{-ik_r l} \end{bmatrix} \ . \tag{2.7.8}$$

Given arbitrary a_L and b_L coefficients at the far left of a guide with n layers, the corresponding a_R and b_R coefficients at the right of the guide may be found by multiplication of the $\mathcal{F}$ and $\mathcal{I}$ matrices:

$$\begin{bmatrix} a_R \\ b_R \end{bmatrix} = \begin{bmatrix} A & B \\ C & D \end{bmatrix} \begin{bmatrix} a_L \\ b_L \end{bmatrix} \tag{2.7.9}$$

where

$$\mathcal{M} \equiv \begin{bmatrix} A & B \\ C & D \end{bmatrix} = \mathcal{I}_n \mathcal{F}_n \mathcal{I}_{n-1} \mathcal{F}_{n-1} \cdots \mathcal{I}_2 \mathcal{F}_2 \mathcal{I}_1 \tag{2.7.10}$$

and the layers are numbered from left to right.

For a real index waveguide, the fields must be evanescent in the cladding region, so that k_L and k_R are imaginary. If we write

$$k_{L,R} = i\, g_{L,R} \tag{2.7.11}$$

the exponential functions then have real arguments $g_{L,R}$:

$$\begin{bmatrix} e^{+ikx} \\ e^{-ikx} \end{bmatrix} \longrightarrow \begin{bmatrix} e^{-gx} \\ e^{+gx} \end{bmatrix} \ . \tag{2.7.12}$$

For a guided mode, the coefficients a_L and b_R to the exponentially growing terms must be zero. This leads to the dispersion relationship

$$D = 0\ . \tag{2.7.13}$$

This result may also be derived by invoking the radiation condition that allows only outward traveling waves to contribute to the field of a guided mode. Gain guided waveguides are similar, but the condition (2.7.11) becomes $\Im m\{kx\} < 0$. The dispersion relation (2.7.13) remains unchanged, but the k_r are complex.

As an example, consider the symmetric three layer slab waveguide

$$n(x) = \begin{cases} n_1 = n_e & -\infty < x \le 0^- \\ n_2 = n_0 & 0^+ \le x \le \ell^- \\ n_3 = n_e & \ell^+ < x < \infty \end{cases} \tag{2.7.14}$$

where n_e and n_0 are (possibly complex) constants. The evanescent wave vectors in regions 1 and 3 are imaginary, $k_L = k_R = ig$ and the propagation matrix is simply $\mathcal{M} = \mathcal{I}_2 \mathcal{F}_2 \mathcal{I}_1$. The eigenvalue condition becomes

$$0 = D_{\text{three layer}} = \frac{(ig+k)^2 e^{-ik\ell} - (-ig+k)^2 e^{+ik\ell}}{4ikg} \tag{2.7.15}$$

where k and g are given by Equation (2.6.5). Equation (2.7.15) reduces to

$$\tan(k\ell/2) = \begin{cases} -k/g & \text{(positive root} \rightarrow \text{symmetric modes)} \\ -g/k & \text{(negative square root} \rightarrow \text{antisymmetric modes)} \end{cases} \tag{2.7.16}$$

which is the eigenvalue equation (2.6.6).

This method may be extended to slab waveguides with more layers, although the analytic results rapidly become unwieldly. The multilayer slab approximation to a continuous waveguide is a good one provided that $k_r l_r$ is not too large. From a numerical point of view the series of 2×2 matrix computations (2.7.10) are easy to perform for any number of layers. D may be considered a function of η, with the zeros to be found numerically. For real index waveguides, η is real, and the zeros of D are easy to find. If, however, the effects of gain and/or loss are to be considered, η becomes complex, and it is necessary to search a two-dimensional parameter space $\Re\mathrm{e}\{\eta\} \otimes \Im\mathrm{m}\{\eta\}$. The problem is further complicated because D is not analytic due to the branch points arising from the square-root dependence of k on η in Equation (2.7.2). Therefore, complex root finders which make use of the analyticity of the function cannot be easily used. Furthermore, from the point of view of semiconductor laser design, it is important to find *all* of the modes with high modal gains, and especially the mode that has the highest modal gain because that will be the lasing mode at threshold.

In waveguides in which gain is not a perturbation (*e.g.*, in a gain guided laser), the task of finding the zeros of D is considerably simplified by the equivalent technique of minimizing $|D|$. We find that it is not unusual for $\nabla |D|$ to be very large, often as much as 10^{20}. As a result, automated root finders often miss roots. This problem can be minimized by making use of a contour plot of $|D|$; roots may be approximately located merely by the structure they introduce into the contour lines.

For example, inspection of the contour plot of Figure 2.17 shows that there is almost certainly a root within the area enclosed by box B, while there may be one in the box marked C. Note that the minimum value of $|D|$ in box B is 10^3; the gradients are so steep in this region that an automated root finder will probably miss the root unless the program is given a good initial guess. Furthermore, it is obvious that there are no roots to be found within box A; this is the most effective way of insuring that all the high gain modes have been found.

Once the eigenvalues have been found, the electric field may be calculated by setting $\binom{a_L}{b_L}$ to $\binom{0}{1}$, multiplying by I_1 to get the a and b coefficients inside the first

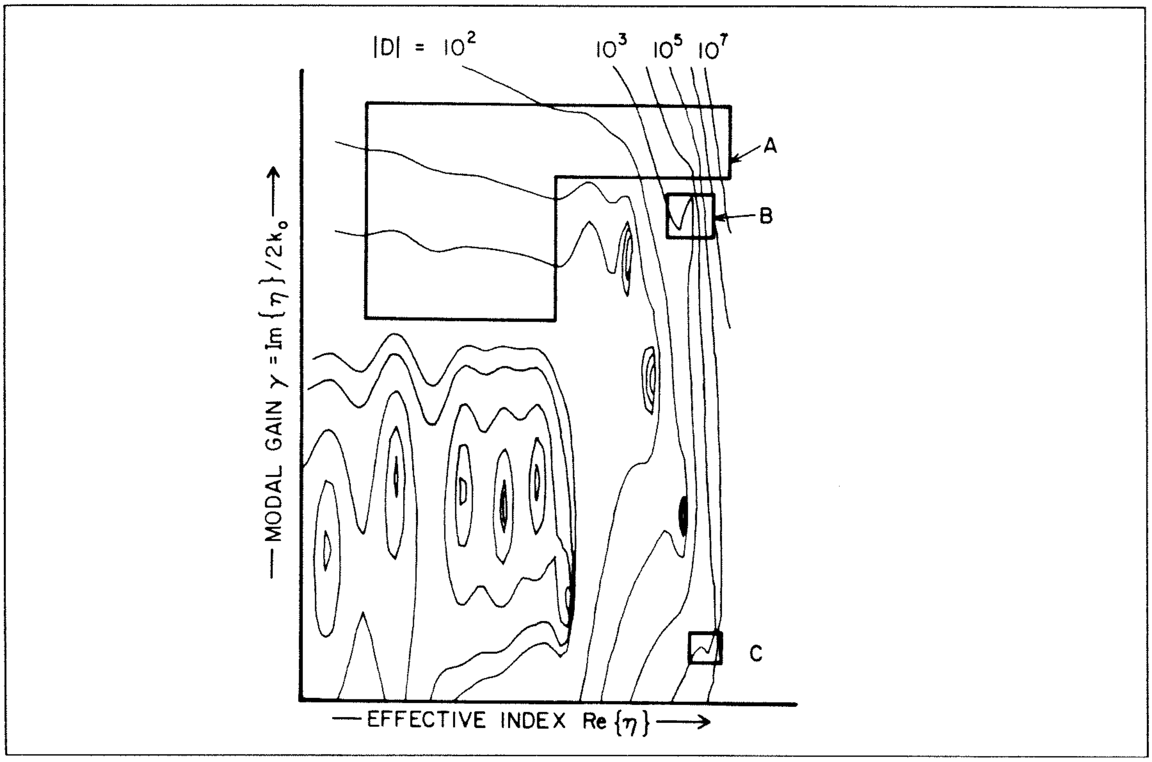

FIGURE 2.17 Contour plot of the level lines of the magnitude of the dispersion function of a complicated waveguide showing several regions of particular interest.

layer, using (2.7.1) with $x = 0$ taken to be the left edge of the layer to get the electric field within the layer, then using (2.7.4) to cross the boundary, *etc.*

Finally, we remark that, if one starts with an *a priori* index and gain distribution, the method applied here is valid only for the unsaturated waveguide (*i.e.*, only at threshold). However, an iterative scheme could easily be devised which includes the effects of gain saturation via the rate equations. The effect of gain saturation is to reduce the mode discrimination between the modes; therefore, an accurate model requires that *all* the high gain modes be identified. This can be easily done with the method described here.

A listing of the essential parts of the MODES and the CONTOUR plotting computer programs used to calculate the dispersion function D, and to calculate the nearfield and farfield patterns of a mode are given in the Appendix. We have made extensive use of these programs throughout this thesis.

CHAPTER
THREE
Two Coupled Lasers

Better two than one by himself,
since thus their work is really profitable.

—Ecclestiastes 4:9

In this Chapter, we consider in detail the very simplest possible array, that of two coupled box waveguides. When two waveguides are placed close together so that their optical fields overlap, an optical eigenmode of one of the individual waveguides will not be an eigenmode of the composite two waveguide system. If each waveguide supports only the fundamental mode, to an excellent degree of approximation, the new eigenmode will be given by a *linear combination* of the two individual waveguide modes. In a laser, the mode of the composite system with the highest modal gain will be the lasing mode. We therefore need to find an expression for this mode's effective index, as well as its nearfield and farfield pattern.

We consider weakly coupled real index guided waveguides in §3.1, strongly coupled waveguides in §3.2, show which classes of coupled waveguides have phase matching wavelengths in §3.3, and give a means of designing two coupled waveguides with a given phase matching wavelength in §3.1(a). We then take up the effect of gain on weakly coupled waveguides in §3.4. Finally, the complex character of the wavevectors for the case of two strongly coupled gain induced waveguides makes these systems especially interesting; they are studied both theoretically and experimentally in §3.5.

§3.1 Coupled Mode Theory of Weakly Coupled Waveguides

The solution of the Helmholtz equation with an index profile consisting of two adjacent waveguides may be found by use of the coupled mode equations. These equations and their derivation have been extensively discussed in the literature; thus here we merely present an outline of their derivation with a view to understanding their applicability and limitations when applied to the understanding of phased array semiconductor lasers.

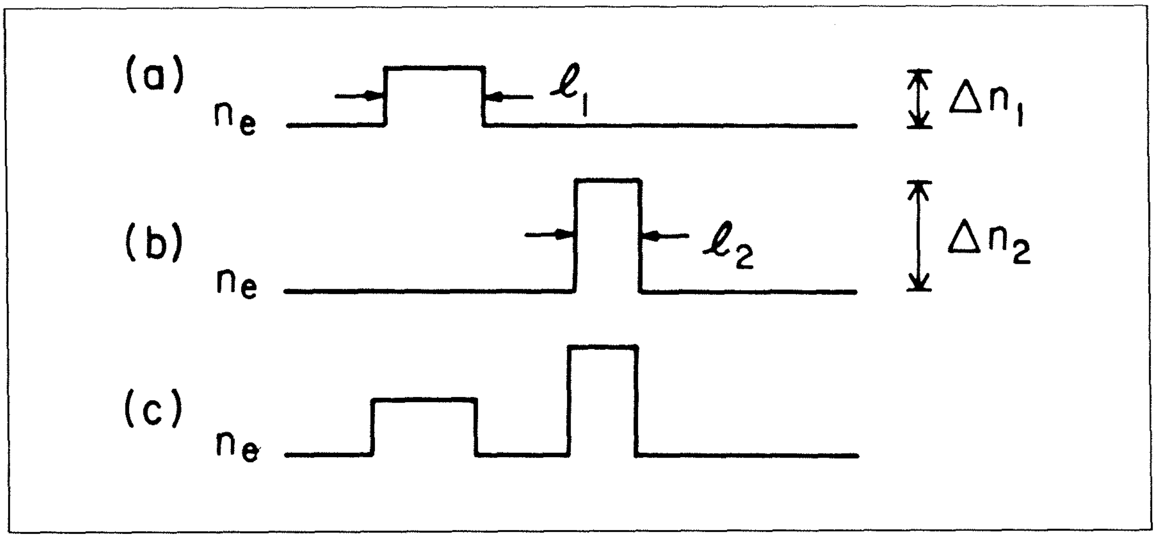

FIGURE 3.1 Spatial variation of the refractive index for two uncoupled waveguides (a) $n_1(x)$ and (b) $n_2(x)$, and (c) the two coupled waveguides $n(x)$.

Following Yariv,[1,2] we consider the case of the two planar waveguides illustrated in Figure 3.1. Refractive index distributions for the individual two guides are given by $n_1(x)$ in Figure 3.1a and $n_2(x)$ in Figure 3.1b. The spatial refractive index variation for the combined two waveguide system, which is shown in Figure 3.1c, is given by

$$n^2(x) = n_1^2(x) + n_2^2(x) - n_e^2 \tag{3.1.1}$$

where n_e is the common cladding index external to all the core regions. We will often use the term "channel region" interchangably with "core region" and "interchannel region" to refer to the cladding layer between the waveguides.

We denote the eigenmodes of guide 1, 2 as $E_{1,2}(x)e^{i\beta_{1,2}z}$ with both fields assumed normalized by Equation (2.6.4). We also assume without loss of generality that $\beta_2 > \beta_1$. For many purposes, the mode propagation constants $\beta_{1,2} = k_0\eta_{1,2}$ are more convienient to use for analytical calculations than are the mode effective indices $\eta_{1,2}$; we will use both formalisms interchangeably.

The eigenmodes of the combined guide are denoted by $E(x,z)$. In the limit of weak coupling, E may be approximated as a linear combination of the electric fields in the two elemental waveguides:

$$E(x,z) = \frac{1}{2}\left\{A_1(z)E_1(x)e^{i\beta_1 z} + A_2(z)E_2(x)e^{i\beta_2 z}\right\} \qquad + c.\ c. \tag{3.1.2}$$

where $c.\ c.$ represents the complex conjugate. In the absence of coupling — that is, if the distance between the waveguides were infinite — $A_1(z)$ and $A_2(z)$ will not depend on z and will be independent of each other since each of the two terms on the right-hand side of (3.1.2) satisfies the Helmholtz equation (2.5.4) separately. When the guides are placed in close proximity, an eigenmode of the composite system has the property that the shape of the mode (*i.e.*, the ratio $|A_2(z)|\,/\,|A_1(z)|$ is independent of z). This implies that (3.1.2) may be rewritten as(§3.2)

$$E(x,z) = \left[E_1(x) + \varrho\, E_2(x)\right] e^{i\beta z}\ . \tag{3.1.3}$$

We desire to find the new mode propagation constant β and the admixture factor ϱ which relates the optical amplitude in one guide to that in the other.

If we define a column vector $\mathbf{E}(z)$ to represent the two terms in (3.1.2)

$$\mathbf{E}(z) = \begin{bmatrix} A_1(z)e^{i\beta_1 z} \\ A_2(z)e^{i\beta_2 z} \end{bmatrix} \equiv \begin{bmatrix} E_1(z) \\ E_2(z) \end{bmatrix} \tag{3.1.4}$$

then the evolution of $\mathbf{E}(z)$ is described by the matrix equation

$$\frac{d\mathbf{E}}{dz} = i\mathcal{C}\mathbf{E} \tag{3.1.5}$$

with

$$\mathcal{C} = \begin{bmatrix} \beta_1 & \kappa_{12} \\ \kappa_{21} & \beta_2\,. \end{bmatrix} \tag{3.1.6}$$

The coupling coefficients $\kappa_{\substack{12\\21}}$ are given by[3]

$$\kappa_{\substack{12\\21}} = \frac{1}{4}\frac{k_0}{Z_0}\int_{-\infty}^{\infty}\left[n_{\substack{1\\2}}^2(x) - n_e^2\right] E_1(x)E_2(x)\,dx\ . \tag{3.1.7}$$

where $Z_0 = \sqrt{\frac{\mu_0}{\epsilon_0}}$ is the impedance of free space. The new propagation constants β and the admixture factor ϱ are given by the eigenvalues and eigenvectors of the matrix (3.1.6).

The eigenvalues of (3.1.6) are given by the roots of the secular equation

$$\begin{vmatrix} \beta_1 - \beta & \kappa_{12} \\ \kappa_{21} & \beta_2 - \beta \end{vmatrix} = 0\ . \tag{3.1.8}$$

Since the two basis vectors $E_{1,2}(x)$ are assumed to be orthogonal, the diagonalization of the perturbed matrix (3.1.6) also yields two eigenvectors, denoted $E^{\pm}(x)$, which are known as the "supermodes"[4] of the composite waveguide. They may be written as

$$\mathbf{E}^{\pm}(z) = \begin{bmatrix} 1 \\ \varrho^{\pm} \end{bmatrix} e^{i\beta^{\pm}z} \tag{3.1.9}$$

where

$$\beta^{\pm} = \tilde{\beta} \pm \sqrt{\Delta^2 + \kappa^2} \tag{3.1.10}$$

is the propagation constant of the $(\pm)$ supermode and $\kappa \equiv \sqrt{\kappa_{12}\kappa_{21}}$ is the mean coupling constant. The average propagation constant $\tilde{\beta}$ and phase mismatch parameter Δ are defined to be

$$\begin{aligned} \tilde{\beta} &= \tfrac{1}{2}(\beta_1 + \beta_2) \\ \Delta &= \tfrac{1}{2}(\beta_1 - \beta_2)\ . \end{aligned} \tag{3.1.11}$$

Finally, the admixture factor $\varrho^{\pm}$ is given in terms of the normalized phase mismatch parameter δ

$$\begin{aligned}\varrho^{\pm} &= \delta \pm \sqrt{1+\delta^2} \\ &= \pm \exp(\pm \sinh^{-1}\delta)\end{aligned} \qquad \delta \equiv \frac{\Delta}{\kappa} \,. \tag{3.1.12}$$

The special condition $\delta = 0$ (which corresponds to $\beta_1 = \beta_2$) is referred to as the *phase matching point.* Obviously, identical waveguides will be phase matched at all wavelengths, while nonidentical waveguides, having differing dispersion curves (see Figure 3.3), will not be phase matched except at a possible *phase matching wavelength* λ_p. We note in passing that not all waveguides have a phase matching wavelength; we will discuss this point further in §3.3.

The phase matching wavelength is a very important number which characterizes a system of two coupled waveguides. Equation (3.1.12) shows that far away from the phase matching wavelength $\delta \to \infty$ and the supermodes are identical to the modes of the isolated waveguides:

$$E^{+}(z) \longrightarrow \begin{bmatrix}0\\1\end{bmatrix} e^{i\beta_2 z} \qquad E^{-}(z) \longrightarrow \begin{bmatrix}1\\0\end{bmatrix} e^{i\beta_1 z} \qquad (\beta_2 > \beta_1) \,. \tag{3.1.13}$$

As the two waveguides become more closely phase matched, the supermode becomes more equally distributed between the two waveguides. At the phase matching wavelength $\delta = 0$, the admixture factor is unity, and equal power flows in each guide. The solutions $E^{\pm}(z)$ become

$$E^{+}(z) \longrightarrow \begin{bmatrix}1\\1\end{bmatrix} e^{i\beta^{+} z} \qquad E^{-}(z) \longrightarrow \begin{bmatrix}1\\-1\end{bmatrix} e^{i\beta^{-} z} \,. \tag{3.1.14}$$

This is, of course, to be expected in the special case of two identical waveguides where, by symmetry, $|\varrho|$ must be unity, and since all the quantities in (3.1.12) are real, the phase of the fields can only be either 0 or π. The inphase addition of the two modes (corresponding to β^{+}) is usually referred to as the (++) supermode, while the out-of-phase combination (corresponding to β^-) is referred to as the $(+-)$ supermode. Equation (3.1.14) also applies to two dissimilar waveguides at the phase matching wavelength.

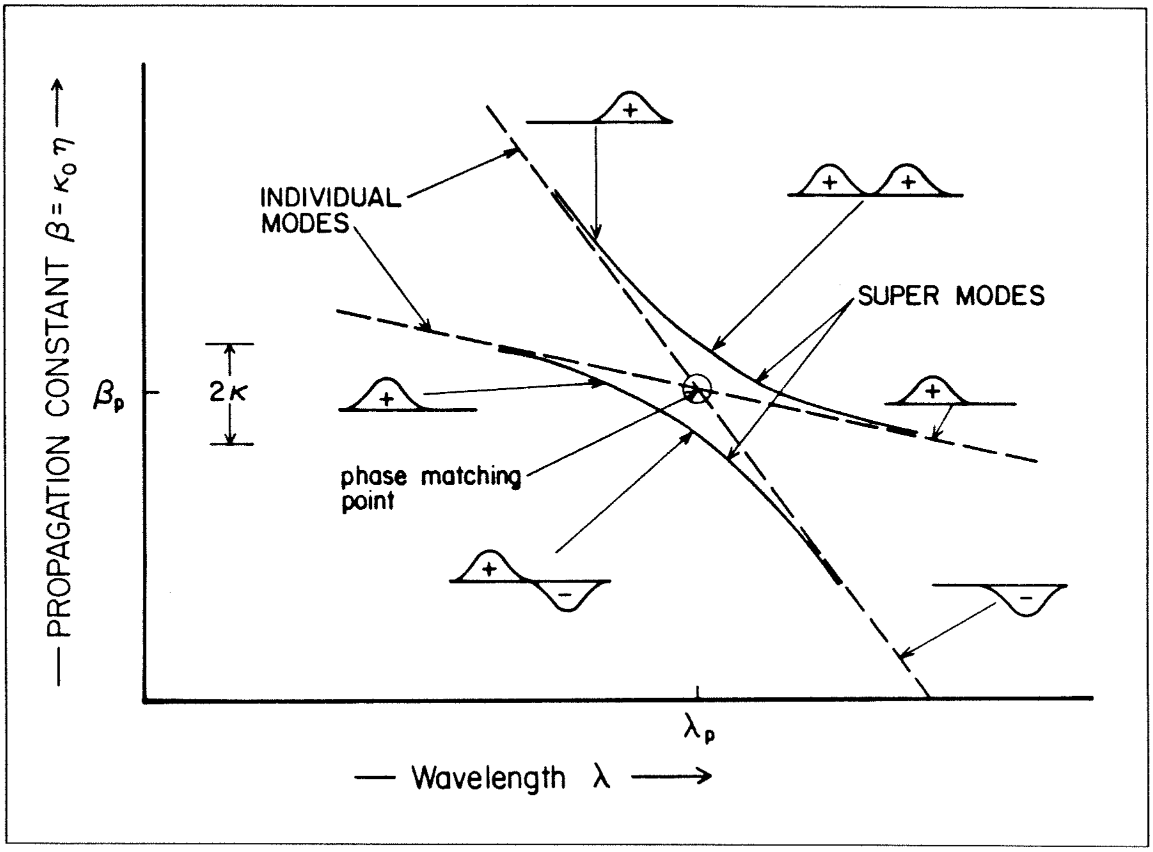

FIGURE 3.2 Schematic diagram of supermodes near the phase matching wavelength.

These results are shown schematically along with the dispersion curves for the coupled waveguide system in Figure 3.2. The individual unperturbed dispersion curves are indicated by the straight dashed lines, while the supermodes of the composite waveguide are shown as the solid curves. The phase matching wavelength is indicated by the intersection of the two dashed lines. Far away from the phase matching wavelength, the dispersion curves for the two supermodes are asymptotic to the dispersion curves for the uncoupled individual waveguide modes. Near the phase matching wavelength at which the two individual waveguide modes cross, the dispersion curves of the supermodes separate. The difference in the supermode propagation constants at the phase matching point is then simply twice the coupling constant.

(a) Calculation of the Phase Matching Wavelength

From the point of view of optoelectronic device design utilizing two nonidentical waveguides, it is important to know the location of the phase matching wavelength λ_p. Given two arbitrary waveguides, the phase matching wavelength can usually be found only by numerically solving the dispersion equation (2.6.6) for each individual uncoupled waveguide separately. However, for the case of two nearly identical coupled waveguides, it is possible to derive a general relationship between the waveguide parameters so that two guides may be designed around a predetermined phase matching wavelength (*e.g.*, within the spectral gain curve of $GaAs$).[5]

We start with the dispersion equation (2.6.6) for the fundamental mode of a box waveguide, and write it as an explicit function of the parameters defining the guide. Equation (2.6.6) is of the form

$$D(x_i^0) = D(n_e, n_0, \lambda, \ell, \eta) = k\ell/2 \tan k\ell/2 - g\ell/2 = 0 \tag{3.1.15}$$

where$^{(\S 2.6)}$

$$\begin{aligned} k &= \frac{2\pi}{\lambda}(n_0^2 - \eta^2)^{1/2} \\ g &= \frac{2\pi}{\lambda}(\eta^2 - n_e^2)^{1/2} \end{aligned} \tag{3.1.16}$$

and the x_i^0 represent the five parameters $n_e, n_0, \lambda, \ell, \eta$ which define a mode in a box waveguide. Equation (3.1.15) is an implicit relationship among these five parameters. If we expand the dispersion equation (3.1.15) for the second waveguide about the unperturbed parameter values of the first guide using a first order Taylor expansion, we can write

$$D(x_i^0 + \delta x_i) \simeq D(x_i^0) + \sum_i \frac{\partial D}{\partial x_i}\bigg|_{x_i = x_i^0} \delta(x_i) = 0 \tag{3.1.17}$$

where x_i represent the parameters corresponding to the first guide and $\delta(x_i)$ represent the differences between the two waveguides. Since the dispersion equation $D(x_i^0) = 0$ is satisfied for the unperturbed parameter values, Equation (3.1.17) establishes a linear relationship between the partials of D and changes in at most four of the five parameters:

$$A\,\delta(n_e) + B\,\delta(n_0) + C\,\delta(\lambda) + E\,\delta(\ell) + F\,\delta(\eta) = 0\ . \tag{3.1.18}$$

For example, if we allow changes only in the width ℓ of the guide and the core index n_0, $\delta(\ell)$ and $\delta(n_0)$ are related by

$$\delta(\ell) = -\frac{B}{E}\delta(n_0) = \frac{a\,b}{g - a\,k}\,\delta(n_0) \tag{3.1.19}$$

where

$$\begin{aligned} a &= \frac{k\ell/2}{\cos^2(k\ell/2)} + \tan(k\ell/2) \\ b &= \frac{k_0\ell}{(k/k_0)} n_0 \end{aligned} \tag{3.1.20}$$

and k and g are given by Equation (3.1.16). We remark that essentially the same relationships may be obtained using first order perturbation theory;[6,7] the present method has the great advantage that it does not require *a priori* knowledge of the electric field and power filling factors, and also that the method may be easily extended to any waveguide for which the dispersion equation is known. It can also be used to derive simple relationships between any other two or three of the parameters in Equation (3.1.18).

§3.1(a) Calculation of the Phase Matching Wavelength

We now consider a numerical example to help explore the limitations of the coupled mode theory. If we start with a guide with the parameters $n_e = 3.550$, $\Delta n \equiv n_0 - n_e = 0.050$, $\ell_1 = 1.0\mu$m, and require the phase matching wavelength to occur at 0.85μm, we find that a waveguide with $\Delta n = 0.051$ will phase match to the first waveguide at $\lambda_p = 0.846975446\mu$m if the width of the second guide has a width $\ell_2 = 0.943274347\mu$m. Equation (3.1.19) does not exactly predict the phase matching wavelength due the effect of the Coulomb self-energy term (see §3.2) on η and the effect of higher order terms in (3.1.17), both of which have been ignored; the exact phase matching wavelength was found numerically. The dispersion curves for these two guides at infinite separation is plotted in Figure 3.3 along with the electric field amplitude at three different wavelengths. Note that the fields become less well-confined at longer wavelengths, and so the coupling between two adjacent waveguides a fixed distance apart will increase as the wavelength increases. Also, there is only one phase matching wavelength; this point will be discused further in §3.3.

(b) Comparison of the Coupled Mode Theory With the Exact Theory

We use the two waveguides of Figure 3.3 to illustrate the predictions of the coupled mode solutions of §3.1 by plotting the exact numerical eigenmodes near the phase matching wavelength (Figure 3.4) and far away from it (Figure 3.5). Close to the phase matching wavelength the predictions of the coupled mode theory appear to be correct: away from the exact phase matching wavelength, the optical field is concentrated in either one or the other of the two guides, while at the phase matching point the admixture factor is unity, as expected.

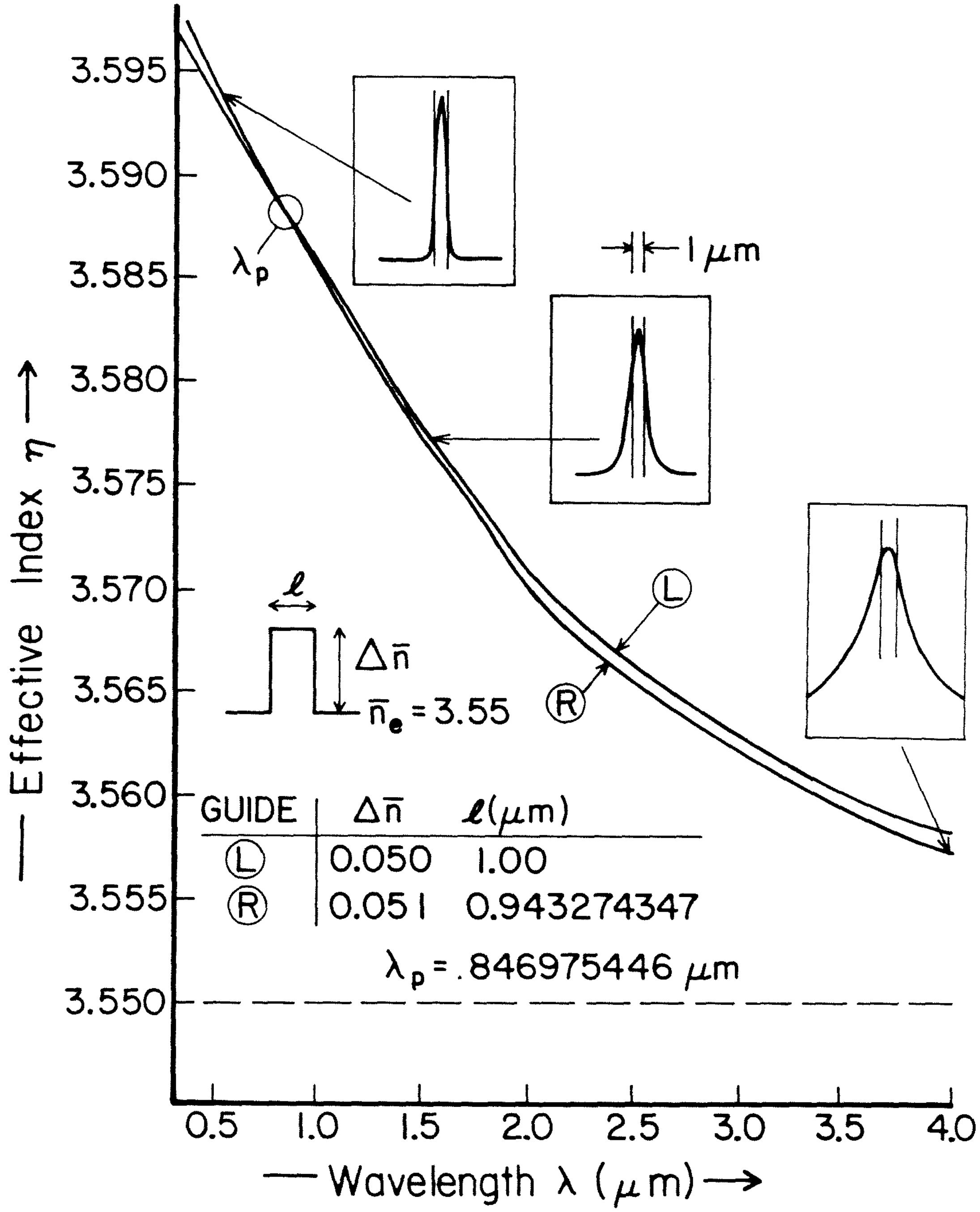

FIGURE 3.3 Dispersion curves for two slightly different real index guided box waveguides. The insets indicate the extent of the field amplitude relative to the guide width t at various wavelengths.

§3.1(b) Comparison of the Coupled Mode Theory With the Exact Theory

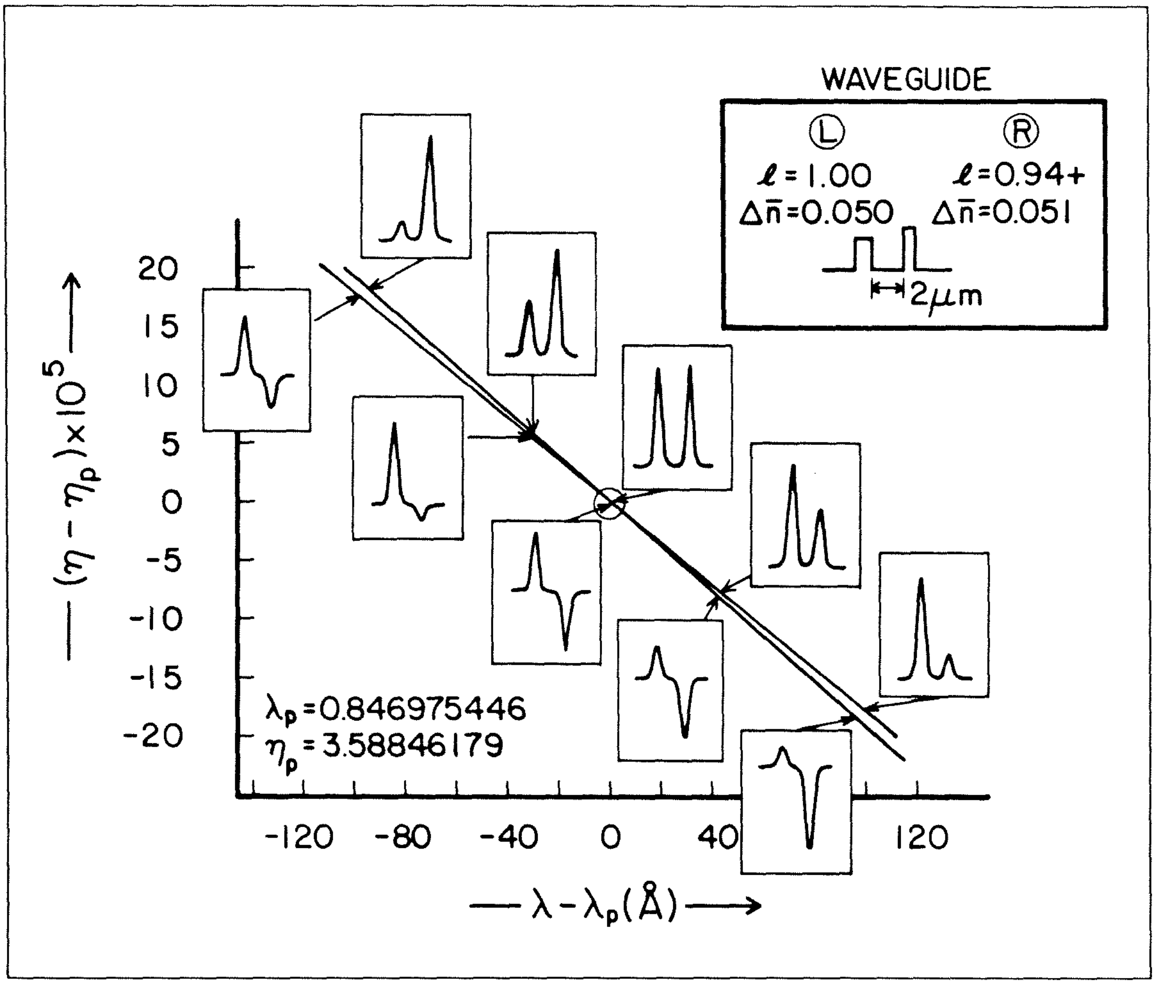

FIGURE 3.4 Exact solutions near the phase matching wavelength for the two waveguides of Figure 3.3 separated by 2μm. Note that they compare well with the coupled mode theory predictions of Figure 3.2.

However, Figure 3.5 shows that far away from the phase matching wavelength in the direction of longer wavelength the admixture factor (which is predicted by the coupled mode theory to *decrease* indefinitely) actually *increases* towards a limiting value of unity! The reasons for this behavior will be discussed in the next section, especially in §3.2(b).

§3.1(b) Comparison of the Coupled Mode Theory With the Exact Theory

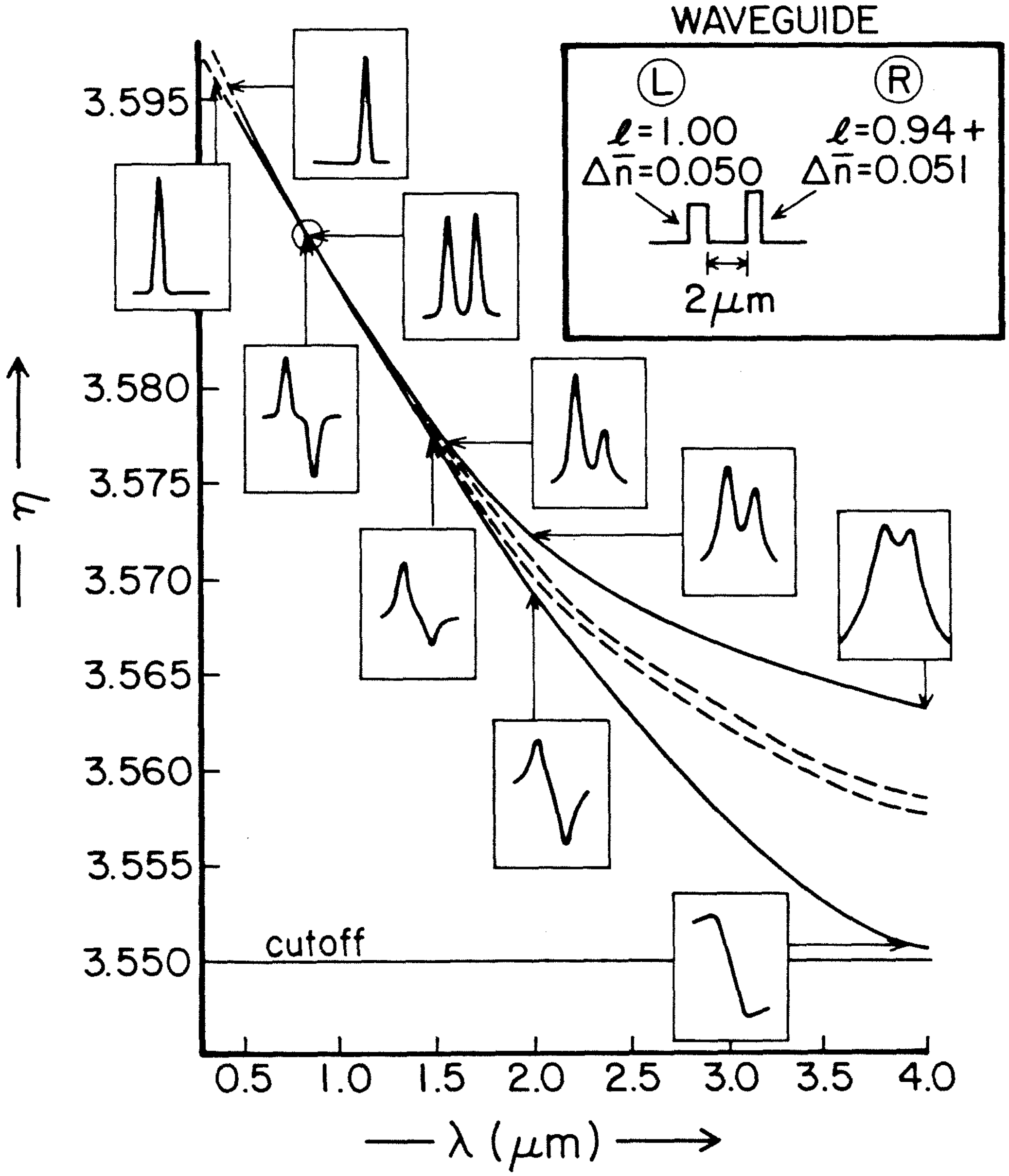

FIGURE 3.5 The solid lines plot the exact solutions far away from the phase matching wavelength for the waveguide of Figure 3.4. The dahsed line shows the dispersion curve of the individual isolated waveguides of Figure 3.3. Note that the coupled mode theory prediction that power flows in only one guide or the other when the waveguides are very phase mismatched is correct at short wavelengths, but is incorrect at long wavelengths (or equivalently, large overlap between the fields).

§3.2 The Quantum Chemistry of Strongly Coupled Waveguides

Three assumptions have been made in the derivation of the coupled mode equations:

(1) that the composite eigenmode can be expressed as a linear combination of the individual eigenmodes (Equation (3.1.2)),

(2) an adiabatic approximation[8] which makes the coupled mode equations (Equation (3.1.5)) first order in z, and

(3) that the individual eigenmodes $E_{1,2}(x)$ in (3.1.2) are orthogonal.

These assumptions restrict application of the coupled mode theory to weakly coupled waveguides in which the optical fields do not overlap strongly. However, as we pointed out in Chapter 1 (and discuss further in §4.6), there are a variety of reasons for wanting to make strongly coupled arrays. We therefore take up the study of two strongly coupled waveguides.

Assumption (1), that the composite eigenmode can be expressed as a linear combination of the individual waveguide modes, ignores the fact that even in the case of a single isolated waveguide, the guided modes are an incomplete basis set because leaky and radiation modes have been ignored.[9] We will show in §3.2(c), however, that for the *symmetric* single slab waveguides we are interested in assembling into laser arrays, the contribution of the leaky and radiation modes can be safely ignored except for the case of very strong coupling.

We will now construct a more precise theory of the coupling between two waveguides that does not assume weak coupling (Assumption (2)) and explicitly takes into account the nonorthogonality of the basis states $E_{1,2}(x)$ (Assumption (3)). This theory is in many ways similar to the quantum mechanical approach known as LCAO theory (for "Linear Combination of Atomic Orbitals")[10] that is used to calculate the wavefunctions and eigenenergies of simple molecules such as the H_2^+ ion; hence the title of this section as "The Quantum Chemistry of Strongly Coupled Waveguides." (This problem has recently been treated by Hardy and Streifer[11] from a slightly different perspective.)

If we rewrite the Helmholtz equation (2.5.4) as

$$\left\{ -\frac{1}{k_0^2}\frac{d^2}{dx^2} + [-n^2(x)] - [-\eta^2] \right\} E(x) = 0 \tag{3.2.1}$$

and compare it with the time independent quantum mechanical Schroedinger Equation

$$\left\{ -\frac{\hbar^2}{2m}\frac{d^2}{dx^2} + V(x) - E \right\} \psi(x) = 0 \tag{3.2.2}$$

we see that the equations are mathematically identical if we make the correspondence

$$\frac{1}{k_0^2} \Leftrightarrow \frac{\hbar^2}{2m} \qquad -n^2(x) \Leftrightarrow V(x) \qquad -\eta^2 \Leftrightarrow E \ . \tag{3.2.3}$$

Although the equations are mathematically similar, there are some differences between the quantum mechanical and electromagnetic theories. First, the time dependent Schroedinger Equation is of first degree in the time variable, while Maxwell's equations are of second degree in both the time and spatial variables. However, as we will show below, this difference is not important for the waveguides of interest here. Secondly, there is no quantum mechanical analog of the optical dispersion curve. Equation (3.2.3) shows the correspondence between the optical wavelength and the quantum mechanical particle mass. Since the free space quantum mechanical electronic mass is a fundamental constant of nature, the optical analogy corresponds to considering only one wavelength. Finally, we note that the effect of gain and/or loss may be conveniently included in the optical formulation through a complex potential which has no analog in the quantum mechanical formulation.

§3.2 The Quantum Chemistry of Strongly Coupled Waveguides

The optical problem of finding the effective indices and electric field for a single real index guided dielectric slab waveguide is therefore essentially equivalent to the quantum mechanical problem of finding the energy levels and wavefunctions for a particle in a finite potential well. As remarked earlier, the problem of two coupled real index guided dielectric waveguides is mathematically similar to the quantum chemical problem of the Hydrogen molecule-ion. In particular, since both the Helmholtz equation (3.2.1) and the Schroedinger equation (3.2.2) are both Sturm-Liouville eigenvalue problems, we can adopt the powerful and elegant Dirac notation of quantum mechanics to simplify the mathematical manipulations. We therefore rewrite the Helmholtz equation (3.2.1) as an eigenvalue equation:

$$\mathcal{H}|E>=\beta^2|E> \tag{3.2.4}$$

with $\mathcal{H}$ being the "optical Hamiltonian":

$$\begin{aligned}\mathcal{H} &= \frac{d^2}{dx^2}+k_0^2n^2(x)\\ n^2(x) &= n_1^2(x)+n_2^2(x)-n_e^2\end{aligned} \tag{3.2.5}$$

where $n_1(x)$, $n_2(x)$, and n_e are given by Figure 3.1.

We keep the LCAO approximation (Assumption (1)) by writing the electric field $E(x)$ (which is denoted in the Dirac notation by $|E>$) as a linear combination of the electric fields $E_1(x)$ and $E_2(x)$ (or $|1>$ and $|2>$, respectively):

$$|E>=c_1|1>+c_2|2> \tag{3.2.6}$$

where $c_{1,2}$ are constants (note that the coupled mode theory admixture factor $\varrho=c_2/c_1$). The single guide field $|1>$ satisfies the Helmholtz equation

$$\mathcal{H}_1|1>=\left[\frac{d^2}{dx^2}+k_0^2n_1^2(x)\right]|1>=\beta_1^2|1> \tag{3.2.7}$$

and similarly for $\mathcal{H}_2|2>$. For $|E>$ to be an eigenvector of $\mathcal{H}$ it is necessary and sufficient that

$$< i|\mathcal{H}|E >= \beta^2 < i|E > \qquad \text{for } i = 1,2 \tag{3.2.8}$$

that is:

$$\sum_{j=1}^{2} c_j < i|\mathcal{H}|j >= \beta^2 \sum_{j=1}^{2} c_j < i|j > \ . \tag{3.2.9}$$

This system of equations has a nontrivial solution only if

$$\begin{vmatrix} H_{11} - \beta^2 S_{11} & H_{12} - \beta^2 S_{12} \\ H_{21} - \beta^2 S_{21} & H_{22} - \beta^2 S_{22} \end{vmatrix} = 0 \tag{3.2.10}$$

where $S_{ij} =< i|j >$, $\mathcal{H}_{ij} =< i|\mathcal{H}|j >$, and

$$\begin{aligned} \mathcal{H}_{11} &=< 1|\mathcal{H}|1 > \\ &=< 1|\frac{d^2}{dx^2} + k_0^2 n_1^2(x)|1 > + < 1|k_0^2[n_2^2(x) - n_e^2]|1 > \ . \\ &= \beta_1^2 + C_1 \end{aligned} \tag{3.2.11}$$

Similarly,

$$\begin{aligned} \mathcal{H}_{22} &= \beta_2^2 + C_2 \\ \mathcal{H}_{12} &= \beta_2^2 S_{12} + R_{12} \\ \mathcal{H}_{21} &= \beta_1^2 S_{21} + R_{21} \end{aligned} \tag{3.2.12}$$

where $\beta_{1,2} = k_0 \eta_{1,2}$ are the mode propagation constants, the terms C_1 and C_2 represent a small correction to the propagation constants β_1^2 and β_2^2, respectively, due to the presence of the other guide. $R_{\substack{12\\21}}$ is the coupling coefficient between the first and second (second and first) guide; its relation to the coupled mode coupling parameter κ will be discussed below. In general, R_{12} need not equal R_{21}. $C_{1,2}$ and $R_{\substack{12\\21}}$ correspond to the Coulomb and resonance coupling integral in the quantum mechanical formulation. For the optical problem considered here, the integrals S, C, and R are given by

$$
\begin{aligned}
< i|j > \equiv S_{ij} &= \int_{-\infty}^{\infty} E_i(x)E_j(x)\,dx \quad \text{for } i,j=1,2 \\
C_{\substack{1\\2}} &= k_0^2 \int_{-\infty}^{\infty} \left[n^2_{\substack{2\\1}}(x) - n_e^2 \right] E^2_{\substack{1\\2}}(x)\,dx \\
R_{\substack{12\\21}} &= k_0^2 \int_{-\infty}^{\infty} \left[n^2_{\substack{1\\2}}(x) - n_e^2 \right] E_1(x)E_2(x)\,dx
\end{aligned}
\tag{3.2.13}
$$

where for convenience we have used the normalization condition $< i|i >= 1$ instead of the power normalization normally used in electromagnetic theory for which $< i|i >= \frac{2k_0 Z_0}{\beta}$ (see Equation (2.6.4)).

Since the fields $|1>$ and $|2>$ are assumed to be normalized, we have $S_{11} = S_{22} = 1$. However, both of the electric fields of the individual waveguides are TE modes and so they are *not* orthogonal: S_{12} and S_{21} are non-zero. For real index waveguides $S_{12} = S_{21} = S$, and the eigenvalue condition (3.2.10) becomes

$$
\begin{vmatrix} \beta_1^2 - \beta^2 + C_1 & (\beta_2^2 - \beta^2)S + R_{12} \\ (\beta_1^2 - \beta^2)S + R_{21} & \beta_2^2 - \beta^2 + C_2 \end{vmatrix} = 0 \, . \tag{3.2.14}
$$

The solutions derived from (3.2.14) make no assumptions about the strength of the coupling constant $R_{1,2}$, and are limited only by the validity of the assumption that the total electric field may be written as a linear combination of the individual electric fields in Equation (3.2.6). This is usually a very good assumption; however, we will briefly discuss the limit of its validity in §3.2(c).

Aside from the explicit inclusion of the overlap and Coulomb integrals, we note one major difference between the coupled mode formulation of this problem in Equation (3.1.8) and the LCAO approach summarized by Equation (3.2.14). The coupled modes solution is expressed in terms of the first power of β while the the more exact LCAO approach gives the eigenvalue as β^2. This difference actually has no significant effect on the numerical values of the propagation constants for the waveguides of interest here.

The term β^2 occurs in the Helmholtz equation because Maxwell's wave equation is second order in the spatial z variable. However, in the derivation of the coupled mode equations (3.1.5), an adiabatic approximation (Assumption (2)) has been made which assumes "slow variation" of the $A_{1,2}(z)$ in Equation (3.1.2), effectively replacing β^2 by β. For the adiabatic approximation to be valid, it is necessary that[8]

$$\left|\frac{d^2 A_{1,2}(z)}{dz^2}\right| \ll \beta_{1,2} \left|\frac{dA_{1,2}(z)}{dz}\right| \; . \tag{3.2.15}$$

Using Equations (3.1.2) and (3.1.10), we can write $A_2^+(z)$ as

$$A_2^+(z) = e^{i(\Delta + \sqrt{\Delta^2+\kappa^2})z} \tag{3.2.16}$$

and similarly for $A_1^+(z)$ and for the $(+-)$ supermode. The inequality which expresses the validity of the adiabatic approximation (3.2.15) becomes

$$\Delta + \sqrt{\Delta^2 + \kappa^2} \ll \beta_{1,2} \; . \tag{3.2.17}$$

It is easy to show that this condition is always satisfied for *GaAs/GaAlAs* waveguides by overestimating the left-hand side and underestimating the right-hand side of Equation (3.2.17). Using Equations (2.6.4), (3.1.7), and (3.1.11), we arrive at

$$\begin{aligned}
\Delta &= \frac{k_0}{2}\Delta\eta \le \frac{k_0}{2}\Delta n \\
\kappa &= \frac{1}{4}\frac{k_0}{Z_0}\int_{-\infty}^{\infty}\left[n_{\substack{1\\2}}^2(x) - n_e^2\right] E_1(x)E_2(x)\,dx \\
&\le \frac{1}{4}\frac{k_0}{Z_0}\,(2n\Delta n)\,\frac{2k_0 Z_0}{\beta} \approx k_0\Delta n \\
\beta_{1,2} &\ge k_0 n_e \; .
\end{aligned} \tag{3.2.18}$$

For a *GaAs/GaAlAs/GaAs* waveguide, the inequality (3.2.17) reduces to $\Delta n/n_e \ll 0.6$. The worst case Δn, corresponding to a $GaAs/Ga_{0.6}Al_{0.4}As$

heterojunction, gives $\Delta n/n_e \approx 0.3/3.5 \ll 0.6$, and so the adiabatic approximation (3.2.15) is a good one. (In fact, for a typical laser waveguide, the left-hand side of (3.2.15) has been overestimated by several orders of magnitude!) We therefore conclude that the adiabatic approximation of Assumption (2) is never violated in the waveguides of interest here. This also implies that the presence of the squared terms in Equation (3.2.14) are not important.

The coupled mode theory secular equation Equation (3.1.8) may be derived from the corresponding LCAO (3.2.14) by (1) multiplying $R_{\substack{12\\21}}$ by $1/2$ to account for the fact that the coupled mode theory expression for the electric field ((3.1.2)) is written in terms of complex exponentials and complex conjugates, whereas the LCAO electric field ((3.2.6)) is not; (2) taking the different normalization convention for $< i|i >$ into account by multiplying $R_{\substack{12\\21}}$ by $\beta_{1,2}/2k_0 Z_0$; (3) ignoring the mode nonorthogonality by setting $S = 0$; (4) absorbing the Coulomb term $C_{1,2}$ into the propagation constant $\beta^2_{1,2}$; and finally by (5) dividing through by $\beta_{1,2}$.

Of far greater importance than the adiabatic approximation is the appearance of the overlap integral S. This term is nonzero because the two overlapping TE modes are not orthogonal to each other. The effect of the overlap integral becomes increasingly important as the two waveguides become more closely coupled. Unfortunately, we find that for the general case of two phase mismatched waveguides the effect of this integral is about the same order as the effect of the Coulomb and resonance integrals. In the coupled mode formulation of the problem, the individual propagation constants $\beta_{1,2}$ appear only in the diagonal elements of the matrix Equation (3.1.8), and hence the Coulomb term C may be absorbed into the propagation constant. However, in the LCAO formulation, the individual guide propagation constants also appear *without* C in the off diagonal matrix elements of Equation (3.2.14). Unlike the coupled mode theory, the Coulomb term *cannot* be absorbed into the propagation constant in the LCAO formulation of the problem. As a result, the exact analysis becomes analytically intractable due to the large number of independent parameters (*e.g.*, β_1, β_2, C_1, C_2, R_{12}, R_{21}, and S).

(a) Two Identical Waveguides

However, considerable insight may be obtained by considering several special cases. We start with two identical coupled waveguides, for which Equation (3.2.14) becomes

$$\begin{vmatrix} \tilde{\beta}^2 - \beta^2 + C & (\tilde{\beta}^2 - \beta^2)S + R \\ (\tilde{\beta}^2 - \beta^2)S + R & \tilde{\beta}^2 - \beta^2 + C \end{vmatrix} = 0 \tag{3.2.19}$$

where $\tilde{\beta} = \beta_1 = \beta_2$, $C = C_1 = C_2$, and $R = R_{12} = R_{21}$. Equation (3.2.19) has the solution

$$\begin{aligned} (\beta^+)^2 &= \tilde{\beta}^2 + \frac{R+C}{1+S} \\ (\beta^-)^2 &= \tilde{\beta}^2 - \frac{R-C}{1-S} \end{aligned} . \tag{3.2.20}$$

The splitting between the eigenvalues is given by

$$(\beta^+)^2 - (\beta^-)^2 = 2\frac{R - CS}{1 - S^2} . \tag{3.2.21}$$

This gives the well-known coupled mode theory result that when C and S are ignored, the splitting is given by twice the coupling constant. When the effects of the nonorthogonality of the TE mode basis states and the Coulomb integral are included, the splitting between the eigenvalues becomes *greater* than the coupled mode theory predicts. The term $(1 - S^2)$ in the denominator of (3.2.21) shows that the splitting increases as the overlap between the fields increases.

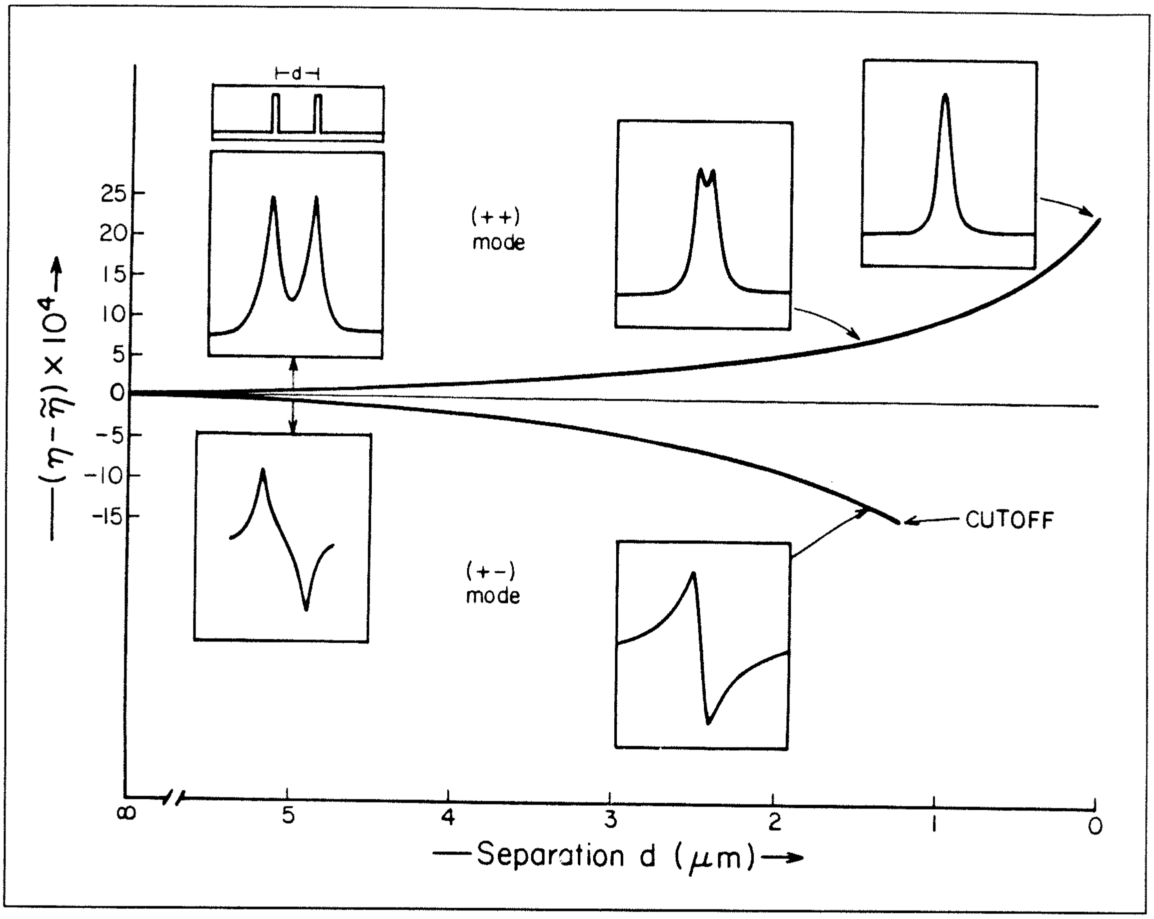

FIGURE 3.6 Cut-off of the highest order supermode. The strong coupling drives the effective index of the highest order supermode below the cladding effective index, and into cut-off.

The effect of the overlap integral on the eigenvalues has an interesting effect on the number of guided supermodes. This is illustrated in Figure 3.6, which plots the effective index $\eta^{\pm}$ as a function of the separation d between two waveguides. As $S \rightarrow 1$, the term $(1-S)$ in Equation (3.2.20) goes to zero faster than does the term $(R-C)$, and so $(\beta^{-})^2$ decreases relative to $(\tilde{\beta})^2$; however, since $(\beta^{-})^2$ can never be less than β_e^2, the $(+-)$ mode is eventually driven into cut-off and we are left with a single mode system.

At first glance, it appears that there is a paradox in the disappearance of this second mode because, as indicated on page 70, the effect of the perturbation produced by the second waveguide upon the first is to introduce nondiagonal elements (κ or R) into the optical Hamiltonian. By rediagonalizing this perturbed matrix, we obtained the supermodes of the coupled waveguides, and since we started out with a basis set consisting of two elements, we expect to find two supermodes — which we do, *provided that the overlap between the fields is small.* When the effect of the overlap integral is considered, it becomes apparent that the original basis set does not span a true two-dimensional space, and in fact, in the limit that the distance between the waveguides decreases to zero, the two guides become one — with only a *one-dimensional* basis set, and hence only one "supermode," the (++) mode, remains.

Equation (3.2.20) shows that $(\beta^+)^2 \rightarrow \tilde{\beta}^2 + (R+C)/2$ as the distance between the two waveguides decreases. In that limit, the resonant coupling integral R becomes almost identical to the Coulomb integral C so that $(\beta^+)^2$ approaches $(\beta_1)^2 + C$, which is simply the value that first order perturbation theory gives for the change in β^2 for the fundamental mode of a single waveguide that has been perturbed by doubling its width.

We close this section by noting that this latter result could have been anticipated by considering the two waveguides in the limit $\lambda \rightarrow \infty$. In that case, the wavelength becomes very much larger than the dimensions of the coupled waveguides. The electric field is then so poorly confined that it comes to resemble the field of a single-element waveguide twice the width of the original one. (*cf.* Figure 3.7c).

(b) Two Nonidentical Waveguides

We next examine the case of two nonidentical coupled waveguides, taking into account the differences in the propagation constants but ignoring the the Coulomb integrals $C_{1,2}$. This case corresponds closely to the coupled mode theory of §3.1 except that we now explicitly include the effect of the overlap integral. In this way, we will be able to show that the effect of the overlap integral is to *decrease* the effective phase mismatch between the two individual waveguides, thus leading to admixture factors that approach unity as the overlap increases — exactly as shown by Figure 3.5.

The eigenvalue secular equation (3.2.14) becomes

$$\begin{vmatrix} \beta_1^2 - \beta^2 & (\beta_2^2 - \beta^2)S + R \\ (\beta_1^2 - \beta^2)S + R & \beta_2^2 - \beta^2 \end{vmatrix} = 0 \; . \qquad (3.2.22)$$

This equation has the solution

$$(\beta^{\pm})^2 = \tilde{\beta}^2 - \frac{RS}{1 - S^2} \pm \frac{1}{1 - S^2}\left((\Delta')^2 + R^2\right)^{1/2} \qquad (3.2.23)$$

where $\tilde{\beta} = \frac{1}{2}(\beta_1^2 + \beta_2^2)$ and the effective phase mismatch parameter Δ' is given by

$$\begin{aligned} \Delta' &= (1 - S^2)\hat{\Delta} \\ \hat{\Delta} &= 1/2(\beta_1^2 - \beta_2^2) \\ &\simeq 2\beta_{1,2}\Delta \end{aligned} \qquad (3.2.24)$$

where Δ is the coupled mode theory parameter of Equation (3.1.11). Note that in the limiting case $S \rightarrow 0$ Equation (3.2.23) reduces to the equivalent coupled mode theory results of Equation (3.1.10). We also see that at the other extreme, when $S \rightarrow 1$, the effect of the overlap integral is to *decrease* the effective phase mismatch Δ' relative to its coupled mode theory value Δ (recall that when comparing coupled mode theory and LCAO theory parameters, it is necessary to divide the LCAO parameters by $\beta_{1,2}$). We therefore anticipate that the admixture factor ϱ will tend to unity as $S \to 1$.

In the limit $S \to 1$, $\Delta' \ll R$ and $(\beta^-)^2$ becomes cut-off, as before. The propagation constant for the remaining (++) supermode is then given by

$$\begin{aligned}(\beta^+)^2 &\simeq \tilde{\beta}^2 + R\alpha \\ \alpha &\equiv \frac{1}{1+S} + (1-S^2)\frac{\hat{\Delta}^2}{2R^2} \quad .\end{aligned} \tag{3.2.25}$$

The admixture factor ϱ is obtained from Equation (3.2.22) as

$$\begin{aligned}\varrho &= -\frac{(\beta_1^2 - \beta^2)S + R}{\beta_2^2 - \beta^2} \\ &= \frac{(\hat{\Delta} - R\alpha)S + R}{\hat{\Delta} + R\alpha} \quad .\end{aligned} \tag{3.2.26}$$

If we write $\sigma = 1 - S$ and $\delta = \hat{\Delta}/R$ as the normalized phase mismatch parameter, the limiting admixture factor as $S \to 1$ becomes

$$\begin{aligned}\varrho &= \frac{(\delta - \alpha)(1-\sigma) + 1}{\delta + \alpha} \\ \alpha &= \frac{1}{2-\sigma} + \sigma\delta^2 \quad .\end{aligned} \tag{3.2.27}$$

As $S \to 1$ so that $\sigma \to 0$, $\varrho \to 1$ no matter what the value of δ. In other words, no matter how badly phase mismatched the two waveguides might be when they are far apart, as they come closer together (or the wavelength increases), the overlap becomes stronger, and the effect of the phase mismatch on the admixture factor becomes weaker, thus leading to roughly equal power flowing in each waveguide. We have therefore fully explained the long wavelength result of Figure 3.5.

(c) Breakdown of the LCAO Theory

To summarize: we have shown that the adiabatic approximation (Assumption (2) in the derivation of the coupled mode theory) is never violated for *GaAs/GaAlAs* dielectric waveguides, and we have developed a more accurate theory which relaxes Assumption (3), that the individual eigenmodes be orthogonal. We now briefly examine the single remaining approximation inherent in both the coupled mode and LCAO theories. Assumption (1) on page 79 states that the total electric field may be written as superposition of the two individual waveguide fields in Equations (3.1.2) and (3.2.6). To simplify the analysis, we consider the special case of two identical guides. The symmetry of the problem implies that the admixture factor must be unity. The coupled mode theory and the LCAO theory will give different values for the propagation constants, but both theories must yield the *same* admixture factor of unity.

Figure 3.7 presents a graphical comparison of the exact electric fields (dashed lines) which were obtained numerically using the MODES program$^{(\S 2.7)}$ and the equal admixture of the individual waveguide fields which are separated by varying amounts (solid lines). The waveguide parameters are $n_e = 3.50$, $\Delta n = 0.01$, $\ell = 0.5\mu$m, and $\lambda = 1\mu$m. Portions of the individual electric fields are indicated by the dotted lines, while the shaded region corresponds to the overlap between the two fields. In Figure 3.7a with a separation $d = 2\mu$m between the two waveguides, we see that although the overlap is fairly large (approximately 40%), there is only a very small difference between the superposition field and the exact field, thus indicating that the superposition hypothesis is a very good one even when the overlap integral is quite large. As the separation between the guides decreases to 1μm in Figure 3.7b, the differences between the exact and superposition fields increases. Finally, when the waveguides just touch each other, we see that the

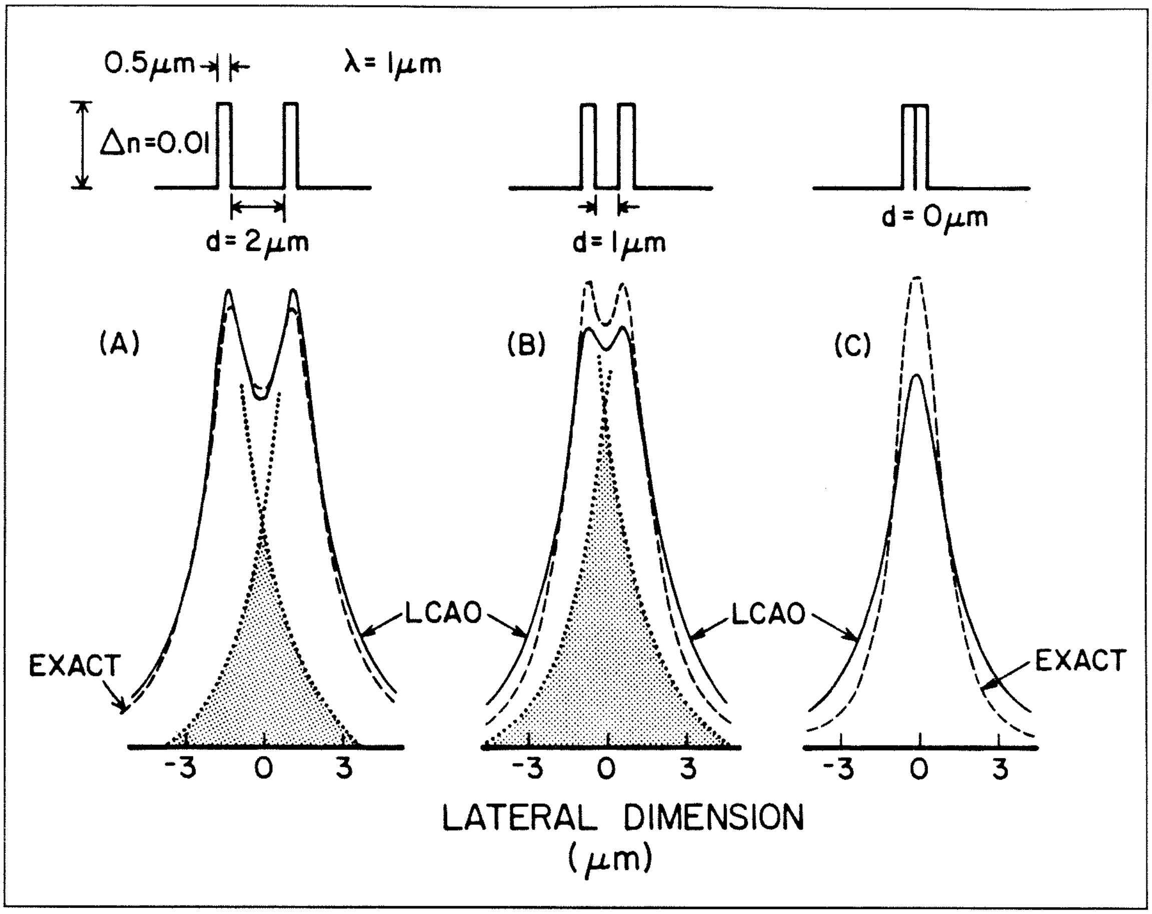

FIGURE 3.7 Comparison of the amplitude superposition (solid curve) and exact (dashed curve) modes for strongly coupled waveguides (a) separated by 2μm (b) separated by 1μm (c) just touching.

superposition field is less clearly well-confined than the exact result. This occurs, of course, because the exponential decay of the field in the cladding region depends upon the product $\sqrt{\Delta n \ell}$, which is greater for the two touching waveguides than it is for the separate individual waveguides.[12]

§3.3 Coupled Waveguides Without a Phase Matching Wavelength

In the previous sections we have seen the paramount importance of the phase matching wavelength λ_p in determining the properties of two coupled waveguides, and described a method for designing a coupled waveguide structure with a given λ_p in §3.1(a). We will now show that the class of real index guided waveguides typified by those of Figure 3.4 in which $\delta(n) \cdot \delta(\ell) < 0$ are the *only* types of coupled waveguides which have a phase matching wavelength. In particular, we will show that a technologically very important class of waveguides, two ridge guided structures (see Figure 2.5), are not phase matched at any wavelength.

Ridge guided (mesa stripe) lasers are fabricated by etching away selected regions of the low index upper cladding layer in a standard four layer heterojunction laser such as that of Figure 1.3a. In a ridge guided structure the only parameter that can be conveniently varied is the width of the guide and the etching depth. In an array of such ridge guided waveguides, it is not technologically possible to easily and controllably vary the etching depth across the array; hence, for all practical purposes, the only degree of freedom is the width ℓ of the waveguide(s). Therefore, for this type of guide $\delta(n) = 0$ and $\delta(\ell) \neq 0$. The index profiles for two such ridge waveguides are shown superimposed by the solid and dashed lines in Figure 3.8a. The first waveguide, denoted by the solid curve, satisfies the Helmholtz equation (3.2.1)

$$\mathcal{H}_s|s>=\left[\frac{d^2}{dx^2}+k_0^2 n_s^2(x)\right]|s>=\beta_s^2|s> \tag{3.3.1}$$

where we have used the Dirac notation of §3.2, $n_s(x)$ represents the refractive index of the solid curve in Figure 3.8a, and $|s>$ represents the corresponding electric field of the fundamental mode for that waveguide. The refractive index $n_d(x)$ of the second guide is indicated by the dashed line in Figure 3.8a. The core index n_0 for this waveguide is the same as that of the first waveguide, but is of

§3.3 Coupled Waveguides Without a Phase Matching Wavelength

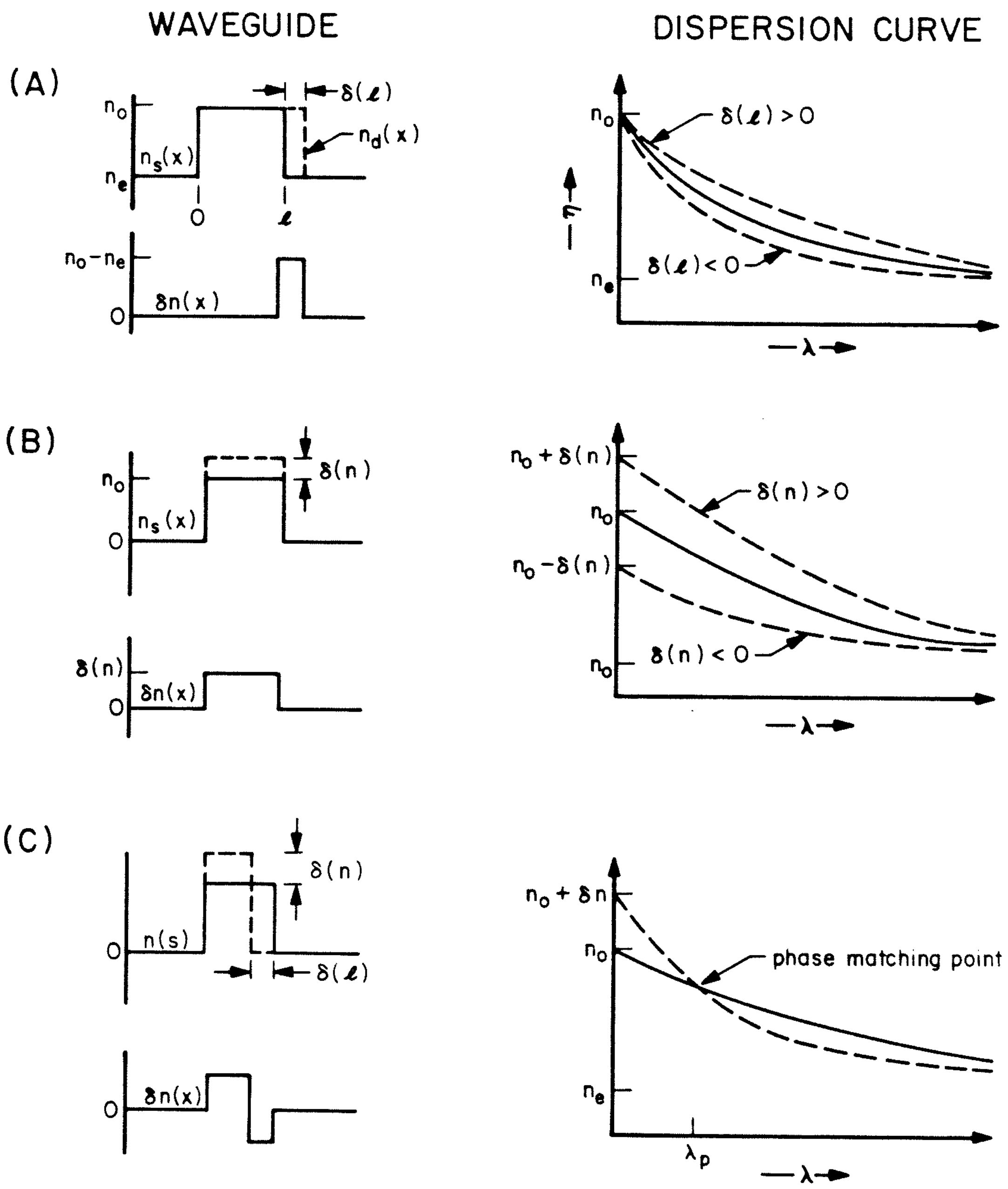

FIGURE 3.8 Dispersion curves for various coupled waveguides (a) Schematic diagram of an air ridge laser suitable for use in phased arrays; waveguides and schematic dispersion curves for various cases (b) $\delta n = 0$, $\delta \ell \neq 0$ (air ridge) (b) $\delta n \neq 0$, $\delta \ell = 0$ (c) $\delta n \neq 0$, $\delta \ell \neq 0$ with $\delta n \cdot \delta \ell < 0$. The solid curve represents the first waveguide, the dashed curve the second.

greater extent in the lateral direction by an amount $\delta(\ell)$. We consider differences between the two guides $\delta n(x)$ to be a perturbation on the first guide:

$$n_d^2(x) = n_s^2(x) + \delta n(x) \tag{3.3.2}$$

where $\delta n(x)$, which is also shown in Figure 3.8a, is non-zero only over the region $\ell < x < \ell + \delta(\ell)$. We can calculate the second guide's propagation constant in terms of the first using first order perturbation theory:[6,7]

$$\begin{aligned} \beta_d^2 &= < s|\mathcal{H}_d|s > \\ &= < s|\mathcal{H}_s + k_0^2 \delta n(x)|s > \\ &= \beta_s^2 + k_0^2 \Gamma_{\ell,\ell+\delta(\ell)} \Delta n \end{aligned} \tag{3.3.3}$$

where $\Delta n = n_0 - n_e$ and the power filling factor Γ is defined by

$$\Gamma_{a,b} = \int_a^b |E_s(x)|^2 \, dx \ . \tag{3.3.4}$$

The phase mismatch parameter $\Delta = \frac{1}{2}(\beta_d - \beta_s)$ is then given by

$$\Delta = \frac{k_0}{\eta_s} \Gamma_{\ell,\ell+\delta(\ell)} \Delta n \ . \tag{3.3.5}$$

Although the numerical values of the power filling factor $\Gamma_{\ell,\ell+\delta(\ell)}$ and the propagation constant η_s depend upon the wavelength, they are both positive definite quantities, and so the sign of Δ is the same as that of $\delta(\ell)$. As a result the two dispersion curves never touch or cross; *i.e.*, *two coupled ridge guided waveguides do not have a phase matching wavelength.* A schematic dispersion curve for $\delta(\ell)$ both positive and negative are shown in Figure 3.8a. The two curves touch asymptotically as λ → 0 or ∞, but due to the absence of a phase matching wavelength, do not touch in between.

Similarly, it can easily be shown that waveguides with $\delta(n) \neq 0$, and $\delta(\ell) = 0$ also do not have a phase matching wavelength. This result may also be shown using the Taylor expanson of (3.1.17) because if only one of the $\delta(x_i) \neq 0$ then the corresponding $\partial D/\partial x_i$ must be zero if the guides are to be phase matched at λ_p, which is not true except fortuitously. Equation (3.1.17) is better for numerical calculation because it does not require *a priori* knowledge of the $\Gamma_{a,b}$, while the method of this section has the advantage that it shows the general trends and gives the correct result for the case $\delta(n)$, $\delta(\ell) \neq 0$ with $\delta(n) \cdot \delta(\ell) > 0$ (the latter result is not readily apparent from Equation (3.1.19)).

We therefore conclude that the only types of waveguides which will have phase matching wavelengths are those for which an increase in one parameter is offset by a decrease in the other — *i.e.*, $\delta(n) \cdot \delta(\ell) < 0$ with the ratio between the two given by Equation (3.1.19). To summarize these results, schematic dispersion curves for the other various types of waveguides are presented in Figure 3.8.

The fact that two nonidentical ridge waveguides do not have a phase matching point has an extremely important consequence for the operation of an array of such lasers because it implies (through Equations (3.3.5), (3.1.12), and (3.1.3)) that the only supermode with a single lobed farfield pattern, the fundamental (++) supermode, is preferentially concentrated in the wider waveguide. We show in §4.4(a) that this idea extends itself in a natural way to *chirped arrays* of ridge guided lasers with widths that vary monotonically across the array. The spatial segregation of the (++) supermode in one half of the array, and of the (+−) supermode in the other, combined with a nonuniform gain profile designed to favor the fundamental supermode, provides the clues we need to design an array which will have a single lobed farfield pattern. The chirping concept is extended to gain guided arrays in §4.4, and ultimately leads to the concept of a tailored gain *broad area* laser in Chapter 5.

§3.4 The Effect of Gain on Weakly Coupled Waveguides

We now consider the case where gain and/or loss are present.[13] To simplify the analysis, we make use of the coupled mode theory for weakly coupled waveguides, and note that extension of the results to the more strongly coupled case using LCAO theory is possible. We will discuss strongly coupled gain guided lasers from a slightly different perspective in §3.5.

When gain is present, the quantities $\beta_{1,2}$, $\beta^{\pm}$, κ, and δ are complex numbers. We write the complex propagation constant as $\beta_{1,2} = \bar{\beta}_{1,2} + i\bar{\bar{\beta}}_{1,2}$ with $\bar{\bar{\beta}}_{1,2} = \gamma_{1,2}/2$, where $\gamma_{1,2}$ is the power modal gain of the first (second) mode. We then write the normalized mismatch parameter $\delta = \delta\beta + i\delta\gamma$ where $\delta\beta = (\bar{\beta}_1 - \bar{\beta}_2)/2\kappa$ is the normalized phase mismatch and $\delta\gamma = (\bar{\bar{\beta}}_1 - \bar{\bar{\beta}}_2)/2\kappa$ is the normalized *amplitude* gain mismatch.

At the phase matching wavelength ($\bar{\beta}_1 = \bar{\beta}_2 = \tilde{\beta}$) the complex propagation constant (Equation (3.1.10)) is given by

$$\beta^{\pm} = \tilde{\beta} + i\,\tfrac{1}{2}(\bar{\bar{\beta}}_1 + \bar{\bar{\beta}}_2) \pm \kappa\sqrt{1 - (\delta\gamma)^2}\ . \tag{3.4.1}$$

The eigenvectors $\mathbf{E}(z)$ are (compare with (3.1.12))

$$\mathbf{E}^{\pm}(z) = \begin{cases} \begin{bmatrix} 1 \\ \pm\exp(\mp i\sin^{-1}\delta\gamma) \end{bmatrix} & |\delta\gamma| \leq 1 \\ \begin{bmatrix} 1 \\ \pm i\,\exp(\mp i\cosh^{-1}\delta\gamma) \end{bmatrix} & |\delta\gamma| > 1 \end{cases}\ . \tag{3.4.2}$$

The amplitude admixture factor ϱ is now a complex number which we write as $\varrho^{\pm} = |\varrho|^{\pm}\, e^{i\phi^{\pm}}$; its behavior is described in Figure 3.9. When $|\delta\gamma| \leq 1$, $\sin^{-1}\delta\gamma$ is real, and so the gain mismatch does not appreciably affect the optical intensity distribution: both supermodes have equal intensity in each waveguide.

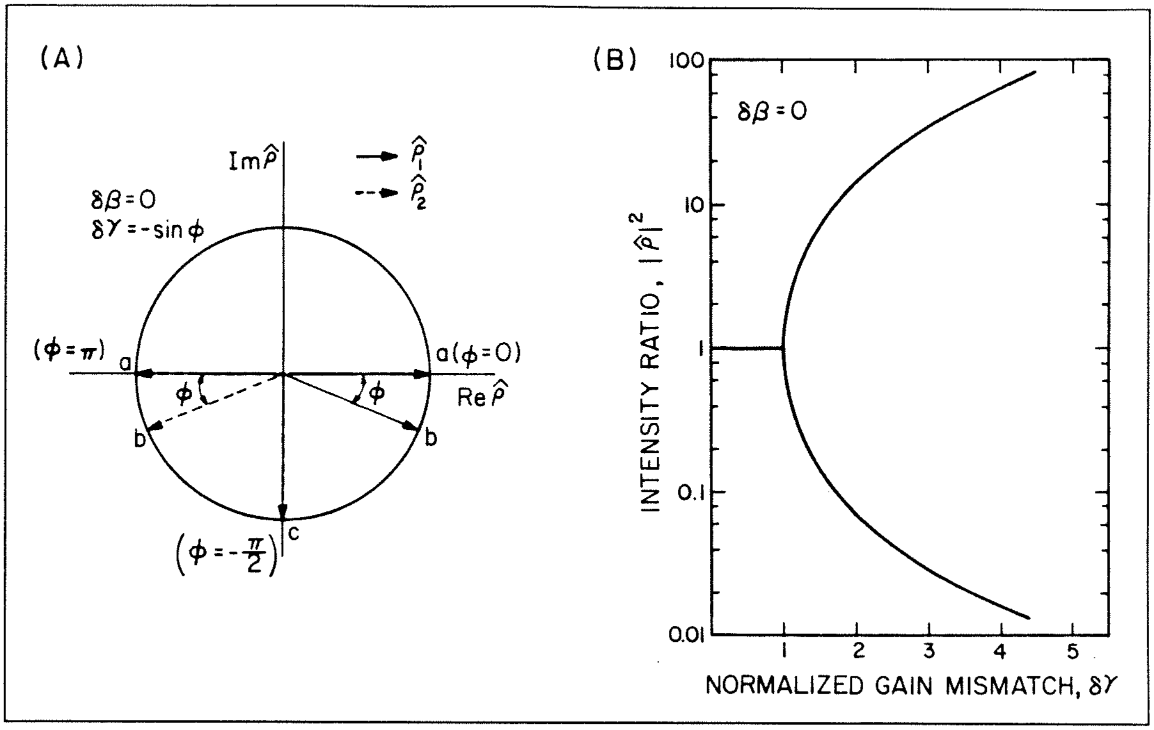

FIGURE 3.9 Effect of gain on the admixture factor for two phase matched waveguides (a) phase angle ϕ (b) intensity $|\varrho|^2$.

The relative phase shift $\phi^{\pm}$ between the electric fields in each guide varies continuously with $\delta\gamma$ as shown in Figure 3.9a.

When there is no gain mismatch ($\delta\gamma = 0$), $\phi^{+} = 0$ for the inphase (++) supermode (solid arrow) and $\phi^{-} = \pi$ for the out-of-phase (+−) supermode (dashed arrow). As $\delta\gamma$ increases, so does ϕ. When $\delta\gamma = 1$ (*i.e.*, $\bar{\bar{\beta}}_1 - \bar{\bar{\beta}}_2 = 2\kappa$), $|\varrho^{\pm}| = 1$ and $\phi^{\pm} = -\pi/2$, so that the modes become degenerate. They then have the same propagation constant and field distribution, and have $\pi/2$ phase shift between the individual waveguide fields.

The term $\sin^{-1}\delta\gamma$ becomes imaginary when there is a large gain mismatch at the phase matching wavelength. When $|\delta\gamma| > 1$, the relative phase shift between the guides is always $\pi/2$, but the intensity distributions of the supermodes are now different from each other. As is illustrated in Figure 3.9b, one supermode has most of its power in one channel, and the optical field of the other supermode is concentrated in the other channel.

Figure 3.10 plots the intensity admixture factor $|\varrho|^2$ and relative phase angle ϕ for the (++) supermode versus the normalized phase mismatch parameter $\delta\beta$ for several values of the normalized gain mismatch parameter $\delta\gamma$.

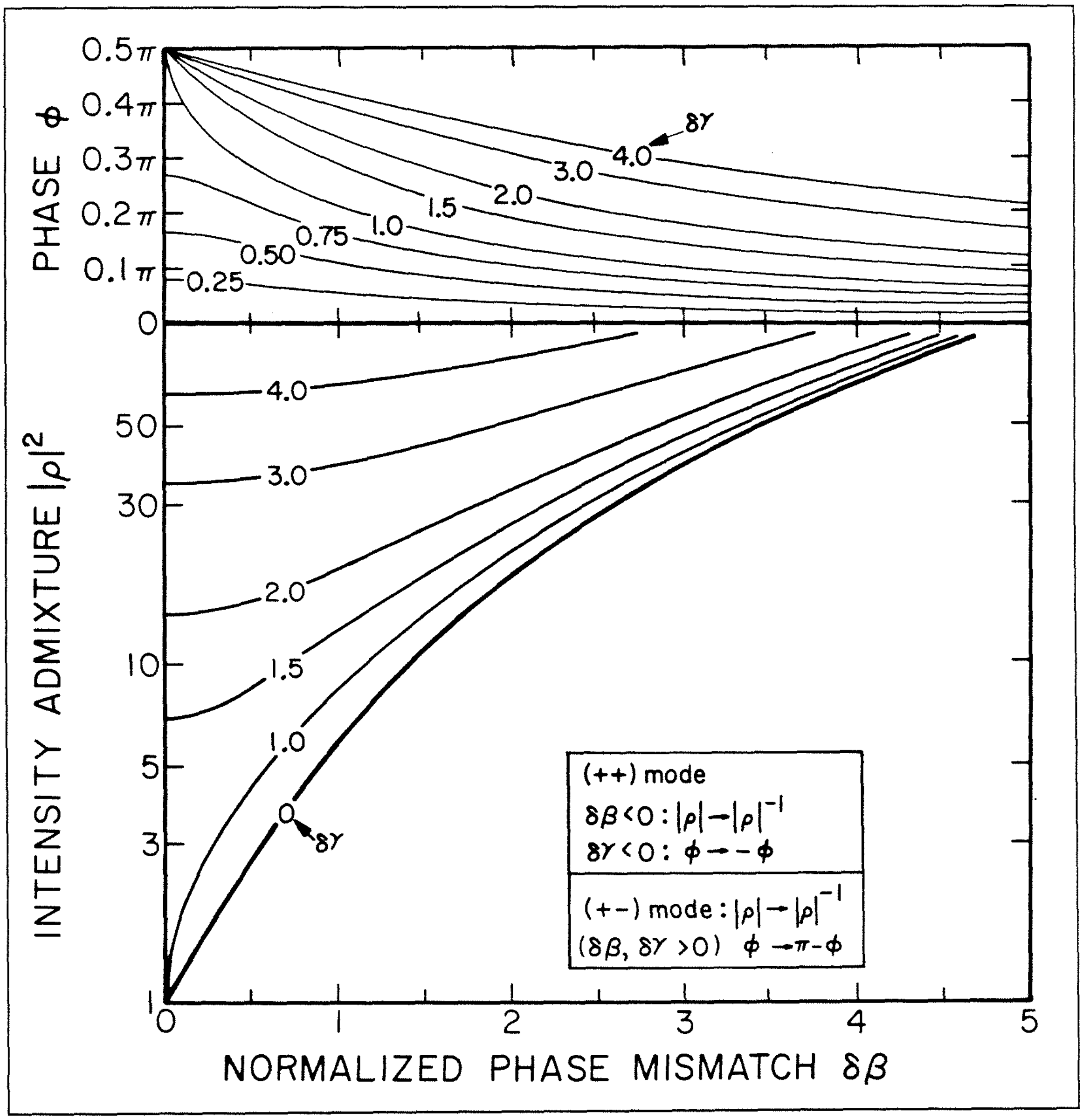

FIGURE 3.10 Effect of gain on the admixture factor for two phase mismatched waveguides.

The corresponding values for the $(+-)$ supermode may be obtained by reflecting the curves about $|\varrho|^2 = 1$ and $\phi = \pi/2$, respectively. It is interesting to note that when $|\delta\gamma| \geq 1$, none of the supermodes can have an admixture factor $|\varrho| = 1$ even at the phase matching wavelength $\delta\beta = 0$, and that the *intensity* admixture factor $|\rho|^2$ does not depend on the sign of $\delta\gamma$. We therefore conclude that if equal power is to flow in each waveguide, they must be both phase and gain matched.

Figure 3.11 plots the exact numerical results for the same waveguide as Figure 3.5, but with $\delta\gamma > 1$. We see that as $\lambda \to \infty$, the intensity admixture factor approaches unity while the relative phase difference approaches 0 for the $(++)$ supermode and π for the $(+-)$ supermode. Comparison of two coupled waveguides without gain in Figure 3.5 with the same two waveguides with a gain mismatch in Figure 3.11 shows that as $\lambda \to \infty$, the effect of the gain mismatch becomes subdominant to the phase mismatch, and that eventually both of these are overcome by the effect of the overlap integral.

Finally, although Figure 3.10 shows that the modified coupled mode theory of this section works for weakly coupled waveguides, we will find in §4.4(a) that it gives entirely *incorrect* results for the case of a strongly coupled gain guided chirped array.

§3.5 Strongly Coupled Gain Induced Waveguides

We have seen in §3.1 that when we consider the case of two weakly coupled real index guided waveguides, we found two new modes to describe the field in the composite cavity. When we considered that the two individual waveguide modes are not orthogonal in §3.2, we found that the strong coupling drove the higher order supermode into cut-off so that only one supermode remained. The addition

§3.5 Strongly Coupled Gain Induced Waveguides

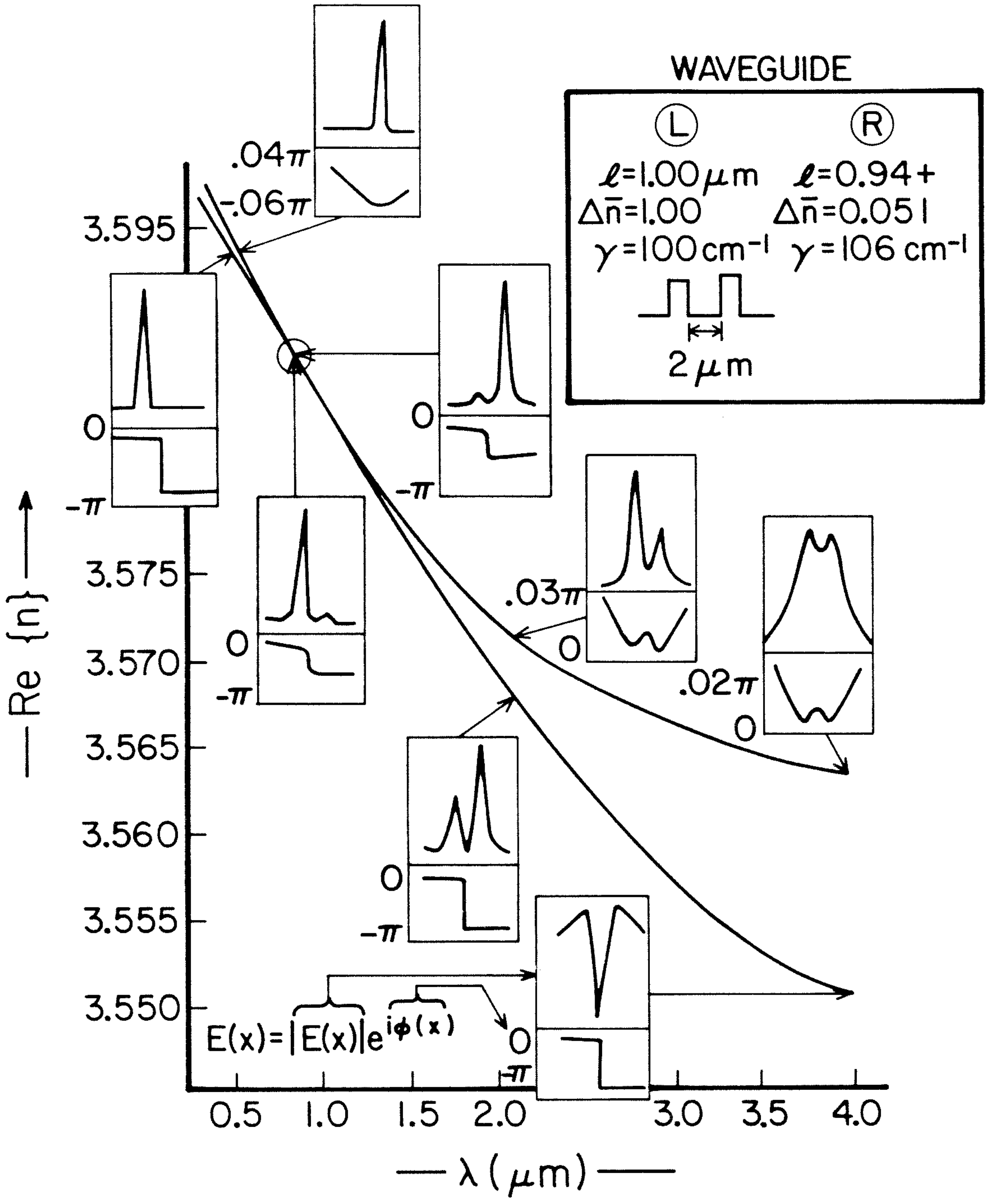

FIGURE 3.11 Exact solutions of two coupled real index waveguides with large gain mismatch. Note that the admixture factor is not unity at the phase matching wavelength. At longer wavelengths, the solutions are very similar to those of Figure 3.5.

of gain (§3.5) did not change the situation appreciably; we still found two modes for weakly coupled waveguides.

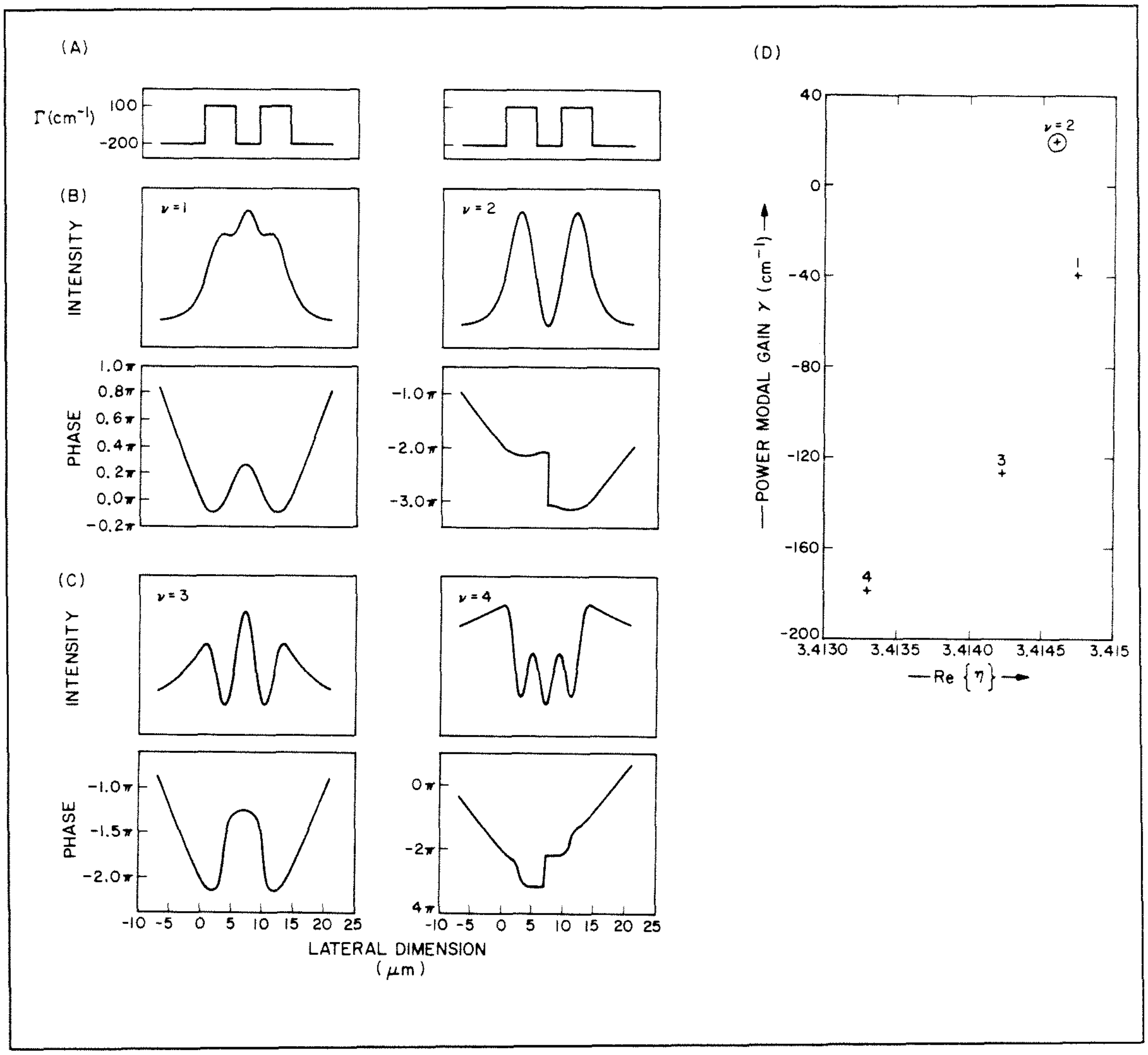

FIGURE 3.12 Eigenmodes of two strongly coupled gain guided box waveguides (a) gain profile (b) nearfield patterns for the expected $\nu = 1$ and $\nu = 2$ supermodes (c) nearfield patterns for the unexpected $\nu = 3$ and $\nu = 4$ supermodes (d) modal diagram.

When we numerically solve for the supermodes of two strongly coupled single mode gain waveguides, we find an entirely unexpected surprise: as is illustrated in Figure 3.12, even if each individual gain waveguide supports *only one* guided mode, the two coupled waveguides support not just one or two but *four* modes!

Notice that the intensity nearfield pattern for the $\nu = 3$ supermode has three peaks, while that of the $\nu = 4$ supermode has four, and that the number of approximate nulls in the nearfield pattern is one less than the mode number. This suggests that the unexpected $\nu = 3$ and $\nu = 4$ modes are higher order modes of the composite structure. The reason why we obtain four modes when we expected only two is not fully understood at the present time. However, we will now examine some interesting aspects of gain guided waveguides that make them qualitatively different from their more intuitive real index guided counterparts and which may have a bearing on this puzzle.

(a) Two Coupled Multimode Real Index Guided Waveguides

Finding four modes suggests that although we claimed that the single-element waveguide was single mode, perhaps in some sense it isn't. We therefore first examine the simpler case of two identical coupled *real index* waveguides each of which supports *two* guided modes, and then consider the corresponding gain guided case. We consider the four possible mode combinations $\nu_{\text{left}} \otimes \nu_{\text{right}}$: $1 \otimes 1$, $1 \otimes 2$, $2 \otimes 1$, and $2 \otimes 2$. The $1 \otimes 1$ combination (coupling between the two fundamental modes) is the usual one we have studied before; the nearfield patterns for the inphase and antiphase combinations of the two fundamental modes are shown in Figure 3.13b.

Since the modes of a symmetric waveguide must have a definite parity,[14] symmetry rules out the possibility of $1 \otimes 2$, and $2 \otimes 1$ (symmetric $\otimes$ antisymmetric) coupling (this is analagous to a quantum mechanical selection rule). Figure 3.13c presents the inphase ($\nu = 3$) and out-of-phase ($\nu = 4$) supermodes of the coupled waveguides that arise from the $2 \otimes 2$ coupling. Notice that the intensity nearfield

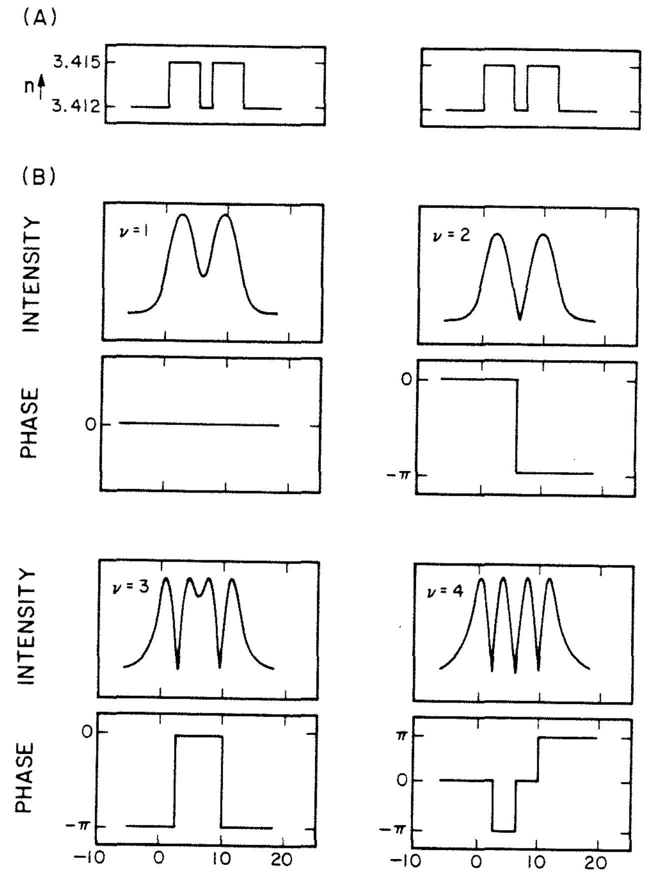

FIGURE 3.13 Eigenmodes of two coupled double mode box waveguides (a) waveguides (b) nearfield patterns for the 1 ⊗ 1 coupling (c) nearfield patterns for the 2 ⊗ 2 coupling. Note the similarities to the modes of Figure 3.12.

pattern for the $\nu = 3$ supermode has three peaks, while that of the $\nu = 4$ supermode has four, and that the number of nulls in the nearfield pattern is one less than the mode number.

These results are very similar to what we found for the gain guided case of Figure 3.12, and suggest that our "single mode" gain guided waveguide of Figure 3.12a is not as "single mode" as we had thought.

(b) Leaky Modes of a Gain Induced Waveguide

It is possible to find solutions of the secular eigenvalue equation (2.6.6) for the box waveguide that satisfy the boundary conditions at $|x| = \ell/2$ but *diverge* at infinity. These modes, referred to as "leaky" modes, are nonphysical because they cannot be normalized to carry finite power. Such modes have been studied in the case of real index guided waveguides[15] but not, to our knowledge, in gain guided structures. We briefly discuss these modes here because, although it does not appear that they play a role in the coupling between two real index guided box waveguides, they may play a role in explaining the two extra supermodes we found in §3.5.

Figure 3.14b presents the modal diagram for the single-element gain guided box waveguide which we considered in §3.5. Since the cladding loss $\Gamma_e = -200\text{cm}^{-1}$, it is physically impossible for a guided mode to have a modal gain smaller than this amount. The line $\gamma = -200\text{cm}^{-1}$ therefore separates the physical guided modes from the nonphysical leaky modes.

The pole at $\eta = n_e$ and the branch cut to the right of this pole are due to the square root dependence of the wavevectors k and g on η in Equation (2.6.5). We find that this waveguide has *two* solutions to the dispersion equation (2.6.6), one of them corresponding to a guided mode, the other to a leaky mode. Use of the CONTOUR program of §2.7 indicates that there are no other solutions in the region indicated in Figure 3.14b. The nearfield patterns of these modes are presented in Figure 3.14c; as expected, the intensity of the leaky mode diverges as $|x| \to \infty$. Notice that the leaky mode has a phase shift of π radians at the middle of the guide; it therefore in some sense corresponds to the "cut-off" $\nu = 2$ guided mode.

§3.5(b) Leaky Modes of a Gain Induced Waveguide

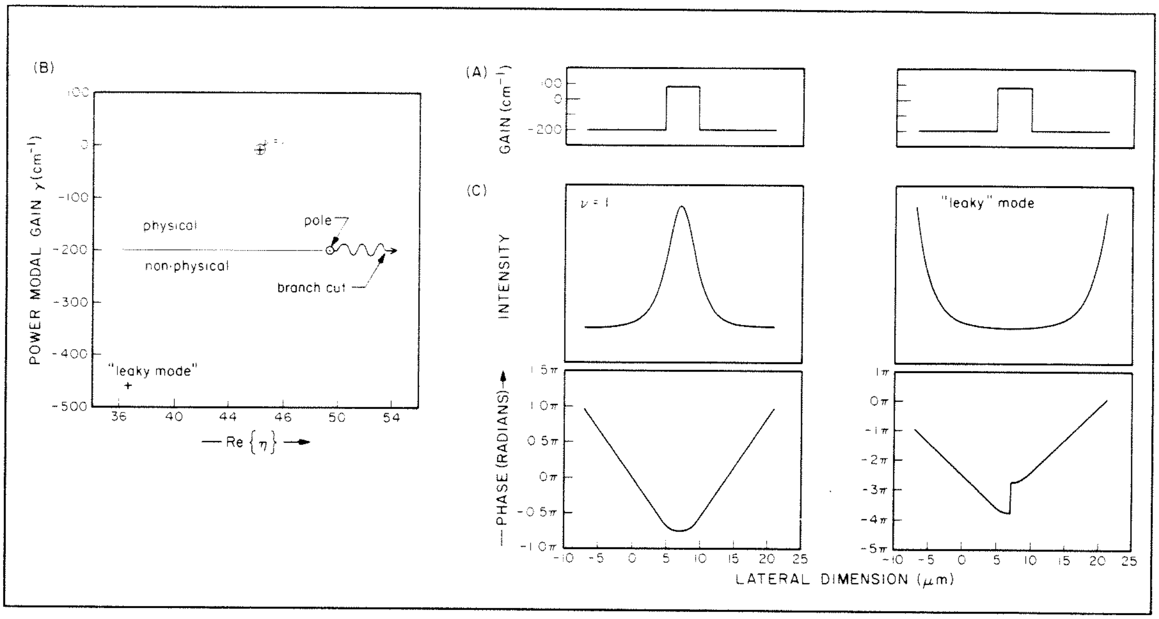

FIGURE 3.14 Leaky modes of the gain guided box waveguide (a) waveguide of Figure 3.12(b) modal diagram showing one guided and one leaky mode (c) nearfield patterns for the $\nu = 1$ and leaky mode.

Examination of the nearfield patterns for the "extra" $\nu = 3$ and $\nu = 4$ modes of the coupled gain guided waveguide system of Figure 3.12 reveals that there is approximately a phase shift of π radians between each of the peaks in the nearfield patterns for the higher order modes. This suggests that although leaky modes do not play a role in the coupling between real index waveguides, they may play a role in the case of strongly coupled *gain induced* waveguides.

(c) Coupling Mechanism Between Gain Guided Lasers

The complex nature of the index of refraction in a gain guided laser makes the coupling between two lasers significantly different than that between two real index guided lasers. Experimentally, we find a standing wave pattern between two gain guided lasers that is not observed between real index guided lasers. We show that this effect is a direct result of the interference of the complex evanescent waves associated with each gain guided laser, and briefly discuss the implications for coupling between gain guided lasers.

<i> *Coupling Between Mechanism Gain Guided Lasers: Experiment*

We have used the separate contact laser developed by Katz, *et. al.*[16] to experimentally investigate the coupling between two gain guided lasers.[17] The laser stripes were delineated by using proton implantation, the separation between the centers of adjacent stripes being 9μm. Separate contacting was accomplished by using two-level metallization. The threshold current of each individual laser was typically $60mA$ (pulsed operation). A schematic cross section of the device used for this experiment is shown in Figure 3.15a.

The spectrally resolved nearfields of pairs of coupled lasers, separated by various multiples of 9μm, were obtained by imaging the nearfield of the lasers on the entrance slit of a spectrometer and displaying the output on a monitor using a silicon-vidicon TV camera. The spatial intensity distribution of the coupled modes at a given frequency could then be obtained by scanning a selected line of the video signal.

Generally, the phase locked modes of the coupled lasers appeared at wavelengths which were $\sim$ 50 to 100 Angstroms longer than the wavelengths of the individual laser modes, and the spectral width of the phase locked lasers was considerably smaller than that of the individual ones. When the interacting lasers were separated by more than 18μm, gain had to be introduced into the coupling region (by pumping current through the intervening stripes) in order to obtain phase locked modes. The nearfield pattern of a phase locked mode consisted of two main lobes, located approximately below the centers of the coupled laser stripes, and secondary peaks in the intervening coupling region. An example of such a phase

§3.5(c.i) Coupling Between Mechanism Gain Guided Lasers: Experiment

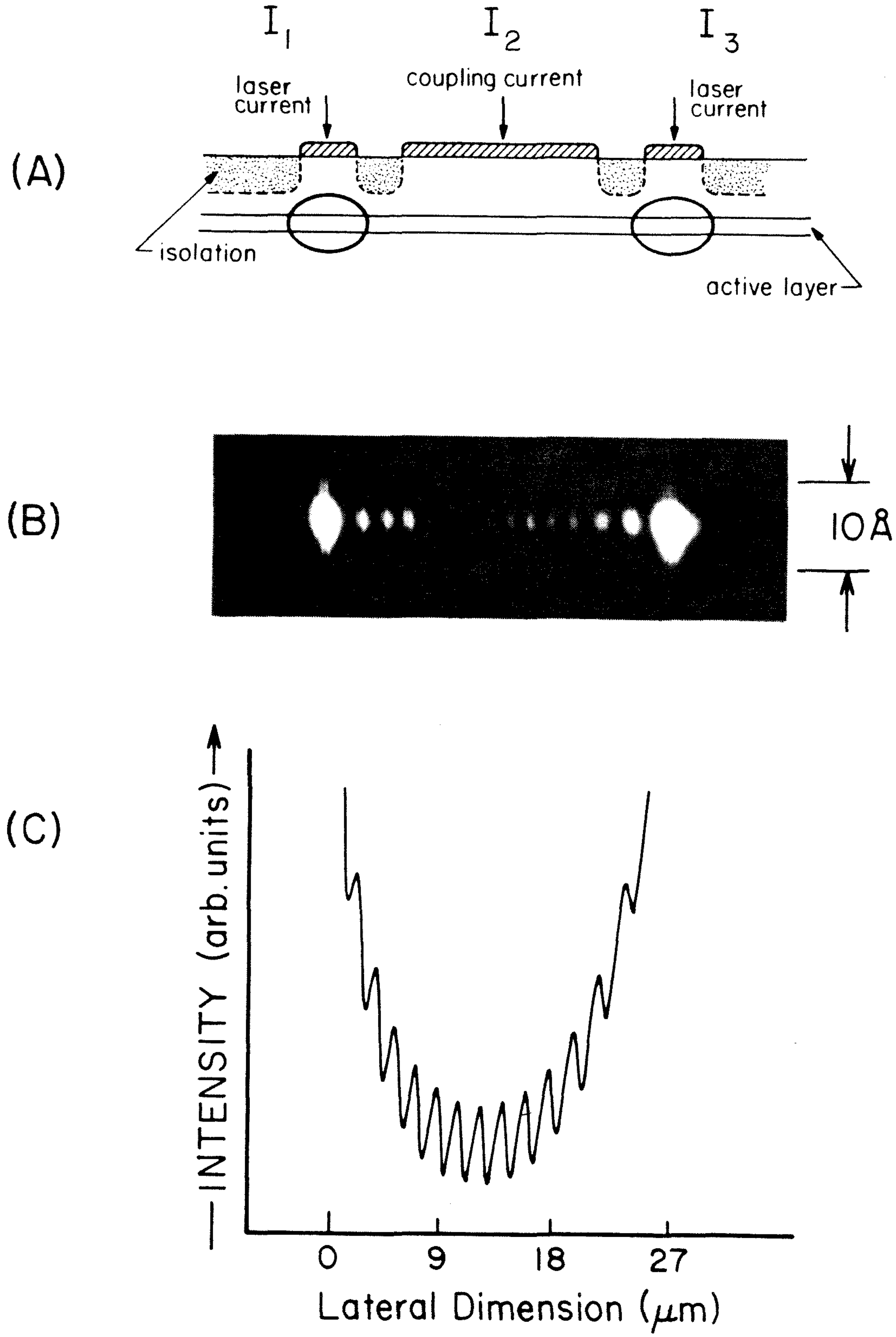

FIGURE 3.15 Standing wave patterns between gain guided lasers (a) exprimental diagram (b) spectrally resolved nearfield pattern demonstrating phase locked operation (c) theoretical nearfield pattern.

locked mode is shown in Figure 3.15. Figure 3.15a illustrates the way in which current injection I_1 and I_3 form the two gain guided lasers with I_2 controlling the coupling between them. The coupled lasers operated in essentially a single longitudinal mode, at $\lambda \approx 0.88$ μm, thereby showing phase locked operation. Figure 3.15b shows the spectrally resolved nearfield pattern of two lasers separated by 27μm. Thirteen approximately equally spaced fringes are visible.

As the current through the contact between the coupled lasers was increased, the lasing modes hopped to shorter wavelengths, resulting in a tuning range of $\sim$ 50 Angstroms. When this current was further increased, the lasing mode hopped back to longer wavelengths, but the spatial mode pattern was now different. This behavior repeated at still higher currents through the intermediate stripe. Figure 3.16 shows the evolution of the spatial mode pattern of the phase locked modes of two lasers separated by 18μm for two sets of laser currents I_1 and I_3. For all the spectrally resolved nearfields of Figure 3.16, the wavelength is $\lambda \sim 0.88\mu$m. It is clear that the separation between the secondary peaks in the mode pattern increases with increasing current I_2.

<ii> *Coupling Mechanism Between Gain Guided Lasers: Theory*

The nearfield patterns presented above can be understood by recalling that the curved phase fronts in a gain guided laser cause power to flow outward from the laser axis.(§2.6(*b*)) As a result, the evanescent lateral wavevector g in Equation (2.6.5) is complex. When two gain guided lasers are placed in close proximity, the radiating modes of the adjacent gain guided lasers interfere to form a lateral standing wave pattern in the intervening region.

To illustrate the phenomenon, first consider a single gain induced waveguide of width ℓ. We take the origin to be located a distance $s/2$ to the right of the

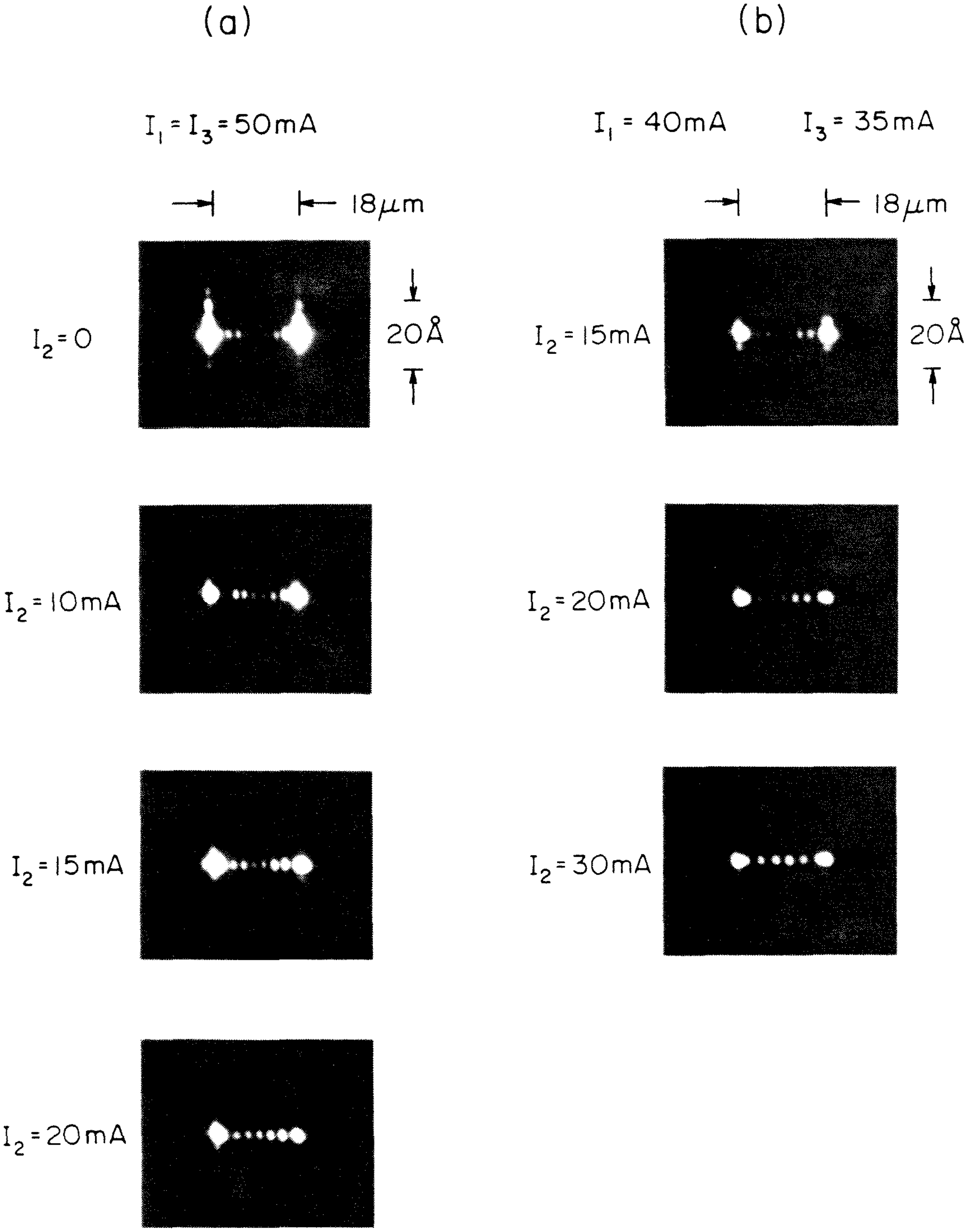

FIGURE 3.16 Variation of the standing wave pattern with coupling current. Note that as the current (*i.e.*, interchannel gain) is increased, the spacing between the fringes also increases.

guide. The electric field amplitude external to the channel region ($x \geq -s/2$) may be written as an evanescent exponential (*i.e.*, $\left|E_{1,2}(x)\right|^2 \rightarrow 0$ as $|x| \rightarrow \infty$) so that we can express the (unnormalized) electric field to the right of the solitary guide as

$$E_1(x) = e^{-(x+s/2)g} \sim e^{-i\bar{\bar{g}}x}\, e^{-\bar{g}x} \tag{3.5.1}$$

where g is the complex evanescent lateral wave vector given by

$$g = \bar{g} + i\bar{\bar{g}} = k_0\sqrt{\eta^2 - n_e^2}\ . \tag{3.5.2}$$

The effect of $\bar{\bar{g}} \neq 0$ is to cause the phase fronts of the evanescent field to be tilted by an angle $\theta = \sin^{-1}(\bar{\bar{g}}/k_0)$ with respect to a plane normal to the mirror facets. Note that in a real index guided laser, $\bar{\bar{g}} = 0$, and so the phase fronts propagate normal to the mirror facets. When we calculate the nearfield intensity pattern external to the waveguide $I(x) = |E(x)|^2$, we see that the effect of the imaginary part of g is masked by complex conjugation:

$$I_1(x) = e^{-2\bar{g}x}\ . \tag{3.5.3}$$

The interchannel nearfield pattern corresponding to a single laser is thus a simple exponential.

Now consider two identical coupled gain induced waveguides separated by a distance s. We take the origin to be located midway between the two guides. The individual fields are given by expressions similar to Equation (3.5.1). The total electric field between the waveguides is therefore given by

$$E_{total}(x) = E_1(x) + E_2(x) = e^{-(x+s/2)g} + e^{+(x-s/2)g} \tag{3.5.4}$$

and the nearfield intensity between the waveguides is

$$I_{total}(x) = \frac{1}{2}(e^{-2\bar{g}x} + e^{+2\bar{g}x}) + \cos 2\bar{\bar{g}}x\ . \tag{3.5.5}$$

This function is plotted in Figure 3.15c with $g = 0.3 + 1.4\pi\, i\, \mu\mathrm{m}^{-1}$. Interference between the two electric fields, expressed by the $\cos 2\bar{g}x$ term, leads to a standing wave pattern which makes visible the imaginary part of the complex wave vector $\bar{\bar{g}}$.

The fringe period depends on the angle $\theta = \sin^{-1}(\bar{g}/k_0)$ between the phase fronts of the interfering fields, larger angles giving more closely spaced fringes. Equation (3.5.2) shows that this angle increases with increasing difference between the peak gain under the laser stripe and the gain in the region outside the laser stripe.(§2.6(b)) The period of the interference fringes in the pattern of the phase locked modes increases when the region between the coupled lasers becomes less lossy, which is experimentally verified by the results of Figure 3.16. We also note that increasing the interchannel gain will decrease the phase front curvature of a mode(§2.6(b)) because less power needs to flow from the high gain regions of the mode to the low gain regions, thus possibly leading to a decrease in the astigmatism of the output beam.

CHAPTER
FOUR
Phased Array Lasers

I am afraid that I rather give myself away when I explain.
Results without causes are much more impressive.

—Sherlock Holmes, *The Stock-Broker's Clerk*
Sir Arthur Conan Doyle

In this chapter, we extend the results of the previous chapter to systems of many coupled waveguides. The coupled mode analysis of §3.1 is extended to a uniform array of waveguides in §4.1, where we show why a uniform array has a twin lobed farfield pattern. In §4.2 we introduce the idea of *chirped arrays* of *nonuniform* lasers as a means of spatially segregating the fundamental supermode from the higher order supermodes. Unfortunately, we find in §4.2(a) that given current technological constraints, it is exceedingly difficult to fabricate a real index guided chirped array, and in any event, such structures are almost certainly to be partially gain guided. We therefore turn our attention to the possibility of using the chirping concept in a gain guided array.

The actual implementation of these ideas into a working device came to resemble a rather exciting detective story (that even Sherlock Holmes might enjoy!) which starts with a single clue — chirping — and evolves as we work out its consequences, discover the limitations of the theoretical results of Chapter 3, modify our ideas, and try again — and again... until we finally arrive at a working device. Along the way, we will discuss a variety of waveguides relevant to phased array laser design so that the reader will, we hope, emerge with a good understanding of the lateral mode control problem in evanescently coupled phased array semiconductor lasers.

In particular, we will stress time and again the importance of a large interchannel gain for device performance. Since the region external to the array is always lossy due to the unpumped *GaAs* active layer, this leads us to discuss the interesting concept of the interplay between array and box modes in §4.3(a) and 4.4(a). We introduce chirped arrays of gain guided lasers in §4.4, and discover the theoretical possibility of suppressing one lobe of a twin lobed farfield pattern in §4.4(a). We discover gain tailoring in §4.5 and fabricate a device based on these principles. The combination of gain tailoring and a high interchannel gain enables us to achieve our goal of fabricating an array with a single lobed farfield pattern. We demonstrate that such *tailored gain chirped arrays* are able to operate with both single lobed diffraction limited operation (1.5° beamwidth) or high output power ($450mW$ into 3.5°).

Finally, in §4.6, we summarize the many advantages of an array with a very high interchannel gain, and pose the question: are such devices really arrays, or should they be considered as tailored gain *broad area* lasers? This then leads naturally into Chapter 5, where we fabricate and analyze a truly *tailored gain broad area laser.*

§4.1 Uniform Arrays of Real Index Guided Lasers

The coupled mode analysis of Chapter 3 may be readily extended to the case of more than two channels. Following Kapon, Katz, and Yariv,[1] we presume that each individual waveguide, when isolated from its neighbors, supports only the fundamental spatial mode. This elemental mode is described by its electric field

$E_l(x)e^{i\beta_l z}$, where $l = 1, 2 \dots N$ and β_l is the propagation constant for the elemental mode in the l^{th}-channel. In a manner entirely analogous to Equation (3.1.2) the total electric field for the array supermode may then be written as a linear combination of the elemental modes:

$$E(x,z) = \frac{1}{2}\sum_{l=1}^{N} A_l(z)E_l(x)e^{i\beta_l z} + c.\ c. \tag{4.1.1}$$

where $N = 2$ for the two coupled waveguides of Figure 3.1 and the z dependence of the $A_l(z)$ is due to the interaction between the waveguides. The coupled mode equations for the array may once again be written in the form

$$\frac{d\mathbf{E}}{dz} = i\mathcal{C}\mathbf{E} \tag{4.1.2}$$

where $\mathbf{E}$ is a vector n whose elements are $E_l = A_l e^{i\beta_l z}$. We assume weak overlap between the fields so that coupling occurs only between nearest neighbors, and so the only nonvanishing elements of the matrix $\mathcal{C}$ are $\mathcal{C}_{l,l} = \beta_l$ with $l = 1, 2, \dots N$ and $\mathcal{C}_{l,l+1} = \kappa_{l,l+1}$, $\mathcal{C}_{l+1,l} = \kappa_{l+1,l}$ with $l = 1, 2 \dots N-1$. The definition of the coupling coefficients κ_{ij} is the same as in the case of a pair of coupled waveguides (3.1.7).

The array supermodes are, by definition, the eigenvectors of Equation (4.1.2), *i.e.*, those vectors that satisfy

$$\mathbf{E}^{\nu}(z) = \mathbf{E}(0)e^{i\beta^{\nu} z} \tag{4.1.3}$$

where β^{ν} is the propagation constant of the supermode $\mathbf{E}^{\nu}(z)$. Substitution of (4.1.3) into (4.1.2) gives the matrix eigenvalue problem

$$(\mathcal{C} - \beta^{\nu}\mathcal{I})\mathbf{E}^{\nu} = 0 \tag{4.1.4}$$

where $\mathcal{I}$ is the identity matrix.

A solution of Equation (4.1.4) yields the N supermodes that are supported by an array of N single-mode lasers. The eigenvectors $\mathbf{E}^{\nu}$, $\nu = 1, 2, \ldots N$ can be used in Equation (4.1.2) to evaluate the nearfield of each supermode; each such mode, say $\mathbf{E}^{\nu}$, describes a phase locked combination of the individual laser modes with amplitude $\varrho_l^{\nu} E_l$:

$$E^{\nu}(x) = \frac{1}{2} e^{i\beta^{\nu} z} \sum_{l=1}^{N} \varrho_l^{\nu} E_l(x) + c.\ c.\ . \tag{4.1.5}$$

Generally, the eigenvalues of an arbitrary N-channel array must be found by solving Equation (4.1.4) numerically. The special case of a *uniform array* of identical lasers on equispaced centers may be solved analytically. In this case $\beta_l = \tilde{\beta}$ and $\kappa_{ij} = \kappa$ and the solution of Equation (4.1.4) is[1,2]

$$\begin{aligned} \beta^{\nu} &= \tilde{\beta} + 2\kappa \cos\left(\frac{\nu\pi}{N+1}\right) \\ \varrho_l^{\nu} &= \sin\left(l \frac{\nu\pi}{N+1}\right) \end{aligned} \qquad \nu = 1, 2, \ldots N\ . \tag{4.1.6}$$

Figure 4.1 shows the nearfield patterns of the five supermodes which are supported by an index guided array of five identical channels. The lateral distribution of the effective index (in the junction plane) was taken, for definiteness, as that corresponding to an array of typical *GaAs/GaAlAs* ridge waveguide lasers such as those of Figure 2.5. The channels are 4μm wide and the interchannel spacing is 2μm; the index step $\Delta\bar{n} = 0.002$. The supermode patterns were calculated by using the numerical methods of §2.7, and confirm the predictions of the coupled mode theory. The supermodes designated by $\nu = 1, 2, 3, 4, 5$ correspond to $(+ + + + +)$, $(+ + 0 - -)$, $(+0 - 0+)$, $(+ - 0 + -)$, and $(+ - + - +)$ field amplitudes in the various array channels, respectively. The $+$, $-$, and 0 symbols indicate whether the field is positive, negative, or zero in the corresponding channel. The $(+ + + + +)$ supermode of the five-element uniform array (which

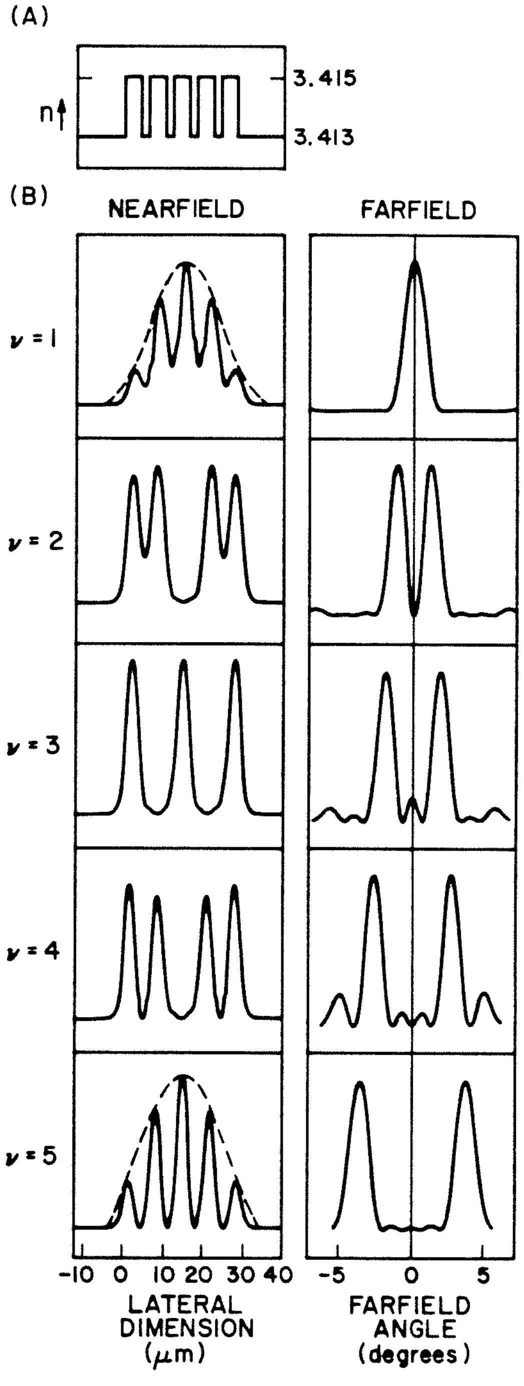

FIGURE 4.1 Supermodes of a five-element real index guided uniform array. The channel width is 4μm and the channel spacing is 2μm with an index step $\Delta\bar{n} = 0.002$. (a) refractive index profile (b) intensity nearfield and farfield patterns. Note the envelope functions (dashed lines) of the fundamental and highest order supermode nearfield patterns are very similar. The two modes differ only in the lossy interchannel regions.

is referred to as the fundamental mode) corresponds to the $(++)$ supermode of the two-element array studied in Chapter 2, while the highest order completely antisymmetric supermode $(+-+-+)$ corresponds to the $(+-)$ supermode in the two-element array. It is clear that the nearfield envelopes (given by the dashed line in Figure 4.1) of the $\nu = 1$ and the $\nu = 5$ supermodes are very similar. (In fact, as shown by (4.1.6), in the limit of very weak coupling between the channels they become identical.) The intensity nearfield patterns differ only in that the $\nu = N$ supermode has nulls in the interchannel region. This has an extremely important effect on the operation of a uniform array of semiconductors.

Almost all semiconductor laser structures are designed so that the gain is greatest in the core region of the waveguide; the cladding region is therefore relatively lossy when compared with the core region. In a single-element semiconductor laser, this minimizes the threshold current density and leads to more efficient operation.(§1.2) However, the very properties that lead to low threshold currents in a single-element laser promote the undesirable twin lobed farfield pattern in an uniform *array*. Since the highest order completely antisymmetric supermode has *nulls* in the lossy interchannel region, relatively more of its light is concentrated in the high gain core regions of the laser channels than is the case for the fundamental supermode. The highest order supermode therefore has a higher modal gain than the fundamental supermode and will thus be the lasing mode at threshold. This in turn leads to the undesirable twin lobed farfield patterns characteristic of uniform arrays such as that of Figure 1.6d.

Finally, we note that the farfield pattern of the fundamental supermode is similar to that of an array of uniformly illuminated slits, and thus will have a single lobed farfield pattern only if the elemental waveguides are closely spaced.[3] This is the case for all the array waveguides considered in this thesis.

§4.2 Chirped Arrays of Real Index Guided Lasers

We showed in Chapter 2 that two phase mismatched waveguides will support two supermodes that have *unequal* power distributions in each channel. If we consider two coupled ridge waveguides of unequal widths, we know from the results of §3.1 and Figure 3.8 that the fundamental supermode will be concentrated in the wider channel. If we can then also preferentially concentrate the gain in this channel, the fundamental supermode will have the highest modal gain and will therefore be the lasing mode. This in turn should lead to the desired single lobed farfield pattern.

These ideas extend themselves in a natural way to a *chirped array* of lasers in which the widths of the individual channels increase monotonically across the array.[4] (The term *chirp* is borrowed from the communication theory term for a signal with a temporal frequency that varies linearly with time; in a chirped array, however, it is the *spatial* frequency which varies with *distance*). We consider real index guided arrays in this section, and discuss and gain guided chirped arrays in §4.4*ff*.

Figure 4.2 shows the supermodes supported by a real index guided chirped array with channel widths that are linearly chirped from 5μm to 3μm across the array. The channel spacing is uniform (2μm). Comparison of Figure 4.1b (which plots the mode profiles for a uniform array) with Figure 4.2c (which plots the mode profiles for a chirped array) reveals a striking difference between the two types of arrays. Unlike the uniform array, the fundamental supermode in the chirped array is preferentially concentrated at one side of the waveguide, and the completely antisymmetric supermode is concentrated at the other side.

In principle, the lasing of higher order supermodes in a chirped array could be suppressed by tailoring the spatial gain profile across the array so as to favor the

§4.2 Chirped Arrays of Real Index Guided Lasers

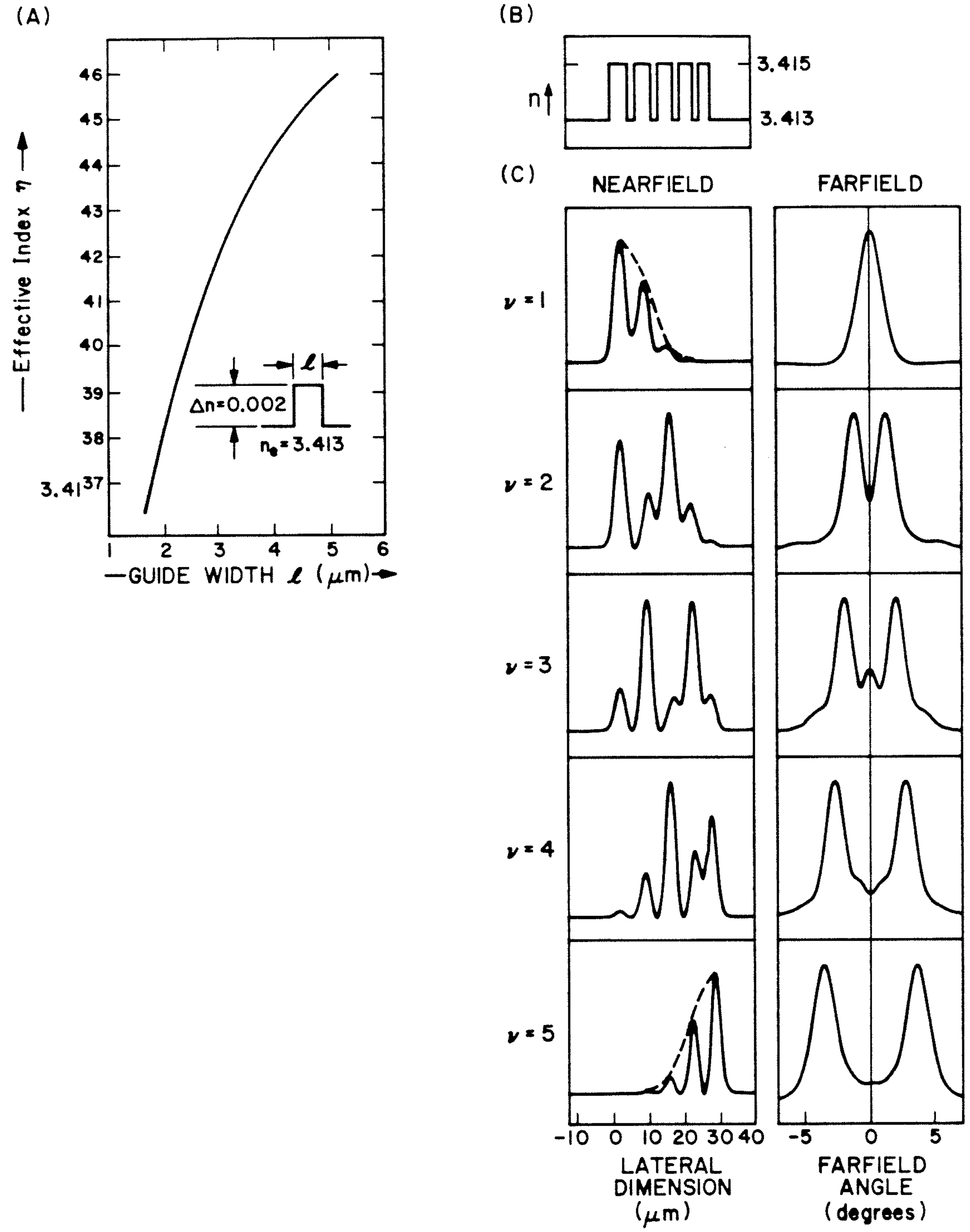

FIGURE 4.2 Supermodes of a five-element real index guided chirped array. The channel widths vary linearly between 5μm and 3μm in steps of 0.5μm. The channel spacing is 2μm, and the index step $\Delta\bar{n} = 0.002$. (a) plot of guide width ℓ *vs.* effective index η. (b) refractive index profile (c) intensity nearfield and farfield patterns. Note that the fundamental $\nu = 1$ supermode is located to one side of the array and the highest order $\nu = 5$ supermode is at the other. Also note that despite the asymmetric nearfield patterns, the farfield patterns are all symmetric.

fundamental supermode. Since the other supermodes are increasingly localized at the other side of the array, their overlap with the gain distribution will be smaller, and they will not lase until well above threshold.

(a) Limitations of Real Index Guided Chirped Arrays

Unfortunately, there are both fundamental and technological limitations that make real index guided chirped arrays impractical. The fundamental limitations result from the interplay between real index and gain guiding discussed in §2.3, while the technological limitations result from the limited precision with which it is possible to fabricate real index guided structures.

Reference to Figure 2.10 in our discussion of the types of lasers suitable for integration into arrays shows that if an array is to be considered real index guided, the size of the built-in index step must be sufficient to overcome the antiguiding effect due to the carriers. This implies that the built-in index step $\Delta\bar{n}$ must be greater than about 0.003, and so a single mode waveguide must be no wider than $\sim 2\mu\text{m}$ ($5\mu\text{m}$ if the waveguide is allowed to support at most two modes). If $2\mu\text{m}$ is adopted as the smallest feature size, and 0.5 microns for the precision with which the guide width may be varied, we see that at best we could fabricate a five-element array with a maximum width of about $22\mu\text{m}$. The volume of the lasing mode has then been increased by only a factor of four from that of a single-element laser. Thus, we expect only moderately high power outputs from real index guided chirped arrays.

Furthermore, given a variation in the stripe width of $0.5\mu\text{m}$, the phase mismatch parameter between adjacent waveguides will be quite large. This is illustrated by Figure 4.3, which plots the nearfield pattern of the fundamental mode for the same array as Figure 4.2 but with various values of the refractive index

§4.2(a) Limitations of Real Index Guided Chirped Arrays

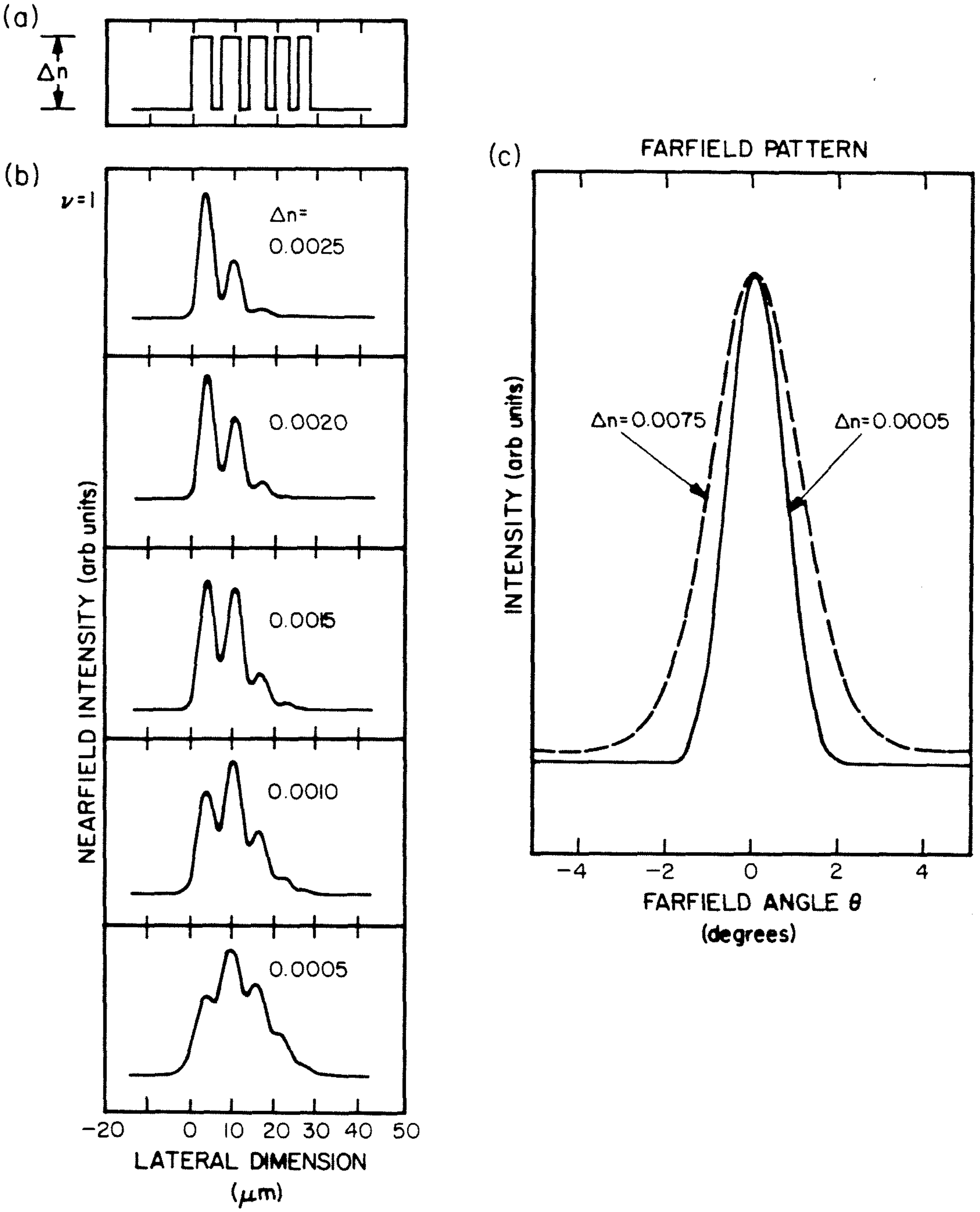

FIGURE 4.3 Limitations of strongly coupled chirped arrays due to phase mismatching. (a) refractive index profile, the same as Figure 4.2 but for various index steps $\Delta\bar{n}$; (b) the fundamental supermode for various index steps $\Delta\bar{n}$; (c) corresponding farfield patterns.

step $\Delta\bar{n}$. (The effect of gain has been ignored for the moment). We see that for $\Delta\bar{n} = 0.0025$ the admixture factor between adjacent channels is 3:1, and thus there is significant optical intensity in only the first two channels. Power may be spread out over more of the lasers (*i.e.*, the admixture factor may be decreased) by decreasing the size of the index step; however, Figure 4.3 shows that as the index step becomes even slightly smaller, the channels become more strongly coupled and the fundamental mode shifts to the *center* of the waveguide. If the index step is too great, power will be concentrated in only a few elements of the array. If the index step is too small, the beneficial effects of the spatial segregation of the supermodes is lost. Figure 4.3 indicates that it is therefore necessary to control the refractive index step across the array to about ±0.0002.

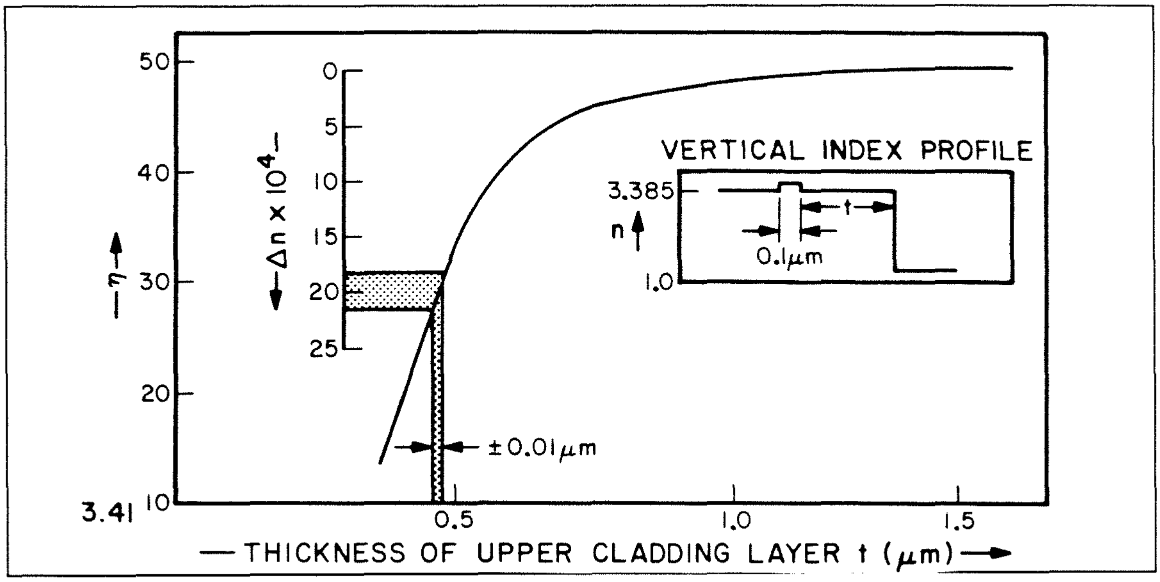

FIGURE 4.4 Plot of the refractive index step $\Delta\bar{n}$ in an air ridge waveguide as a function of the thickness of the upper cladding layer.

This number implies some extraordinary constraints on the precision with which the channels must be etched. Figure 4.4 shows that the etching depth into the upper cladding region must stop just under 0.5μm from the active layer (which is easily possible), but that the *uniformity* with which the etching must occur over the array must be better than 200 Angstroms! At the present time this is impossible.

Furthermore, even if new technology made it possible to control the etching to this precision, there is the question as to whether or not this device could be considered a real index guided laser at all. Figure 4.5a shows the waveguide model for the chirped array of Figure 4.4, but now the effect of gain has been included.

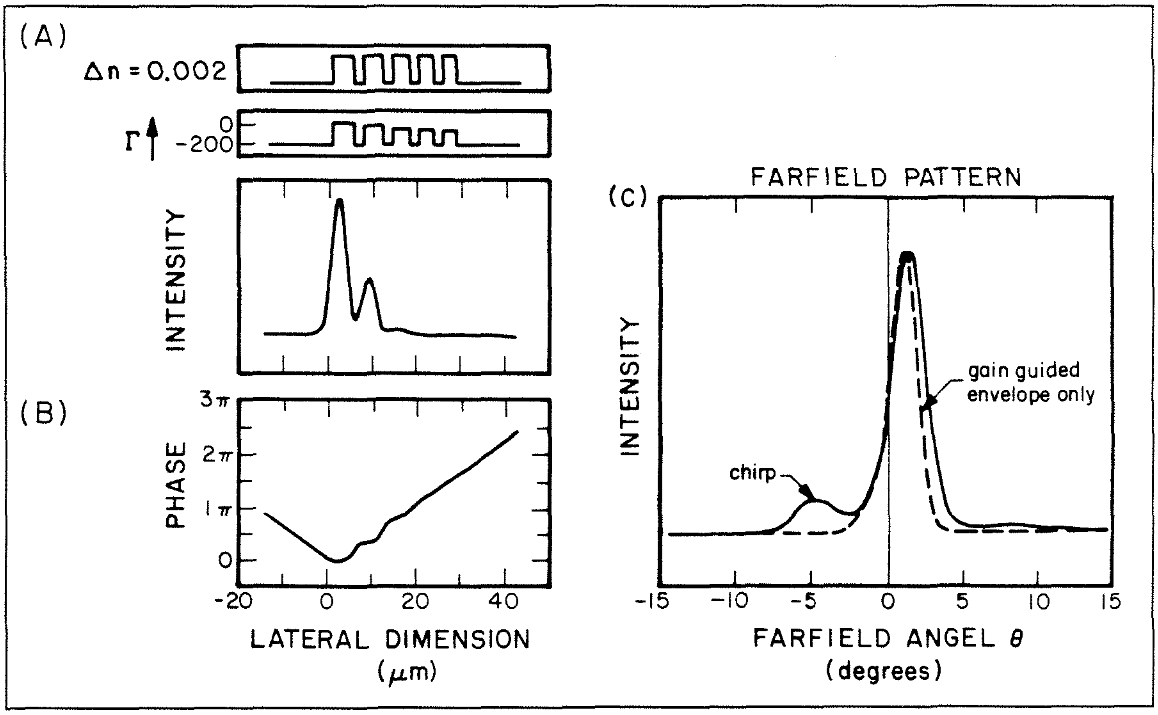

FIGURE 4.5 Limitions of chirped arrays due to the effect of gain. (a) Waveguide model and (b) nearfield pattern for the chirped array of Figure 4.2 including the effect of gain. (c) Farfield patterns (solid line) for the array of part (a), and (dashed line) for a gain guided waveguide with a spatial gain profile given by the envelope function of the gain profile of the waveguide of part (a). The nearly superimposed solid and dashed lines of part (c) indicate that the chirped array of part (a) is essentially gain guided.

The gain profile is tailored to match the fundamental mode, thus assuring single lobed operation. The solid curve in Figure 4.5b shows the farfield pattern for this chirped array. Note that it is essentially single lobed, but slightly displaced from the facet normal. We will see in §5.12 that the off-axis farfield pattern is the result of an asymmetric gain profile. Here, it provides a convenient measure of the extent to which this chirped array should be considered either real index or gain guided. The dashed curve in Figure 4.5b shows the farfield pattern for a gain guided laser with no variation in the refractive index profile and with a spatial gain profile that matches the gain envelope function for the waveguide of Figure 4.5a. The fact that the two curves are almost superimposed indicates that this array is almost entirely gain guided.

In conclusion, we have shown that fundamental and technological limitations make the fabrication of real index guided chirped arrays difficult, if not impossible. We therefore turn our attention to arrays of gain guided lasers.

§4.3 Uniform Arrays of Gain Guided Lasers

We have seen in previous sections that reducing the size of the index step which confines the mode allows it occupy a larger volume of space. However, as we have shown in §2.3 and §4.2(a), there is a lower limit on the minimum possible index step due to the presence of gain, and that laser waveguides with index step differences of $\Delta\bar{n} \leq 0.003$ should be considered as gain guided.

Although suffering from the disadvantage that their spectral properties are less desirable than those of strongly real index guided lasers, gain guided arrays offer several important advantages over their real index counterparts.

(1) Most importantly, from a research point of view, gain guided lasers are far easier to fabricate than real index guided lasers, thus allowing more rapid improvements in device design.

(2) The spatial gain profile simultaneously determines both the eigenmodes as well as the modal gains, thus potentially simplifying device design.

(3) The interchannel gain in a proton implanted laser may be controlled by simply reducing the depth of the proton implantation.(§4.3)

(4) A gain guided laser confines the optical field significantly less strongly than a real index guided laser. The modal volumes can therefore be much larger, thus potentially increasing the device's power output and decreasing the beamwidth. Accordingly, all the high power records to date have been set with gain guided lasers.

(5) Finally, in a *nonuniform* structure the intrinsically weak nature of the gain guiding reduces the effect of phase mismatching, effectively increasing the size of the device.

We commence our study of arrays of gain induced waveguides by noting that the formalism used in §4.1 to predict the supermodes of a uniform array of real index guided lasers may also be used to calculate the supermodes of a weakly coupled gain guided structure. However, for the more important case of strong coupling, we must make use of the numerical methods of §2.7. This is especially so because, as we will see in §4.4(a), the exact (numerical) results are quite different from what we would expect based on a naive application of the theory of §3.4 to strongly coupled gain guided lasers.

In most of the waveguide models we discuss, the antiguiding factor has been ignored for simplicity. Its exclusion in no way alters any of the conclusions we will draw from our work. We will incorporate the antiguiding effect into our models when appropriate.(§2.2(*e*),4.5(*b*))

Figure 4.6 presents (a) the gain profile, (b) the nearfield and farfield patterns, and (c) the modal plot for a uniform array of five lasers 4μm wide on 9μm centers. Comparison with the corresponding Figure 4.1 for a uniform array of real index guided lasers shows that the nearfield and farfield patterns are essentially identical.

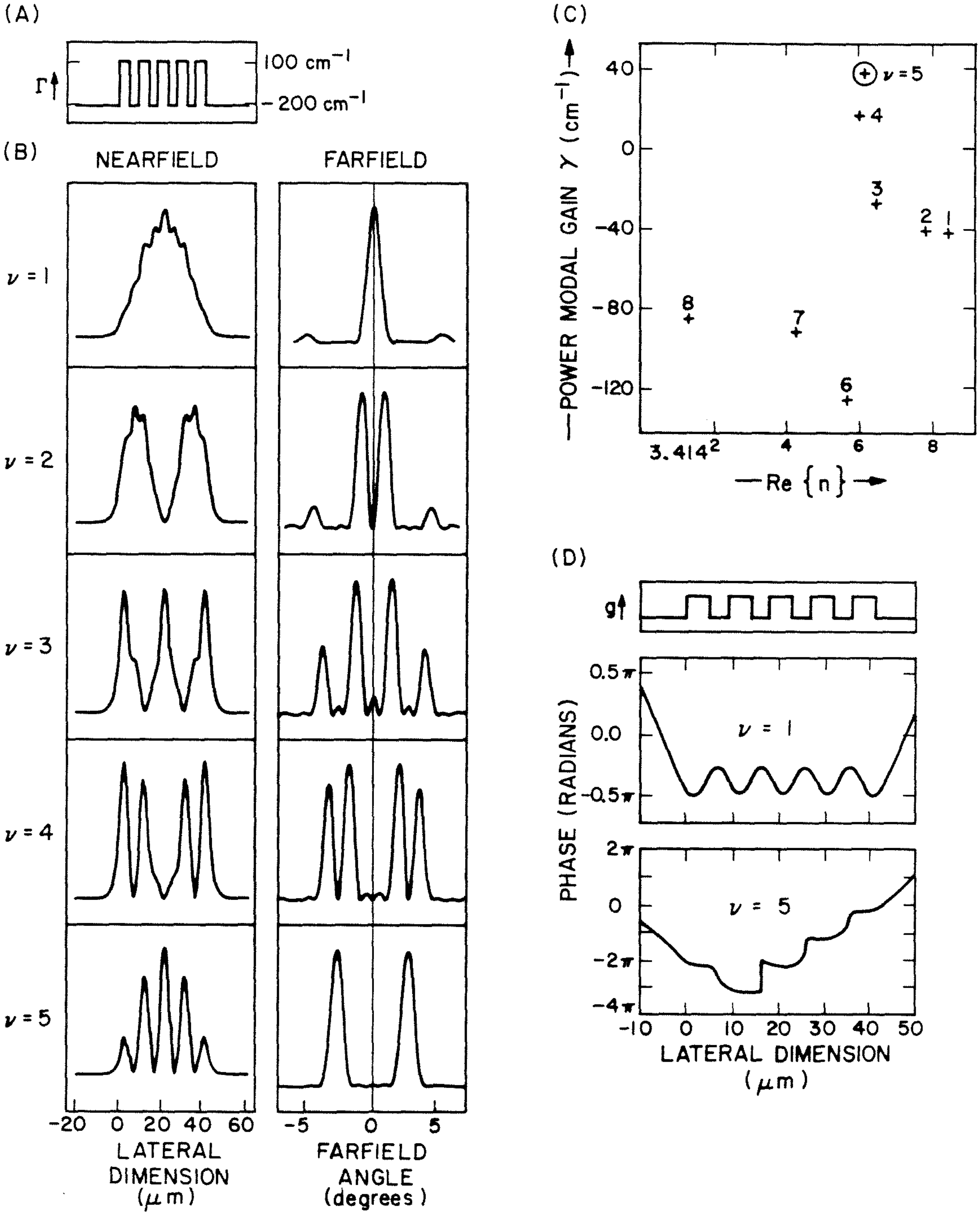

FIGURE 4.6 Supermodes of a gain guided uniform array of five lasers 5μm wide on 9μm centers: (a) gain profile (b) intensity nearfield and farfield patterns (c) modal diagram with the lasing $\nu = 5$ supermode circled (d) phase plots for the $\nu = 1$ and $\nu = 5$ supermodes. Note the symmetric farfield patterns.

Note that the phase plot diagram in Figure 4.6d shows that the phases of each of the lasers is the same for the $\nu = 1$ fundamental mode, but that the effect of the phase curvature is the same as that of a single-element laser. Since the astigmatism of gain guided lasers is proportional to the phase front curvature, this array will also be astigmatic.

Of somewhat more interest is the modal diagram of Figure 4.6c. Not surprisingly, the $\nu = 5$ mode, which has nulls in the lossy interchannel regions, has the highest modal gain. It is of interest, however, to note that the pattern of the modes is reminiscent of a resonance curve. We will see below that a type of "resonance" between the nearfield pattern and the spatial frequency of the peaks in the gain distribution does occur. This concept will prove helpful in understanding strongly coupled gain guided chirped arrays.(§4.4(*a*))

(a) Box Modes and Array Modes

Figure 4.7 illustrates another interesting point about waveguide models for array structures in which the interchannel gain has been increased to enhance phase locking among the array elements. Starting from an array picture, Figure 4.7a shows the mode pattern and nearfield pattern for the lasing $\nu = 5$ supermode (*i.e.*, the one with the highest modal gain) for a five-element array in which both the interchannel regions and the region external to the waveguide have been pumped to transparency. The mode pattern and nearfield pattern for the lasing mode are also shown.

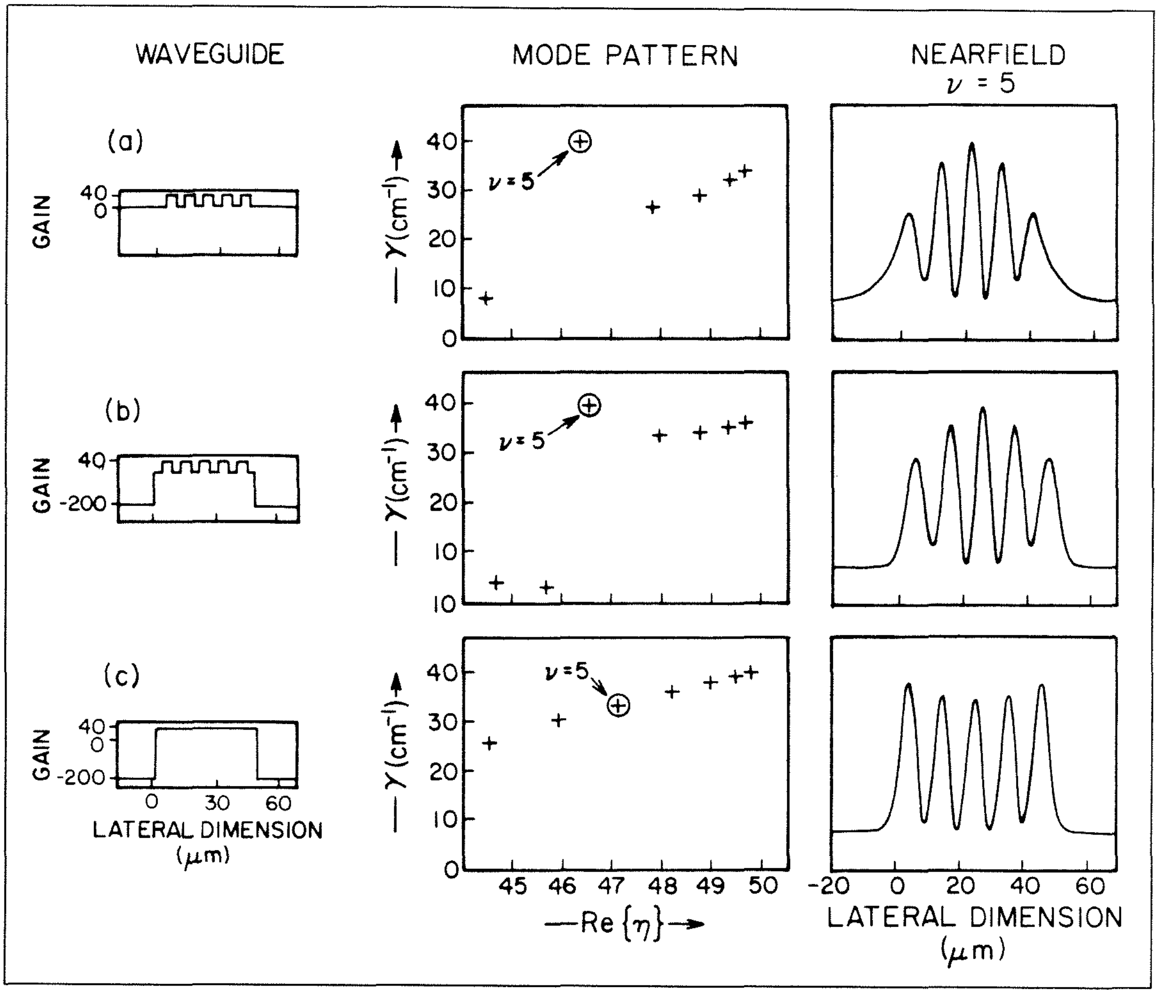

FIGURE 4.7 Comparison of the mode patterns and nearfield and farfield patterns for (a) an array, (b) a "box plus array" and (c) a box waveguide.

When the effect of the unpumped active region external to the array is added in, we obtain the "array plus box" waveguide of Figure 4.7b. Note that, as might be expected from elementary perturbation theory, the effect of the lossy external region that defines the "box" has only a minimal effect on the eigenmodes because the field is small in that region. The effect of the "box" may then be considered as a small perturbation on the array structure.

The interesting point is to compare the modes of Figure 4.7b with the $\nu = 5$ mode of the wide box waveguide with the same width in Figure 4.7c, where we see that (except for a relatively minor change in the envelope functions), the $\nu = 5$ box mode is very similar to the array and "array plus box" modes. In fact, another way of thinking about the same waveguide of Figure 4.7b would be to start with a uniform gain *box* waveguide and add the *array* as a perturbation to form a "box plus array" waveguide. Elementary perturbation theory predicts that the *box* mode which has the greatest overlap with the high gain region of the perturbation (*i.e.*, the array) will have the highest modal gain. The high modal gain of the $\nu = 5$ mode may then be viewed as coming about because the spatial frequency of the perturbation (*i.e.*, the array) is "resonant" with that of the $\nu = 5$ *box* mode (both have five periods over the width of the waveguide), thus enhancing the modal gain of the $\nu = 5$ mode.

We remark that examination of Figure 4.7 reveals that for the special case of a strongly coupled *uniform* array either the "box plus array" picture or the "array plus box" picture works equally well, although the "array plus box" viewpoint is probably somewhat better. However, we will see in §4.4(a) that making a distinction between the two perspectives aids understanding of strongly coupled *nonuniform* gain guided arrays.

§4.4 Chirped Arrays of Gain Guided Lasers

In a single-element laser the modal gain of the fundamental mode is approximately proportional to the overlap between the optical intensity profile and the gain distribution inside the laser. If we make a chirped array of gain guided lasers, the wider lasers should have higher individual channel modal gains than the narrower ones, and hence in a manner entirely analogous to the way in which we have effectively tailored the real index profile in a real index guided chirped array, we should also achieve some degree of gain tailoring in a gain guided chirped array.

In such an array, we can take advantage of the fact that in a gain guided laser the gain profile determines the eigenmodes as well as the modal gains to devise an array structure that favors the fundamental single lobed supermode.

(a) Chirped Arrays of Gain Guided Lasers: Theoretical

For example, Figure 4.8 plots the increase in the real part of the effective index $\bar{\eta}$ and the power modal gain γ of the fundamental mode in a single-element gain guided laser as a function of the width ℓ for a laser with a channel gain Γ_0 of 60cm^{-1} and a cladding loss of 200cm^{-1}.

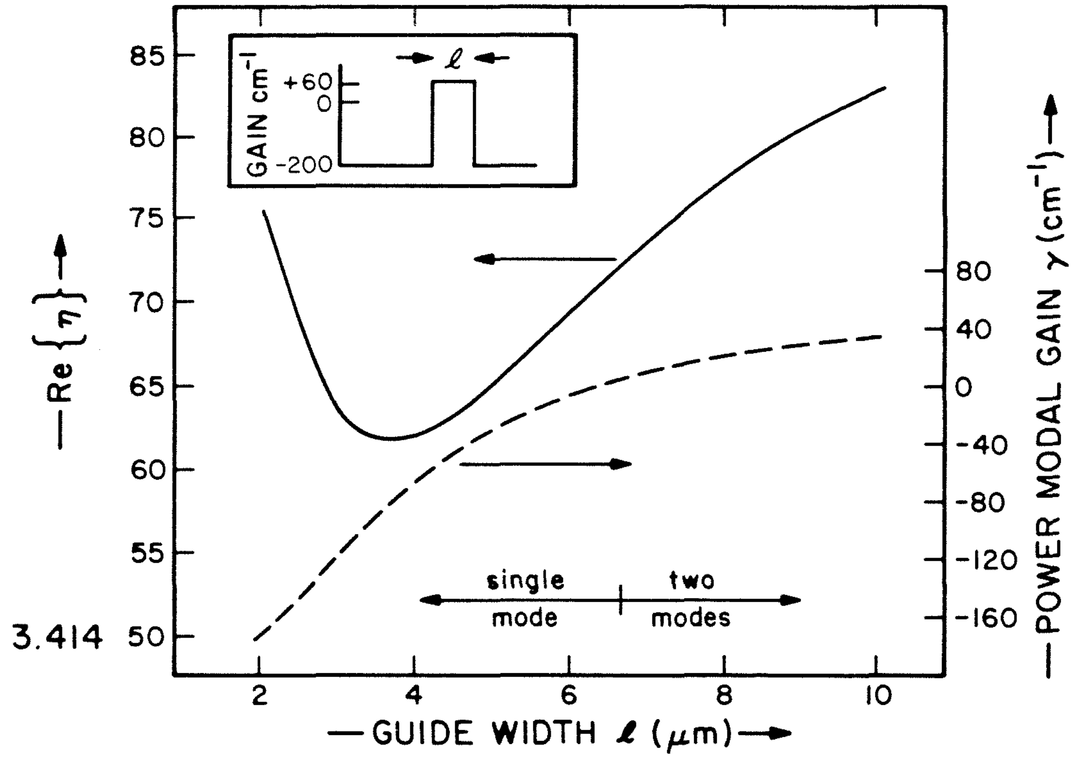

FIGURE 4.8 Variation of effective index and modal gain in a gain guided laser. The channel effective index (solid line) and modal gain (dashed line) are shown for a gain guided box waveguide as a function of the waveguide's width.

We see that as long as the widths of the laser channels are greater than about 4μm, the wider channels will have both higher effective indices and modal gains. The theory of §3.4 then leads us to expect the fundamental supermode to be concentrated in the wider channels. Since the gain is also greatest there, we then expect the fundamental supermode to have the highest modal gain, which in turn should yield the desired single lobed farfield pattern.

Figure 4.9 illustrates the waveguide model for such a chirped array of five-elements with widths ranging between 8μm and 4μm in 1μm increments with 5μm separations between the lasers. The heavy solid horizontal lines indicate the effective refractive index in each channel, while the dashed lines indicate the effective modal gain in each channel.

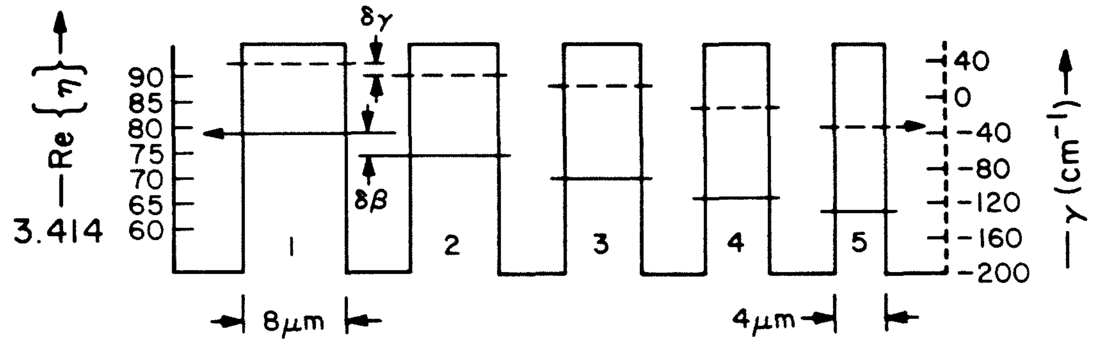

FIGURE 4.9 Schematic diagram of a five-element gain guided chirped array based on the plot of Figure 4.8 showing the variation of the channel index and gain. $\delta\beta$ and $\delta\gamma$ are the phase and gain mismatch parameters of §3.4.

If we number the channels sequentially from the wider to the narrower, then both the phase mismatch parameter $\delta\beta$ and gain mismatch parameter $\delta\gamma$ of §3.4 are negative. Figure 3.10 then indicates that the fundamental supermode should have more power in the wider guides than in the narrower ones. Since the confinement factor of the channel mode is greater in a wider guide than in a narrower one, the fundamental supermode should also have the highest modal gain. We therefore hope that we might be on the verge of achieving our goal of designing a laser array that favors the fundamental supermode.

Unfortunately, when we compute the supermodes of this array, we discover the actual situation is very different from what we had anticipated. Figure 4.10 presents the modal distribution diagram for the first six modes of this waveguide. To our surprise, we find that the fundamental supermode does not have the highest modal gain as we had expected. In fact, the fundamental supermode has one of the *lowest* modal gains of all the modes! Furthermore, when we examine the phase plots for the $\nu = 2$ supermode (in Figure 4.10d), we see that the phase difference between adjacent channels is approximately π radians, which implies that the so-called $\nu = 2$ supermode is actually the "highest order antisymmetric" supermode. Figure 4.10 shows that the supermodes in complicated gain guided structures can no longer be characterized simply by means of ranking them in order of decreasing effective index.

More importantly, as a result of the π phase shift between adjacent channels, the $\nu = 2$ high gain supermode has the undesirable twin lobed farfield pattern, so we have not yet achieved our goal. When we examine the intensity nearfield patterns of Figure 4.10, we see why this supermode has the highest modal gain of all the supermodes: once again, the lossy interchannel regions favor the supermode which has nulls in the interchannel regions.

We also note that the $\nu = 2$ "antisymmetric" mode is localized under the relatively *wider* channels, while the $\nu = 1$ fundamental mode is localized under the *narrower* channels. This result is also completely unexpected. The reasons for this anomalous behavior is unknown; however, it may be related to the fact that

§4.4(a) Chirped Arrays of Gain Guided Lasers: Theoretical

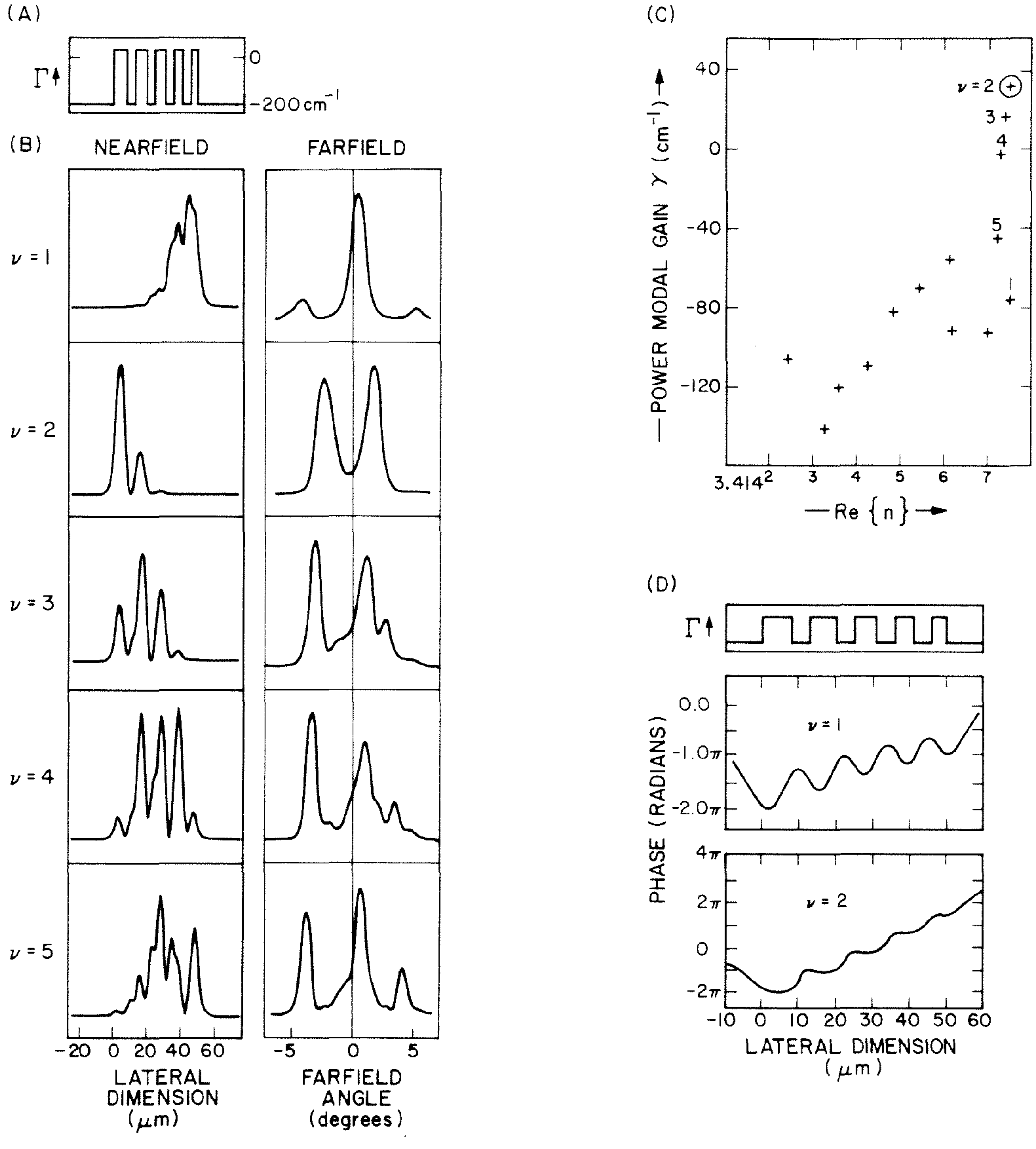

FIGURE 4.10 Supermodes of a weakly coupled gain guided linearly chirped array of five lasers with widths between 8μm and 4μm, and separated by 5μm. (a) gain profile (b) intensity nearfield and farfield patterns (c) modal diagram (d) phase plots for the $\nu = 1$ and $\nu = 2$ supermodes. Note that the farfield patterns are no longer symmetric about 0°.

this particular array is both gain guided and very strongly coupled; these results clearly show the limitations of the theory of §3.4.

We also observe another interesting aspect of asymmetric gain-induced waveguides: unlike the symmetric real index guided waveguides of Figures 2.11 and 4.1, the symmetric gain-induced waveguides of Figures 2.12 and 4.6 and the *asymmetric* real index waveguide of Figure 4.2 for which all the higher order modes have *symmetric* farfield patterns, the farfield patterns of this asymmetric gain-induced waveguide are *asymmetric* about 0°. Asymmetric gain induced waveguides are a unique class of waveguide because of the complex nature of the electric field due to gain guiding and the lack of left-right inversion symmetry of the waveguide. We will explore this point further in §5.12.

Finally, note that both the $\nu = 1$ and $\nu = 2$ supermodes have appreciable intensity over approximately one half the array, thus indicating that although gain guiding has reduced the effective phase mismatch between the channels, there is still too large a degree of phase and gain mismatch present. Although the mismatch between the channels could be reduced by decreasing the variations in the widths of the waveguides, as is pointed out in §4.2(a), there is a practical lower limit on the the attainable photolithographic resolution which makes this difficult, and especially so for proton isolated lasers. We therefore consider another method of reducing the channel mismatch by increasing the interchannel gain. This is also advantageous from the point of view of promoting phase locked operation of the array.[5] Now, however, we see that there are at least two additional advantages to be derived from an enhanced interchannel gain. Firstly, the phase and gain mismatch between adjacent channels will be reduced (because the fields of the isolated lasers will be less well-confined, and hence less sensitive to variations in the width of the laser). This should also cause the mode to spread out over more of the array, thus making more effective use of the gain distribution. Secondly, if we recall that the twin lobed antisymmetric supermode is favored over the single lobed fundamental supermode because it has nulls in the lossy interchannel regions, we might surmise that increasing the interchannel gain will tend to favor the fundamental supermode more than it will the antisymmetric supermode.

Figure 4.11a shows just such a waveguide. This waveguide is identical to that of Figure 4.10 except that the interchannel gain has been increased from $-200\mathrm{cm}^{-1}$ to transparency ($0\mathrm{cm}^{-1}$). When we examine the theoretical farfield patterns of this waveguide, we immediately receive another surprise, this time rather pleasant: whereas in all of the waveguides we have studied so far only the fundamental mode has the desired single lobed farfield pattern, we now find *many* modes with single lobed farfield patterns! Understanding how and why this come about will lead us down some exceedingly interesting mathematical paths in the next chapter.

Figure 4.11b shows that one possible exception to this pattern is the $\nu = 5$ supermode, which is quite unlike the other supermodes plotted in Figure 4.11 because it alone has a twin lobed, nearly symmetrical, farfield pattern. The reason that this mode is so different from the others may be best understood in the light of §4.3(a), where we showed that due to the lossy unpumped *GaAs* active region at the edges of the array, it is possible to consider a strongly coupled array (*i.e.*, one with a large interchannel gain) as either an array perturbed by a box ("array plus box" picture) or as a box waveguide perturbed by an array ("box plus array" picture). In the case of a *uniform array*, we remarked that it was immaterial which description is used, although the "array plus box" description is probably a little better.

However, it is clear from Figure 4.11b that the effect of the small nonuniform array perturbation, while only slightly affecting the nearfield patterns, has

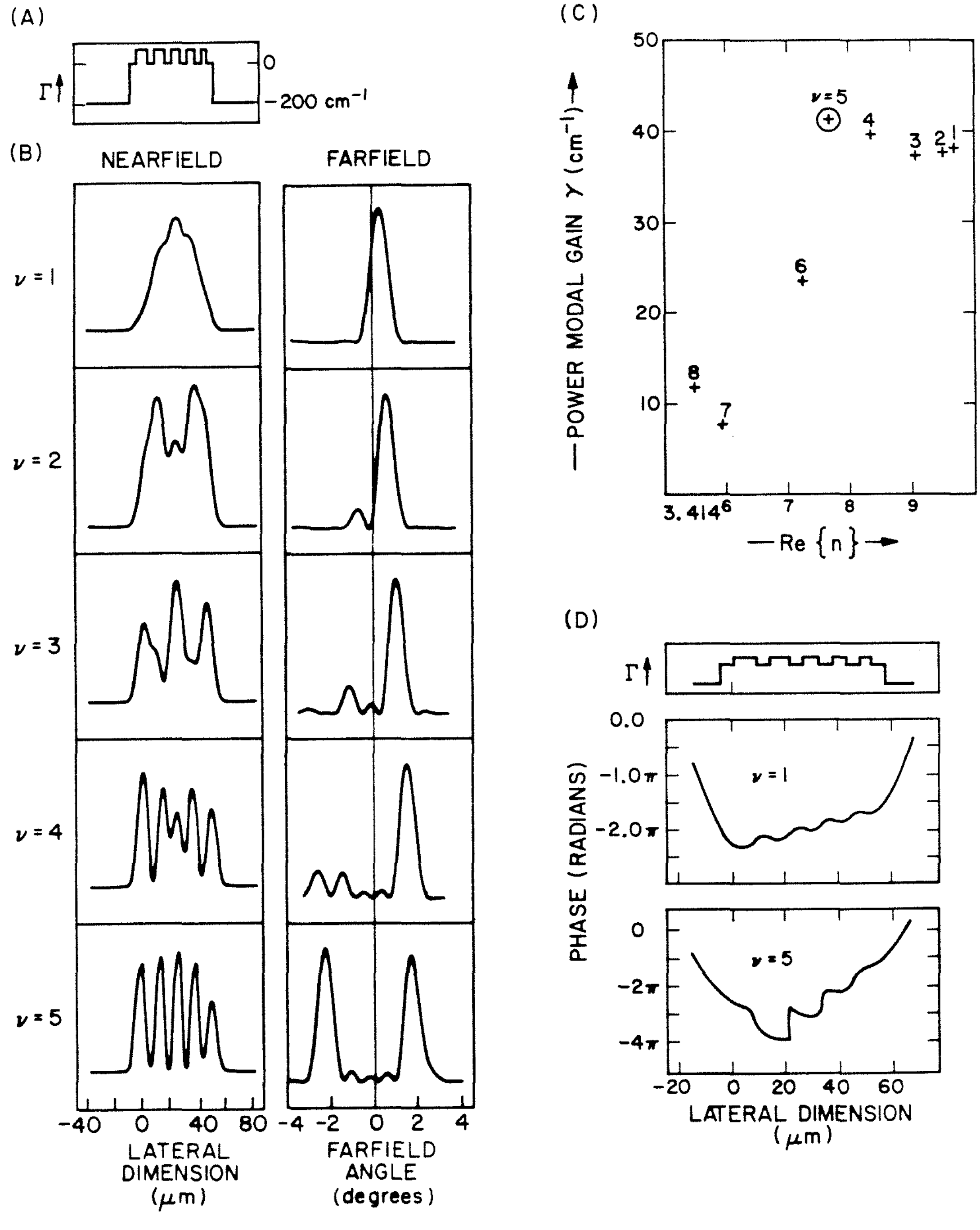

FIGURE 4.11 Supermodes of a five-element strongly coupled gain guided chirped array (same as Figure 4.10 but with the interchannel gain set to transparency (0cm^{-1}). (a) gain profile (b) intensity nearfield and farfield patterns (c) modal diagram (d) phase plots for the $\nu = 1$ and $\nu = 5$ supermodes. Note that all the farfield patterns except that of the $\nu = 5$ supermode are single lobed.

introduced a radical change in all of the farfield patterns save that of the $\nu = 5$ supermode. We note that the spatial frequency of the nearfield intensity distribution for the $\nu = 1 \ldots 4$ box modes are non-resonant with that of the perturbation, while the $\nu = 5$ mode, having as many peaks as there are array elements, is resonant with the array structure. In a manner entirely analogous to the uniform array case of §4.3(a), this explains why the $\nu = 5$ supermode has the highest modal gain of all the waveguide modes. When we compare the strongly coupled uniform array of Figure 4.7b with the strongly coupled asymmetric nonuniform array of Figure 4.11, we see that the asymmetrical nature of the gain perturbation alters the character of the nonresonant box modes by suppressing one of the twin lobes of the farfield pattern. However, the asymmetric gain perturbation is incapable changing the character in the resonant $\nu = 5$ mode so that this mode has the usual twin lobed farfield pattern. We therefore see that, unlike the strongly coupled uniform array of Figure 4.7b, which was better described as an array perturbed by a box, the strongly coupled *nonuniform* gain guided array *must* be thought of in terms of a box waveguide perturbed by the array. This will be true for any strongly coupled gain guided array: whatever the array design, the interaction of the array and box modes cannot be ignored.

Given our quest to design an array with a single lobed farfield pattern, the discovery of a means of supressing one lobe of a twin lobed farfield pattern is an exceedingly interesting one.

(b) Chirped Arrays of Gain Guided Lasers: Experimental

At this point in our work, a rather fortuitous accident occurred. We noted in our discussion of numerical techniques in §2.7 that it was important to find *all* the modes of a waveguide, and especially so for the mode with the highest modal gain (because that mode will be the lasing mode). Unfortunately, the automated root finding routine in the MODES program described in §2.7 occasionally misses roots of the dispersion equation (2.7.13), and in fact it first missed finding the $\nu = 5$ mode discussed above. It therefore seemed (erronously, as it turned out) as if *all* the modes of the strongly coupled gain guided chirped array had the desired single lobed farfield pattern, and so we therefore decided to fabricate a chirped array of gain guided lasers.

Figure 4.12 presents a cross-sectional schematic diagram of two such nonuniform gain guided proton implanted chirped arrays in which the damage created by the implanted protons creates the high resistivity regions that separate the laser channels. Two channel configurations were used. In the first[6] (pattern A in Figure 4.12a), the widths of the laser channels vary from 8μm to 3 μm in steps of 1μm with 5μm between channels.

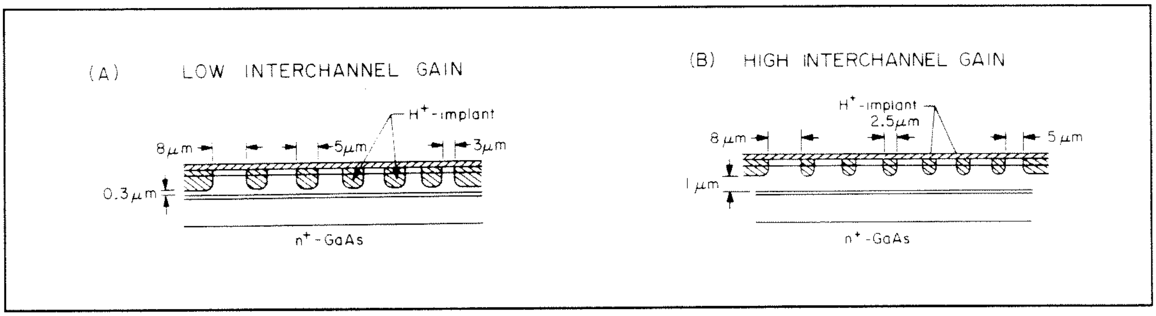

FIGURE 4.12 Schematic diagram of a (a) weakly and (b) strongly coupled proton implanted chirped array.

§4.4(b) Chirped Arrays of Gain Guided Lasers: Experimental

For the second configuration[7] (pattern B in Figure 4.12b), which is essentially the same as the first but allows enhanced interchannel coupling, the widths of the laser channels vary from 8μm to 5μm in steps of 0.5μm with 2.5μm between channels. The width of each laser array was approximately 60μm.

To fabricate the array, four layers were grown by molecular beam epitaxy (MBE) on a n^+GaAs substrate (Si doped, $2 \times 10^{18} cm^{-3}$). The composition and thickness of the layers are as follows: n $Ga_{0.6}Al_{0.4}As$ lower cladding layer (2.0μm thick), Si doped, $3 \times 10^{17} cm^{-3}$; undoped $GaAs$ active region (0.15μm thick); p $Ga_{0.6}Al_{0.4}As$ upper cladding layer (1.8μm thick), Be doped, $3 \times 10^{17} cm^{-3}$; p^+GaAs cap layer, (0.2μm thick), Be doped, $1 \times 10^{18} cm^{-3}$. Immediately after growth a single contact of Cr/Au was deposited to form the p contact. Thick photoresist was patterned to define the array, and protons were implanted to define the laser channels. Various proton implant energies were used to demonstrate the importance of strong interchannel coupling (*i.e.*, gain) for achieving single lobed farfield operation; dosages were typically $3 \times 10^{16} cm^{-3}$. After implantation, the photoresist was removed, the devices were lapped to ~ 75μm, $AuGe/Au$ was deposited to form the n contact, and the contacts were annealed at 380°C for 20 seconds in an H_2 atmosphere. Devices were then cleaved into bars ~ 250μm long and tested under low duty cycle, pulsed conditions.

The interchannel gain in a chirped array of proton implanted lasers may be conveniently varied by changing the depth (energy) of the proton implantation; a smaller implant energy increases the distance between the bottom of the insulating proton damaged regions and the active layer. If the proton penetration depth does not extend to the active layer, current will spread into the regions between the laser channels, thus increasing the interchannel coupling (gain). For a given implantation pattern, it is therefore possible to vary the interchannel coupling from its minimum value (deep implant, minimum interchannel gain) to a maximum value (shallow implant, maximum interchannel gain). The maximum interchannel gain is determined by the envelope function for the spatial gain distribution.

We remark that our early work[6] used wafers grown by liquid phase epitaxy (LPE) while later work[7] utilized wafers grown by molecular beam epitaxy (MBE). Better results were obtained with the MBE grown wafers; we attribute this to the greater uniformity of the MBE process.

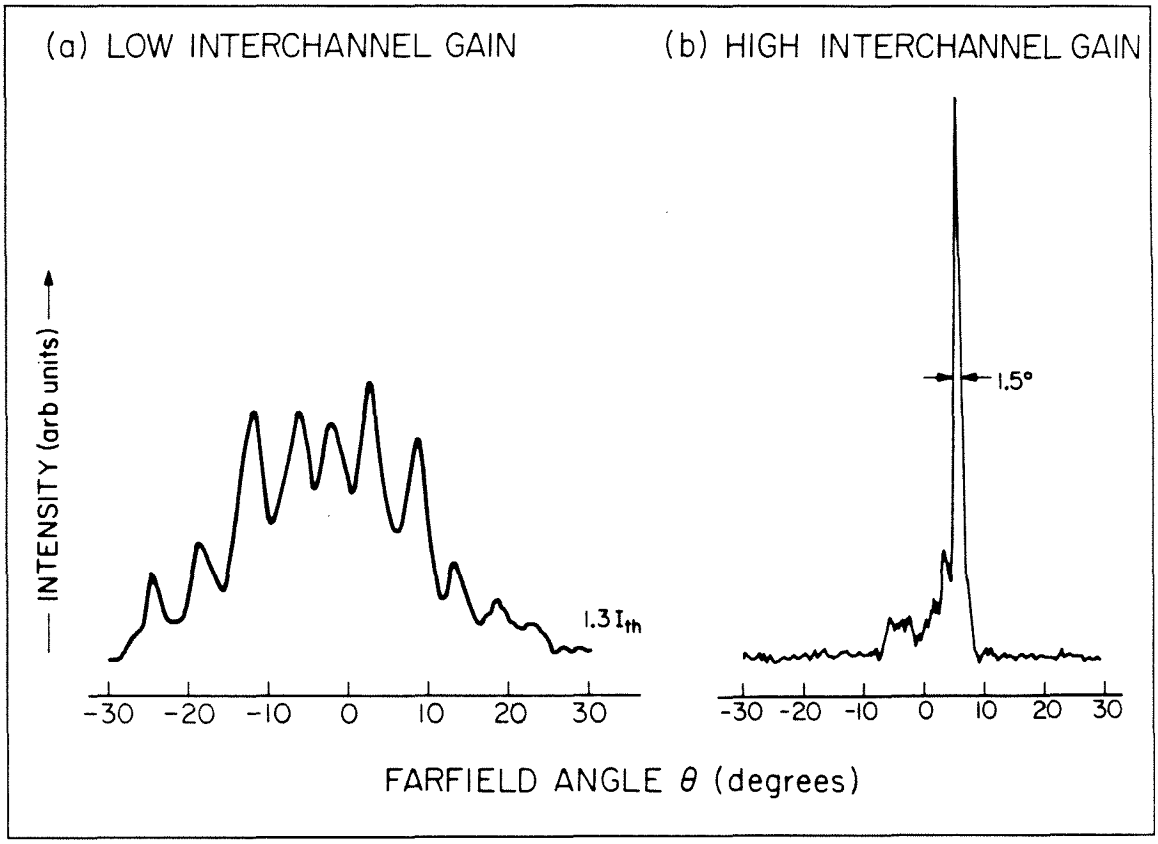

FIGURE 4.13 Experimental farfield patterns for (a) weakly and (b) strongly coupled proton implanted chirped arrays. Note the importance of a high interchannel gain.

The farfield patterns just above threshold for an array with small interchannel gain (Figure 4.12a, pattern A, deep implant of $160KeV$, 0.5μm spreading thickness), and an array with very much larger interchannel gain (Figure 4.12b, pattern B, shallow implant of $80KeV$, 1.1μm spreading thickness) are shown in Figure 4.13a and 4.13b, respectively. Notice that, as expected from the model of Figure 4.10, the farfield pattern of the deeply implanted array is multilobed. However, Figure 4.13b shows that the farfield pattern of the shallowly implanted, strongly coupled array is a very narrow, single lobed beam.

Figure 4.14 shows the experimental farfield patterns at various current levels for two shallowly proton implanted chirped arrays from the same wafer. Figure 4.14a demonstrates a single lobed, very narrow diffraction limited beam at approximately $1.3I_{th}$, while Figure 4.14b demonstrates high power ($450mW$ into $3\frac{1}{2}^\circ$ at $5.3I_{th}$) operation. Both beams are emitted at an angle of about 4° with respect to the facet normal in the direction of the smaller stripes. At high power, the single lobed beams broaden slightly, and some power starts to appear in a sidelobe at -4°. These effects will be discussed in Chapter 5.

We have therefore finally achieved our goal of creating a high power phased array with a single lobed farfield pattern.

§4.5 Tailored Gain Chirped Arrays

After achieving single lobed operation of a strongly coupled proton implanted chirped array, we carefully rechecked the theoretical results of §4.4(a) by using the CONTOUR program of §2.7 and discovered that *we had missed the* $\nu = 5$ *mode which had the highest modal gain and a twin lobed farfield pattern*! We were now in the curious position of having developed a theory which predicted that our array should *not* work — only to find that *did*!

We noted in §4.4(a) that the $\nu = 5$ mode has the highest modal gain and the twin lobed farfield pattern because it is "resonant" with the array perturbation, and therefore excites the $\nu = 5$ "box" mode. This higher order mode will always be

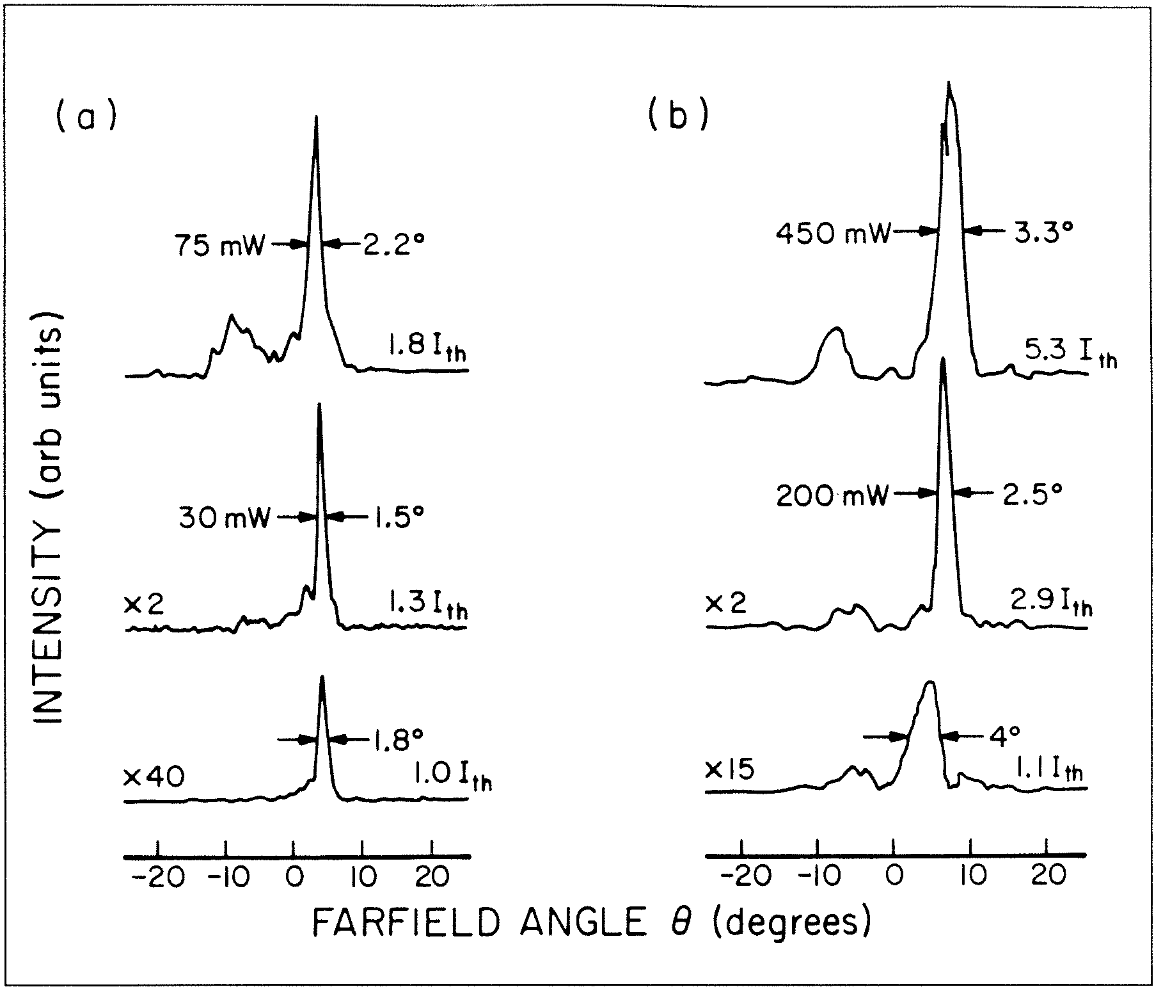

FIGURE 4.14 (a) Diffraction limited operation at $1.3 I_{th}$ and (b) high power operation at $5.3 I_{th}$ of a proton implanted chirped array with a high interchannel gain.

favored as long as there is less gain in the interchannel regions than there is in the channel regions. The only parameter left in our model which might be changed is the spatial gain envelope function. Up until now, we have assumed that the peak gain in each laser was identical; the "gain tailoring" effect described in §4.4(a) resulted from our use of the effective index method to analyze a two-dimensional waveguide in terms of a simpler one-dimensional slab waveguide.

We are greatly indebted to Dr. Shlomo Margalit for pointing out that it was quite possible that the spatial gain profile across the array was not uniform as we had first assumed. In the proton implanted chirped array of Figure 4.12, each of the laser channels share common contacts and are thus electrically connected in parallel. The voltage drop across all the lasers is the same and hence, to a first approximation, the current density flowing through each laser is also. It is known that narrower proton implanted lasers have larger threshold current *densities* than wider lasers. This effect has been described in terms of a "leakage current"[8] and implies that, when the array is operated below threshold and for a given current flowing through the entire device, the wider lasers will be closer to threshold than the narrower ones. In other words, the gain will be greater under the wider stripes than it is under the narrower ones.

(a) Tailored Gain Chirped Arrays: Experimental

The gain tailoring effect in a proton implanted chirped array is confirmed by an examination of the nearfield spontaneous emission pattern just below threshold which makes visible the spatial gain profile across the array. Figure 4.15a shows the spatial gain profile in the deeply implanted array of Figure 4.12a, while Figure 4.15b does the same for the shallowly implanted array of Figure 4.12b. The considerably greater light intensity under the wider stripes indicates that the gain is greater there than it is under the narrower stripes, thus making visible the *nonuniform gain profile* across the array.

The weak interchannel coupling due to the deep implant in Figure 4.15a is evidenced by the large modulation of the spontaneous emission pattern which results from the well isolated lasers, while the very strong interchannel gain of the shallowly implanted laser in Figure 4.15b shows very little, if any, modulation in the spontaneous emission pattern.

§4.5(a) Tailored Gain Chirped Arrays: Experimental

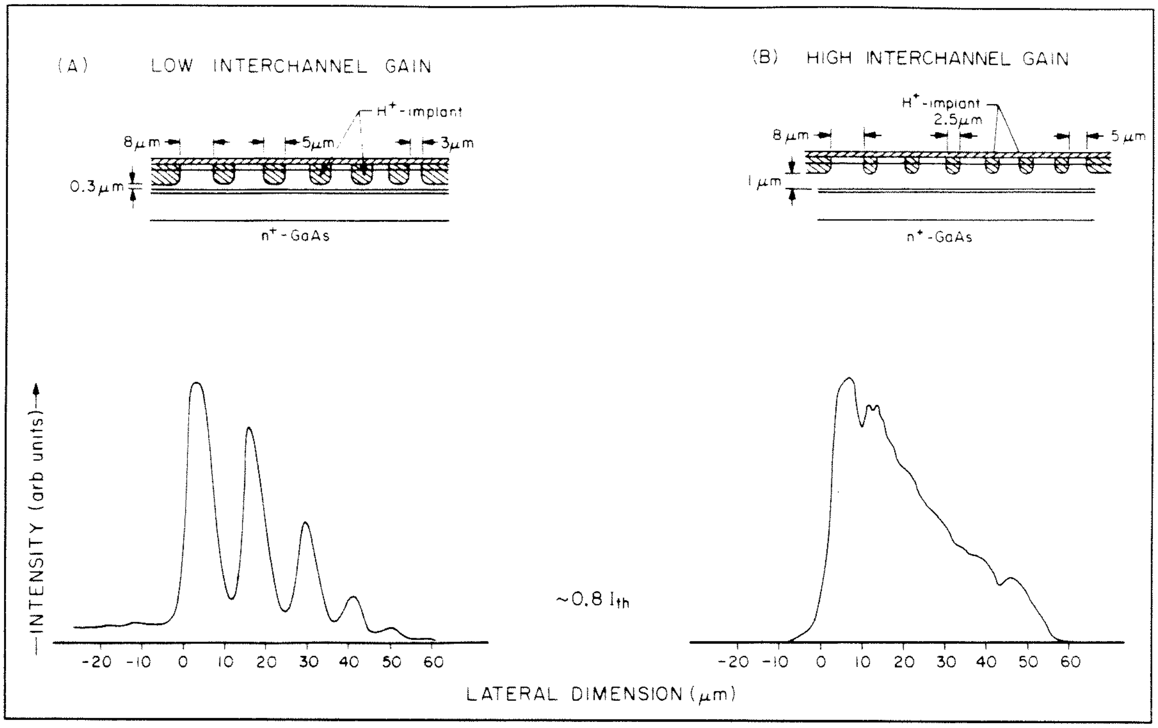

FIGURE 4.15 Spontaneous emission pattern showing gain tailoring in (a) weakly coupled (b) strongly coupled proton implanted chirped arrays.

We have therefore discovered a very effective means of intentionally controlling the spatial gain profile within a proton implanted laser array; such lasers will be referred to as *tailored gain* semiconductor lasers. Evidently, the effect of gain tailoring in the strongly coupled chirped array is sufficient to overcome the propensity to excite the twin lobed box modes, thus yielding the desired single lobed farfield pattern of Figure 4.13b. This is a result of great importance, and understanding the mechanism behind the suppression of the twin lobed farfield patterns will form the bulk of the remainder of this thesis.

(b) Tailored Gain Chirped Arrays: Theoretical

We now need to incorporate gain tailoring into our waveguide model. The most important new parameter to be determined is the spatial gain gradient. This parameter may be estimated by noting that the experimental results indicate that light is emitted over the entire width of the array, which implies that the low gain edge of the array is pumped at least to transparency. The value of the gain at the high gain edge of the array is then fixed by the requirement that the modal gain of the lasing mode be equal to the mirror losses.(§1.5) The only other parameter needed is the value of the gain in the interchannel region. This is not an easy parameter to estimate either experimentally or theoretically; however, we will see that of the three it is the least important because we will want it to be as large as possible.

We have discussed at length several advantages of a high interchannel gain, among them a decrease in the phase mismatch parameter(§4.4(*a*)) and an improvement in the phase locking characteristics of the array.[5] We now add one more.[7] Since the farfield pattern of the array is given by the Fourier transform of the device's nearfield pattern, and the power radiated into the central lobe is proportional to the Fourier coefficient with zero spatial frequency (*i.e.*, the DC term), it is clearly desirable to make the nearfield pattern of the array as uniform as possible. This may also be achieved by strongly coupling the array elements. This second point is illustrated in the theoretical waveguide models of Figure 4.16, which are used to predict the theoretical intensity nearfield and farfield patterns of the lasing supermode in a tailored gain chirped array 60μm wide. Figure 4.16a models an array with small interchannel gain, and Figure 4.16b an array with large interchannel gain. The laser channel widths varied from 8μm to 5μm in steps of 0.5μm.

§4.5(b) Tailored Gain Chirped Arrays: Theoretical

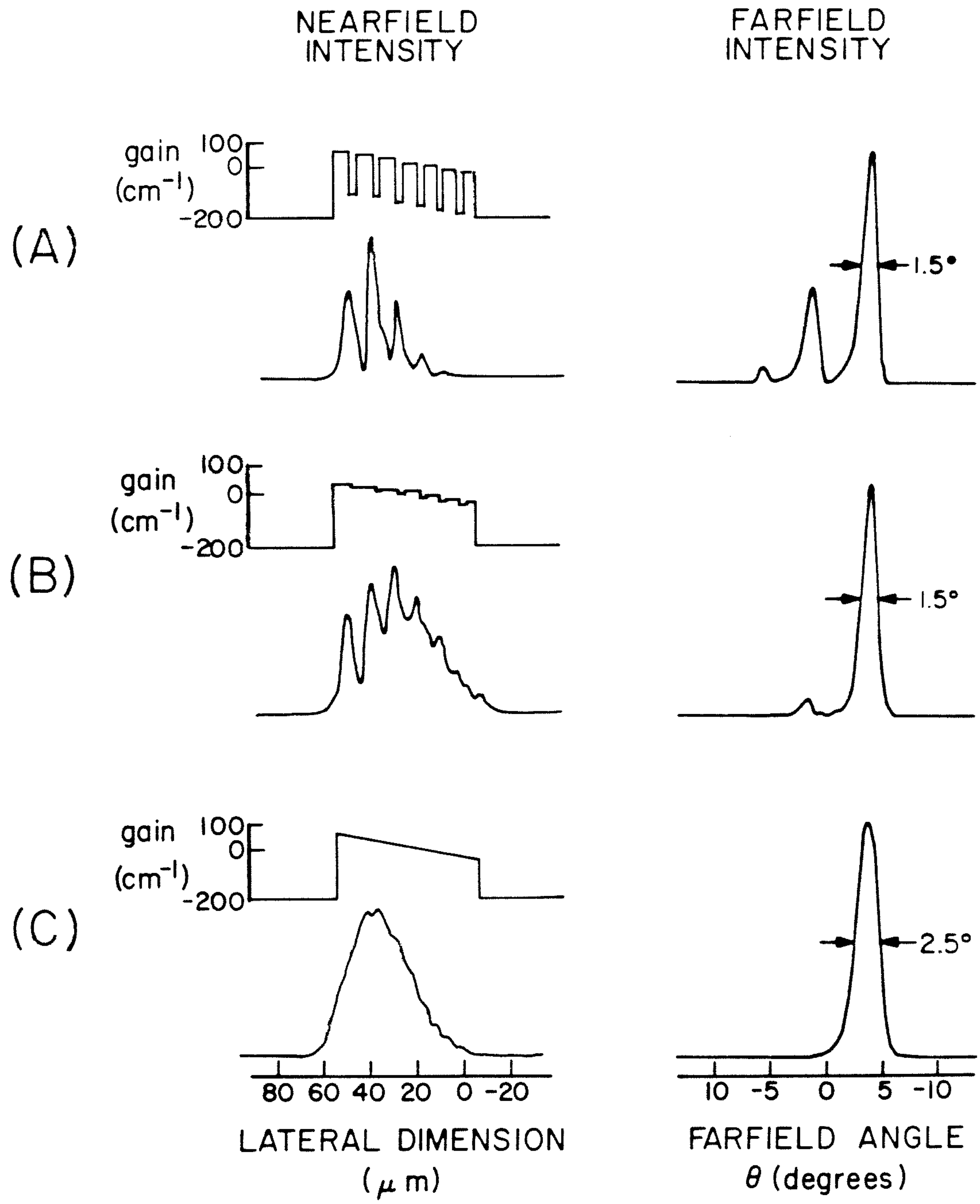

FIGURE 4.16 Theoretical nearfield and farfield patterns for the predominant lasing mode in a (a) weakly and (b) strongly coupled tailored gain chirped array with the antiguiding parameter $b = 3$. (c) shows the same mode for a truly tailored gain broad area laser in which there is no trace of the array structure. Note that increasing the interchannel gain decreases the amount of power radiated into the sidelobes, with the natural limit of this process being the tailored gain broad area laser shown in (c).

The interchannel thickness was 2.5μm. These dimensions correspond to the device shown schematically in Figure 4.12b.

Up to this point, we have considered gain guided lasers in which there is no variation in the real part of the spatial index of refraction. In actual devices, however, there is an approximately linear relationship between the value of the gain at any point in the laser and a *depression* in the real part of the index of refraction profile; this effect is known as the antiguiding effect.(§1.5) It is usually assumed that this ratio, referred to as the antiguiding factor b, is a constant which is approximately equal to three. (An experimental determination of this ratio will be made in §5.13, where we find $b = 2.5 \pm 0.5$.) Including the antiguiding factor does not appreciably change the results of this chapter. However, since we are now attempting to make a simple model for a working device, we will henceforth incorporate this parameter into our waveguide models.

Figure 4.16 demonstrates how increasing the interchannel gain decreases the spatial modulation of the nearfield pattern, with the result that the farfield pattern becomes increasingly single lobed. Figure 4.16a shows that a tailored gain chirped array with small interchannel gain (well defined individual laser channels) will not have a single lobed farfield pattern. On the other hand, Figure 4.16b illustrates that a device with large interchannel coupling *will* have a single lobed farfield pattern 1.5° wide. The experimental single lobed diffraction pattern for the shallowly implanted chirped array of Figure 4.13b is thus diffraction limited.

Figure 4.16c shows the limiting case of a tailored gain chirped array in which the interchannel gain has been made so strong that all traces of the array — and the sidelobe — have disappeared. Obviously, since the gain tailoring effect in a proton implanted laser depends upon chirping the widths of the array elements, Figure 4.16c is an idealization which cannot be achieved by the methods of this chapter. We will fabricate and analyze such a true *tailored gain broad area laser* in Chapter 5.

The theoretical nearfield and farfield patterns for the shallowly implanted chirped array of Figure 4.16b are shown in Figure 4.17. Unlike all the other waveguides we have previously encountered, the farfield patterns of all the modes of this waveguide are single lobed. It therefore no longer matters whether or not the "fundamental" mode has the highest modal gain. This point will be further discussed in Chapter 5.

Notice also that the fundamental $\nu = 1$ mode has a nearfield pattern which is strongly localized towards the high gain side of the array and a very wide farfield pattern much closer to 0° than that of the other modes. Despite the fact that this mode has the highest modal gain, experimental farfield patterns corresponding to this mode have not been observed. We suggest three reasons for this. First, the narrow mode width causes this mode to saturate rapidly, thereby reducing its *saturated* modal gain relative to that of the other modes. Second, the $\nu = 1$ mode does not utilize the gain medium as effectively as the broader high gain $\nu = 3$ mode does and as a result it will contribute less power to the output beam. Finally, there can be no step discontinuity in the spatial gain profile in an actual device. The model of Figure 4.17a therefore is not a good one for that mode. We therefore refer to the $\nu = 3$ mode as the "principal" lasing mode and will henceforth ignore the $\nu = 1$ mode.

Notice that unlike the uniform gain box waveguide of Figure 4.7c in which the mode discrimination between the the fundamental and the higher order modes is less than 1cm^{-1}, in the shallowly implanted tailored gain chirped array the mode discrimination between the principal $\nu = 3$ and $\nu = 4$ modes is 9cm^{-1}.

§4.5(b) Tailored Gain Chirped Arrays: Theoretical

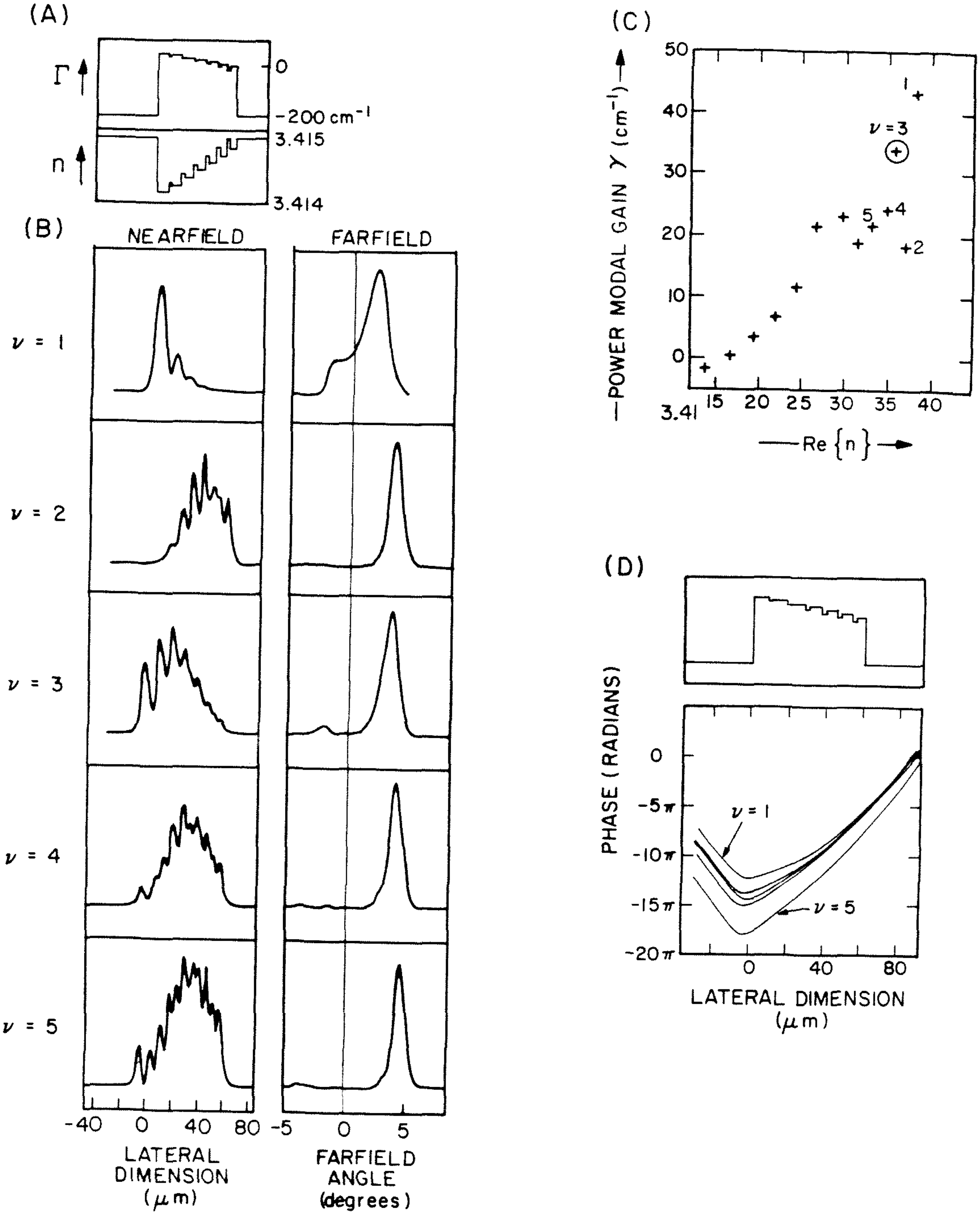

FIGURE 4.17 Theoretical supermodes of the strongly coupled tailored gain chirped array of Figure 4.16b (a) waveguide model with the antiguiding factor $b = 3$, (b) nearfield and farfield patterns, (c) modal plot, and (d) phase variations for the nearfield patterns. Note that all modes have single lobed farfield patterns.

Near threshold (where the effects of gain saturation are less important) a strongly coupled tailored gain array will lase in predominantly one supermode.

Figure 4.17d shows that the phase fronts of both modes are nearly linear and *tilted* with respect to the waveguide axis. This leads to the off-axis beam emission angle.(§5.11) Furthermore, the phase front curvature of the fundamental mode of the tailored gain chirped array of Figure 4.17a is much less than that of the uniform array of Figure 4.6, thus implying a possibly less astigmatic output beam. This comes about because less power flows from the high gain channel regions into the low gain interchannel regions of a strongly coupled array than in a weakly coupled device with a lossy interchannel region.

Finally, Figure 4.17b shows that the farfield patterns of the modes of the strongly coupled tailored gain chirped array have single lobed farfield patterns only slightly displaced from that of the fundamental. This is a direct result of the complex nature of the electric field and the lack of left-right symmetry in the asymmetric structure of Figure 4.17a and will be extensively discussed in Chapter 5. From a practical point of view, however, this is an important result because when the array is operated well above threshold, gain saturation will cause higher order modes to lase. In any symmetric waveguide, or any real index waveguide, these modes emit power on both sides of $\theta = 0$,(§5.12) thus leading to rapid degradation of the farfield pattern. In a strongly coupled tailored gain chirped array, however, the farfield pattern of the higher order modes are all single lobed and only slightly displaced from the fundamental, so that when these modes lase the effect will be to merely broaden the beam slightly and cause a small shift in the emission angle. These predictions are confirmed by the experimental results of Figure 4.14.

§4.6 Tailored Gain Phased Array or Broad Area Laser?

Throughout this work, we have emphasized the importance of a high interchannel gain in a phased array laser. In summary, the high interchannel gain

(1) enhances the ability of the array to operate in a phase locked mode;[9]

(2) reduces the phase and gain mismatch between nonidentical waveguides, thus causing the optical field to spread out over a larger volume, thereby potentially increasing the power output and decreasing the beamwidth;(§4.4(*a*))

(3) decreases the tendency of the array to operate in a high order mode with a twin lobed farfield pattern;(§4.4(*a*))

(4) decreases the amount of power radiated into the sidelobes in a tailored gain array.(§4.5(*b*)) In fact, as the experimental multilobed farfield pattern of the deeply implanted array with small interchannel gain of Figure 4.13 shows, a high interchannel gain is *crucial* to achieving single lobed operation in a tailored gain chirped array.

(5) reduces the phase front curvature, thus potentially reducing the astigmatism of the output beam.(§4.5(*b*))

(6) may increase the reliability of the array. If any laser element in a weakly coupled array fails, the two halves of the array are effectively decoupled, and will be unlikely to operate in a phase locked mode. This problem is reduced in a strongly coupled array because there will be coupling between second nearest neighbors as well.

It is interesting to note that although the schematic diagrams of Figure 4.15b superficially resemble those of an array, examination of the gain profiles via the spontaneous emission patterns below threshold reveal that the effect of the array has been nearly, if not completely, obliterated by current spreading in the upper cladding layer. Therefore, it is actually better to refer to such a device as a tailored gain *broad area* laser than as an array. We will extensively explore this topic in the next chapter.

Finally, the work of Welch, Scifres, *et al.*[10,11] should be mentioned. We utilized the proton implanted chirped array structure to provide gain tailoring, and achieved large interchannel gains by the simple expedient of a shallow proton implantation so that current spreading in the upper cladding layer created gain in the active layer between the array elements. Welch and Scifres have also used proton implanted chirped arrays to provide gain tailoring, but they achieved the necessary high interchannel gain by means of an offset stripe structure that effectively creates gain in the interchannel region. A schematic view of their device is shown in Figure 4.18a&b, which is reproduced from their work.

As shown in Figure 4.18c, they demonstrated that best results were obtained when the length of the center section of the laser was equal to the length of the two offset end sections.[10] Thus, there is effectively no distinction between the channel and interchannel regions because the total integrated gain along the length of the laser is (approximately) the same in the center channel regions as it is in the interchannel regions. This indicates that their device also resembles a *tailored gain broad area laser* more than it does an array of individual lasers, providing independent confirmation of our own work. Figure 4.18c demonstrates that the published description of their device as an "array" is actually a misnomer. Like our own version, it is more properly referred to as a tailored gain *broad area* laser and not as an array. We remark in passing that we can see no advantage to the offset stripe version of the proton implanted chirped array over our own shallowly implanted version, and especially so since the presence of lossy unpumped regions

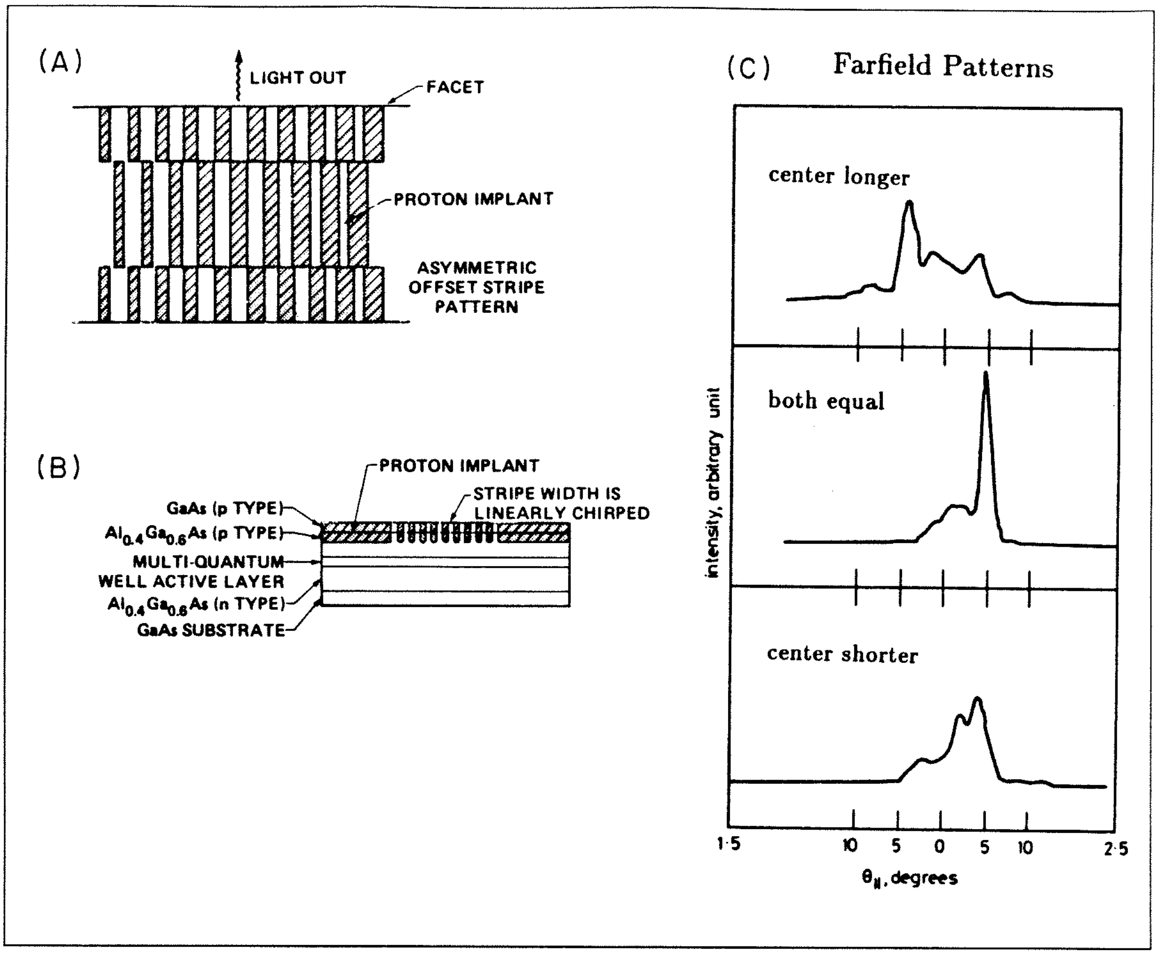

FIGURE 4.18 "Offset Stripe" geometry tailored gain chirped array. (a) top view showing offset stripe pattern of proton implantation (b) side view showing chirped structure (c) experimental farfield patterns. When the length of the center section equals the length of the two end sections, there is effectively no distinction between the channel and interchannel regions, making the device resemble a broad area laser more than an array.

can only increase the device threshold relative to that of our own version of the device.

§4.7 Summary of Chapter 4

To summarize: one way to achieve single lobed operation in a semiconductor laser array is to meet three criteria: (1) the fundamental supermode must be spatially segregated from the other supermodes (*e.g.*, by chirping the widths of the lasers); (2) the gain profile must be tailored so as to favor the fundamental supermode (*e.g.*, in a proton implanted chirped array); and (3) the interchannel coupling must be sufficiently increased so as to bring about single lobed operation (*e.g.*, by shallow proton implantation in a tailored gain chirped array — really a tailored gain broad area laser).

CHAPTER
FIVE
Tailored Gain Broad Area Lasers

God created man simple;
man's *complex* problems are of his own devising.

—Ecclestiastes 7:30

§5.1 Introduction

As we have shown in Chapters 1 to 4, conventional broad area semiconductor lasers with *uniform* spatial gain profiles and widths greater than ~ 10μm have very wide, poorly characterized, and unstable farfield patterns many times the diffraction limit. These undesirable farfield patterns result from the poor mode discrimination between the fundamental and higher order lateral modes, and the presence of uncontrolled filamentation.$^{(\S 1.2(a))}$

One method for achieving high power semiconductor laser operation is to place many individual lasers in close proximity to form a phase locked laser array.$^{(\S 1.2(c))}$ Although the filamentation problem has been suppressed in an array, the lateral mode problem remains. The well-known undesirable twin lobed farfield pattern of a uniformly spaced array of identical lasers (Figure 1.6) comes about because the lossy interchannel regions in the uniform array cause the highest order supermode to have the highest modal gain, and this mode has a twin lobed farfield pattern.$^{(\S 4.1)}$ In principle, fundamental mode operation in an array could be achieved by chirping the widths of the array elements so that the fundamental mode is localized in a different spatial region than the higher order modes.$^{(\S 4.2)}$ If the gain profile within the laser is then tailored to match the intensity pattern of the desired fundamental mode, the fundamental mode will be the preferred lasing mode at threshold, and the desired single lobed farfield pattern will be obtained.

In an index guided laser, the electric field is determined by the spatial dependence of the variation in the real part of the refractive index, and the modal gains are then determined by the overlap between the electric field and the spatial gain distribution. In Chapter 4, we explored the idea of a real index guided chirped array which achieves fundamental mode operation by spatially segregating the fundamental from the higher order modes.(§4.2) Unfortunately, the fundamental and technological limitations of the real index guided chirped array structure make this structure very difficult, if not impossible, to fabricate.(§4.2(*a*)) However, by taking advantage of the fact that in a *gain guided laser* the spatial gain profile determines both the electric field as well the modal gain, we demonstrated a single contact tailored gain array of semiconductor lasers in which gain tailoring was achieved by chirping the widths of the proton implanted laser elements comprising the array.(§4.4(*b*)) Subsequently, we showed that the desired single lobed farfield patterns could best be obtained in devices in which the interchannel gain had been made so strong that the distinction between an array and a broad area laser became blurred.(§4.6) The proton implanted chirped array structure provided gain tailoring, while the shallow proton implantation provided a large interchannel gain.

Nevertheless, it is possible that some residual effect due to the chirped array structure gave the improved results. In §5.2 we will demonstrate the "halftone process" of achieving gain tailoring which does not use an array geometry. The halftone process works by varying the fractional coverage of injecting (metal to p^+GaAs) contact relative to Schottky blocking (metal to $pGaAlAs$) contact over the surface of the laser. We will obtain single lobed diffraction limited beams from such tailored gain broad area lasers 40μm wide.

We will also show in §5.9 that the highly nonuniform gain profile made possible by either tailored gain proton implanted chirped arrays or in tailored gain broad area lasers plays an important role in the suppression of the lateral mode control problem in these devices. It may also possibly contribute to the suppression of the filamentation problem as well. In this thesis, however, we restrict our attention primarily to the analytic study of the (unsaturated) optical eigenmodes of a linear asymmetric tailored gain waveguide, leaving the complicated subject of the above threshold behavior (*e.g.*, filamentation problem) of these devices for further study.

To analyze asymmetric ramp waveguides, we make use of the method of Path Analysis introduced in §2.6(c), first considering the somewhat simpler case of a real index guided waveguide with a linear variation of the refractive index in §5.3. However, it is for the complex asymmetric tailored gain waveguides that the technique of Path Analysis proves its elegance and power. We will find that by following the path of the argument of the optical eigenfunction (in this case the Airy function) throughout the complex plane,(§5.8) we will be able to determine all the important properties of asymmetric tailored gain laser waveguides. In particular, we are able to give simple closed form expressions for the eigenvalues, mode discriminations (§5.9), nearfield patterns (§5.10), and farfield patterns (§5.11) using fairly simple algebraic and geometric arguments.

We find that the linear asymmetric tailored gain waveguide has several unusual properties that make it very different from either real index guided or symmetric waveguides, thus making them especially interesting from both a theoretical and a practical point of view. Unlike all real index guided lasers or symmetric gain guided lasers in which higher order modes have nulls in their nearfield patterns and multilobed farfield patterns, the higher order modes of linear asymmetric tailored gain lasers do not have nulls in their intensity nearfield patterns(§5.10), and as a result also have farfield patterns that are all single lobed and only slightly displaced from the fundamental (§5.11). Thus, when gain saturation at high power operation causes several lateral modes to lase, the farfield pattern remains single lobed, albeit with a slightly larger beamwidth. These unusual properties come about as a result of the Stokes phenomenon,[1] which plays a prominent role in the theory of the asymptotic approximations of complex valued functions. In §5.12 we discuss some general Fourier Transform relationships which relate a device's geometry to its farfield pattern.

The beam emission angle at threshold is sensitive to the exact value of the antiguiding parameter,[2] and in §5.13 we are able to make use of asymmetric halftone tailored gain lasers with varying spatial gain gradients to make a measurement of this important parameter.

Finally, in §5.14, we briefly discuss the effects of gain saturation on the farfield patterns, and touch upon some design criteria and engineering tradeoffs for practical tailored gain broad area lasers.

§5.2 Tailored Gain Broad Area Lasers: Experimental

In our discussion of proton implanted lasers in §2.2(e) we pointed out that current into the $GaAs$ crystal is either fully injected (into the p^+GaAs cap layer) or completely blocked (by the proton implantation); there is no simple way to achieve intermediate values of injected current. In §4.5(a) we discovered that gain tailoring could be achieved in a proton implanted chirped array by making use of the "leakage current" effect, but that the desired single lobed farfield patterns could be achieved only if the interchannel gain was very large. We did this by means of a shallow proton implantation. Obviously, the leakage current model is inadequate for explaining the gain tailoring effect when the implant depth is very small.

A moment's reflection will reveal that our goal of achieving intermediate values of the gain using contacts that either fully inject or completely block current flow is conceptually identical to the problem that the graphics artist faces when he (or she) desires to print a photograph with many shades of grey in a newspaper using black ink on white paper. We therefore consider solving our problem the same way graphics artists solve theirs: by means of a *halftone* pattern. A halftone pattern such as that of Figure 5.1 achieves the illusion of grey tones by varying the fractional surface coverage of black ink to white paper over the newspaper's surface by using many very closely spaced dots of varying size.

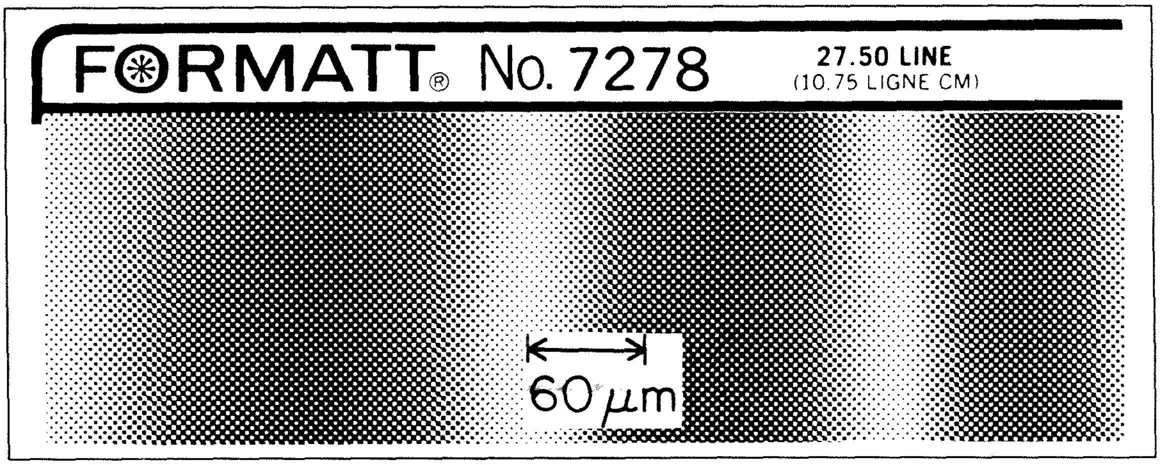

FIGURE 5.1 Graded halftone screen obtained from an artist's supply store. This pattern was used to create the "halftone" laser of Figure 5.2 and Figure 5.3.

The eye's limited spatial resolution causes the discrete nature of the dot to be smeared out so that the illusion of a uniformly varying grey scale is created. A quick glance at any newspaper or magazine photograph fully illustrates the versatility of the halftone process for achieving complicated patterns with varying shades of grey.

We did something very similar to this when we made the shallowly implanted chirped array. Another way of thinking about this structure would be to realize that for a very shallow proton implantation depth it is the *fractional surface coverage* of injecting to noninjecting contact that varies over the surface of the chirped array. For example, in the strongly coupled array of Figure 4.12b the fractional surface coverage of injecting contact varies from $\frac{8}{8+2.5} \approx 80\%$ on the left to $\frac{5}{5+2.5} \approx 70\%$ on the right. This is very similar to the idea of a halftone pattern, but unfortunately the thick photoresist required to block the protons limits the usefulness of this method to very simple patterns such as those of Figure 4.12.

Much smaller feature sizes, on the order of $1\mu\text{m} - 2\mu\text{m}$, may be obtained by utilizing a halftone pattern in conjunction with Schottky isolation that has been described in §2.2(e). The practical difficulty with this method lies in obtaining the desired pattern of dots. Linearly graded halftone may be readily obtained at any artist's supply store for only a few dollars. A typical pattern is illustrated in Figure 5.1. The photolithographic mask used to create the microscopic halftone pattern on the surface of the wafer was made by photoreducing the graded halftone screen of Figure 5.1 by 250×.

A plan view of an asymmetric tailored gain broad area laser based on the halftone method for achieving gain tailoring[3] is shown in Figure 5.2a. The standard four layer heterostructure was grown by molecular beam epitaxy (MBE). The thickness of the upper cladding layer has been increased to enhance lateral carrier diffusion in the region between the p^+GaAs cap layer and the active layer. The layers were grown on an n^+GaAs substrate (Si doped, $2\times10^{18}\text{cm}^{-1}$). The composition and thickness of the layers are as follows: $n\ Ga_{0.7}Al_{0.3}As$ lower cladding layer

§5.2 Tailored Gain Broad Area Lasers: Experimental

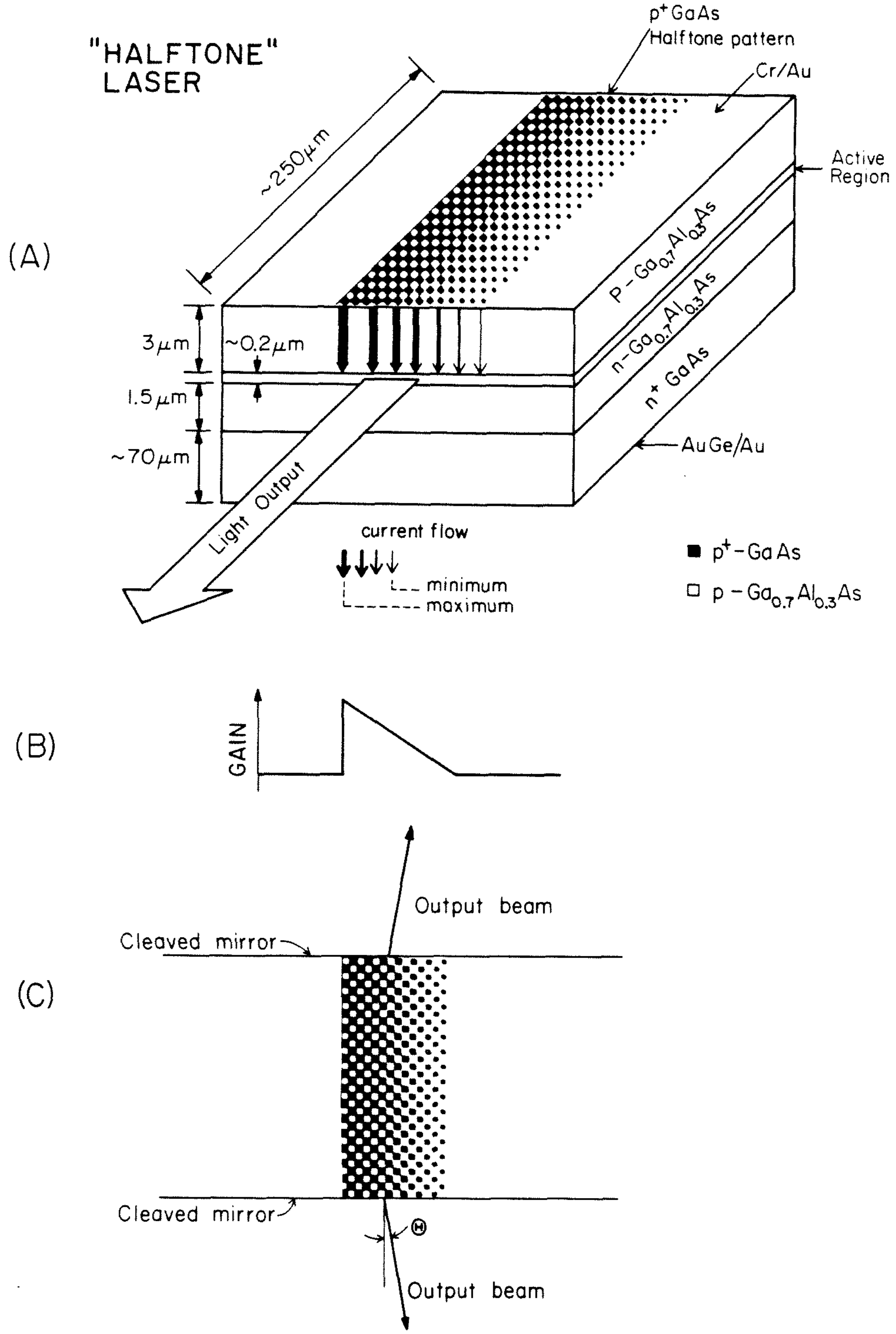

FIGURE 5.2 (a) Plan view of a "halftone" asymmetric linear tailored gain broad area laser, (b) waveguide model showing nonuniform spatial gain profile, and (c) top view of a halftone laser showing direction of output beam. The black dots on the surface of the laser represent injecting p^+GaAs while the white areas represent noninjecting $GaAlAs$. The varying fractional surface coverage of injecting to noninjecting contact creates a controlled nonuniform spatial gain profile within the device.

1.5μm thick, Si doped, 3×10^{17}cm^{-1}; active region composed of a four layer multiple quantum well (MQW) of 200 Angstroms of GaAs separated by 200 Angstroms of $Ga_{0.7}Al_{0.3}As$; p $Ga_{0.7}Al_{0.3}As$ upper cladding layer 3.0μm thick, Be doped, 3×10^{17}cm^{-1}; p^+GaAs cap layer, 0.2μm thick, Be doped, 1×10^{18}cm^{-1}.

The 0.2μm p^+GaAs cap layer was etched away using H_2SO_4:H_2O_2:H_2O :: 1:8:40 according to the pattern of Figure 5.1. As described in §2.2(e), the metal to p^+GaAs interface forms an injecting ohmic contact, while the metal to $pGa_{0.7}Al_{0.3}As$ forms a Schottky blocking contact. The black areas of the pattern block the etch, leaving the injecting p^+GaAs cap layer, while the white areas on the mask allow the etch to remove the cap layer, leaving the $pGa_{0.7}Al_{0.3}As$ blocking contact. The current injection density (and hence gain) thus decreases from left to right with the decrease of fractional coverage by p^+GaAs. The enhanced lateral carrier diffusion provided by the thick upper cladding layer smears out the effects of the discrete dots and makes for a smooth, nonuniform spatial gain distribution within the active layer. Since the dot size varies linearly across the laser, to a first approximation the gain profile varies linearly as well. Thus, halftone tailored gain lasers provide a well-characterized means of experimentally studying strongly asymmetric linear tailored gain waveguides.

Although the halftone laser of Figure 5.2a has only a one-dimensional variation in the spatial gain profile, the same idea may be easily extended to create nearly arbitrary *two-dimensional* spatial gain distributions within a broad area laser, offering an entirely new degree of freedom to the designer of semiconductor lasers. In such halftone tailored gain lasers, the nature of the halftone pattern, combined with the enhanced current spreading in the upper cladding layer, removes all traces of the array structure; such devices are truly *broad area* lasers, with the desired spatially nonuniform gain profiles controlled by the $p^{+}GaAs$ dot density on the surface of the laser.

Figure 5.2b shows a schematic waveguide model with a linear spatial gain profile for the halftone tailored gain broad area laser of Figure 5.2a. Figure 5.2c shows a top view of the laser of Figure 5.2a, and schematically illustrates how the output beams are directed at an angle Θ to the mirror facets in the direction of the low gain side of the laser. As will be shown in §5.11, this is a direct result of the asymmetric spatial gain profile.

The pulsed, low duty cycle nearfield and farfield patterns for the linear asymmetric halftone laser are shown in Figure 5.3. This figure demonstrates that linear asymmetric tailored gain halftone *broad area lasers* are capable of nearly diffraction limited high power ($\sim 200mW$ into $2\frac{1}{2}^{\circ}$) single lobed farfield operation. Note also that the farfield patterns are strongly asymmetric (the beam is emitted about 4° off-axis), and that the beamwidth increases gradually at high power. The reasons for this behavior will be discussed below.

The structure in the nearfield pattern at $3.2I_{th}$ in Figure 5.3a may be due to either lateral modes, filamentation, or both. The detailed experimental resolution of this question (by very careful measurements of the spectrally resolved nearfield patterns)(§3.5(c.i),5.9) and the theoretical analysis of filamentation(§1.2(a.i)) in tailored gain broad area lasers are beyond the scope of this thesis.

§5.3 Linear Tailored Real Index Waveguide

We begin our analysis of tailored gain broad area lasers by first considering the much simpler example of a *real index guided* ramp waveguide with a refractive

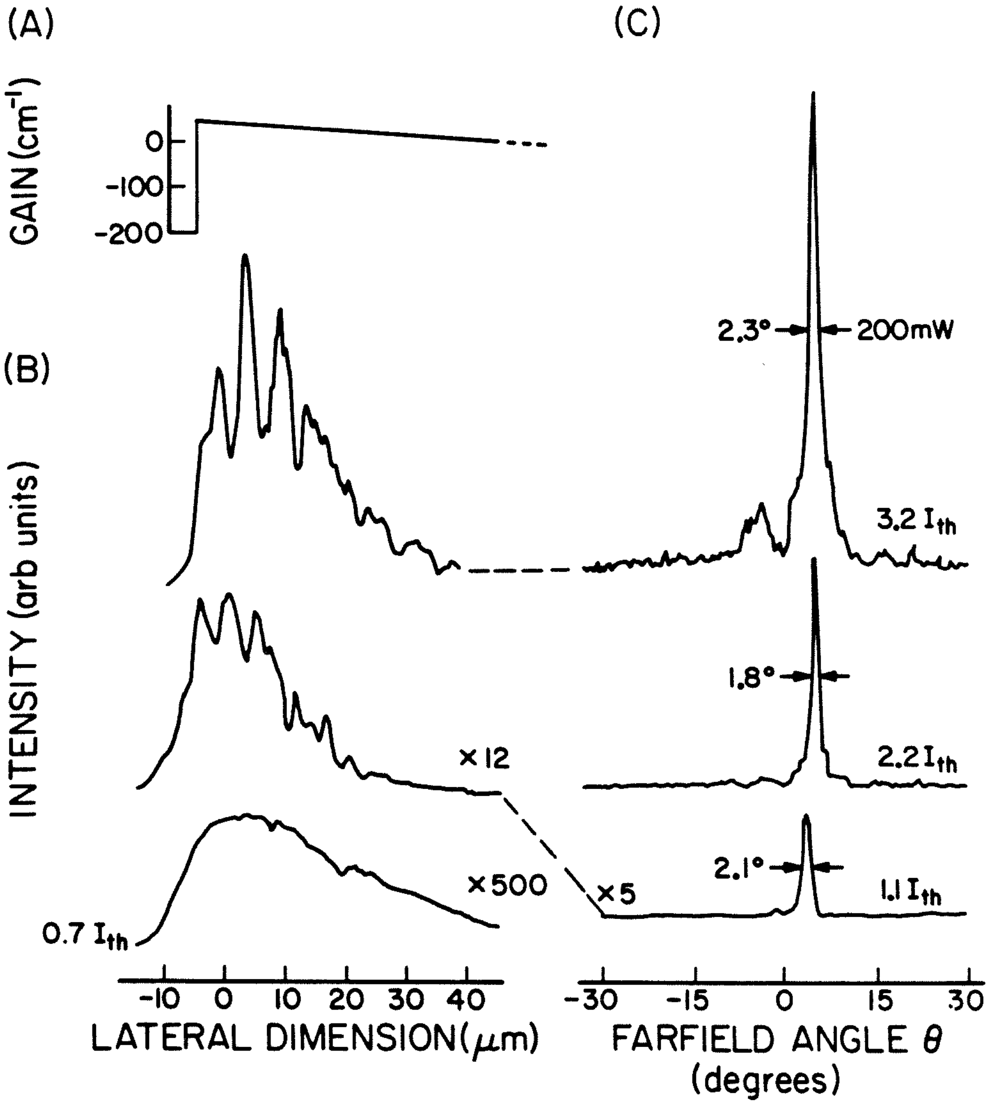

FIGURE 5.3 (a) Nearfield patterns and (b) high power single lobed farfield patterns for the "halftone" laser of Figure 5.2. Note the nearly linear spatial gain profile as evidenced by the spontaneous emission pattern at $0.7 I_{th}$.

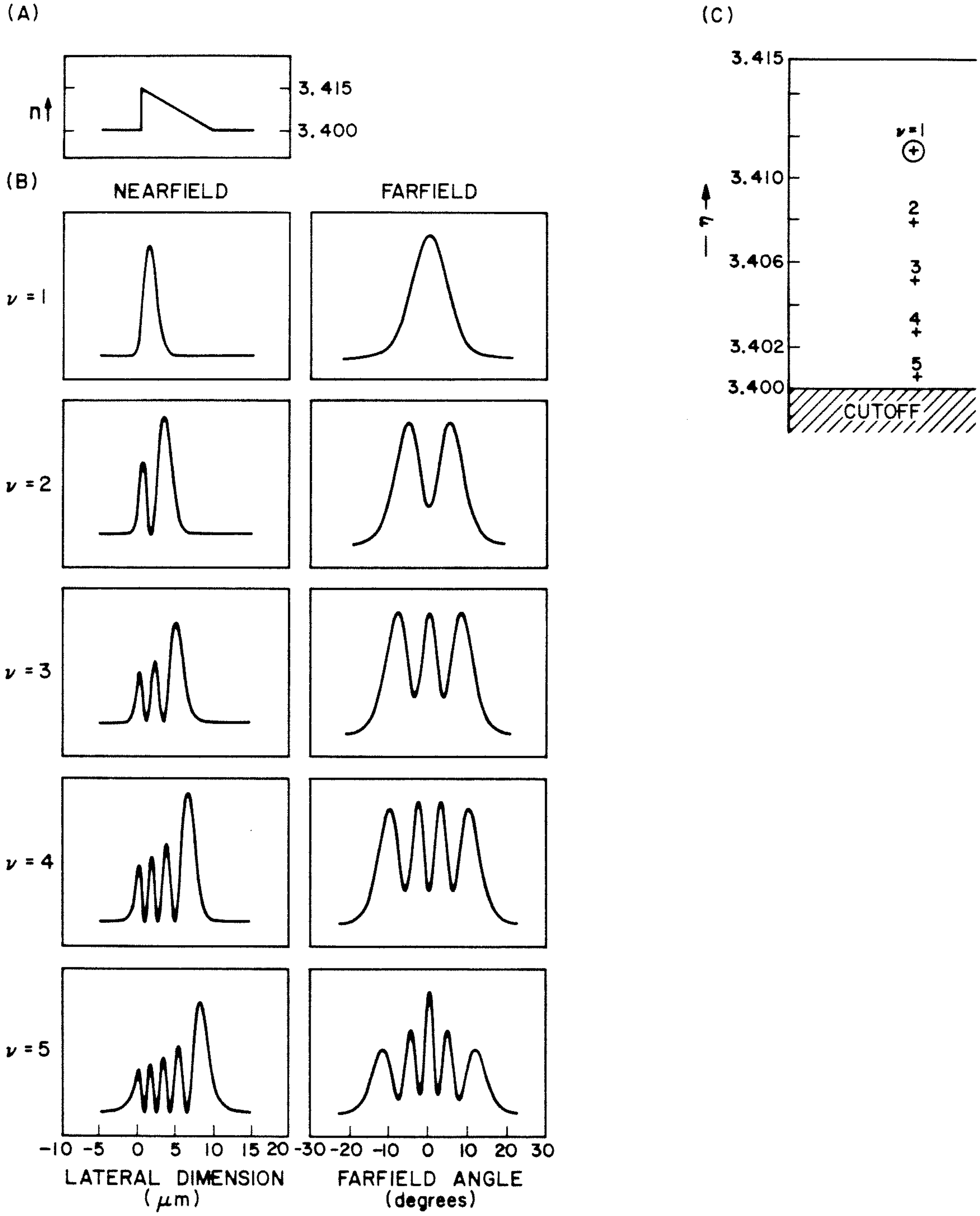

FIGURE 5.4 Modes of the asymmetric tailored real index ramp waveguide (a) refractive index profile (b) intensity nearfield and farfield patterns (c) mode pattern.

index profile described by

$$n(x) = \begin{cases} n_e & -\infty < x \le 0^- \\ n_0 - \sigma k_0 x & 0^+ \le x \le \ell^- \\ n_e & \ell^+ < x < \infty \end{cases} \tag{5.3.1}$$

where n_e is the (constant) index of refraction external to the waveguide, n_0 is the index of refraction at $x = 0^+$, and σ is the gradient of the index of refraction profile within the core region of the waveguide.

After substituting Equation (5.3.1) into Equation (2.5.4) and dropping the term second order in x, the Helmholtz equation inside the guide becomes

$$\frac{d^2}{dx^2}E + k_0^2((n_0^2 - \eta^2) - 2n_0 k_0 \sigma x)E = 0 \tag{5.3.2}$$

which has the solution

$$E(x) = a\,\mathrm{Ai}(\xi) + b\,\mathrm{Bi}(\xi) \qquad \xi = \rho + \omega x \tag{5.3.3}$$

where a and b are real constants, $\mathrm{Ai}(\xi)$ and $\mathrm{Bi}(\xi)$ are the Airy functions, and

$$\begin{aligned} \rho &= \frac{k_0^2}{\omega^2}(\eta^2 - n_0^2) \\ \omega &= k_0(2n_0\sigma)^{\frac{1}{3}} \end{aligned} \quad . \tag{5.3.4}$$

The secular equation yielding the eigenvalue condition may be found by matching the boundary conditions at $x = 0$ and $x = \ell$:$^{(\S5.6)}$

$$\frac{\sqrt{\rho_e}\mathrm{Bi}(\rho) - \mathrm{Bi}'(\rho)}{\sqrt{\rho_e}\mathrm{Ai}(\rho) - \mathrm{Ai}'(\rho)} - \frac{\sqrt{\rho_e}\mathrm{Bi}(\rho + \omega\ell) + \mathrm{Bi}'(\rho + \omega\ell)}{\sqrt{\rho_e}\mathrm{Ai}(\rho + \omega\ell) + \mathrm{Ai}'(\rho + \omega\ell)} = 0 \tag{5.3.5}$$

where

$$\rho_e = \frac{k_0^2}{\omega^2}(\eta^2 - n_e^2) \ . \tag{5.3.6}$$

Figure 5.4b presents the intensity nearfield patterns for the first five modes of the tailored real index ramp waveguide shown in Figure 5.4a. Notice that, like the real index and box waveguides of Figure 2.11 and 2.12, the higher order modes of the real asymmetric linear tailored index waveguide all have nulls in their nearfield patterns, but unlike the box waveguides the peak intensity within the waveguide gradually shifts from the high index side of the waveguide to the low index side. This is similar to the real index guided chirped array of Figure 4.2, and may be understood by using the method of Path Analysis$^{(\S 2.6(c))}$ to follow the path of the argument ξ of the Airy function along the real axis.

§5.4 Path Analysis of the Linear Tailored Real Index Waveguide

Before we make use of Path Analysis, it is necessary to determine which one of the functions $\mathrm{Ai}(\xi)$ or $\mathrm{Bi}(\xi)$ dominates the contribution to $E(x)$ in Equation (5.3.3). (If both were equally important, it would not be possible to analyze the waveguide in terms of any simple function, and the analysis would have to be carried out numerically.) Figure 5.5 plots $\mathrm{Ai}(\xi)$ (solid line) and $\mathrm{Bi}(\xi)$ (dashed line), showing that along the negative real ξ axis as $\xi \to -\infty$, both functions are sinusoidal with a gradually decreasing period and amplitude, while along the positive real axis $\mathrm{Ai}(\xi)$ decays exponentially and $\mathrm{Bi}(\xi)$ grows exponentially.

Since $E(x)$ must match to a decaying exponential outside the waveguide, the function $\mathrm{Bi}(\xi)$ will not satisfy the boundary conditions and hence will not contribute appreciably to $E(x)$. (This point will be discussed in detail when we discuss the asymmetric linear tailored gain waveguide in §5.8.) We can therefore approximate the electric field inside the waveguide by

$$\begin{aligned} E(x) &\simeq \mathrm{Ai}(\xi) & \xi &= \rho + \omega x \\ &\sim \begin{cases} \pi^{-1/2}(-\xi)^{-1/4}\sin[\frac{2}{3}(-\xi)^{\frac{3}{2}} + \frac{\pi}{4}] & \xi \leq 0 \\ \frac{1}{2}\pi^{-1/2}\xi^{-1/4}e^{-\frac{2}{3}\xi^{3/2}} & \xi \geq 0 \end{cases} \end{aligned} \tag{5.4.1}$$

where we have used the appropriate asymptotic approximation for the Airy function.[4]

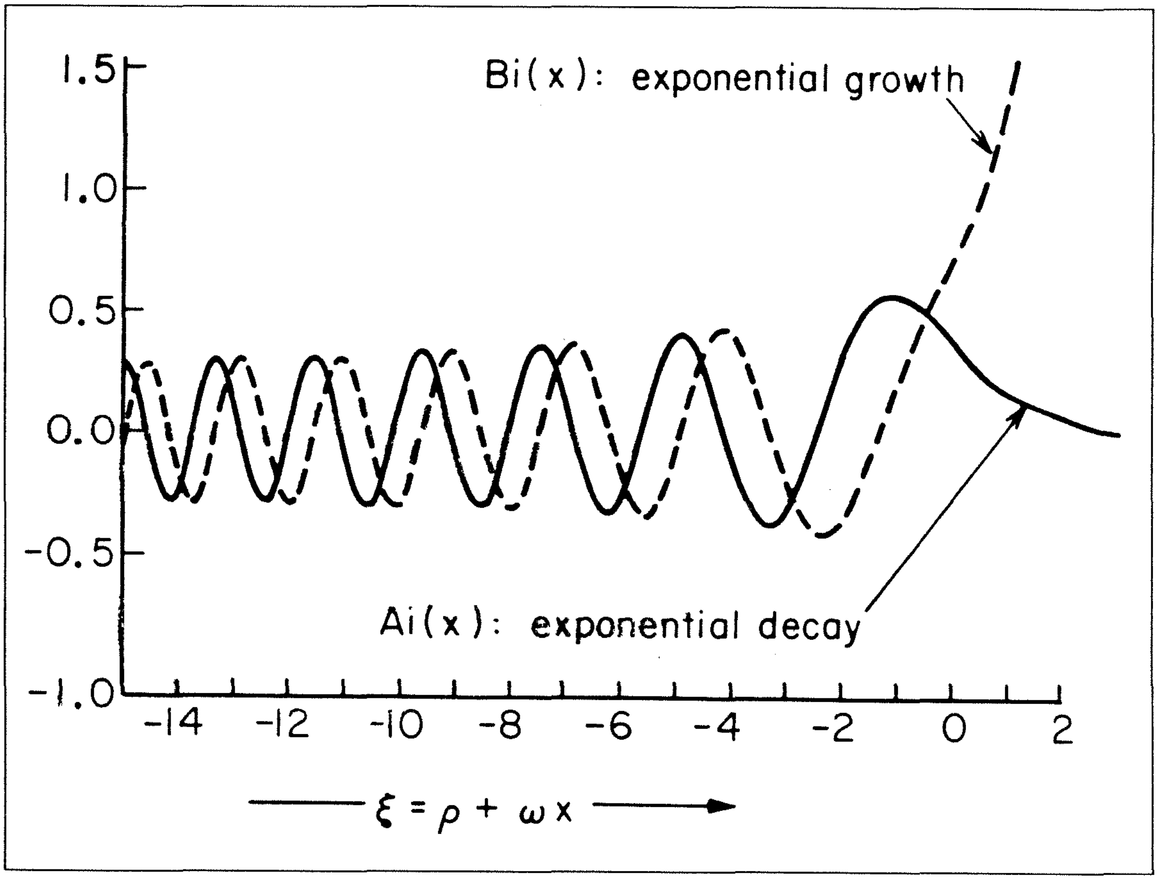

FIGURE 5.5 Plot of Ai(ξ) and Bi(ξ) along the real axis showing that Bi(ξ) does not satisfy the boundary conditions because it grows exponentially as $x \to \infty$.

We saw in §2.6(c) that each of the modes of the box waveguide could be associated with a zero of the sine or cosine function, the parity condition determining which function to associate with each mode. In the case of the linear tailored index waveguide however, the boundary conditions require that *all* of the well-confined modes be determined by the Airy function Ai(ξ). Each mode is then associated with a zero $-r_n$ of Ai(ξ).

In a manner entirely analogous to the case of the box waveguide, for a well-confined mode the path $\mathcal{L}$ of the argument of the Airy function $\xi = \rho + \omega x$ has one endpoint at at the r^{th} zero of the Airy function $\rho = -r_n$ and the other endpoint at $\rho + \omega \ell$. The length of this line is $|\omega \ell|$ with ω given by Equation (5.3.4).

The quantity ω corresponds to the lateral wavevector k of the box waveguide in Equation (2.6.5). Note that while $|k|$ (and hence the length of $\mathcal{L}$ for the box guide) depends on the eigenvalue η, for the case of the linear guide $|\omega|$ is *independent* of η: the eigenvalue dependence of the argument to the Airy function is contained entirely in ρ. Thus, unlike the argument kx for the box waveguide,(§2.6(c)) for the various modes of the real ramp waveguide the line $\mathcal{L}$ translates along the real axis but does not change its length.

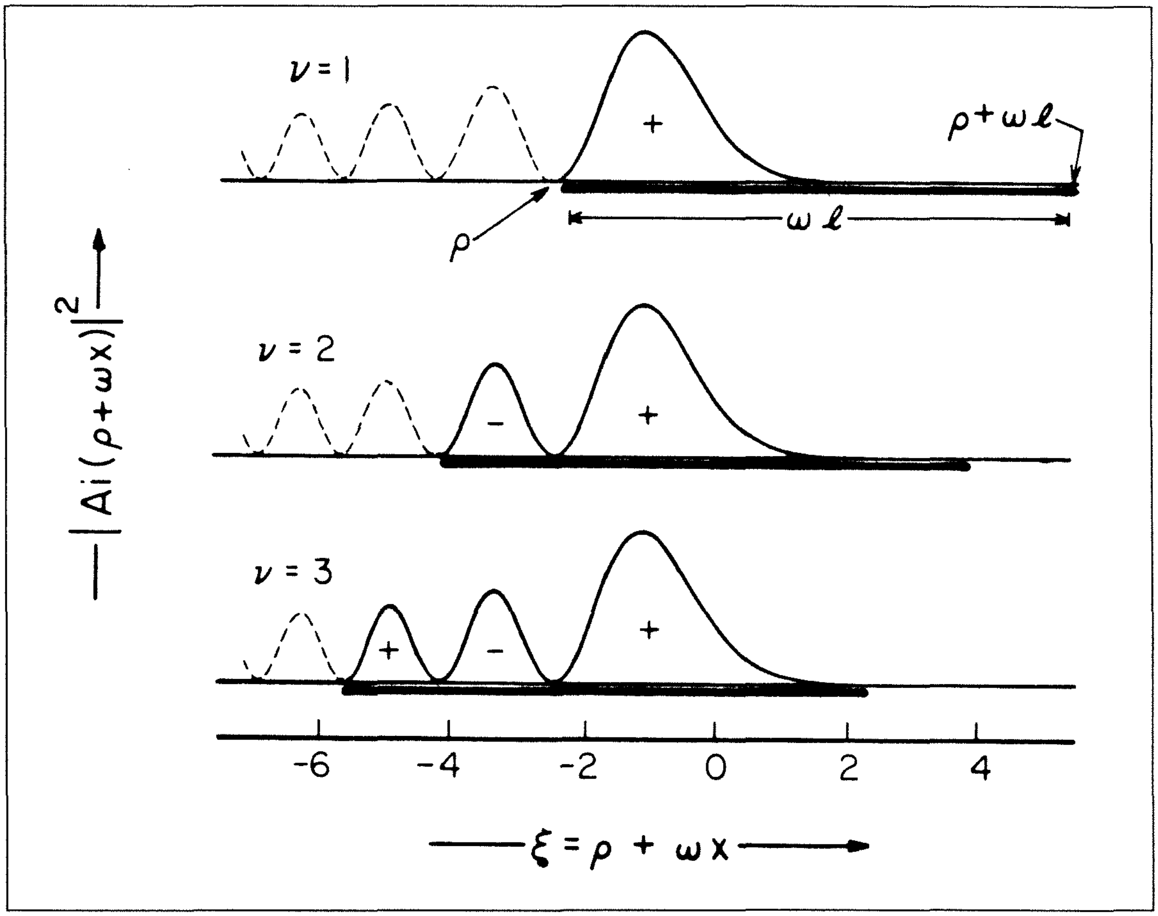

FIGURE 5.6 The path of the argument to the Airy function along the real axis for the first three modes of the tailored real index ramp waveguide is shown by the heavy horizontal line. Compare with the corresponding Figure 2.14 for the real index box waveguide.

Figure 5.6 plots the intensity $|\mathrm{Ai}(\xi)|$ (dashed line), the path $\mathcal{L}$ along the real ξ axis (heavy solid line), and the mode shape (medium solid line) for the first three modes of a real ramp waveguide. It is of particular interest to note that the optical power of the fundamental mode is located to the far left of the guide (at $x = 0$ and $\xi = \rho$) due to the exponential tail of $\mathrm{Ai}(\xi)$ when $\xi = \rho + \omega\ell > 0$, while the peak intensity for the higher order modes gradually moves to the other side of the waveguide due to the $(-\xi)^{1/4}$ amplitude dependence in the sinusoidal approximation of $\mathrm{Ai}(\xi)$ in Equation (5.4.1).

Path Analysis may be used to derive an approximate expression for the cut-off condition for a mode. A guided mode given by $\mathrm{Ai}(\rho + \omega x)$ must match to a decaying exponential at $x = \ell$, and this can occur only if the rightmost endpoint of $\mathcal{L}$ ($\xi = \rho + \omega\ell$) lies to the right of the first zero of the *derivative* of $\mathrm{Ai}(\xi)$ at $\xi \approx -1.02$. The condition for the ν^{th} mode to be guided is thus $|\omega\ell| + 1.02 < -r_\nu$. This condition is approximate because our assumption that one end of $\mathcal{L}$ starts at a zero of the Airy function is only satisfied for a well-confined mode, and this is not true near cut-off.

§5.5 The Linear Tailored Gain Waveguide

If we allow the constants in Equation (5.3.1) to be complex numbers, the solutions of the Helmholtz equation (5.3.2) are once again linear combinations of the Airy functions, but now with a *complex* argument. For convenience, we split n_e and n_0 into their real and imaginary parts:

$$\begin{aligned} n_e &= \bar{n}_e - i\Gamma_e/2k_0 \\ n_0 &= \bar{n}_0 - i\Gamma_0/2k_0 \; . \end{aligned} \tag{5.5.1}$$

The gradient of the complex index of refraction within the guide $0 \le x \le \ell$ is given by σk_0. σ is a dimensionless quantity which plays a key role in determining the properties of the waveguide. It is a real number in a real index guided laser, imaginary in a gain guided laser in which antiguiding has been ignored, and becomes complex when either intentionally introduced real index guiding is present or in a gain guided structure in which the effects of antiguiding are included. It is defined by

$$\sigma = s(b - i) \qquad (s > 0) \tag{5.5.2}$$

where b is the antiguiding factor which relates the depression in the real part of the index of refraction due to the presence of gain through the free carrier and band edge effects. The antiguiding parameter b (sometimes referred to by R) has been assigned values in the literature[5] between 2 and 6. In (§5.13) we experimentally measure $b = 2.5$. The real constant s is related to the guide parameters by

$$s = \frac{\Gamma_0 - \Gamma_\ell}{2k_0^2\ell} . \tag{5.5.3}$$

It should be noted that in this model there will always be a step discontinuity in the index of refraction $n(x)$ at the left edge of the guide $x = 0$, while there will be a corresponding step discontinuity at the right edge of the guide $x = \ell$ only if $n_e \neq n_\ell = n_0 - \sigma k_0 \ell$. The effect of the discontinuity in $n(x)$ at the right edge of the guide depends upon the magnitude of the discontinuity and also upon the particular eigenmode as well as the width ℓ of the guide. Of course, in an actual device there can be no real discontinunity in the spatial gain profile. However, since it is only the value of the *gradient* which is important, to first order at least, the discrepancy between the model waveguide and an actual device may be ignored.

The solution to the Helmholtz equation (5.3.2) is given by a linear combination of the two Airy functions

$$E(x) = a\,\mathrm{Ai}(\rho + \omega x) + b\,\mathrm{Bi}(\rho + \omega x) \tag{5.5.4}$$

where a and b are complex constants, and

$$\begin{aligned} \rho &= \frac{k_0^2}{\omega^2}(\eta^2 - n_0^2) \\ \omega &= k_0(2n_0\sigma)^{\frac{1}{3}} \end{aligned} \tag{5.5.5}$$

Recall that(§5.4) the equation $z = \rho + \omega x$ describes a straight line $\mathcal{L}$ in the complex z–plane with one endpoint at $z = \rho$ and the other endpoint at $z = \rho + \omega\ell$. The length of this line is $|\omega\ell|$, but the line $\mathcal{L}$ now no longer lies on the real axis. The angle ψ that $\mathcal{L}$ makes with the real axis is given by $\psi = \angle\omega \simeq \frac{1}{3}\tan^{-1}\frac{\Im\mathrm{m}\{\sigma\}}{\Re\mathrm{e}\{\sigma\}}$. Notice that the orientation of $\mathcal{L}$ in the complex plane does not depend on either the width of the waveguide or the gain gradient but only on the antiguiding factor. For the case of index guiding with no gain, ψ is zero. For the case of gain guiding, with no index antiguiding ($b = 0$), σ may be written as an imaginary number $\imath\, s$ with s real:

$$\sigma = -\imath\, s \qquad \text{(pure gain guiding, } s \text{ real)} \tag{5.5.6}$$

where s is related to the guide parameters by Equation (5.5.3). We can then write ω as

$$\omega = k_0(2n_0 s)^{\frac{1}{3}}(-\imath)^{\frac{1}{3}} \; . \tag{5.5.7}$$

Each branch of the cube root gives rise to a physically meaningful mode, leading to three distinct families of modes, which will be referred to as the (+) , (0) , and (–) branches. Since $\bar{n}_0 \ll \bar{n}_0$, ψ is determined almost entirely by the cube root of $-\imath$ which takes the values $e^{-\imath\pi/6}$, $e^{-\imath 5\pi/6}$, and $e^{+\imath\pi/2}$. The angle ψ then takes on the values ∓30°, and +90°. The inclusion of index antiguiding ($b \neq 0$) effects a rotation in the complex plane; this will be discussed in §5.13.

§5.6 Dispersion Equation and Eigenvalue Branch Structure

Once again, for a well-confined mode, the path $\mathcal{L}$ will start near a zero of $\mathrm{Ai}(z)$. Since the quantity ωl is now a complex quantity, $\mathcal{L}$ is no longer restricted to the real axis. To determine its origin, the eigenvalue η is required. The normalized eigenmodes will then be completely specified when the ratio of coefficients a/b is known. Both of these quantities are determined by the boundary conditions which require E and dE/dx to be continuous at the edges of the guide and bounded at infinity. If we require the field to decay exponentially as $x \to -\infty$ and match the boundary conditions at the left edge of the guide, we may derive an expression for the ratio a/b inside the guide:

$$\left.\frac{a}{b}\right|_{x=0} = -\frac{\sqrt{\rho_e}\mathrm{Bi}(\rho) - \mathrm{Bi}'(\rho)}{\sqrt{\rho_e}\mathrm{Ai}(\rho) - \mathrm{Ai}'(\rho)} \tag{5.6.1}$$

where the prime $(')$ denotes a derivative with respect to x, and

$$\rho_e = \frac{k_0^2}{\omega^2}(\eta^2 - n_e^2) \ . \tag{5.6.2}$$

Similar consideration at the right side of the guide leads to

$$\left.\frac{a}{b}\right|_{x=\ell} = -\frac{\sqrt{\rho_e}\mathrm{Bi}(\rho+\omega\ell) + \mathrm{Bi}'(\rho+\omega\ell)}{\sqrt{\rho_e}\mathrm{Ai}(\rho+\omega\ell) + \mathrm{Ai}'(\rho+\omega\ell)} \ . \tag{5.6.3}$$

Inside the guide, the ratios $(a/b)|_{x=0}$ and $(a/b)|_{x=\ell}$ both describe the same linear combination of $\mathrm{Ai}(z)$ and $\mathrm{Bi}(z)$. Setting them equal yields the eigenvalue equation for η Equation (5.3.5). This technique for determining the secular equation is reminiscent of the method by which the eigenvalue condition is derived in the WKB method.[6]

Equation (5.3.5) may be solved numerically for the eigenvalues η. The electric fields may then be determined using Equation (5.6.1)and (5.5.4). For comparison with the box waveguides of Figures 2.11 and 2.12 and the real ramp waveguide

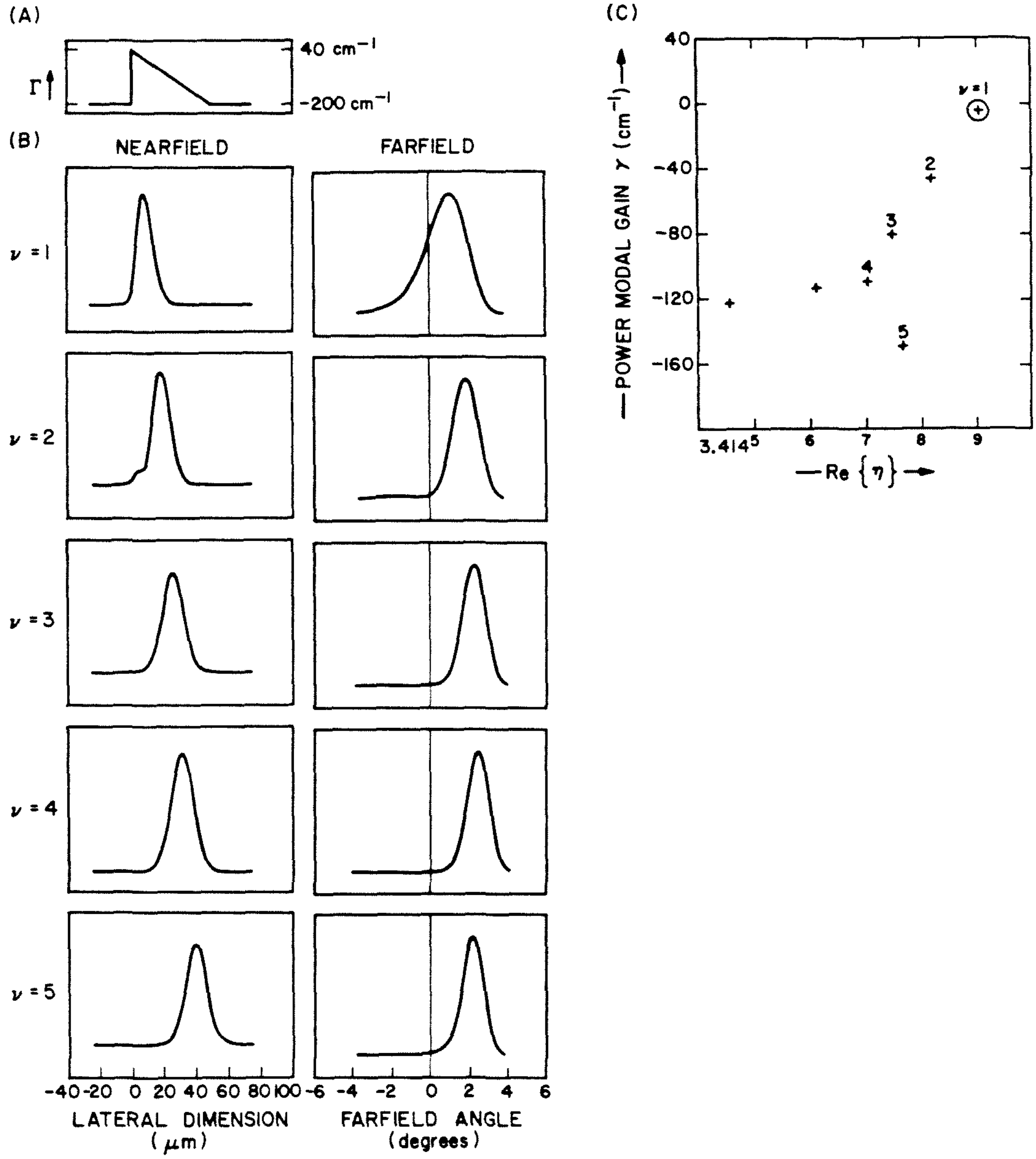

FIGURE 5.7 High gain modes of an asymmetric tailored gain ramp waveguide (a) gain profile (b) intensity nearfield and farfield patterns (c) modal plot. Note that all the nearfield patterns are null-less and that the farfield patterns are all single lobed (*cf.* Figures 2.12and 5.4.

of Figure 5.4, we present the equivalent tailored gain waveguide of Figure 5.7. Only the first five modes with the highest $\bar{\eta}$ are shown. It is interesting to note that while there is very little difference between real index and gain guided box waveguides (Figure 2.11 and 2.12, respectively), comparison of Figure 5.7 with that of the corresponding one for the real index waveguide of Figure 5.4 reveals a striking difference between the two ramp waveguides. The higher order modes of the real index waveguides have nulls in their nearfield patterns, while the tailored gain guide modes do not. For real index waveguides, all higher order modes have multilobed farfield patterns, but the farfield patterns of the tailored gain waveguide have *single lobed* farfield patterns.

To understand these differences, we examine in detail the Airy functions of complex argument.

§5.7 The Airy Functions of Complex Argument

In order to obtain simple analytical expressions for the eigenvalues, nearfield patterns and farfield patterns in terms of elementary functions, it is necessary to eliminate either Ai or Bi from Equation (5.5.4).

As we have shown in §5.4, along the negative real axis, Ai(ξ) resembles a damped sinusoidal function with a gradually decreasing period, while along the positive real axis Ai(ξ) *decays* exponentially without oscillations or zeros. Similarly, along the negative real axis, Bi(ξ) resembles a damped cosinusoidal function with a gradually decreasing period, while along the positive real axis Bi(ξ) *grows* exponentially without oscillations or zeros. However, as gain is introduced into the waveguide, the mode paths deviate from the real axis and the eigenmodes of this complex waveguide are determined by the analytic continuations of Ai(ξ) and Bi(ξ) into the complex z–plane.

§5.7 The Airy Functions of Complex Argument

At this point we introduce the full first order asymptotic expansions to the Airy functions which are valid throughout the complex plane. These approximations will be seen to greatly facilitate the analytic treatment of linear tailored gain waveguides. The leading behavior of Ai(z) and Bi(z) as $|z| \to \infty$ is[4]

$$\mathrm{Ai}(z) \sim \begin{cases} \pi^{-1/2}(-z)^{-1/4}\sin[\frac{2}{3}(-z)^{\frac{3}{2}} + \frac{\pi}{4}] & \frac{\pi}{3} < \angle z < \frac{5\pi}{3} \\ \frac{1}{2}\pi^{-1/2}z^{-1/4}e^{-\frac{2}{3}z^{3/2}} & |\angle z| < \pi \end{cases} \tag{5.7.1}$$

$$\mathrm{Bi}(z) \sim \begin{cases} \pi^{-1/2}(-z)^{-1/4}\cos[\frac{2}{3}(-z)^{\frac{3}{2}} + \frac{\pi}{4}] & \frac{\pi}{3} < \angle z < \frac{5\pi}{3} \\ \pi^{-1/2}z^{-1/4}e^{+\frac{2}{3}z^{3/2}} & |\angle z| < \frac{\pi}{3}\,. \end{cases} \tag{5.7.2}$$

The magnitude and phase of both Airy functions are illustrated over the complex plane in Figure 5.8. Even though the approximations (5.7.1) and (5.7.2) are strictly valid only as $|z| \to \infty$, we have found them (numerically) to be fairly accurate even for $|z|$ as small as 2 or 3. We see that Ai(z) has zeros only along the negative real axis, grows exponentially as $|z| \to \infty$ in the sectors $\frac{\pi}{3} < |\angle z| < \pi$, and decays exponentially as $|z| \to \infty$ in the sector $|\angle z| < \frac{\pi}{3}$. Bi($z$) also has zeros along the negative real axis (but at different locations than those of Ai(z)), as well as along the lines $\angle z = \pm\frac{\pi}{3}$. Otherwise, Bi($z$) grows exponentially everywhere as $|z| \to \infty$. Unlike Ai(z), there is no sector in which Bi(z) decays exponentially as $z \to \infty$.

The various sectors described by Equations (5.7.1)and (5.7.2)are referred to as *Stokes regions*;[1]the negative real axis and the lines $\angle z = \pm\frac{\pi}{3}$ are the *Stokes lines.* The Stokes regions play a crucial role in the analysis of asymmetric linear tailored gain waveguides and will be discussed further in §5.8, and §5.10 to §5.12.

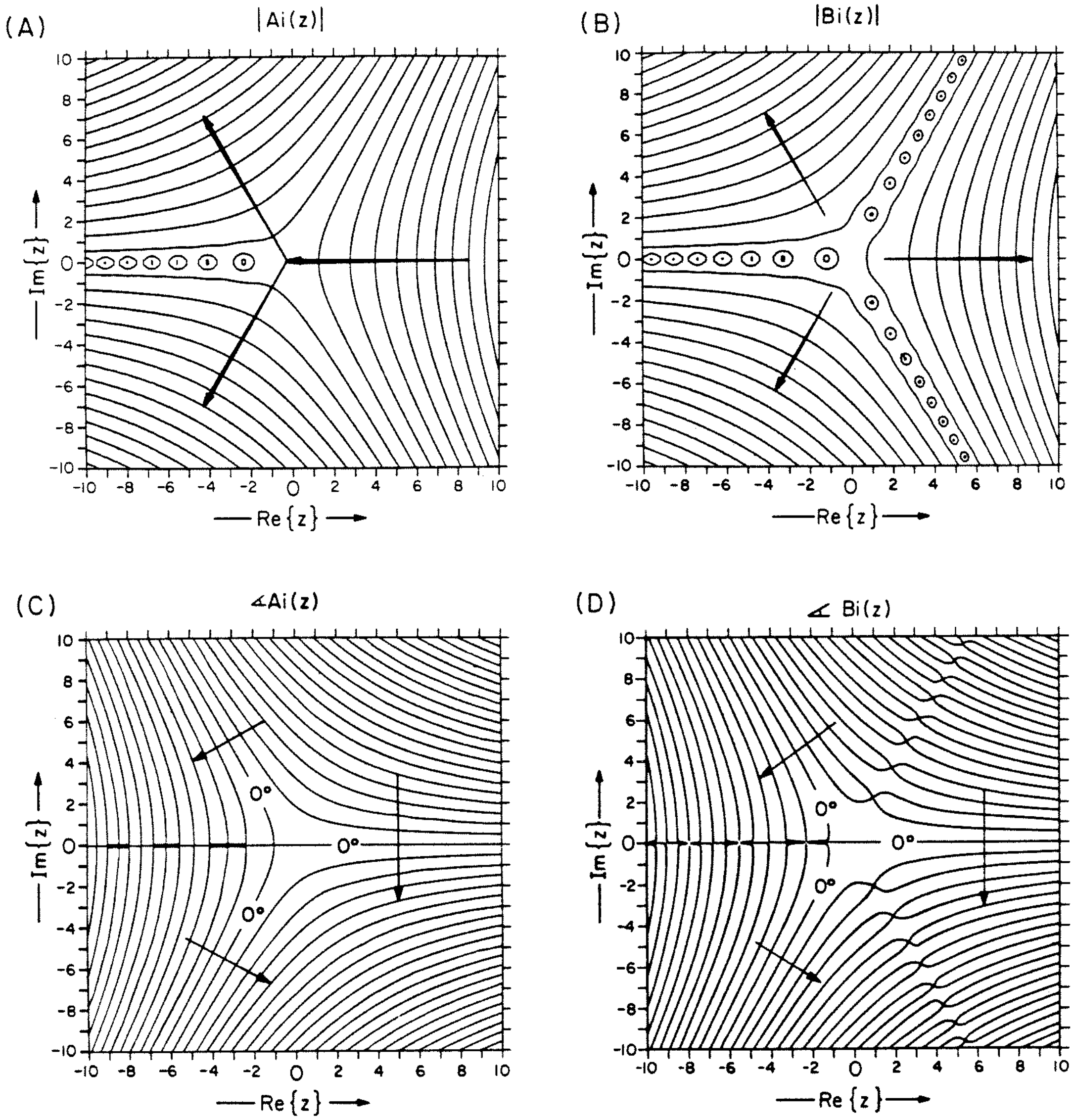

FIGURE 5.8 Airy Functions of Complex Argument. Level lines for the magnitude of (a) Ai(z) and (b) Bi(z); the arrows show the direction of increasing magnitude. Lines of constant phase for (c) Ai(z) and (d) Bi(z); the arrows show the direction of increasing phase. The contours in (a) & (b) differ by a factor of ten and by $\pi/4$ in (c) & (d).

§5.8 Path Analysis for the Linear Tailored Gain Waveguide

In order to proceed with the theoretical analysis, it is necessary to determine which one of the terms $a\,\mathrm{Ai}(z)$ or $b\,\mathrm{Bi}(z)$ provides the dominant contribution to E in Equation (5.5.4). We therefore examine both the ratio a/b as well as $|\mathrm{Ai}(z)|\,/\,|\mathrm{Bi}(z)|$ for modes on the (+) branch. Since the modes on the (−) branch are cut off due to the relatively small width of the waveguide of Figure 5.7, we will make use of the wider waveguide of Figure 5.9 for the remainder of this work.

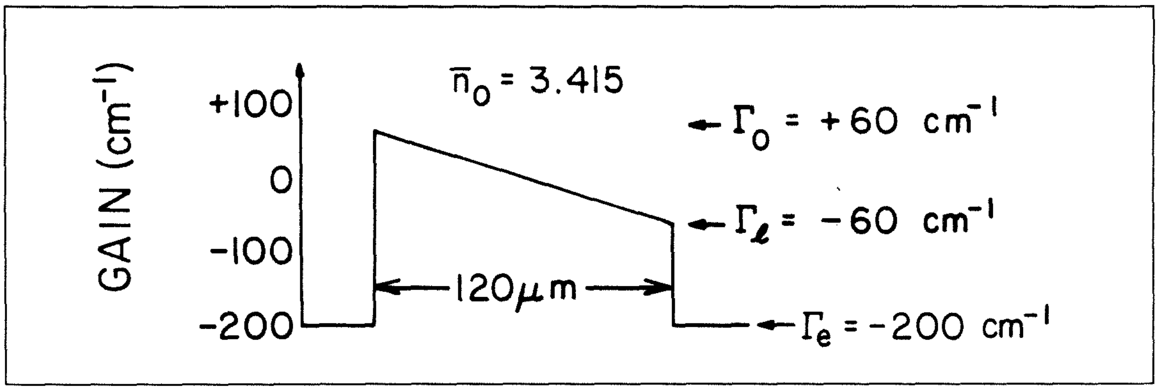

FIGURE 5.9 Asymmetric tailored gain ramp waveguide used for illustrative purposes throughout this chapter.

Using the root of $(-i)^{1/3} = e^{-i\pi/6}$ which is appropriate for the this branch along with (5.6.1) to compute the ratio a/b in the sector $|\angle z| < \frac{\pi}{3}$ for the ν^{th} (+) mode, we get

$$\left|\frac{a}{b}\right|_{\nu}^{(+)} \sim 2\exp\frac{4}{3}\left[|\omega\ell|^{3/2} + \frac{3}{2}\rho_\nu|\omega\ell|^{1/2}\right] \tag{5.8.1}$$

This ratio is plotted in Figure 5.10 for a guide with a constant gain gradient of approximately $1\mathrm{cm}^{-1}/\mu\mathrm{m}$ and varying widths ℓ. The ratio a/b can approach a value as high as 10^{12}, suggesting that the contribution of $\mathrm{Ai}(z)$ to E completely dominates that of $\mathrm{Bi}(z)$ for the first few modes of guides wider than about $50\mu\mathrm{m}$.

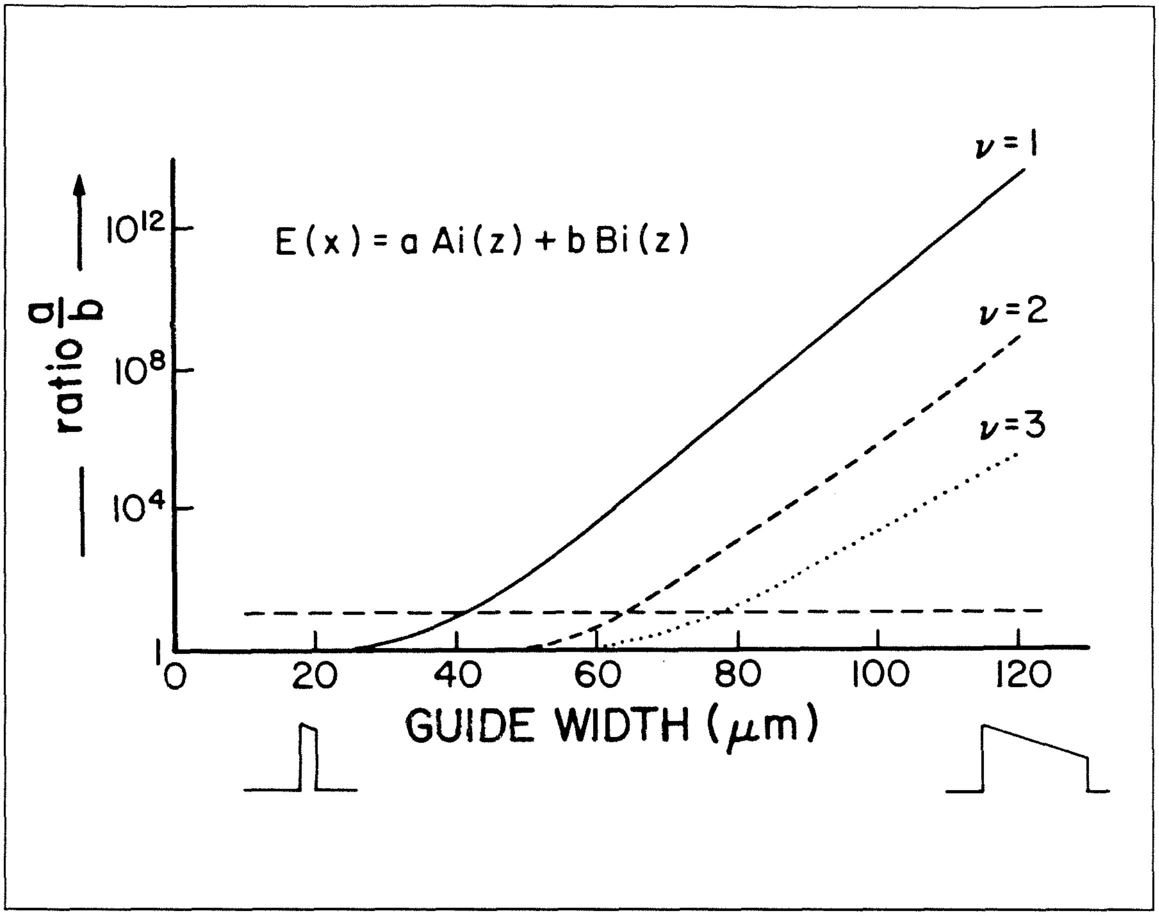

FIGURE 5.10 Ratio of $|\mathrm{Ai}(z)| \,/\, |\mathrm{Bi}(z)|$ for the first three modes on the (+) branch for guides of different widths. To an excellent degree of approximation, the mode is determined almost entirely by the behavior of $\mathrm{Ai}(z)$.

However, this ratio, by itself, is conclusive only when the magnitudes of the two functions $\mathrm{Ai}(z)$ and $\mathrm{Bi}(z)$ are of the same order. Consequently, we must examine the paths $\mathcal{L}$ of the argument $\rho+\omega x$. The various paths taken by $\mathcal{L}$ for each branch are shown superimposed on $|\mathrm{Ai}(z)|$ in Figure 5.11. One endpoint $z = \rho$ $(x = 0)$ lies near a zero of $\mathrm{Ai}(z)$ and the other is in the sector $|\angle z| < \frac{\pi}{3}$ where $|\mathrm{Ai}(z)|$ is exponentially small. This merely expresses the fact that the modes of the wide waveguide of Figure 5.9 are well-confined: the electric field is close to zero at the edges of the guide.

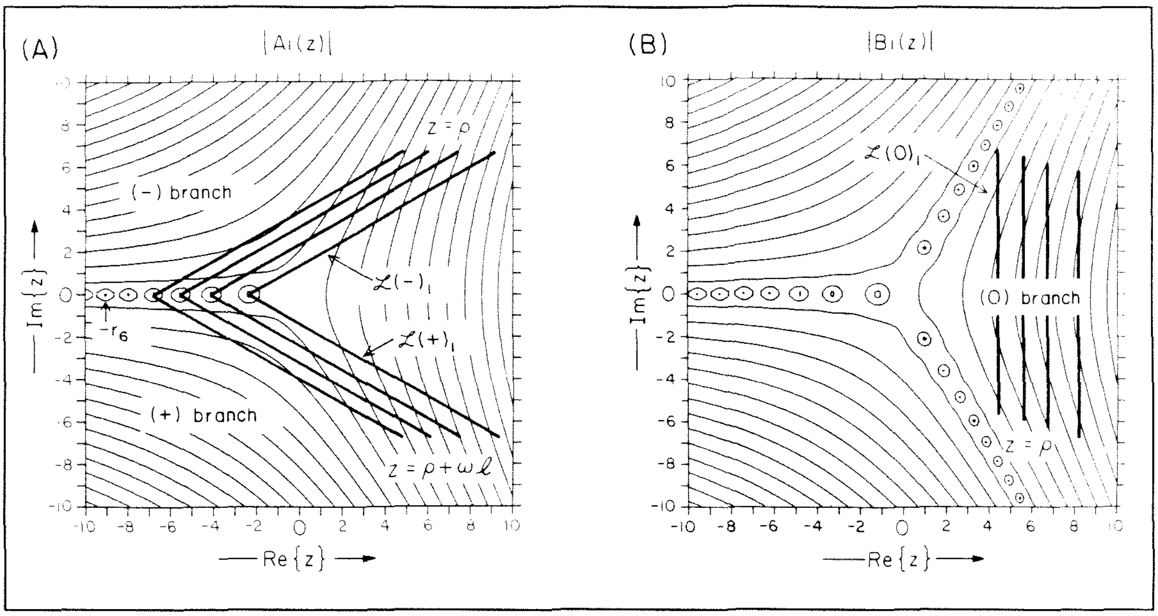

FIGURE 5.11 Path analysis for the asymmetric linear tailored gain ramp waveguide of Figure 5.9 (a) (+) & (−) branches, (b) (0) branch.

From Figure 5.8 we note that in the sector $|\angle z| < \frac{\pi}{3}$, $|\mathrm{Bi}(z)|$ is exponentially large, so that its magnitude at $z = \rho + \omega\ell$ is much larger than it is at $z = \rho$. Consequently, its profile is not consistent with a well-confined mode. This explains why the ratio a/b above is so large for the (+) modes. As the guide width ℓ is increased, the endpoint $z = \rho + \omega\ell$ penetrates deeper into the Stokes region $|\angle z| < \frac{\pi}{3}$ and the increasing ratio a/b reflects the growing dissimilarity between $\mathrm{Ai}(z)$ and $\mathrm{Bi}(z)$. Only when the endpoint $z = \rho + \omega\ell$ lies near the Stokes line at $|\angle z|\, is = \frac{\pi}{3}$ does $\mathrm{Bi}(z)$ make a significant contribution to the eigenmode. Thus the solution $E_\nu^{(+)}(x)$ of the Helmholtz equation can be expressed as a single term for guides wider than some critical width ℓ^*, to be determined in §5.10.

The peak intensity within the waveguide occurs when the line $\mathcal{L}$ is tangent to a level line of $\mathrm{Ai}(z)$. For modes on the (+) branch this point lies near the high gain side of the waveguide near $x = 0$, and so these modes have modal gains higher than those on any other branch. Of these modes, the $\nu = 1$ mode has the largest spatial overlap with the lateral gain profile and hence will be the lasing mode at threshold. As is evident from Figure 5.7, it also has the highest effective index of any mode on the (+) branch and will henceforth be referred to as the "fundamental" mode of the waveguide.

Similar arguments can be applied to both the (0) and (−) branches. The paths $\mathcal{L}(-)$ with $\psi = +30°$ are also illustrated in Figure 5.11 and are similar to $\mathcal{L}(+)$ except that now the zero of the Airy function occurs at $z = \rho + \omega\ell$. As a consequence, these modes are concentrated in the lossy regions of the waveguide.

The path of the argument of the Airy functions for the (0) branch is plotted in Figure 5.11b with $\psi = +90°$. Unlike the previous two cases, $\mathrm{Bi}(z)$ plays a much more prominent role on the (0) branch because the lines $\mathcal{L}(0)$ are nearly symmetric about the real axis, and $\mathrm{Ai}(z)$ grows exponentially towards the Stokes lines at $\angle z = \pm\frac{\pi}{3}$ while $\mathrm{Bi}(z)$ decays. Since the electric field at the interface must match to a decaying exponential that is bounded at infinity, $\mathrm{Bi}(z)$ better satisfies the boundary conditions on the (0) branch than $\mathrm{Ai}(z)$ does, and hence plays a much more important role in determining E. Due to the symmetry of $\mathrm{Bi}(z)$ about the positive real axis, the nearfield patterns of these modes are approximately centered within the waveguide. These modes therefore have a modal gain which is between modes on the (+) branch and modes on the (−) branch. They correspond to the (0) branch of Figure 5.11. We remark that this description of modes on the (0) branch holds for the wide waveguides considered here but becomes considerably more complicated for waveguides in which $|\omega\ell| \to 0$.

§5.9 Analytical Approximations for the Eigenvalues

Once it has been determined that the contribution of $\mathrm{Ai}(z)$ dominates that due to $\mathrm{Bi}(z)$ on the principal (+) branch, it becomes possible to derive very simple analytical expressions for the mode effective indices and modal gains by recalling that $\mathcal{L}$ for the principal branch starts near a zero of $\mathrm{Ai}(x)$ and ends in the sector of exponential decay. At the left edge of the guide $E(0) = a\mathrm{Ai}(\rho)$, where ρ is given by Equation (5.3.4). Setting ρ equal to one of the (real) zeros $-r_\nu$ of the Airy function

$$-r_\nu \simeq \rho_\nu = \frac{k_0^2}{\omega^2}(\eta_\nu^2 - n_0^2) \tag{5.9.1}$$

and approximating $(\eta_\nu^2 - n_0^2)$ by $2n_0(\eta_\nu - n_0)$ yields an expression for the ν^{th} eigenvalue η_ν:

$$\eta_\nu \simeq n_0 - \frac{1}{2n_0}\frac{\omega^2}{k_0^2} r_\nu \tag{5.9.2}$$

where the ν^{th} zero of $\mathrm{Ai}(z)$ is approximately given by (Equation (5.7.1))

$$-r_\nu \simeq \left[\frac{3}{2}\left(\nu - \frac{1}{4}\right)\pi\right]^{2/3} \qquad \nu = 1, 2, 3 \ldots\ . \tag{5.9.3}$$

After using the definition of ω in Equation (5.3.4) for the case of gain guiding with no index antiguiding ($\sigma = -is$), taking the principal (+) branch of ω, and equating the real and imaginary parts we obtain an expression for $\eta = \bar{\eta} + i\bar{\bar{\eta}}$ on the (+) branch:

$$\begin{aligned} \bar{\eta}_\nu^{(+)} &\simeq \bar{n}_0 - \frac{1}{2}\epsilon_\nu \\ \bar{\bar{\eta}}_\nu^{(+)} &\simeq \bar{\bar{n}}_0 + \frac{\sqrt{3}}{2}\epsilon_\nu \end{aligned} \tag{5.9.4}$$

where

$$\epsilon_\nu = \left|\frac{s^2}{2n_0}\right|^{1/3} r_\nu \tag{5.9.5}$$

and the parameter s is related to the guide parameters by Equation (5.5.3). We therefore see that in the complex η plane, the mode structure is particularly simple:

all the modes of the principal branch lie on a straight line emanating from the point $(\bar{n}_0\,,\,\bar{\bar{n}}_0)$ and making an angle $\tan^{-1}\sqrt{3} = 60°$ with the real axis. The modes are spaced along this line according to the zeros of the Airy function, with the higher order modes being more closely spaced together.

Since the modal gain $\gamma_\nu^{(+)}$ is related to $\bar{\bar{\eta}}_\nu$ through $\gamma_\nu = -2k_0\bar{\bar{\eta}}_\nu$ (Equation (2.5.2)),

$$\begin{aligned}\gamma_\nu^{(+)} &\simeq \Gamma_0 - 2k_0\frac{\sqrt{3}}{2}\epsilon_\nu \\ &\simeq \Gamma_0 - \sqrt{3}k_0\left|\frac{s^2}{2n_0}\right|^{1/3} r_\nu\end{aligned} \tag{5.9.6}$$

and $0 < r_1 < r_2 \ldots$, we see that the fundamental mode has the highest modal gain and hence will be the lasing mode at threshold. At threshold, the modal gain $\gamma_1^{(+)}$ of the fundamental mode must equal the mirror losses $-\Gamma_m$ (scattering losses are probably insignificant in a wide gain guided laser). Equation (5.9.6) may thus be inverted to give the required peak gain Γ_0 at threshold in terms of Γ_m and the gain gradient s. Equation (5.9.6) shows that the required peak gain at threshold (*i.e.*, inversion density) increases sublinearly with the gain gradient.

The mode discrimination between any two modes is given by

$$\Delta\gamma_\nu^{(+)} \equiv \gamma_\nu^{(+)} - \gamma_{\nu+1}^{(+)} \simeq \sqrt{3}k_0\left|\frac{s^2}{2n_0}\right|^{1/3}\delta_\nu \tag{5.9.7}$$

where

$$\delta_\nu \equiv |r_\nu - r_{\nu+1}| \tag{5.9.8}$$

is the spacing between the zeros of $\mathrm{Ai}(\xi)$. The mode discrimination scales sublinearly with the gain gradient, and is greatest between the fundamental $\nu = 1$ and the next higher order $\nu = 2$ mode. Equation (5.9.7) is typically accurate to within a few percent for wide waveguides.

Each lateral mode of the waveguide has a slightly different guide wavelength due to the different effective indices of refraction $\bar{\eta}$. Spectrally resolved nearfield patterns$^{(\S 3.5(c.i))}$ may be used to make visible the various lateral modes in a laser operated above threshold. The wavelength separation between any two modes is given by

$$\begin{aligned}\Delta\lambda_\nu^{(+)} &\simeq \frac{\lambda_0}{\bar{n}_0^2}\left|\epsilon_\nu - \epsilon_{\nu+1}\right| \\ &\simeq \frac{\lambda_0}{\bar{n}_0^2}\left|\frac{s^2}{2\bar{n}_0}\right|^{1/3}\delta_\nu \ .\end{aligned} \tag{5.9.9}$$

In an entirely analogous manner, formulae for the propagation constants of modes on the $(-)$ branch may be determined by setting $\rho + \omega\ell$ equal to a zero of the Airy function:

$$-r_\nu \simeq \rho_\nu + \omega\ell = \frac{k_0^2}{\omega^2}(\eta_\nu^2 - n_0^2) + \omega\ell \ . \tag{5.9.10}$$

The the additional term $\omega\ell$ and the $(-)$ root of ω lead to slightly different expressions for the eigenvalues $\eta_\nu^{(-)}$:

$$\begin{aligned}\bar{\eta}_\nu^{(-)} &\simeq \bar{n}_\ell - \frac{1}{2}\epsilon_\nu \\ \bar{\bar{\eta}}_\nu^{(-)} &\simeq \bar{\bar{n}}_\ell - \frac{\sqrt{3}}{2}\epsilon_\nu \\ \gamma_\nu^{(-)} &\simeq \Gamma_\ell + \sqrt{3}k_0\left|\frac{s^2}{2n_0}\right|^{1/3} r_\nu \ .\end{aligned} \tag{5.9.11}$$

As before, the approximations for the eigenvalues on the $(-)$ branch lie on a straight line, but this time they emanate from the point $(\bar{n}_\ell\,,\,\bar{\bar{n}}_\ell)$. The angle that this line makes with the real axis remains 60°, so that it makes an angle of 120° with the corresponding $(+)$ line. Similarly, the modes are spaced along this line according to the zeros of the Airy function, with the higher order modes being more closely spaced together. In this case the $\nu = 1$ mode on the $(-)$ branch has the *lowest* modal gain of all the modes. We remark that Equation (5.9.11) is not as accurate as Equation (5.9.6) for truncated waveguides in which $n_\ell \neq n_0 - \sigma k_0 \ell$

because of the perturbation introduced by the truncated region at the lossy edge of the guide. Modes on the (−) branch will not lase, however, so the error is unimportant from a practical point of view.

Modes on the (0) branch have nearly constant modal gains and are composed almost entirely of $\mathrm{Bi}(z)$. It is not possible to obtain simple closed form analytic expressions for the eigenvalues for these modes. Once again, however, since they have low modal gains and will not lase until much above threshold, the formulae are not required.

We have confirmed these results using the numerical methods of §2.7. Figure 5.12a shows the mode diagram for the waveguide of Figure 5.9. Figure 5.12b shows an enlargement of the boxed region of Figure 5.12a. Note that the spacing of the modes on both the (+) and (−) branches are consistent with the spacing between the zeros of the Airy function, as predicted by Equation (5.9.4).

§5.10 Nearfield Patterns

Qualitative features of the nearfield patterns of the eigenmodes of an asymmetric linear tailored gain waveguide were indicated by Figure 5.11. Considering first the (+) branch, we recall that $\mathcal{L}$ starts from a zero of $\mathrm{Ai}(z)$ and terminates in the sector of exponential decay $|\angle z| < \pi/3$. Since the zeros of $\mathrm{Ai}(z)$ occur only along the negative real axis, we see that unlike the eigenmodes of a symmetric or real index guided structure, *the eigenmodes of an asymmetric linear tailored gain waveguide do not have nulls in their intensity nearfield patterns.*

Quantitatively, this unusual property may be understood by considering the behavior of $\mathrm{Ai}(z)$ off the negative real axis. We expand the sine function in (5.7.1) as a superposition of exponential terms:

$$\mathrm{Ai}(z) \sim \tfrac{1}{2}\pi^{-1/2}(-z)^{-1/4}\left(c\, e^{+\frac{2}{3}z^{3/2}} + c^{*}\, e^{-\frac{2}{3}z^{3/2}}\right) \qquad (5.10.1)$$

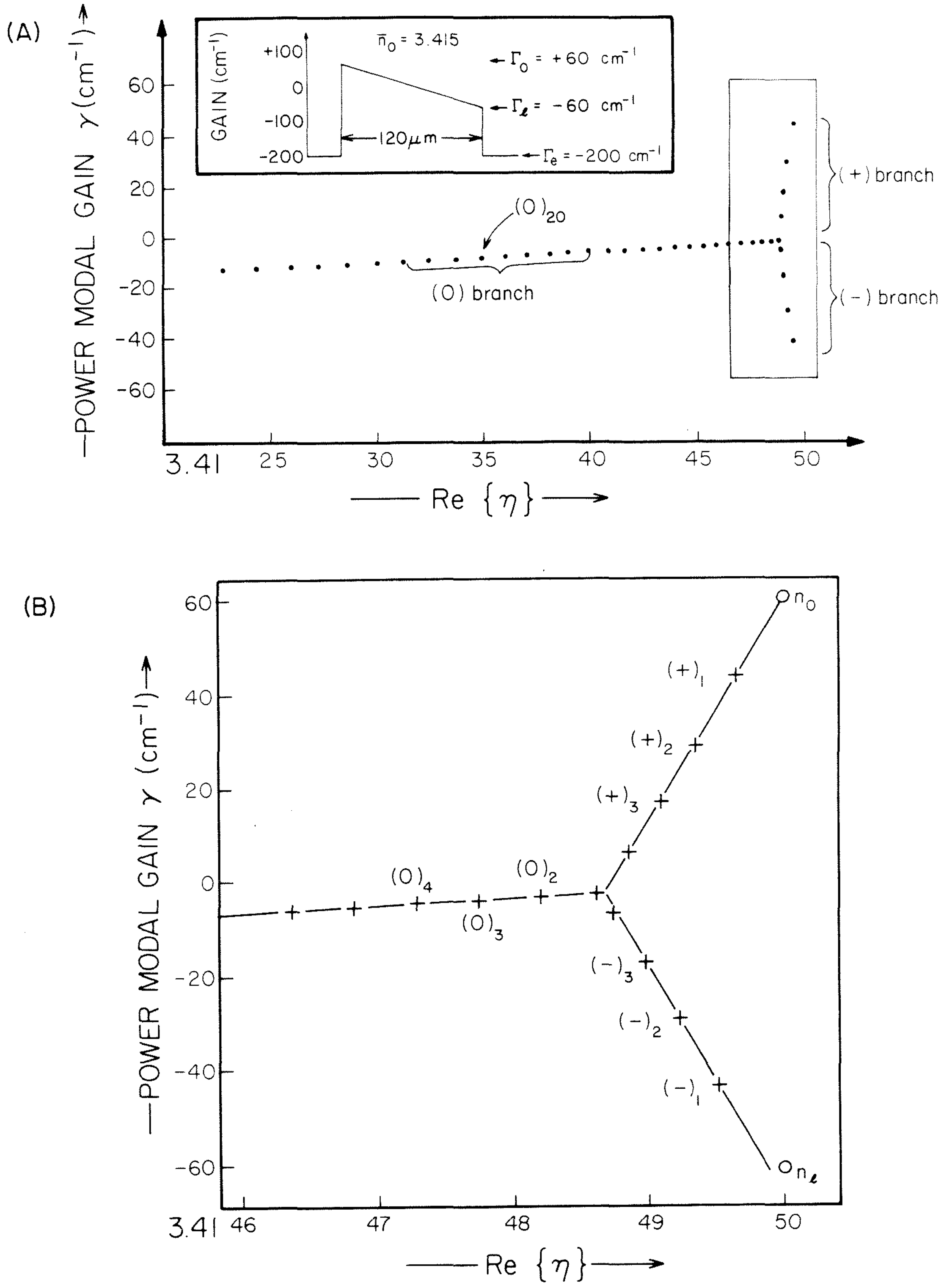

FIGURE 5.12 Summary of the eigenvalues of the asymmetric tailored gain waveguide of Figure 5.9, showing the (+) , (−) , and (0) branches. (a) overview (b) closeup of boxed region of part (a).

where $c = e^{-i\frac{\pi}{4}}$. The relative contribution of each of the two terms to $\mathrm{Ai}(z)$ varies within the region of validity of (5.7.1). If we write z in polar form, $z = r\,e^{i(\pi-\delta)}$, near the negative real axis $\Re\mathrm{e}\{z^{3/2}\} = r^{3/2}\cos(\frac{3}{2}(\pi-\delta)) = -r^{3/2}\sin\frac{3}{2}\delta$. Above the negative real axis $\sin\frac{3}{2}\delta > 0$, so that as $|z| \to \infty$ the second term becomes exponentially larger than the first. Correspondingly, below the negative real axis $\sin\frac{3}{2}\delta < 0$, so as $|z| \to \infty$ the first term becomes exponentially larger than the second. Along the negative real axis (the Stokes line), both terms are of equal magnitude but differ in phase, while along the line $\angle z = \pm\frac{2\pi}{3}$ (the antiStokes lines) the second term in (5.10.1) most dominates the contribution due to the first term. The switching of dominance between the two exponential terms in Equation (5.10.1) (*i.e.*, Stokes phenomenon) plays a central role in the analysis of asymmetric linear tailored gain waveguides because it allows the Airy function to be written as a single term asymptotic expansion in a region of the complex plane away from the Stokes line along the negative real axis. As will be discussed below, this is also directly responsible for the single lobed farfield patterns characteristic of these waveguides.

The nearfield intensity for modes on the (+) branch is given by $I(x) = |\mathrm{Ai}(\rho+\omega x)|^2$. Writing $\mathrm{Ai}(z)$ as a single term asymptotic expansion, the nearfield intensity for the ν^{th} mode becomes

$$I_\nu(x) \simeq \left|(\rho_\nu+\omega x)^{-1/4}e^{-\frac{2}{3}(\rho_\nu+\omega x)^{3/2}}\right|^2 \quad . \tag{5.10.2}$$

We desire to find the position of the maximum χ_ν and the half-width w_ν of mode E_ν. The usual technique of setting $\frac{dI(x)}{dx} = 0$ does not yield an expression giving a closed form solution for χ_ν. However, χ_ν may be determined from the geometrical relationships between $\mathcal{L}$ and the level lines of $\mathrm{Ai}(z)$. Along $\mathcal{L}$ both the real and imaginary parts of $\rho + \omega x$ are approximately equal. By introducing a coordinate rotation such that one coordinate axis lies along $\mathcal{L}$, and the other coordinate axis goes through χ_ν, we can make a Taylor expansion of the radicals in the asymptotic expression for Ai(z) to derive first order approximations for the electric field $E(x)$.

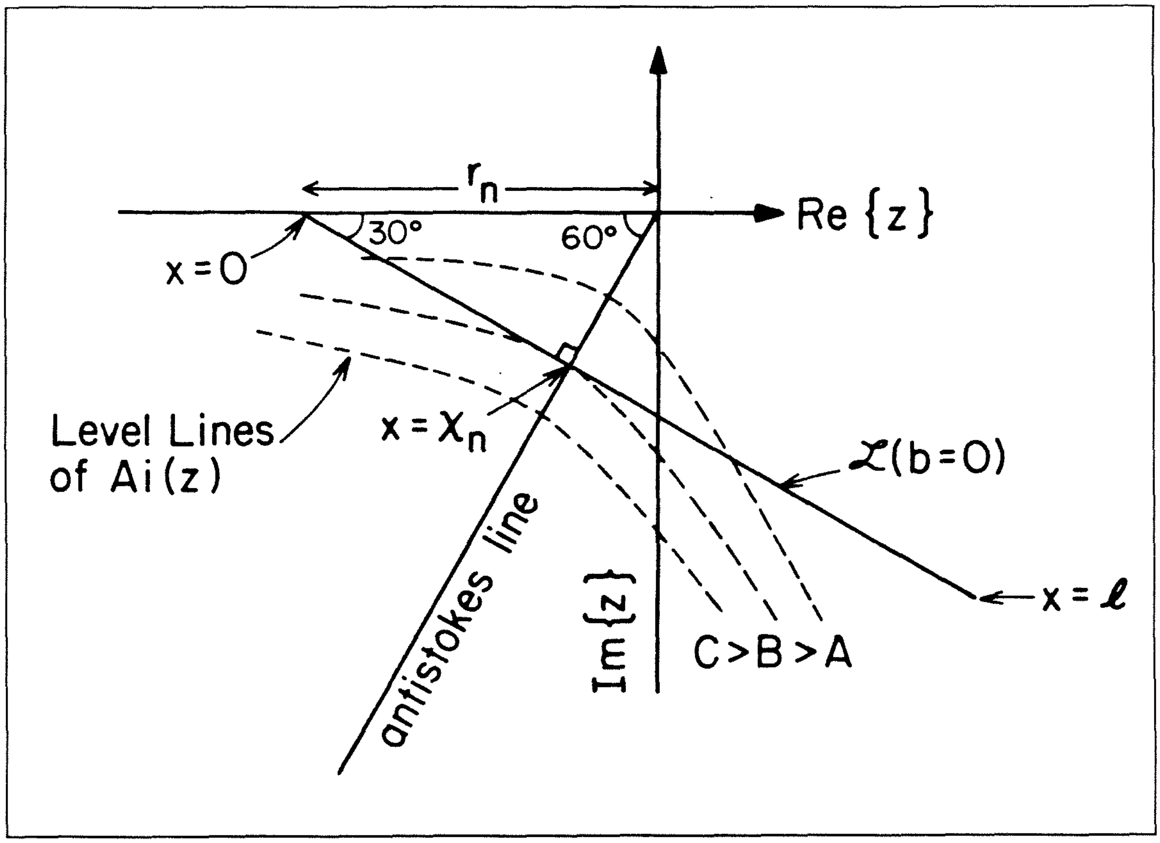

FIGURE 5.13 Geometrical construction to determine the position of the peak intensity χ_ν. The 30° – 60° right triangle makes the calculation of χ_ν especially simple for the special case of no index antiguiding.

Referring to Figure 5.13, we see that along the path $\mathcal{L}$, $|\text{Ai}(z)|$ reaches its maximum when $\mathcal{L}$ is tangent to the level lines of Ai(z). These level lines are perpendicular to the lines of constant phase of Ai(z). The antiStokes line associated with the principal branch is asymptotic to the line of constant phase (see Figure 5.8c), which makes an angle of $-60°$ with the negative real axis. The corresponding tangent lines are at an angle of $-30°$, which is precisely the angle ψ that

$\mathcal{L}$ makes with the negative real axis for the special case of no index antiguiding. The quantity $\rho_\nu - \chi_\nu$ therefore lies on the Airy function's antiStokes line. This happens when

$$\angle z = \angle(\rho_\nu - \chi_\nu) = \pm\sqrt{3} \tag{5.10.3}$$

where the minus sign is used for the principal (+) branch. If we approximate ρ_ν by a (real) zero of the Airy function, use Equation (5.3.4) for the complex quantity ω, and make use of a simple geometric construction shown in Figure 5.13, we can derive an expression for χ_ν:

$$\chi_\nu = \frac{\sqrt{3}}{2}\frac{r_\nu}{|\omega|} \; . \tag{5.10.4}$$

It should be noted that, for a wide guide, the position of the mode within the guide χ_ν depends only on the gain gradient and is independent of both the peak gain Γ_0 and the width ℓ of the guide. The mode maxima are separated within the guide by

$$\Delta\chi_\nu = \frac{\sqrt{3}}{2k_0}\,|2n_0 s|^{-1/3}\,\delta_\nu \tag{5.10.5}$$

where s is given by Equation (5.5.3) and δ_ν by (5.9.8).

Equation (5.10.5) may be used to derive a particularly simple expression for the modal gains on the principal branch. If we take $\Gamma(x)$ as the lateral gain profile and $g = (\Gamma_0 - \Gamma_l)/\ell$ as the spatial gain gradient, the expressions for the modal gain and mode discrimination become

$$\begin{aligned} \gamma_\nu^{(+)} &= \Gamma(\chi_\nu) \\ \Delta\gamma_\nu^{(+)} &= g\Delta\chi_\nu \end{aligned} \; ; \tag{5.10.6}$$

i.e., the modal gain of the mode is given simply by the value of the spatial gain at the point where the electric field has its peak value. This suggests that, to first order, the mode intensity profile is approximately symmetric about its peak position, and that its width is much less than the width of the waveguide.

To find an expression for the nearfield pattern, we write z in terms of the rectangular coordinates $z = u' + iv'$ and rotate the coordinate system (see Figure 5.14) to new variables u and v so that u lies along the antiStokes line $\angle z = e^{-i2\pi/3}$ and v lies perpendicular to it (*i.e.*, along $\mathcal{L}$).

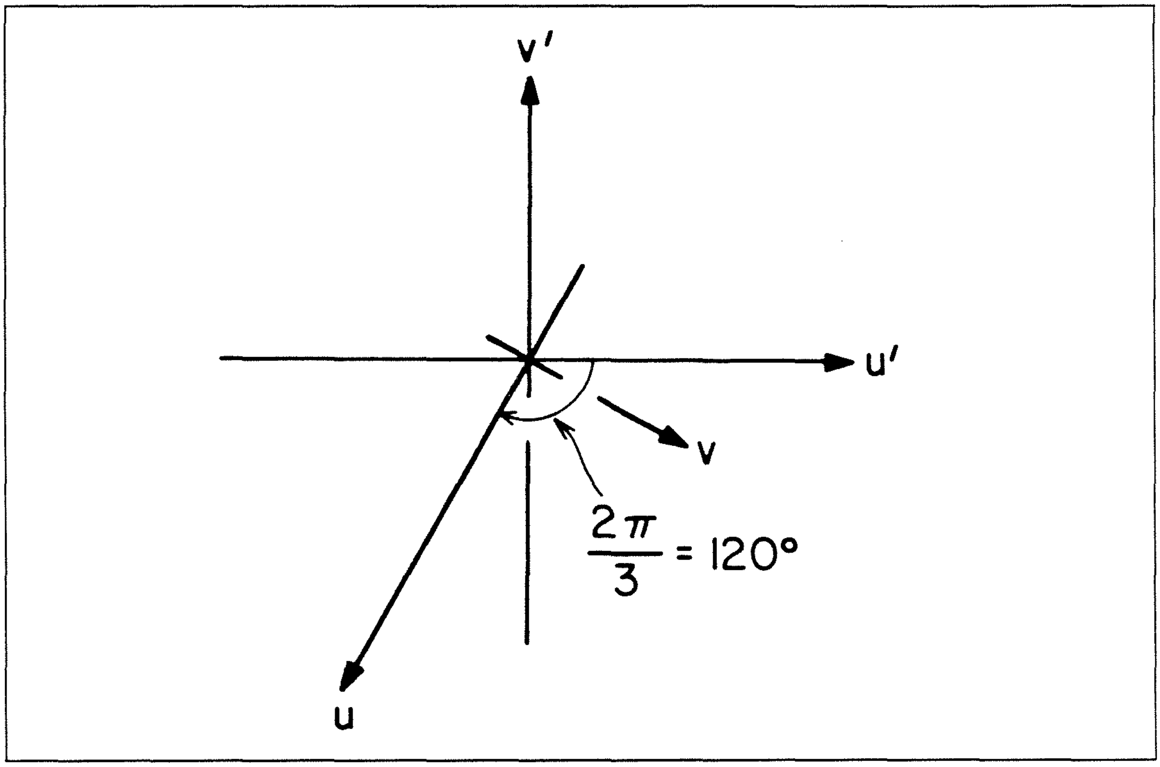

FIGURE 5.14 Coordinate rotation of $-2\pi/3 = 120°$ for used in the calculation of the nearfield pattern.

After making the rotation, near the antiStokes line associated with the (+) branch, the Airy function may be written as a single term asymptotic expansion

$$\mathrm{Ai}(u+iv) \simeq (u+iv)^{-1/4} e^{+\frac{2}{3}(u+iv)^{3/2}} . \tag{5.10.7}$$

where we have dropped some unimportant global constants. The radicals may be simplified by making a binomial expansion about $v = 0$ with $v \ll u$:

$$\begin{aligned}(u+iv)^{3/2} &\approx u^{3/2}\left[1+i\frac{3}{2}\frac{v}{u}-\frac{3}{8}\left(\frac{v}{u}\right)^2\right]\\ (u+iv)^{-1/4} &\approx u^{-1/4}\left[1+\left(\frac{v}{4u}\right)^2\right]^{1/2} e^{-i\frac{v}{4u}} \quad .\end{aligned} \tag{5.10.8}$$

Along the antiStokes line, $v = 0$ while along the line $\mathcal{L}$ u is constant and Figure 5.13 shows that v is linearly related to the lateral position x within the guide:

$$\begin{aligned}u &= \frac{r_\nu}{2}\\ v &= (x-\chi_\nu)\,|\omega| \quad .\end{aligned} \tag{5.10.9}$$

Substituting Equations (5.10.8)and (5.10.9) in (5.10.7), we find that the expression for the electric field reduces to

$$\begin{aligned}E(x) &\simeq \mathrm{Ai}(\frac{r_\nu}{2}+i(x-\chi_\nu)\,|\omega|)\\ &\simeq \mathrm{Bi}\left(\frac{r_\nu}{2}\right)e^{-(x-\chi_\nu)^2/2w_\nu^2}\,e^{i\phi_\nu(x-\chi_\nu)}\end{aligned} \tag{5.10.10}$$

which is a Gaussian centered at χ_ν with half width w_ν multiplied by a linear phase variation ϕ_ν, where χ_ν is given by Equation (5.10.4), and w_ν and ϕ_ν are given by

$$\begin{aligned}w_\nu &= \frac{(2r_\nu)^{1/4}}{|\omega|}\\ \phi_\nu &= \left[\left(\frac{r_\nu}{2}\right)^{1/2}-\frac{1}{2r_\nu}\right]|\omega| \quad .\end{aligned} \tag{5.10.11}$$

The normalized nearfield intensity $I_\nu(x)$ is hence

$$I_\nu(x) \simeq \frac{1}{\sqrt{\pi w_\nu^2}}e^{-(x-\chi_\nu)^2/w_\nu^2} \, . \tag{5.10.12}$$

The intensity nearfield patterns may be found for the (−) branch in a similar manner. The exact (numerical) nearfield intensities and phases for representative modes on each of the three branches is plotted in Figure 5.15. All of the modes are approximately Gaussian in shape with essentially linear phase variations over the

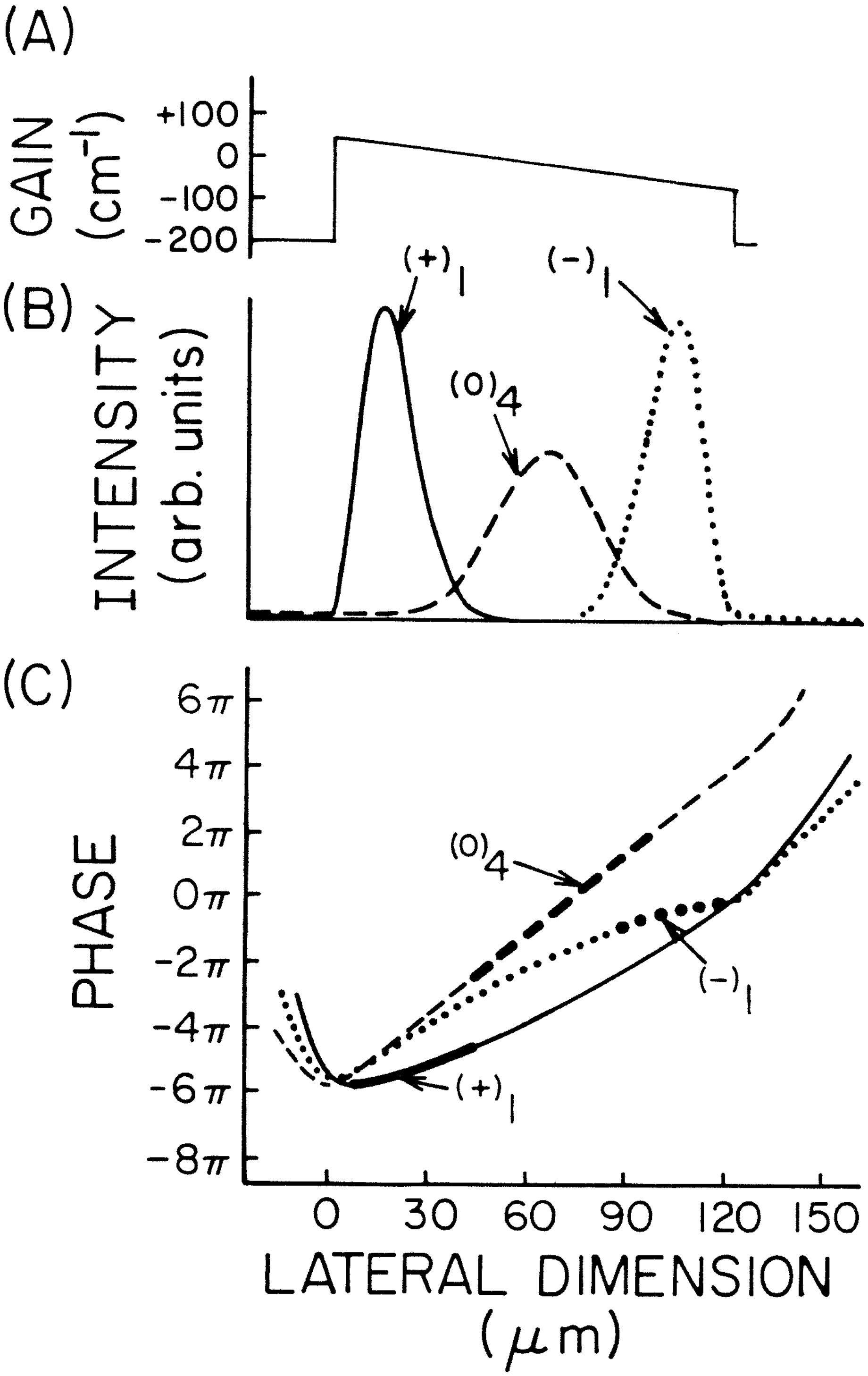

FIGURE 5.15 (a) the asymmetric linear tailored gain ramp waveguide of Figure 5.9, (b) the nearfield patterns of representative modes on each of the three branches (c) the correspoinding phases. Note that all the nearfield patterns are all approximately Gaussian in shape, and that the phase fronts are nearly linear over the region of appreciable light intensity.

region of appreciable light intensity. The linear phase variation reflects the fact that power flows from the high gain region of a mode towards a low gain region (the phase fronts of a gain guided mode are curved for a similar reason.$^{(\S 2.6, 3.5(c))}$) The small amount of power which travels in the opposite lateral direction is described by the term of Equation (5.10.7) which we neglected, and contributes to farfield emission at an angle $-\Theta_\nu$ off-axis. Thus it is the *asymmetry* of the lateral gain profile which is responsible for suppressing the farfield emission at $-\Theta_\nu$ and leads to the off-axis single lobed farfield patterns characteristic of linear tailored gain semiconductor lasers. Higher order terms in the expansion of Equation (5.10.8) lead to slightly asymmetric nearfield patterns with some curvature in the phase fronts.

The fact that the nearfield patterns of all of the modes are single lobed is a direct result of the fact that the path $\mathcal{L}$ is constrained by the argument of the cube root of $(-i)$ in Equation (5.5.7) for the high gain modes to make an angle of $-30°$ with the real axis, and so (see §5.8) the point of peak intensity χ_ν lies well within a Stokes region. This allowed $\mathrm{Ai}(z)$ to be expressed in terms of a single exponential in Equation (5.10.12). Since a single exponential term has no zeros (except at infinity) the nearfield pattern cannot have any nulls. The null-less nearfield patterns are therefore a direct result of the Stokes phenomenon. We will discuss this point further in §5.11.

The experimental nearfield patterns of Figure 5.3 show a structure similar to the mode patterns of Figure 5.7. However, it should also be noted that the effect of filamentation$^{(\S 1.2(a.i))}$must be included in the discussion of the above-threshold experimental results. The role of filamentation in an asymmetric linear tailored gain laser is a complicated one, and is beyond the scope of this thesis.

The nearfield patterns of the low order eigenmodes of the tailored gain broad area lasers considered here are strongly localized near the left edge of the guide, and are hence relatively unaffected by the gain distribution in the right half of the guide. The eigenvalues and nearfield patterns of the low order modes on the (+) branch will not be significantly affected if the the guide is truncated in a region where the field does not penetrate. The critical guide width ℓ^* is approximately given by

$$\begin{aligned}\ell^* &\equiv \chi_\nu + 2w_\nu \\ &\simeq \frac{\sqrt{3}}{2}\frac{r_\nu}{|\omega|} + 2\frac{(2r_\nu)^{1/4}}{|\omega|} \quad .\end{aligned} \tag{5.10.13}$$

If ℓ is sufficiently greater than ℓ^* so that part of the waveguide is pumped below transparency (but above $-\Gamma_e$), the optical field of the low order modes will not extend into that region, and the injected carriers will be wasted. This will tend to both raise the threshold currents and lower the differential quantum efficiency. These effects will be discussed further in §5.14.

§5.11 Farfield Patterns

Once $E_\nu(x)$ has been found to have such a simple form, it is easy to find the mode's farfield pattern. In the Fraunhofer approximation, the farfield pattern $F_\nu(\theta)$ is given by the square of the Fourier transform of $E_\nu(x)$ times an obliquity factor $\cos\theta$.[7] The wide asymmetric tailored gain broad area lasers of interest here have very narrow farfield patterns near the axis, and thus the obliquity factor may be ignored. The electric field $E_\nu(x)$ in Equation (5.10.10) is the product of two functions of the spatial variable x. Making use of the shift and convolution Fourier

Transform theorems,[8] the intensity farfield pattern may be written as

$$\begin{aligned} F_\nu(\theta) &= \left|\mathcal{F}\{e^{-(x-\chi_\nu)^2/2w_\nu^2}\} \star \mathcal{F}\{e^{i\phi_\nu(x-\chi_\nu)}\}\right|^2 \\ &= \left|e^{-\theta^2/4\Sigma_\nu^2} \star \delta(\theta-\Theta_\nu)\right|^2 \\ &= e^{-(\theta-\Theta_\nu)^2/2\Sigma_\nu^2} \end{aligned} \tag{5.11.1}$$

where $\mathcal{F}\{\}$ denotes a $(-i)$ Fourier Transform,(§2.6) $\star$ denotes the convolution operation, and the emission angle Θ_ν and beamwidth Σ_ν are given by

$$\begin{aligned} \Theta_\nu(^\circ) &= \left(\frac{180}{\pi}\right)\frac{\phi_\nu}{k_0} = \left(\frac{180}{\pi}\right)\left[\left(\frac{r_\nu}{2}\right)^{1/2} - \frac{1}{2r_\nu}\right]|\omega| \\ \Sigma_\nu(^\circ) &= \left(\frac{180}{\pi}\right)\frac{1}{k_0}\frac{1}{w_\nu} = \left(\frac{180}{\pi}\right)\frac{|\omega|}{k_0(2r_\nu)^{1/4}} . \end{aligned} \tag{5.11.2}$$

Intensity farfield patterns for the (−) branch may be calculated similarly, and are, in fact, identical (except for an unimportant global phase factor) to those on the (+) branch.

Figure 5.16 summarizes the nearfield and farfield patterns for the first three modes on each branch. We see that the farfield patterns for all modes are single lobed, and approximately Gaussian in shape, in agreement with Equation (5.10.12).

Of some practical importance is the fact that the farfield patterns of the higher order modes on the (+) branch are only slightly displaced from the fundamental. From (5.9.3) and (5.11.2) we see that the emission angle Θ_ν of the higher order modes scales approximately as $\nu^{\frac{1}{3}}$. Thus, when gain saturation at high power operation causes many lateral modes to lase, the beamwidth will degrade gradually, becoming slightly broader and shifting very slightly in angle. This analytical result is borne out by the experimental data of Figure 5.3.

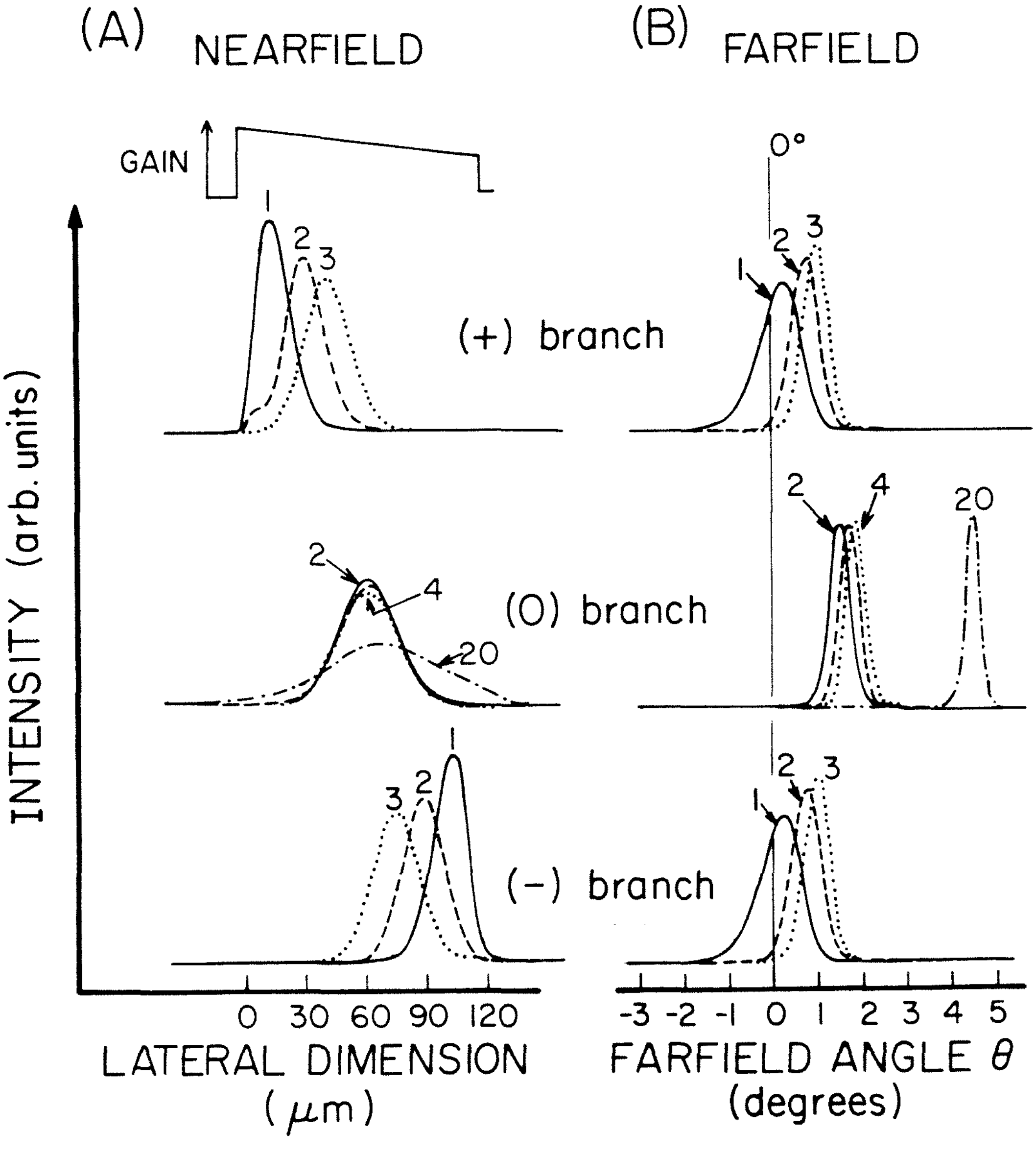

FIGURE 5.16 Summary of nearfield and farfield patterns for all branches of the asymmetric linear tailored gain waveguide (a) intensity nearfield patterns (b) intensity farfield patterns.

§5.12 Effect of Fourier Transform Symmetry Relations on Farfield Patterns

In this work, we have considered several examples from each of the four general classes of waveguides: real index guided symmetric (§2.6), real index guided asymmetric (§4.3 & §5.3), gain guided symmetric (§2.6), and gain guided asymmetric (§5.5 to §5.11). We have seen that with the exception of the asymmetric gain waveguide, all the higher order modes of the other waveguides have nulls in their nearfield patterns and symmetric, multilobed farfield patterns.

The particularly interesting property that the farfield patterns of asymmetric tailored gain waveguide are all single lobed and asymmetric about 0° is the result of some fundamental Fourier Transform relations which relate a mode's nearfield patterns to its farfield pattern.

Let us consider symmetry and asymmetry as it relates to Fourier Transform pairs. It is easy to understand why symmetry in the nearfield pattern of either a real index guided or gain guided waveguide results in a symmetric farfield pattern, but less easy to understand why an *asymmetric* real index guided waveguide should have a *symmetric* farfield pattern.

One possible approach would be to quote the Fourier Transform theorem which states that the power spectrum of a real valued function is symmetric in the transform plane.[9] If the indices of refraction of the waveguide are real, so also will be the electric field, and hence the farfield pattern must be symmetric.

However, it is possible to give a much more satisfying answer that is based on physical principles. The nulls in a mode's nearfield pattern result from the complete destructive interference of two waves of equal amplitude (*cf.* Equation (2.7.1), (5.10.1), or the zig-zag ray model[10] for a real index box waveguide).

§5.12 Effect of Fourier Transform Symmetry Relations on Farfield Patterns

Inside any waveguide, the optical field may be considered as a Fourier superposition of many plane waves, each traveling at an angle $\theta = \sin^{-1} \bar{k}/k_0$ relative to the axis of the guide. In a real index guided waveguide for which there is no gain or loss, there can be no power flow perpendicular to the waveguide axis (because of total internal reflection at an index step, or because of ray bending in a nonuniform real index media such as the quadratic index fiber).[11] Thus, the magnitude of a Fourier component at $+k$ must be precisely equal to the magnitude of the corresponding component at $-k$, where k is the lateral wavevector in the x direction. The vector sum of the two then has no component perpendicular to the waveguide axis, so that the sum of the components of all the waves moving in $+x$ direction must equal the sum of the components of the waves moving in $-x$ direction. This in turn leads to complete cancellation (*i.e.*, nulls) in the electric field at isolated points, and explains the nulls in the nearfield pattern of any real index guided waveguide.

Furthermore, since the waveguide's farfield pattern is essentially given by the Fourier Transform of the nearfield pattern, the equality condition on the Fourier components mentioned above implies that the farfield patterns of a real index guided laser must be symmetric about $\theta = 0°$ — even if the waveguide is *asymmetric.* A symmetric farfield pattern implies a single lobed (more precisely, a null-less) farfield pattern for the fundamental mode (because all Fourier components interfere constructively along $\theta = 0°$). Since the *Fourier Transform* of a high order mode must be orthogonal to that of the fundamental mode, the farfield pattern of the high order mode must contain at least one null — *i.e.*, it is multilobed. We therefore see that the requirement that there be no power flow perpendicular to the axis of a real index guided waveguide implies multilobed farfield patterns for the higher order modes, even if the nearfield pattern is asymmetric, as in the case of the chirped array of Figure 4.2 or the real ramp waveguide of Figure 5.4.

The case of an *asymmetric complex valued function* such as that of an asymmetric (not necessarily linear) gain induced waveguide is very different. As we have seen, the electric field is now a *complex* quantity, and there is in general no symmetry relation between an asymmetric complex valued function and its Fourier Transform.[9] This makes possible the unique nearfield and farfield patterns of the linear asymmetric tailored gain waveguides.

First consider the null-less nearfield patterns. Mathematically, Equation (5.10.1) represents two superimposed traveling waves. Since the exponential function itself has no zeros, the zeros of the asymptotic representation of $\mathrm{Ai}(z)$ result from the complete cancellation when the two terms of (5.10.1) have equal magnitude and opposite phase. This can occur only when $\mathcal{L}$ lies along the Stokes line on the negative real axis and implies that $\psi \propto \bar{\bar{\omega}} = 0$, which in turn can only occur if there is no gain or loss—*i.e.*, in a real index waveguide. For an asymmetric gain induced waveguide for which $\psi \neq 0$, the path of the argument to $\mathrm{Ai}(z)$ will not lie along a Stokes line (negative real axis), and cannot pass through a zero of $\mathrm{Ai}(z)$. As we remarked earlier, $\mathcal{L}$ near the peak in the nearfield intensity is restricted to lie in a Stokes region, and therefore since ψ depends only upon the slope of the gain gradient σ and not upon the eigenvalue η, the higher order modes of an asymmetric linear gain induced waveguide will not have nulls in the nearfield patterns.

The farfield patterns are given by the Fourier Transform of Equation (5.10.1). We showed that the Stokes phenomenon allowed dropping one of the terms in this equation. This led to the expression (5.10.12) for the electric field as a Gaussian times an exponential of a linear phase term ϕ. If we had kept the other term in

Equation (5.10.1), we would arrive at the same result with ϕ replaced by $-\phi$; *i.e.*, power would be radiated at $-\theta$. The fact that the the latter beam is suppressed is directly due to the necessity for power to flow from the high gain region of the mode to the low gain region(§5.10). This is reflected mathematically in the tilted phase fronts arising from the effect of the Stokes phenomenon which comes into play because of the complex nature of the electric field in a gain guided laser and the lack of left-right inversion symmetry in the asymmetric linear tailored gain waveguide.

It is a very beautiful thing to see such an abstract mathematical concept as the Stokes phenomenon come to life in the laboratory every time we increase the current to a tailored gain broad area laser and see a narrow, single lobed farfield pattern such as that of Figure 5.3.

§5.13 Measurement of the Antiguiding Parameter

In the interest of simplicity, the preceding analysis considered only the case of a pure gain waveguide with no index variation within the waveguide. In actual devices, however, the effect of gain created by the carriers in the active region gives rise to a change in the real part of the refractive index within the waveguide through both the free carrier plasma effect and the band-edge effect.[12] In a semiconductor laser, this relationship between the real and imaginary parts of the complex index of refraction is usually assumed to be linear. The effect of the antiguiding parameter b on the eigenmodes may be determined by recalling the definition of σ in Equation (5.5.2), *viz.* $\sigma = -s(b+i)$. Rewriting σ as

$$\sigma(b) = \sigma(0)\,(1 - ib) \tag{5.13.1}$$

then

$$\begin{aligned} \omega(b) &= \omega(0)\,(1-ib)^{1/3} \\ |\omega(b)| &= |\omega(0)|\;(1+b^2)^{1/6}\;. \\ \angle\omega(b) &= \angle\omega(0) - \frac{1}{3}\tan^{-1}b \end{aligned} \tag{5.13.2}$$

Aside from a slight increase in its length, the principal effect on $\mathcal{L}$ (which is of length $|\omega\ell|$ and makes an angle $\psi = \angle\omega$ with the real axis) is a clockwise rotation about $-r_\nu$ of $\frac{1}{3}\tan^{-1}b$ radians. The expression for the eigenvalues on the $(\pm)$ branch becomes slightly more complicated:

$$\eta_\nu^{(\pm)} \simeq n_{\binom{0}{\ell}} \mp \left|\frac{\sigma}{2n_0}\right|^{1/3} e^{-i\Phi^{(\pm)}}\, r_\nu \tag{5.13.3}$$

where $\Phi^{(\pm)} = \frac{2}{3}\tan^{-1}b \pm \frac{\pi}{3}$. The mode discrimination for the $(\pm)$ branch becomes

$$\Delta\gamma_\nu^{(\pm)}(b) = (1+b^2)^{1/3}\left[\cos\varphi \pm \frac{1}{\sqrt{3}}\sin\varphi\right]\Delta\gamma_\nu^{(\pm)}(0) \tag{5.13.4}$$

where $\varphi = \frac{2}{3}\tan^{-1}b$. When compared with the special case of no index antiguiding, for $b = 2.5$, the mode discriminations on the $(+)$ branch are increased by a factor of about two. The cluster of modes centered about the middle of the guide (*i.e.*, the (0) branch) is relatively insensitive to the effect of the antiguiding parameter. The number of modes on the $(+)$ branch actually decreases with increasing b, consistent with the notion that index antiguiding should shift the high-gain modes towards the lower-gain regions of the waveguide.

Mathematically, the effect of antiguiding on the nearfield patterns may be qualitatively determined with the aid of Figure 5.17 and a simple geometrical argument. As b increases from 0, the angle that $\mathcal{L}$ makes with the real axis increases. As a result, $\mathcal{L}$ becomes tangent to the level lines of $\mathrm{Ai}(z)$ at a point further removed from $x = 0$, implying that the position χ_ν of the maximum intensity of E has shifted towards the low gain side of the waveguide. Furthermore, as these latter level lines are less strongly curved than those near the origin, the

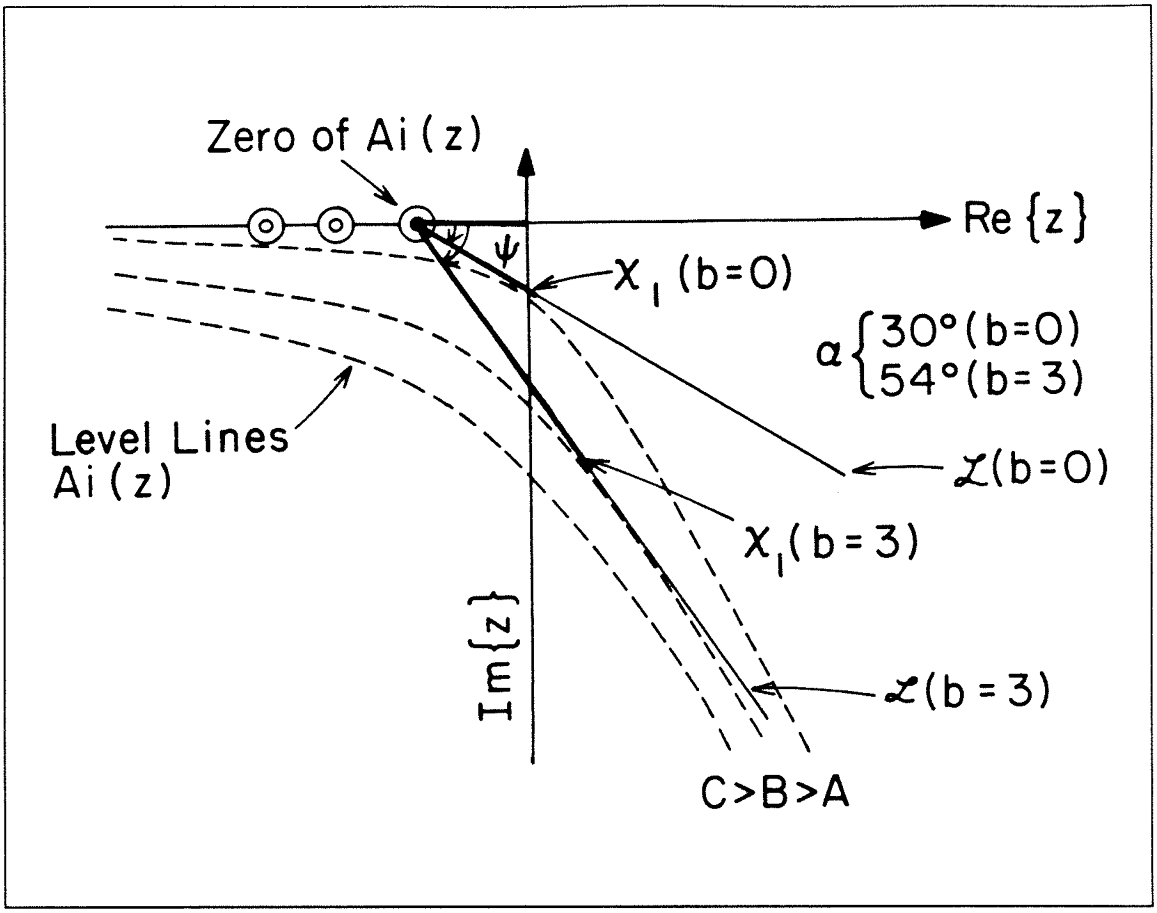

FIGURE 5.17 Effect of the antiguiding factor on the path of the argument to the Airy function throughout the complex plane. The line $\mathcal{L}$ rotates about $-r_n$ and slightly changes its length.

width of the mode increases as well. Nearfield profiles along the two lines of Figure 5.17 are compared in Figure 5.18.

When the antiguiding factor is included, the farfield beamwidth remains approximately constant because the increase in the width of the nearfield is offset by an increase in the phase curvature. The major effect of antiguiding on the farfield patterns is to shift Θ_ν to larger angles. Θ_ν is a sensitive function of b, and therefore knowledge of the guide parameters (made possible via the halftone process described in §5.2) allows a determination of the antiguiding factor.

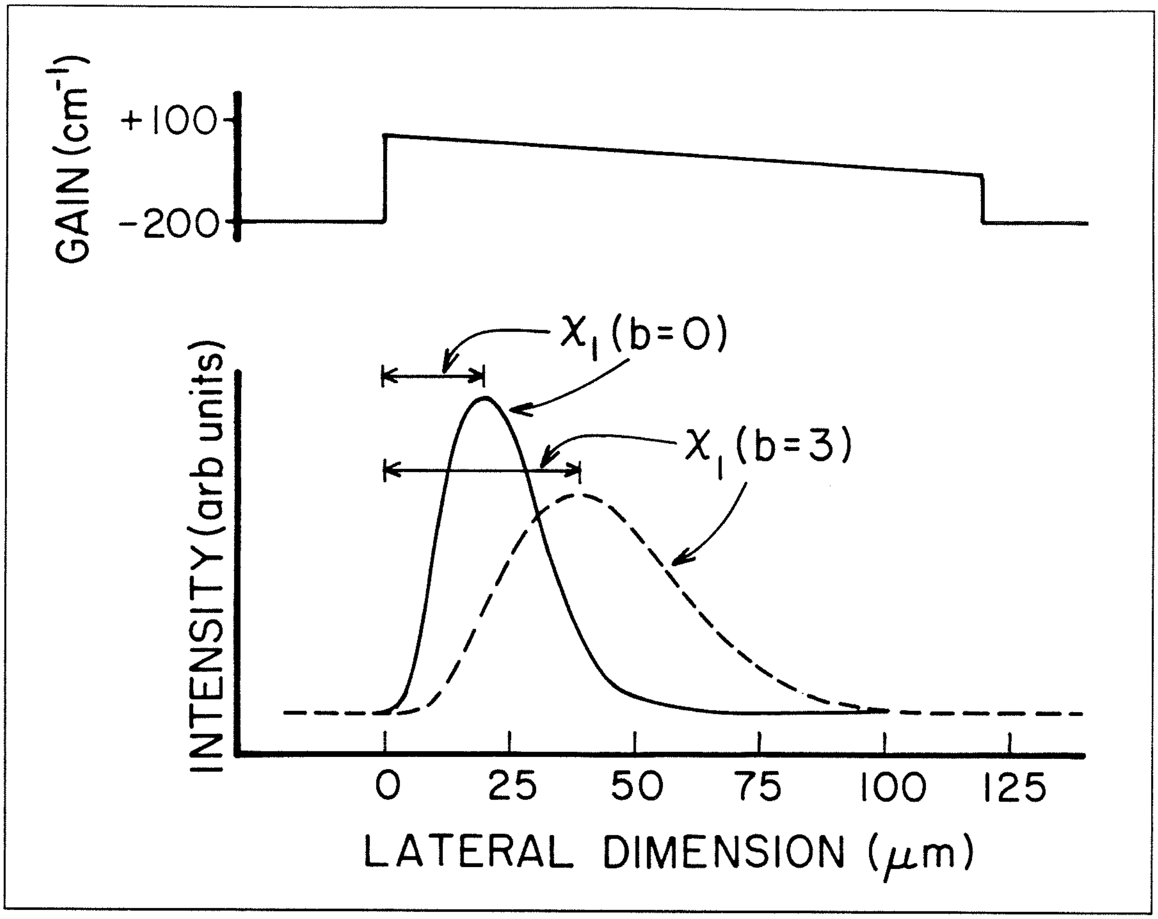

FIGURE 5.18 Effect of the antiguiding factor on the nearfield patterns. Antiguiding causes the mode move towards the center of the waveguide and its width to broaden slightly.

To make an experimental determination of the antiguiding factor it is necessary to know the values of the three parameters Γ_0, Γ_ℓ, and ℓ which define the parameter s in Equation (5.5.3). The constant Γ_0 is fixed by the requirement that at threshold the modal gain of the lasing mode $\gamma_1^{(+)}$ must precisely equal the sum of losses, which are principally due to the mirrors, and are typically about 40cm^{-1} for a device 250μm long. Γ_0 is then given by inverting Equation (5.9.6). We estimate Γ_ℓ by measuring the gradient of the spontaneous emission profile just below threshold. In an asymmetric tailored gain halftone laser in which the fraction of injecting contact varies between 100% at the left edge of the laser and 0% at the right edge, light will be emitted only where the gain is greater than zero. Knowledge of the gradient of the spontaneous emission pattern, Γ_0, and the width of the device ℓ (which is determined by photolithography) then allows estimation of Γ_ℓ. Assuming for simplicity a linear gain-carrier relationship gives $\Gamma_\ell \simeq -170 \pm 20\text{cm}^{-1}$.

The position of the off-axis farfield beam position $\Theta_1^{(+)}$ as a function of the antiguiding factor b may be computed numerically. Figure 5.19 plots the theoretically expected emission angles for several values of the antiguiding factor along with experimental data from halftone asymmetric tailored gain lasers with differing gain gradients. We find a value $b = 2.5 \pm 0.5$, which is consistent with earlier published results.

§5.14 Design Considerations for Tailored Gain Broad Area Lasers

In §5.10 we determined the minimum width ℓ^* of a waveguide in terms of the number of modes we wanted to be well-confined. If the width of the guide is made larger than ℓ^*, carriers that are injected to the right of ℓ^* will not contribute to the optical output near threshold, thus leading to unnecessarily high thresholds and low quantum efficiencies.

This is confirmed experimentally by Figure 5.20 which plots the excess current above threshold $I - I_{th}$ *versus* the optical power emitted per facet for pulsed, low duty cycle operation of lasers similar to that of Figure 5.2 for several gain gradients s. The total (two mirror) differential quantum efficiency η_{ext} is also indicated. As expected, η_{ext} increases as the width of the laser decreases. We therefore see that it is advantageous to decrease the width of the laser.

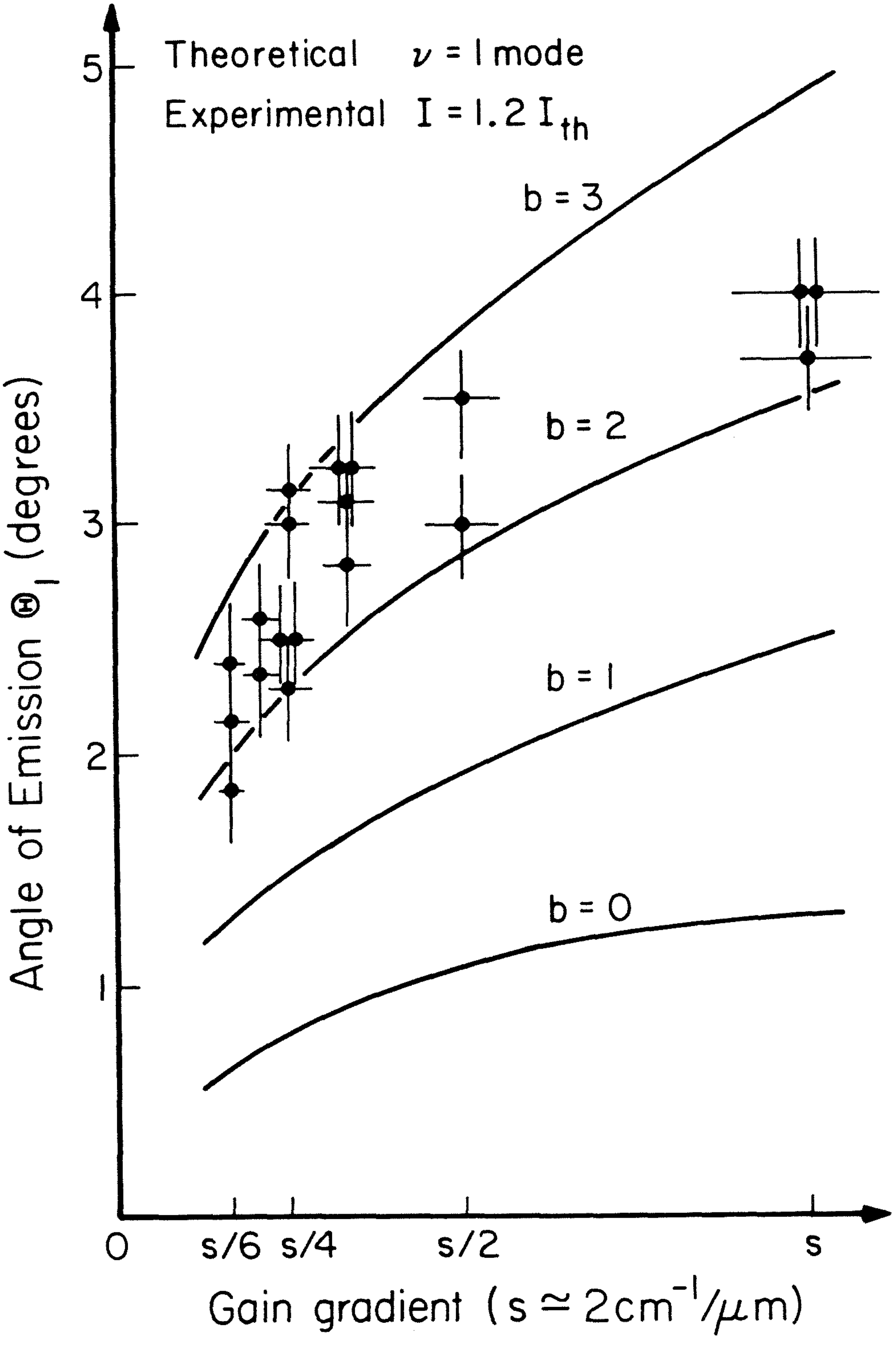

FIGURE 5.19 Experimental determination of the antiguiding factor. Solid line: Plot of the beam emission angle Θ as a function of the antiguiding parameter and spatial gain gradient. The experimental data points fit $b = 2.5 \pm 0.5$, in agreement with previously published results.

§5.14 Design Considerations for Tailored Gain Broad Area Lasers

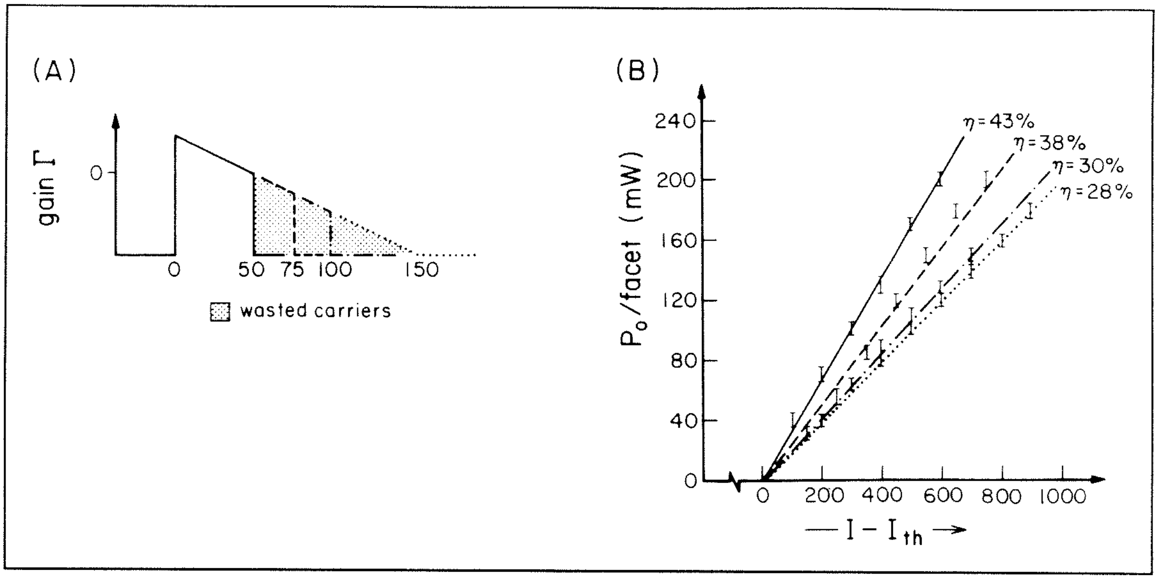

FIGURE 5.20 Light-Current curves for tailored gain broad area lasers. (a) Waveguide model for various truncated waveguides. The shaded areas represent regions of the waveguide which are pumped below transparency, and therefore waste carriers. (b) Experimental light-current curves showing variation of two mirror differential quantum efficiency η as a function of device width. Truncated lasers have higher differential quantum efficiencies because fewer carriers are wasted; they are, however, less resistant to the effects of gain saturation at high power.

Decreasing the width of the laser is roughly equivalent to decreasing the gain gradient across the laser, both of which decrease the product $\omega\ell$ and shorten the path $\mathcal{L}$. Equation (5.8.1) shows that, as $\omega\ell$ decreases, the contribution of Bi(z) increases, and so it is no longer possible to use Path Analysis. We therefore resort once again to the numerical methods of §2.7 to calculate the eigenvalues and eigenmodes.

We have seen that the beneficial effects of both good mode discrimination between the fundamental and the higher order modes, and the single lobed nature of the farfield result from the gain tailoring across the laser waveguide. Above threshold gain saturation will reduce the gain in the regions of high optical intensity (*i.e.*, the high gain side of the waveguide),[13] effectively reducing the gain gradient. While this will not affect the single lobed farfield pattern of the $\nu = 1$ mode, it will add a sidelobe to the $\nu = 2$ farfield pattern.

In any waveguide, the $\nu = 1$ mode is always single lobed. In all except a strongly asymmetric tailored gain waveguide, the $\nu = 2$ mode has a twin lobed farfield pattern, and is thus primarly responsible for the degradation of the single lobed farfield beam. Figure 5.21 presents a numerical study of the effect of a decrease in the amount of gain tailoring on the single lobed nature of the farfield pattern by plotting the farfield pattern of the $\nu = 2$ mode for various values of the gain gradient.

The mode discrimination between the fundamental and the $\nu = 2$ mode is also shown. We see the rather remarkable result that even when the gain tailoring amounts to only $\frac{20}{260} = 8\%$ of the total possible value, the suppression of the sidelobe at $-\theta$ as a result of the Stokes phenomenon is very good indeed. This figure shows that a little bit of gain tailoring goes a long way towards bringing about a single lobed farfield pattern.

The mode discrimination for this case has *decreased* to only 2.7cm^{-1}; this implies that this mode will start lasing just above threshold. The actual effects of gain saturation must be determined by carrying out a simultaneous solution of the rate equations and the Helmholtz equation.[14] However, we can arrive at a qualitative feeling for the situation by considering the waveguides of Figure 5.22a.

Figure 5.22a shows a waveguide with a very small amount of gain tailoring. The unsaturated waveguide is shown in the heavy solid line, and the mode shape in the light solid line. The increased stimulated emission resulting from the high intensity regions of the modal field will deplete the carriers, thereby changing the shape of the gain induced waveguide. We can then roughly approximate the gain profile of the saturated guide by the dotted line. (The actual situation is much

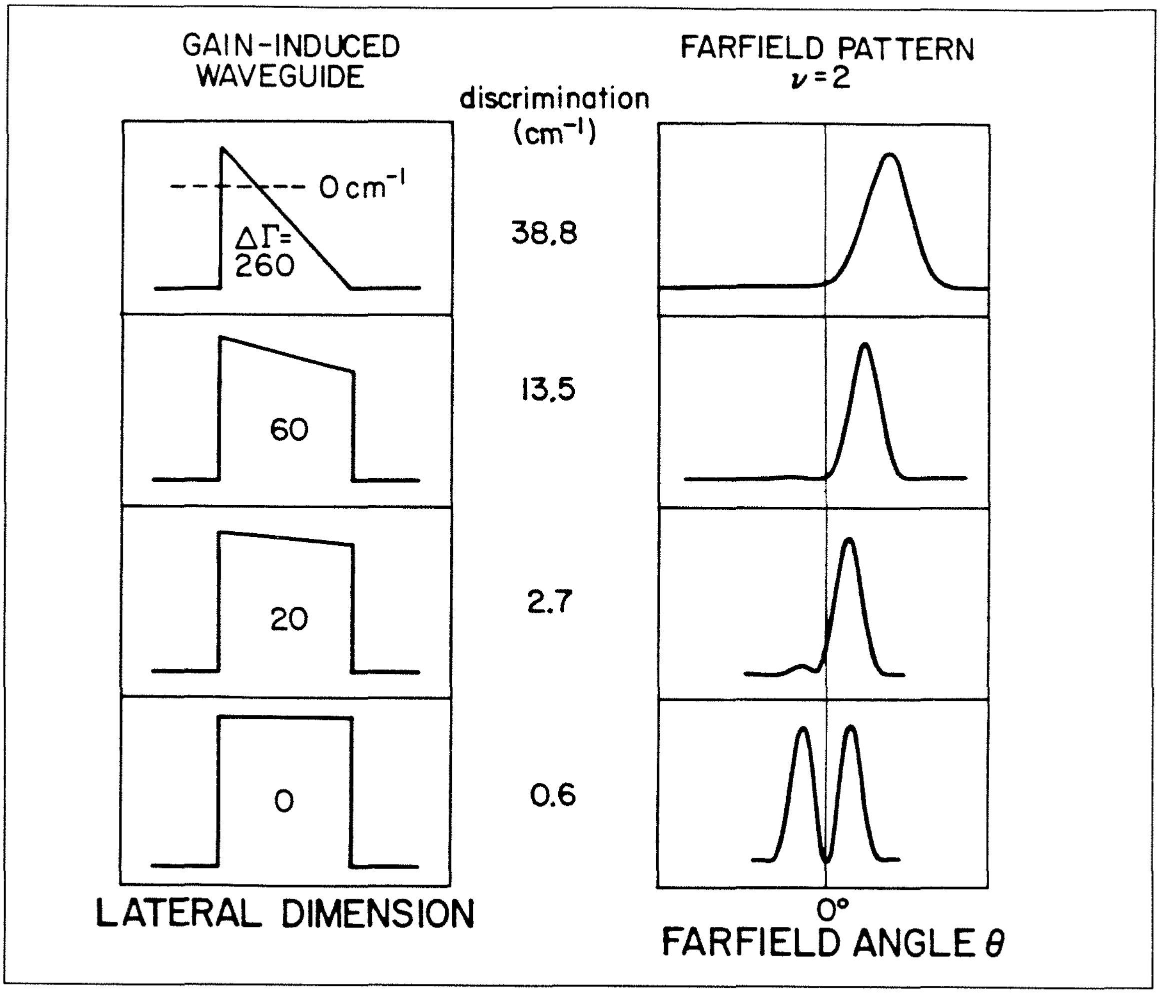

FIGURE 5.21 Design considerations for tailored gain broad area lasers: mode discrimination. The figure shows the suppression of the sidelobe of the $\nu = 2$ mode by the Stokes phenemonon for various values of the gain gradient. The number inside the waveguide gives the gain gradient in cm^{-1}. Notice that even a small amount of gain tailoring is sufficient to suppress the sidelobe.

more complicated, and beyond the scope of this thesis.) The farfield patterns corresponding to the unsaturated and saturated waveguides are shown in the right half of the figure. Once again, we consider the $\nu = 2$ mode. We see that a small $\omega\ell$ product due to either a truncated guide or a small gain gradient combined with gain saturation over a large fraction of the guide leads to multilobed farfield patterns.

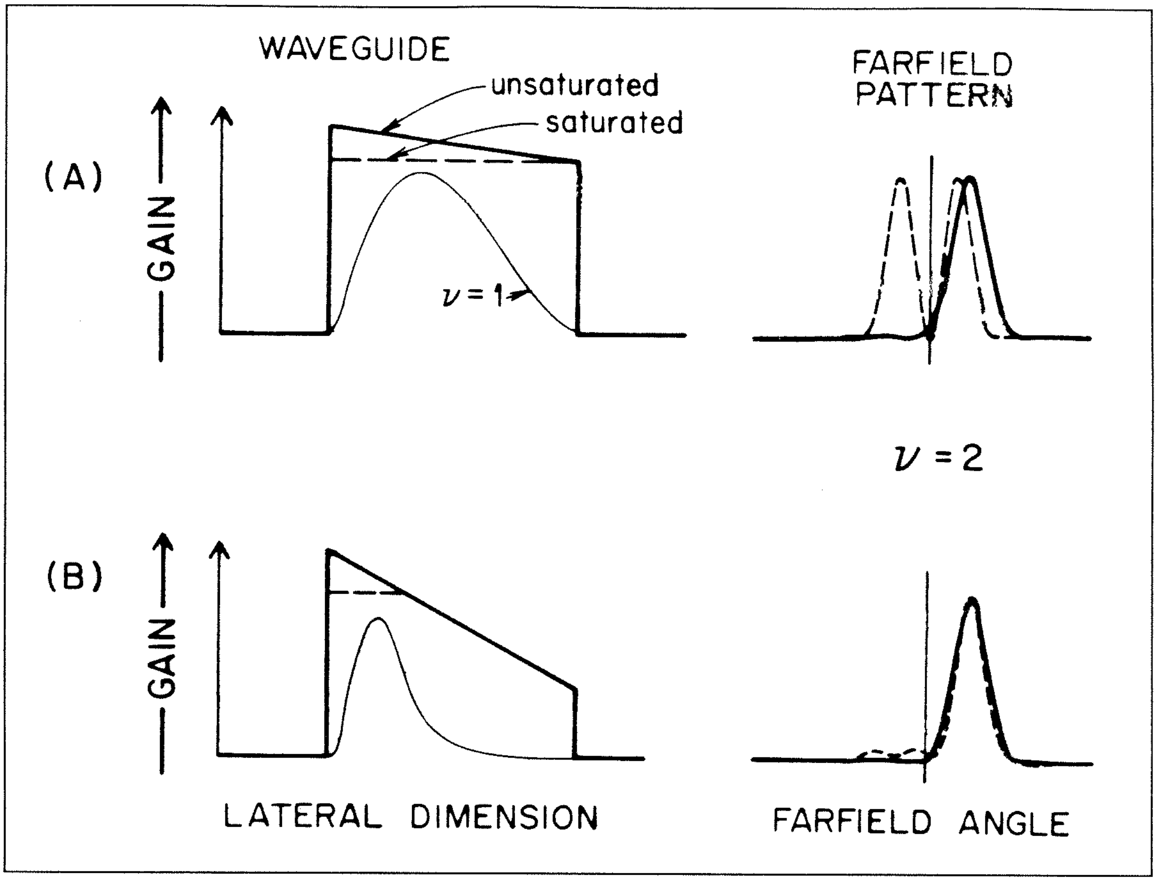

FIGURE 5.22 Effect of gain saturation on the farfield pattern of the $\nu = 2$ mode. (a) weak gain tailoring (b) strong gain tailoring. Notice that increased gain tailoring gives better resistance to gain saturation.

Figure 5.22b presents another unsaturated guide (heavy solid line) and saturated guide (light solid line), but this time with a steeper gain gradient. We see that the corresponding farfield patterns are both essentially single lobed. Waveguides with increased gain gradients are therefore less susceptible to the effects of gain saturation than are guides with smaller gradients.

We can therefore summarize some of the engineering tradeoffs which need to be considered when designing asymmetric tailored gain broad area lasers.

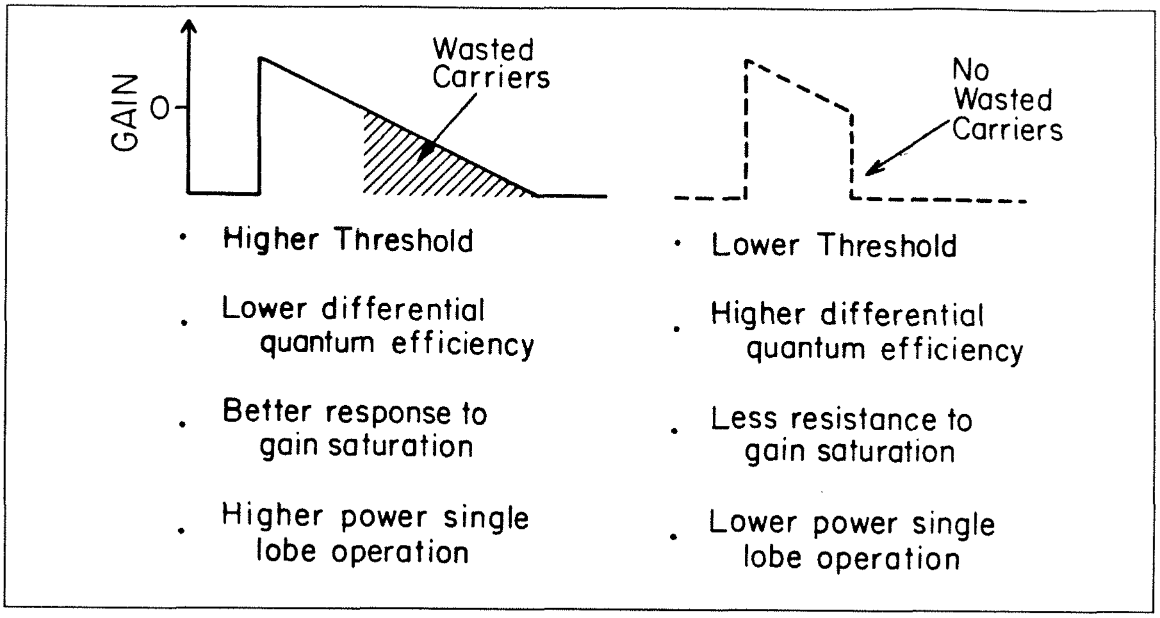

FIGURE 5.23 Design tradeoffs for tailored gain broad area lasers. (a) Nontruncated waveguide (solid line) truncated waveguide (dashed line). (b) Design tradeoffs.

These considerations are summarized in Figure 5.23, and have been borne out by experimental study. Nontruncated waveguides (solid line Figure 5.23a) offer better response to gain saturation and better high power single lobe operation, but have higher threshold currents and lower differential quantum efficiencies. On the other hand, truncated waveguides (dashed line, Figure 5.23b) offer lower threshold currents and higher differential quantum efficiencies but are less resistant to the effects of gain saturation and will give relatively low power single lobed operation.

§5.15 Conclusion

In conclusion, we have come full circle. We started by stating that a uniform gain *broad area laser* was unsuitable for many applications due to the filamentation and lateral mode control problems.$^{(\S 1.2(a))}$ The filamentation problem was solved by using an array structure,$^{(\S 1.2(c))}$ while the lateral mode control problem was solved by introducing gain tailoring.$^{(\S 4.5(b))}$ However, we discovered that in order to make gain tailoring work, it was necessary to increase the interchannel gain to the point where the device resembled a broad area laser more than it did an array.(§3.2(*c*)) We then demonstrated a tailored gain ***broad area laser*** (!) which is capable of single lobed, high power operation.(§5.2)

It is interesting to note that, although we began by assuming that an array was necessary for high power operation, we have found that the introduction of gain tailoring makes the array structure superfluous. In fact (as we showed in §4.5) it may be that since the modulation of the laser's nearfield pattern introduced by the array structure increases the power present in the sidelobes and decreases the ability of the device to operate in a phased locked mode, it may well be advantageous to consider other structures that resemble broad area lasers more than they do arrays of individual lasers. In particular, it would be very interesting to combine our work with gain tailoring with new methods of tailoring the *real* part of the refractive index to create *tailored index tailored gain* broad area lasers that would potentially combine some of the benefits of both real index and gain guiding. Furthermore, in one sense what we have done in this thesis is essentially to *redefine* the maximum upper width of a semiconductor laser from 10μm – 15μm to perhaps 60μm – 100μm. One might then speculate about the possibility of creating ***arrays*** of ***broad area*** semiconductor lasers!

However, one crucial question remains unanswered: What is the role of filamentation in a tailored gain broad area laser? Do filaments exist at all, and if so, why do they not they degrade device performance? Unfortunately, the resolution of these exceedingly interesting questions is beyond the scope of this thesis.

Appendix

Computer Program to Calculate Eigenvalues of a One Dimensional Waveguide

(see §2.7)

```
c   GUTS OF MODES PROGRAM by Chris Lindsey, Applied Physics Department
c   Caltech 128-95 Pasadena CA 91125  or Polaroid Corp, Cambridge, MA
c
c complex dispersion function
c
c  input complex effective index cneff     [exp(+i beta z) convention]
c  output value of complex dispersion function cdisp
c
      complex*16  function  cdisp(cneff
     &              index, t, nregion, k0)
      implicit real *8 (a-h), (o-z)
      complex *16 index(nregion)   ! complex refractive indicies
      real *8 t(nregion)           ! thickness of each region
      complex*16 k(nregion)
      complex *16 cneff, cdisp
      complex *16 neff2, arg
      complex*16 i / (0.0,1.0d0) /
      complex*16 m(2,2), mt(2,2)
      neff2 = cneff**2
      do 1 L = 1, nregion   ! calculate lateral kvectors in each region
        k(L) = k0 * sqrt (index(L)**2 - neff2)
    1 continue
      call interface (m, k, 1)   ! calculate propagation matricies
      do 2 L = 2, nregion-1
        call freespace (mt, k, t, L)
        call mult22r (mt,m)      ! m = mt * m
        call interface (mt, k, L)
        call mult22r (mt,m)
    2 continue
      cdisp = m(2,2)
      return
      end
c
      subroutine interface (mt, k, L)
      implicit real*8 (a-h), (o-z)
      complex*16 mt(2,2), k(L+1)
      integer L
      complex*16 ct
      ct = k(L) / k(L+1)
      mt(1,1) = ( 1.0 + ct ) / 2.0
      mt(1,2) = ( 1.0 - ct ) / 2.0
      mt(2,1) = mt(1,2)
      mt(2,2) = mt(1,1)
      return
      end
c
```

```
        subroutine freespace (mt, k, t, L)
        implicit real*8 (a-h), (o-z)
        complex*16 mt(2,2), k(L), ct
        real *8 t(L)
        integer L
        complex*16 i / (0,1.0d0) /
        mt(1,2) = 0.0
        mt(2,1) = 0.0
        ct = i * k(L) * t(L)
        mt(1,1) = exp ( ct )
        mt(2,2) = 1.0 / mt(1,1)
        return
        end
c
        subroutine mult21 (m, a, b)     ! matrix multiplication routines
        implicit real*8 (a-h), (o-z)
        complex*16 m(2,2)
        complex*16 a,b
        complex*16 an, bn
        an = m(1,1) * a + m(1,2) * b
        bn = m(2,1) * a + m(2,2) * b
        a = an
        b = bn
        return
        end
c
        subroutine mult22r (ml, mr)    ! mr = ml * mr
        implicit real*8 (a-h), (o-z)
        complex*16 ml(2,2), mr(2,2), a, b, c, d
        a =  ml(1,1)*mr(1,1) + ml(1,2)*mr(2,1)
        b =  ml(1,1)*mr(1,2) + ml(1,2)*mr(2,2)
        c =  ml(2,1)*mr(1,1) + ml(2,2)*mr(2,1)
        d =  ml(2,1)*mr(1,2) + ml(2,2)*mr(2,2)
        mr(1,1) = a
        mr(1,2) = b
        mr(2,1) = c
        mr(2,2) = d
        return
        end
c
c  calculate electric field
c
        subroutine efield (npoints, x, xleft, xright,
     &                    e, neff, wavelength)

        implicit real*8 (a-h), (o-z)
        integer npoints               ! number of x,e data points
        real*8 x(npoints)             ! put x values here starting at
        real*8 xleft, xright          ! xleft & ending at
                                      ! <thickness of guide> + xright
        complex*16 e(npoints)         ! electric field
        complex*16 neff               ! effective index of mode
```

```
        real*8 wavelength              ! wavelength in microns
        complex*16 neff2, cdisp, a, b, ekp, ekx
        complex*16 mi(2,2), mf(2,2)
        complex*16  enorm, enorml, enormr
        real*8 mag2
        if (abs(cdisp(neff)) .gt. .01) ! set up kvectors & see if root
     &     type *, 'efield: cdisp <> 0', neff, cdisp(neff)
        tsum = xleft + xright
        do 2 kr = 2, nregion-1
          tsum = tsum + t(kr)
    2   continue

        t(1) = 0.0d0
        t(nregion) = 1.1 * xright
        dx = tsum / (npoints-1)
        xx = - xleft - dx
        xt = xx
        kr = 1
        a = dcmplx (0.0d0,0.0d0)
        b = dcmplx (1.0d0,0.0d0)
        enorm = 0.0d0                 ! normalization
        enorml = mag2(b) / dimag ( 2.0d0 * k(1) )
        do 200 kp = 1, npoints
          xx = xx + dx
          xt = xt + dx
          x(kp) = xx
          if (xt .le. t(kr)) go to 210
c here if we pass into a new region
            call freespace (mf, k, t, kr) ! propagate over free space region
                                          !    we just passed through
            call interface (mi, k, kr)    ! then through the interface
            call mult22r (mi, mf)
            call mult21 (mf, a, b)        ! get new a,b coefficients
            kr = kr + 1
            xt = 0.0d0
  210     ekx = exp ( dcmplx(0.0d0,xt) * k(kr) )
          ekp = a * ekx + b / ekx
          if ((kr.ne.1).and.(kr.ne.nregion))
     &                    enorm=enorm+ekp*conjg(ekp)
          e(kp) = ekp
  200   continue
        enorm = enorm * dx      ! numerical integral
        enormr = mag2(a) / (2.0d0 * dimag(k(nregion)))  ! analytic integrals
        enorm = enorm + enorml + enormr
        enorm = sqrt ( enorm )
        do 300 kp = 1, npoints
          e(kp) = e(kp) / enorm
  300   continue
        return
        end
```

```
c
c FARFIELD PATTERN   (uses IMSL routines)
c
        subroutine farfield (x,nearfield,np,theta,fi,nfp,cut,
     &                       lambda,cwork,npoints)
c
c  x(np)           real*8      array of x data values for nearfield points
c  nearfield(np)   complex*16  array of nearfield electric field points
c  np              integer     number of nearfield points (200 suggested)
c  theta(nfp)      real*4      theta values for farfield
c  fi(nfp)         real*4      farfield intensity pattern
c  nfp             integer     number of points in farfield
                               !   (20*np or 4000 suggested)
c  cut             real*8      threshold value for plot (0.01 suggested)
c  lambda          real*8      wavelength in microns
c  cwork           complex*16  working array
c  npoints         integer     number of points in working array
                               !   (10*np or 2000 suggested)
c
        parameter PWORK = 200
        implicit real*8 (a-h), (o-z)
        real*8 x(np), lambda, mag2
        complex*16 nearfield(np), cwork(npoints)
        real theta(*), fi(*)
        integer iword
        equivalence (work(1),iwork(1))
        real*8 work(PWORK)
        integer iwork(PWORK)
        radtodeg = 180.0d0 / acos(-1.0d0)

        nextra = (npoints - np) / 2 ! get extra resolution by padding with
        do 101 j = 1, nextra        ! zeros to the left and right of the
  101   cwork(j) = dcmplx(0.0d0,0.0d0)  ! waveguide
        l = 0
        do 102 j = nextra+1, nextra+np
        l = l + 1
  102   cwork(j) = nearfield(l)
        do 103 j = nextra+np+1, npoints
  103   cwork(j) = dcmplx(0.0d0,0.0d0)

        dx = x(2) - x(1)
        xr = (npoints-1) * dx
        fmax = 1.0d0 / ( 2.0d0 * dx )
        df = 2 * fmax / (npoints-1)
        if (iword(npoints) .gt. PWORK) pause 'farfield: work too small!'
        call fftccm (cwork, npoints, iwork, work) ! complex FFT

        fnorm2 = 0.0d0  ! find areas where there is appreciable power
        do 210 j = 1, npoints/2
          save = mag2 (cwork(j+npoints/2))
          cwork(j+npoints/2) = dcmplx ( mag2(cwork(j)),0.0d0)
          cwork(j) = dcmplx (save, 0.0d0)
```

```
          if (save .gt. fnorm2) fnorm2 = save
          if (dreal(cwork(j)) .gt. fnorm2) fnorm2 = dreal(cwork(j))
  210   continue

        flim = 1.0/lambda   ! sin(90)/lambda
        jl = flim / df - 1
        j1m = max ( npoints/2 - jl +1  ,  1  )
        j2m = min ( npoints/2 + jl     ,  npoints  )
        nfpm = 2 * jl
        cutoff = cut * fnorm2
        do 221 j1 = j1m, npoints/2
          if (dreal(cwork(j1)) .gt. cutoff) go to 222
          if (dreal(cwork(npoints-j1+1)) .gt. cutoff) go to 222
  221   continue
  222   j2 = npoints - j1 + 1

        nfp = j2 - j1 + 1

        l = 0
        do 223 j = j1, j2
          l = l + 1
          sf = (l - nfp/2) * df
          sint = sf * lambda
        if (sint .gt. 1.0d0) type *, 'sint .gt. 1'
          cos2 = 1.0d0 - sint**2
          fi(l) = cos2 * dreal(cwork(j))/fnorm2
  223   continue

        do 224 l = 1, nfp
          sf = (l - nfp/2) * df     ! spatial frequency
          sint = sf * lambda
          if (abs(sint) .gt. 1.0d0) sint = sign (1.0d0,sint)
          theta(l) = asin (sint) * radtodeg
  224   continue
        return
        end

c compute minus i transform req'd by exp(i beta z) convention

        subroutine fftccm (cwork, npoints, iwork, work)
        complex*16 cwork(*)
        integer npoints, iwork(*)
        real*8 work(*)
        do 10 i = 1, npoints
10      cwork(i) = conjg(cwork(i))
        call fftcc (cwork, npoints, iwork, work)
        do 20 i = 1, npoints
20      cwork(i) = conjg(cwork(i))
        return
        end
```

References

Chapter 1

[1] A. L. Schawlow and C. H. Townes, *Phys. Rev.*, **112**, p. 1940, 1958.

[2] T. H. Maiman, "Stimulated Optical Radiation in Ruby Masers," *Nature*, **187**, p. 493, 1960.

[3] R. N. Hall, G. E. Fenner, J. P. Kingsley, T. J. Soltys, and R. O. Carlson, *Phys. Rev. Lett.*, **9**, p. 336, 1962.

[4] M. I. Nathan, W. P. Dumke, G. Burns, F. N. Dill, and G. J. Lasher, *Appl. Phys. Lett.*, **1**, p. 62, 1962.

[5] M. Holonyak and S. F. Beuacqua, *Appl. Phys. Lett.*, **1**, p. 82, 1962.

[6] T. M. Quist, R. H. Rediker, R. J. Keyes, W. E. Kray, R. Lax, A. L. McWhorter, and H. J. Zeigler, *Appl. Phys. Lett.*, **1**, p. 91, 1962.

[7] I. Hayashi, M. B. Panish, W. W. Foy, and S. Sumski, "Junction Lasers Which Operate Continuously at Room Temperature," *Appl. Phys. Lett.*, **17**, p. 109, 1970.

[8] D. Botez, *Appl. Phys. Lett.*, **36**, p. 190, 1980.

[9] W. T. Tsang and R. A. Logan, *Elect. Lett.*, **18**, p. 845, 1982.

[10] H. D. Wolf, K. Mettler, K. H. Zshaure, *Jap. J. Appl. Phys*, **20**, p. L693, 1981.

[11] M. W. Fleming and A. Mooradian, *Appl. Phys. Lett.*, **38**, p. 511, 1981.

[12] J. Salzman, T. Venkatesan, R. Lang, M. Mittelstein, and A. Yariv, "Unstable Resonator Semiconductor Cavity Lasers," *Appl. Phys. Lett.*, **46***(3)*, pp. 218-220, 1 February, 1985.

[13] D. Botez and D. E. Ackley, "Phase-Locked Arrays of Semiconductor Diode Lasers," *IEEE Circuits and Devices Magazine*, **2***(1)*, pp. 8-17, January, 1986.

References for Chapter 1

[14] F. E. Birbeck, "A Gallium Arsenide Laser Array for Communications," *J. Sci. Instr. (J. Phys E, Series 2)*, pp. 788-790, 1968.

[15] D. R. Scifres, W. Streifer, and R. D. Burnham, "Beam Scanning and Wavelength Modulation With Branching Waveguide Stripe Injection Lasers," *Appl. Phys. Lett.*, **33***(7)*, pp. 616-618, 1 October, 1978.

[16] D. R. Scifres, R. D. Burnham, and W. Streifer, "Phase-Locked Semiconductor Laser Array," *Appl. Phys. Lett.*, **33***(12)*, pp. 1015-1017, 15 December, 1978.

[17] D. R. Scifres, W. Streifer, and R. D. Burnham, "Experimental and Analytic Studies of Coupled Multiple Stripe Diode Lasers," *J. Quant. Elect.*, **QE15***(9)*, pp. 917-922, September, 1979.

[18] D. R. Scifres, R. D. Burnham, and W. Streifer, "High Power Coupled Multiple Stripe Quantum Well Injection Lasers," *Appl. Phys. Lett.*, **41***(2)*, pp. 118-120, 15 July, 1982.

[19] D. R. Scifres, C. Lindstroem, R. D. Burnham, W. Streifer, T. L. Paoli, *Elect. Lett.*, **19**, p. 170, 1983.

[20] G. L. Harnagel, D. R. Scifres, H. H. Kung, D. F. Welch, D. P. Worland, P. S. Cross, and R. D. Burnham, paper #ThDD3, presented at Integrated and Guided Wave Optics Conference, Atlanta, Georgia, February 26-28, 1986.

[21] Donald Ackley, "High-Power Multiple-Stripe Injection Lasers With Channel Guides," *J. Quant. Elect.*, **QE18***(11)*, pp. 1910-1917, November, 1982.

[22] D. E. Ackley and R. W. H. Engelmann, "High-Power Leaky-Mode Multiple-Stripe Laser," *Appl. Phys. Lett.*, **39***(1)*, pp. 27-29, 1 July, 1981.

[23] E. Kapon, J. Katz, A. Yariv, "Supermode Analysis of Phase-Locked Arrays of Semiconductor Lasers," *Optics Lett.*, **9**, pp. 125-127, April, 1984.

[24] E. Kapon, C. Lindsey, J. Katz, S. Margalit, and A. Yariv, "Chirped Array of Diode Lasers for Supermode Control," *Appl. Phys. Lett.*, **45***(3)*, pp. 200-202, 1 August, 1984.

[25] C. P. Lindsey, E. Kapon, J. Katz, S. Margalit, and A. Yariv, "Single Contact Tailored Gain Phased Array of Semiconductor Lasers," *Appl. Phys. Lett.*, **45***(7)*, pp. 722-724, 1 October, 1984.

[26] D. F. Welch, D. Scifres, P. Cross, H. Kung, W. Streifer, R. D. Burnham, J. Yaeli, and T. L. Paoli, "High Power CW Operation of a Phased Array Diode Laser With Diffraction Limited Output Beam," *Appl. Phys. Lett.*, **47***(11)*, pp. 1134-1136, 1 December, 1985.

[27] Chris Lindsey, Pam Derry, and Amnon Yariv, "Fundamental Lateral Mode Oscillation via Gain Tailoring in Broad Area Semiconductor Lasers," *Appl. Phys. Lett.*, **47***(6)*, pp. 560-562, 15 September, 1985.

[28] C. Lindsey, P. Derry, and A. Yariv, "Tailored Gain Broad Area Lasers With Single Lobed Farfield Patterns," *Elect. Lett.*, **21***(16)*, pp. 671-673, 1 August, 1985.

[29] Chris Lindsey, David Mehuys, and Amnon Yariv "Tailored Gain Chirped Array and Broad Area Lasers," to be published in *J. Quantum Electron.*

[30] R. A. Smith, *Semiconductors, 2nd ed.*, Cambridge Univ. Press, Cambridge, Gr. Br., p. 309, 1978.

[31] A. Yariv, *Quantum Electronics, 2nd ed.*, John Wiley & Sons, New York, p. 176, 1975.

[32] T. Tamir, *Integrated Optics, 2nd ed.*, Springer-Verlag New York, Chapter 2 1979.

[33] A. Yariv, *Introduction to Optical Electronics 3rd ed.*, Holt, Rinehart & Winston, New York, p. 88, 1985.

References for Chapter 1

[34] G. H. B. Thompson, *Physics of Semiconductor Laser Devices*, John Wiley & Sons, New York, p. 226, 1980.

[35] G. H. B. Thompson, "A Theory for Filamentation in Semiconductor Lasers Including the Dependence of the Dielectric Constant with the Injected Carrier Density," *Opto-Electronics*, **4**, pp. 257-310, 1972.

[36] Yariv, *Quantum Electronics* [31], p. 545.

[37] Thompson [34], p. 535.

[38] William Streifer, Robert D. Burnham, and Don R. Scifres, "Symmetrical and Asymmetrical Waveguiding in Very Narrow Conducting Stripe Lasers," *J. Quant. Elect.*, **QE15***(3)*, pp. 136-141, March, 1979.

[39] Thompson [34], p. 380.

[40] H. C. Casey and M. B. Panish, *Heterostructure Lasers A:Fundamental Properties B:Materials and Operating Characteristics*, Academic Press, Inc., New York, p. B278, 1978.

[41] Thompson [34], p. 196.

[42] Casey and Panish [40], p. 75.

[43] R. N. Bracewell, *The Fourier Transform and its Applications, 2nd ed.*, McGraw Hill Book Co., New York, 1978.

[44] E. Kapon, J. Katz, C. Lindsey, S. Margalit, and A. Yariv, "Control of Mutual Phase Locking of Monolithically Integrated Semiconductor Laser Arrays," *Appl. Phys. Lett.*, **43***(5)*, pp. 421-423, 1 September, 1983.

[45] H. Tempkin, R. A. Logan, J. P. Van der Ziel, C. L. Reynolds, Jr., and S. Tharldsen, "Index Guided Arrays of Schottky Barrier Confined Lasers," *Appl. Phys. Lett.*, **46***(5)*, p. 465, 1 March, 1985.

[46] Frank Stern, "Calculated Spectral Dependence of Gain in Excited GaAs," *J. Appl. Phys.*, **47***(12)*, pp. 5382-5386, December, 1976.

References for Chapter 1

[47] C. H. Henry, R. A. Logan, and F. R. Merritt, "Measurement of Gain and Absorbtion Spectra in AlGaAs Buried Heterostructure Lasers," *J. Appl. Phys.*, **51***(6)*, pp. 3042-3050, June, 1980.

[48] Joseph Katz, Eli Kapon, S. Margalit, and Amnon Yariv, "Rate Equation Analysis of Phase Locked Semiconductor Laser Array Under Steady State Conditions," *J. Quant. Elect.*, **QE20***(8)*, pp. 875-879, August, 1984.

[49] J. Katz, E. Kapon, C. Lindsey, S. Margalit, U. Shreter, and A. Yariv, "Phase-Locked Semiconductor Laser Array With Separate Contacts," *Appl. Phys. Lett.*, **43***(16)*, pp. 521-523, 15 September, 1983.

[50] Chris Lindsey, unpublished; D. F. Welch, private communication.

[51] Kressel and Butler, *Semiconductor Lasers and Heterojunction LEDs*, Academic Press, New York, 1977.

[52] Casey and Panish [40], p. A81.

[53] William Streifer, Robert D. Burnham, and Don R. Scifres, "Symmetrical and Asymmetrical Waveguiding in Very Narrow Conducting Stripe Lasers," *J. Quant. Elect.*, **QE15***(3)*, pp. 136-141, March, 1979.

[54] Dietrich Marcuse *Theory of Dielectric Optical Waveguides*, Academic Press Inc., New York, 1974.

[55] Dietrich Marcuse, *Light Transmission Optics, 2nd ed.*, Van Nostrand, New York, 1982.

[56] M. B. Panish, "Heterostructure Injection Lasers," *IEEE Transactions on Microwave Theory and Techniques*, **MTT23(1)**, 1 January, 1975.

Chapter 2

[1] H. C. Casey and M. B. Panish, *Heterostructure Lasers A:Fundamental Properties B:Materials and Operating Characteristics*, Academic Press, Inc., New York, p. A45, 1978.

[2] Casey and Panish [1], p. B193.

[3] G. H. B. Thompson, *Physics of Semiconductor Laser Devices*, John Wiley & Sons, New York, p. 196, 1980.

[4] William Streifer, Robert D. Burnham, and Don R. Scifres, "Symmetrical and Asymmetrical Waveguiding in Very Narrow Conducting Stripe Lasers," *J. Quant. Elect.*, **QE15***(3)*, pp. 136-141, March, 1979.

[5] Thompson [3], p. 293.

[6] Casey and Panish [1], p. B213.

[7] H. D. Wolf, K. Mettler, K. H. Zshaure, *Jap. J. Appl. Phys*, **20**, p. L693, 1981.

[8] Casey and Panish [1], p. B214.

[9] A. Yariv, *Introduction to Optical Electronics 3rd ed.*, Holt, Rinehart & Winston, New York, p. 352, 1985.

[10] E. Kapon, J. Katz, C. Lindsey, S. Margalit, and A. Yariv, "Control of Mutual Phase Locking of Monolithically Integrated Semiconductor Laser Arrays," *Appl. Phys. Lett.*, **43***(5)*, pp. 421-423, 1 September, 1983.

[11] H. Tempkin, R. A. Logan, J. P. Van der Ziel, C. L. Reynolds, Jr., and S. Tharldsen, "Index Guided Arrays of Schottky Barrier Confined Lasers," *Appl. Phys. Lett.*, **46***(5)*, p. 465, 1 March, 1985.

[12] Casey and Panish [1], p. A252.

[13] Casey and Panish [1], p. B215.

[14] Chris Lindsey, unpublished

References for Chapter 2

[15] D. Botez, J. C. Connolly, "High Power Phase-locked Arrays of Index Guided Diode Lasers," *Appl. Phys. Lett.*, **43***(12)*, 15 December, 1983.

[16] T. Tamir, *Integrated Optics, 2nd ed.*, Springer-Verlag, , New York, p. 62, 1979.

[17] Casey and Panish [1], p. B214.

[18] S. Mukai, C. Lindsey, J. Katz, E. Kapon, Z. Rav-Noy, S. Margalit, and A. Yariv, "Fundamental Mode Oscillation of a Buried Ridge Waveguide Laser Array," *Appl. Phys. Lett.*, **45***(8)*, pp. 834-835, 15 October, 1984.

[19] Casey and Panish [1], p. B212.

[20] Thompson [3], p. 300.

[21] William Streifer, Don R. Scifres, and Robert D. Burnham, "Analysis of Gain-Induced Waveguiding in Stripe Geometry Diode Lasers," *J. Quant. Elect.*, **QE14***(6)*, pp. 418-427, June, 1978.

[22] W. O. Schlosser, "Gain Induced Modes in Planar Structures," *The Bell Sys. Tech. J.*, **52***(6)*, July-August, 1973.

[23] Thompson [3], p. 291.

[24] M. C. Amman, *Elect. Lett.*, **15**, p. 441, 1979.

[25] Casey and Panish [1], p. B208.

[26] Casey and Panish [1], p. B207.

[27] H. Tempkin, R. A. Logan, J. P. Van der Ziel, C. L. Reynolds, Jr., and S. Tharldsen, "Index Guided Arrays of Schottky Barrier Confined Lasers," *Appl. Phys. Lett.*, **46***(5)*, p. 465, 1 March, 1985.

[28] T. Twu, K.-L. Chen, A. Dienes, S. Wang, and J. R. Whinnery, "High Performance Index Guided Phase-locked Semiconductor Laser Arrays," *Elect. Lett.*, **21***(8)*, pp. 324-325, 11 August, 1985.

[29] Casey and Panish [1], p. A34.

[30] Dietrich Marcuse, *Light Transmission Optics, 2nd ed.*, Van Nostrand, New York, pp. 275-282, 1982.

[31] Casey and Panish [1], p. A36.

[32] Casey and Panish [1], p. A37.

[33] Casey and Panish [1], Chapter 2

[34] Tamir [16], Chapter 2

[35] Dietrich Marcuse *Theory of Dielectric Optical Waveguides*, Academic Press Inc., New York, Chapter 2 1974.

[36] Yariv, *Intro. Optical Electronics* [9], p. 412.

[37] Casey and Panish [1], p. 75.

[38] R. N. Bracewell, *The Fourier Transform and its Applications, 2nd ed.*, McGraw Hill Book Co., New York, 1978.

[39] Thompson [3], p. 323.

[40] Eugen Merzbacher, *Quantum Mechanics, 2nd ed.*, John Wiley & Sons, New York, p. 93, 1970.

[41] P. Yeh, A. Yariv, and C. Hong, *J. Opt. Soc. A.*, **67**, p. 423, 1977.

Chapter 3

[1] A. Yariv, *Introduction to Optical Electronics, 3rd.*, Holt, Rinehart & Winston, New York, p. 413, 1985.

[2] Amnon Yariv, "Coupled Mode Theory for Guided Wave Optics," *J. Quant. Elect.*, QE9*(9)*, p. 919, September, 1973.

[3] Yariv, *Intro. Optical Electronics* [1], p. 437.

[4] E. Kapon, J. Katz, A. Yariv, "Supermode Analysis of Phase-locked Arrays of Semiconductor Lasers," *Optics Letters*, **9**, pp. 125-127, April, 1984.

References for Chapter 3

[5] C. H. Henry, R. A. Logan, and F. R. Merritt, "Measurement of Gain and Absorption Spectra in AlGaAs Buried Hetrostructure Lasers," *J. Appl. Phys.*, **51***(6)*, pp. 3042-3050, June, 1980.

[6] Claude Cohen-Tannoudji, Bernard Diu, Franck LaLoe, *Quantum Mechanics*, John Wiley & Sons, New York, p. 1100, 1972.

[7] Assem S. Deif, *Advanced Matrix Theory for Scientists and Engineers*, Halsted Press Division, John Wiley & Sons, New York, p. 206, 1982.

[8] Yariv, *Intro. Optical Electronics* [1], p. 414.

[9] Dietrich Marcuse, *Theory of Dielectric Optical Waveguides*, Academic Press Inc., New York, p. 19, 1974.

[10] CTDL [6], p. 1169.

[11] A. Hardy and W. Streifer, "Coupled Mode Theory of Parallel Waveguides," *J. Lightwave Tech.*, **LT-3***(5)*, p. 1135, October, 1985.

[12] T. Tamir, *Integrated Optics, 2nd ed.*, Springer-Verlag, , New York, pp. 22-25, 1979.

[13] Chris Lindsey and Eli Kapon, unpublished.

[14] CTDL [6], p. 192.

[15] Allan W. Snyder and John D. Love, *Optical Waveguide Theory*, Chapman and Hall, New York, Chapter 24, 1983.

[16] J. Katz, E. Kapon, C. Lindsey. S. Margalit, U. Streeter, and A. Yariv, "Phase-Locked Semiconductor Laser Array With Separate Contacts," *Appl. Phys. Lett.*, **43***(6)*, pp. 521-523, September, 1983.

[17] E. Kapon, C. Lindsey, J. Katz, S. Margalit, and A. Yariv, "Coupling Mechanism of Gain-Guided Integrated Semiconductor Laser Arrays," *Appl. Phys. Lett.*, **44***(4)*, pp. 389-391, 15 February, 1984.

Chapter 4

[1] E. Kapon, J. Katz, A. Yariv, "Supermode Analysis of Phase-locked Arrays of Semiconductor Lasers," *Optics Letters*, **9**, pp. 125-127, April, 1984.

[2] J. K. Butler, D. E. Ackley, D. Botez, "Coupled Mode Analysis of Phase-Locked Injection Laser Arrays," *Appl. Phys. Lett.*, **44***(3)*, 1 February, 1984.

[3] D. R. Scifres, W. Streifer, and R. D. Burnham, "Experimental and Analytic Studies of Coupled Multiple Stripe Diode Lasers," *J. Quant. Elect.*, **QE15***(9)*, pp. 917-922, September, 1979.

[4] E. Kapon, C. Lindsey, J. Katz, S. Margalit, and A. Yariv, "Chirped Array of Diode Lasers for Supermode Control," *Appl. Phys. Lett.*, **45***(3)*, pp. 200-202, 1 August, 1984.

[5] E. Kapon, J. Katz, C. Lindsey, S. Margalit, and A. Yariv, "Control of Mutual Phase Locking of Monolithically Integrated Semiconductor Laser Arrays," *Appl. Phys. Lett.*, **43***(5)*, pp. 421-423, 1 September, 1983.

[6] C. P. Lindsey, E. Kapon, J. Katz, S. Margalit, and A. Yariv, "Single Contact Tailored Gain Phased Array of Semiconductor Lasers," *Appl. Phys. Lett.*, **45***(7)*, pp. 722-724, 1 October, 1984.

[7] Chris Lindsey, Pam Derry, and Amnon Yariv, "Fundamental Lateral Mode Oscillation via Gain Tailoring in Broad Area Semiconductor Lasers," *Appl. Phys. Lett.*, **47***(6)*, pp. 560-562, 15 September, 1985.

[8] G. H. B. Thompson, *Physics of Semiconductor Laser Devices*, John Wiley & Sons, New York, p. 346, 1980.

[9] E. Kapon, J. Katz, C. Lindsey, S. Margalit, and A. Yariv, "Control of Mutual Phase Locking of Monolithically Integrated Semiconductor Laser Arrays," *Appl. Phys. Lett.*, **43***(5)*, pp. 421-423, 1 September, 1983.

[10] D. F. Welch, D. R. Scifres, P. Cross, W. Streifer, R. D. Burnham, and J. Yaeli, *Elect. Lett.*, **21***(14)*, p. 3, 4 July, 1985.

[11] D. F. Welch, D. Scifres, P. Cross, H. Kung, W. Streifer, R. D. Burnham, J. Yaeli, and T. L. Paoli, "High Power CW Operation of a Phased Array Diode Laser With Diffraction Limited Output Beam," *Appl. Phys. Lett.*, **47***(11)*, pp. 1134-1136, 1 December, 1985.

Chapter 5

[1] Carl M. Bender and Steven A. Orszag, *Advanced Mathematical Methods for Scientists and Engineers*, McGraw-Hill, New York, pp. 115-116, 1978.

[2] William Streifer, Don R. Scifres, and Robert D. Burnham, "Analysis of Gain-Induced Waveguiding in Stripe Geometry Diode Lasers," *J. Quant. Elect.*, **QE14***(6)*, pp. 418-427, June, 1978.

[3] C. Lindsey, P. Derry, and A. Yariv, "Tailored Gain Broad Area Lasers With Single Lobed Farfield Patterns," *Elect. Lett.*, **21***(16)*, pp. 671-673, 1 August, 1985.

[4] Bender & Orszag [1], p. 570.

[5] J. Buus, "Principles of Semiconductor Laser Modelling," *IEE Proc.*, **132J***(1)*, pp. 42-51, 1 February, 1985.

[6] Bender & Orszag [1], p. 520.

[7] H. C. Casey and M. B. Panish, *Hetrostructure Lasers A:Fundamental Properties B:Materials and Operating Characteristics*, Academic Press, Inc., New York, p. A75, 1978.

[8] R. N. Bracewell, *The Fourier Transform and its Applications, 2nd ed.*, McGraw Hill Book Co., New York, p. 122, 1978.

[9] Bracewell [8], p. 14.

References for Chapter 5

[10] T. Tamir, *Integrated Optics, 2nd ed.*, Springer-Verlag, , New York, p. 15, 1979.

[11] A. Yariv, *Quantum Electronics, 2nd ed.*, John Wiley & Sons, New York, p. 109, 1975.

[12] G. H. B. Thompson, *Physics of Semiconductor Laser Devices*, John Wiley & Sons, New York, p. 535, 1980.

[13] Thompson [12], p. 380.

[14] Joseph Katz, Eli Kapon, S. Margalit, and Amnon Yariv, "Rate Equation Analysis of Phase Locked Semiconductor Laser Array Under Steady State Conditions," *J. Quant. Elect.*, **QE20***(8)*, pp. 875-879, August, 1984.

Men passionately desire to live after death, but they often pass away without noticing the fact that the memory of a really good person always lives. It is impressed upon the next generation, and is transmitted again to the children. Is not that an immortality worth striving for?

—PETER KROPOTKIN
Memoirs of a Revolutionist